IMPERIAL COLLEGE LONDON

Department of Bioengineering

Investigating the impact of tibial malalignment in OA development in a mechanically induced rodent osteoarthritis model

Luyang (Leah) Xu

Supervised by Prof. Anthony MJ Bull

Submitted in part fulfilment of the requirements for the degree of Doctor of Philosophy in Bioengineering at Imperial College London and the Diploma of Imperial College London

August 2024

Declaration of Originality

I declare that this thesis and the research to which it refers are original and the products of my own work. Any work performed by individuals other than myself has been appropriately acknowledged and referenced.

Luyang (Leah) Xu

August 2024

Copyright Declaration

The copyright of this thesis rests with the author. Unless otherwise indicated, its contents are licensed under a Creative Commons Attribution-Non Commercial 4.0 International Licence (CC BY-NC).

Under this licence, you may copy and redistribute the material in any medium or format. You may also create and distribute modified versions of the work. This is on the condition that: you credit the author and do not use it, or any derivative works, for a commercial purpose.

When reusing or sharing this work, ensure you make the licence terms clear to others by naming the licence and linking to the licence text. Where a work has been adapted, you should indicate that the work has been changed and describe those changes.

Please seek permission from the copyright holder for uses of this work that are not included in this licence or permitted under UK Copyright Law.

Acknowledgements

First of all, I would like to express my gratitude to my supervisor, Prof. Anthony Bull, for his supervision, support, and assistance throughout my PhD. His guidance on both the research and my personal growth has profoundly influenced my work and perspective on life. The four years of study under his mentorship have been an unforgettable experience that I'm certain will benefit my future career and life.

I extend my thanks to all the researchers and support staff at Imperial College who have contributed in various ways to this project. It would be impossible to list everyone, but I am deeply appreciative of the ideas, energy, and enthusiasm that have been crucial in enabling me to complete my PhD.

This work was conducted under the auspices of the Royal British Legion Centre for Blast Injury Studies at Imperial College London. I would like to acknowledge the financial support of the Royal British Legion. I am grateful for the support provided by all involved, especially my second supervisor Dr. Xiancheng Yu, for his readiness to guide me through my PhD challenges, and for his technical advice and insightful discussions. Big thanks to Dr. Ibidumo Igah for his surgical expertise and technical guidance; despite his busy clinical schedule, he has always made time to assist me.

My thanks also go to my colleagues in the Musculoskeletal Mechanics group—Dr. Shuqiao Xie, Dr. Diana Toderita, Dr. Clement Favier, Ms. Yumou Han, Dr Zepur Kasezian, Dr. Pouya Amiri, Dr. Giovanni Milandri, Dr. Tjuy-Tien Nguyen—for their invaluable discussions and suggestions on biomechanics studies and computational simulations.

I have received tremendous support from many technicians across the Bioengineering Department. In particular, I want to thank Dr. Sharad Patel, Dr. Guthrie-Fenty, Kaisheri, Mr. Olivier Dubois, Mr. Joel Eustaquio, and Mr. Nana A. Asamoah-Danso for their technical advice and assistance. My appreciation also extends to the technicians and veterinarians at the Central Biomedical Services at Faculty of Medicine for their help with the animal research study, and to Dr. Nicoleta Baxan at the Biological Imaging Centre for her insightful suggestions.

To my dear friends, for their moral support, the enriching academic discussions that extended beyond our fields, and the countless hours we spent studying together after hours, I extend my sincere thanks. Special thanks to my friends from the Civil Engineering 403 study group—Dr. Chanjie Cui, Dr. Danhui Yang, Dr. Ying Zhang, and Dr. Zeren Jin —and to my friends in China for their emotional companionship during my PhD years. Last but certainly not least, my deepest gratitude goes to my family, who have been the greatest source of encouragement and motivation for me. Thank you.

Abstract

This study aimed to investigate the impact of tibial malalignment, a strong mechanical factor that occurs spontaneously, on the initiation and development of osteoarthritis (OA) in a rodent model. Different degrees of malalignment were induced to create a model of chronic primary OA resulting from natural chronic overloading, with varying levels of severity. This mechanically-induced model was then used to characterize OA in both early and progressive stages through histological cartilage degradation, radiographic structural changes, gait patterns, and cytokine levels, alongside pharmacological treatment effects.

Histological analyses revealed distinct changes in OA cartilage in response to tibial malalignment. Treatment with autologous protein solution (APS) resulted in cartilage that more closely resembled healthy tissue, while bone morphogenetic protein (BMP) treatment stimulated repair but also promoted chondrophyte formation. Micro-CT analysis highlighted adaptive changes in subchondral bone to accommodate the new mechanical demands of OA, including increased subchondral bone plate thickness, decreased trabecular bone volume fraction and trabecular bone thickness, increased trabecular spacing, and osteophyte formation. While BMP treatment showed potential for subchondral bone repair, it also appeared to stimulate osteophyte growth.

Gait analysis proved to be an effective method for distinguishing between different OA states and assessing recovery following pharmacological treatments. Key variables across all discrimination models for both limbs included Paw Area at Peak Stance (indicating weight support) and Max dA/dT (indicating gait coordination), which highlighted compensatory changes in the contralateral limb. Untargeted LFQ-MS proteomics reveals key biological processes such as collagen formation and degradation, endochondral ossification, and metabolic responses involved in OA pathogenesis.

This study successfully linked histological, structural, gait, and molecular changes to OA pathogenesis. It suggests that although early treatment with BMP and APS can mitigate OA progression by modulating these processes through different pathways, they cannot fully halt the progression if mechanical abnormalities persist.

Table of Contents

Declaration of Originality **2**

Copyright Declaration **3**

Acknowledgements **4**

Abstract **5**

1 Introduction **20**

1.1 Motivation and Objectives *20*

1.2 Chapter summary *20*

1.3 Osteoarthritis: an overview of the disease *21*

1.3.1 Epidemiology 21

1.3.2 Phenotypes 21

1.3.3 Diagnosis and risk factors 21

1.4 Biomechanical factors in OA onset *22*

1.5 Animal models of OA *26*

1.5.1 Classical animal models of OA 26

1.5.2 Biomechanical aspects on developing POA model 33

1.6 Pathophysiology of osteoarthritis *37*

1.6.1 Articular cartilage pathological degeneration and remodelling mechanism in OA 37

1.6.2 Subchondral bone defects and remodelling mechanism in OA 41

1.7 OA treatment *45*

1.8 Measures of disease outcome *47*

1.8.1 Histological measurement tools 47

1.8.2 Imaging measurement tools 48

1.8.3 Gait analysis and quantitative biomechanical markers 49

1.8.4 Biochemical markers 53

2 Surgical model development **55**

2.1 Summary *55*

2.2 Introduction *55*

2.2.1 Clinical use of high tibial osteotomy 55

2.2.2 TO used in animal model 56

2.2.3 Literature reviews of reported TO animal models 57

2.2.4 The chosen model to induce OA 58

2.3 Materials and Methods 59

2.3.1 Experimental groups and research design 59

2.3.2 Operative procedure 61

2.4 Results 66

3 Interventions to prevent OA 68

3.1 Summary 68

3.2 Introduction 68

3.3 Materials and methods 69

3.3.1 Blood fraction 69

3.3.2 Workflow for the Preparation of APS Injections 70

3.3.3 Intra-articular injection procedure 72

3.3.4 APS concentration quantitation via ELISA 72

3.4 Result 73

4 Histopathology analysis of assessing cartilage changes in OA 75

4.1 Summary 75

4.2 Introduction 75

4.3 Material and methods 76

4.3.1 Sample processing 76

4.3.2 Toluidine blue staining protocol. 78

4.3.3 Histopathology scoring of articular cartilage. 79

4.3.4 Statistical analysis 84

4.4 Results 84

4.4.1 Characterizing cartilage changes 84

4.4.2 Macroscopic changes and chondrophytes 88

4.4.3 Histological section evolution 89

4.5 Discussion 95

4.5.1 Cartilage degeneration in OA 95

4.5.2 Chondrocyte hypertrophic process and chondrocyte formation during cartilage repair 97

5 Micro CT imaging in characterising OA subchondral bone changes 100

5.1 Summary 100

5.2 Introduction 100

5.3 Material and methods 101
5.3.1 Micro-CT imaging protocol 101
5.3.2 Micro-CT image analysis 103
5.3.3 Statistical analysis 108
5.4 Result 109
5.4.1 Thresholding method comparison and selection 109
5.4.2 Detection of subchondral plate changes by micro-CT 110
5.4.3 Detection of trabecular bone changes by micro-CT 112
5.4.4 Osteophytes 117
5.4.5 Bone remodelling 119
5.5 Discussion 124
5.5.1 The biomechanical aspects of subchondral bone changes 124
5.5.2 The biomechanical aspects of osteophyte formation 126
5.5.3 The biomechanical aspect of loading with OA initiation 128
5.5.4 The biomechanical aspect of loading with bone remodelling 129
5.5.5 Conclusion 131
6 Gait analysis in characterising OA functional changes 132
6.1 Summary 132
6.1.1 Gait analysis in preclinical rat model 132
6.1.2 Spatiotemporal characterization 133
6.2 Materials and methods 137
6.2.1 Digigait imaging system 137
6.2.2 Digigait data processing system 137
6.2.3 *In vivo* data collection 139
6.2.4 Statistical methods 139
6.3 Results 143
6.3.1 Discrimination analysis between sham group, 30ºTO group, and treatment group 143
6.3.2 Discrimination analysis of 30ºTO group with other groups 152
6.3.3 Discriminate analysis between two treatment groups 157
6.4 Discussion 162
6.4.1 Further explanation of the contributory gait features in the discrimination model 163
6.4.2 Gait pattern changes depending on the model used to induce OA 165
6.4.3 Correlation of gait pattern changes with joint structural changes 167
7 Untargeted LFQ-MS proteomics approach in characterising OA cartilage and serum changes 169

7.1 Summary *169*

7.2 Introduction *169*

7.3 Methods *171*

7.3.1 Sample collection 171

7.3.2 Mass spectrometry sample processing 172

7.3.3 Proteomics 172

7.3.4 Data processing 172

7.3.5 Statistical methods 173

7.4 Results *177*

7.4.1 Enrichment analysis of OA cartilage 179

7.4.2 Upregulated pathways in BMP-treated cartilage 183

7.4.3 Upregulated pathways in APS-treated cartilage 189

7.5 Discussion *196*

7.5.1 Understanding enhanced biological processes in OA cartilage 197

7.5.2 Characterizing the effects of BMP treatment on OA cartilage biology 199

7.5.3 Exploring the role of APS treatment in regulating biological processes in OA cartilage 201

7.5.4 Characterizing the overloading effects on left medial compartment of OA cartilage 203

7.5.5 Proteomics results among different animal models. 204

8 Conclusion 207

8.1 Summary of findings *207*

8.2 Perspectives and future works *211*

8.2.1 Further development of chondrophytes as an OA marker in MRI imaging 211

8.2.2 Deepening the understanding of the gait characteristics in OA rat model 212

8.2.3 Deepening the understanding of OA pathogenesis from histology and proteomics perspective 213

8.2.4 Clinical translation 214

9 References 216

List of Figures

Figure 1-1: Biomechanical factors leading to osteoarthritis (OA). A. represents the healthy knee. B. femoral and tibial malalignment with resulting varus or valgus angulation and medial or lateral joint overload, C. quadriceps muscular weakness leading to muscle imbalance and local joint overload, D. meniscus injury leading to increased contact stress, E. ligament injury leading to changes in the overall knee mechanics. All of these will eventually contribute to increasing the mechanical stress on the healthy knee and induce joint structural changes, including cartilage loss, joint narrowing, osteophyte formation, and subchondral microfractures resulting in, F. arthritic knee. 25

Figure 1-2 Molecular components in the extracellular matrix (ECM) of articular cartilage. Articular hyaline cartilage consists of a single cellular component, chondrocyte, embedded in a complex matrix which mainly includes collagen II and the large aggregating proteoglycans (PGs). PGs have a protein core to which glycosaminoglycan molecules are covalently attached. Cartilage oligomeric matrix protein (COMP), functions as a molecular bridge by binding collagen II fibrils11. Integrin is the receptor of mechanical stress, causing stress-induced signalling directly.....38

Figure 1-3 Schematic representation of various insults causing intracellular signaling pathways that regulate the level of molecular expression in chondrocytes. 40

Figure 1-4 Hypothetical model of early and late-stage OA pathogenesis. Adapted from 'Subchondral bone in osteoarthritis: insight into risk factors and microstructural changes,' by Li et al., 2013. Available at https://doi.org/10.1186/ar4405.....43

Figure 1-5 Schematic diagram of endochondral ossification (created with BioRender.com) 45

Figure 2-1. High tibial osteotomy for knee osteoarthritis pain in active people: (a) in a varus knee, the load-bearing axis (mechanical axis, green line) goes through the medial compartment (orange line); HTO surgery is the removal of the bone indicated in red. (b) HTO realigns the weight-bearing axis of the lower limb towards the lateral compartment thereby decreasing contact pressures and loading transmission on the medial compartment and correcting the varus deformity. In some cases even where there is low varus deformity, HTO can still be used to offload the medial compartment.....56

Figure 2-2. Experimental groups and the timepoints of intervention (BMP-7, APS) and assessments.....61

Figure 2-3. Tibial osteotomy surgery using photographs by (Britzman, 2017). (a) A surgical plate is inserted against the lateral side of the tibia (lateral view), aligning the top edge as anterior on the tibia as possible. (b) Three holes are drilled through the top holes of the plate and through the tibia, acting as a guide for the osteotomy. (c) Using the middle of the plate as a guide, the tibia is cut from the medial side by saw and a 10° or 30° wedge is removed. (d) The five-hole plate is inserted into the lateral side of the tibia, thereafter 4 screws are inserted.....64

Figure 2-4. Photographs of dissected tibiae for the 0º TO, 10º TO, and 30º TO groups. 67

Figure 3-1. Workflow for the Preparation of APS Injections (a, b) Blood separation step: Images showing the different blood layers obtained from the density gradient centrifugation before and after spinning. (c) APS concentration step: Schematic illustrating the use of Amicon for APS concentration. (d) Schematic of the intra-articular injection process (Created with BioRender.com) 71

Figure 3-2. (a) The comparison of IL-1RA concentration in PRP and APS collected at week 0 (before surgery) and week 1 (after surgery). (b) The concentration of IL-1RA in APS during the first 12 weeks after surgery (n=4 for week 1, and n=6 for all other time points). 73

Figure 4-1: a. Histology sample preparation: the proximal tibia sample is halved across both compartments, b. Whole view of the slice after Toluidine-blue staining. 77

Figure 4-2. OA cartilage histopathology -- grading methodology, adapted from (Pritzker et al., 2006). 81

Figure 4-3. Histological section evaluation of one joint compartment of the rat with 30ºTO surgery (An example section is from the lateral compartment of a left leg A and right leg B in 30ºTO group). As shown, the entire cartilage is indicated by green tracing, and the cartilage lesion area is delineated by orange tracing. The tibial plateau is divided into three zones equally (marked by red vertical lines), with outer zone 3, central zone 2 and inner zone 1. 83

Figure 4-4: Toluidine-blue stained sections of representative left limb medial compartments from each experimental group at 5X objective magnification, scale bars = 500 µm. The cartilage of the (A) 0ºTO (sham) group, 10ºTO group, 30ºTO group, 10ºTO group with BMP treatment, 10ºTO group with BMP treatment, 30ºTO group with APS treatment, (B) Right limb medial compartment. 85

Figure 4-5: Toluidine-blue stained sections of representative left limb lateral compartments from 30ºTO group at 5X objective magnification, bars = 500 µm. 86

Figure 4-6 (Column A,B) Representative Toluidine-blue stained sections of left limb medial compartment from each experimental group at 5X objective. The boxed area in column B is further magnified (20× objective) in Column C,D. Scales bar: 100 µm (A, B), 20 µm (B, D). Columns A and B display sections from the same group, but the depth of the stain are different due to variations between different staining rounds. 88

Figure 4-7 Representative sections of left limb medial compartment from 0ºTO, 30ºTO, 30ºTO + BMP group at 20X objective in the same scale (bar = 20µm). The cartilage zones are indicated. This highlights the hypertrophic and fibrosis process observed in cartilage of both the 30ºTO and 30ºTO + BMP groups. ..88

Figure 4-8 Macroscopic changes in the articular cartilage of rats in each group. The arrows indicate a clear chondrophyte in the posterior side of the medial compartment. 89

Figure 4-9 Comparison of the histological OA grade among groups in left medial compartment (n = 9 from 3 biological independent rats per group, one-way ANOVA; ns, not significant; *p ≤0.05 ,p < 0.01, ***p<0.001, ****p<0.0001)....91**

Figure 4-10 Comparison of the histological OA stage among groups in left medial compartment (n = 9 from 3 biologically independent rats per group, one-way ANOVA; ns, not significant; *p ≤0.05 ,p < 0.01, ***p<0.001, ****p<0.0001)....92**

Figure 4-11 Comparison of the OA staging between 0ºTO, 30ºTO, 30ºTO + BMP, and 30ºTO + APS in corresponding zones (n = 9 from 3 biologically independent rats per group, one-way ANOVA; ns, not significant; *p ≤0.05 ,p < 0.01, ***p<0.001, ****p<0.0001). 93**

Figure 4-12. Comparison of the average histological OA score among groups in left medial compartment (n = 9 from 3 biological independent rats per group, one-way ANOVA; ns, not significant; *p ≤0.05 ,p < 0.01, ***p<0.001, ****p<0.0001) 95**

Figure 4-13. Schematic of healthy and OA cartilage structure (chondrocytes and collagen fibres). (a) the normal 'stable' articular chondrocytes in healthy articular cartilage; (b) the 'transient' phenotype cartilage in OA. In the cartilage from OA joint, there is chondrocyte hypertrophy and matrix mineralisation. In the deepest zone of cartilage. The calcified cartilage zone is increased. 96

Figure 5-1. Outline of the CT-measured regions in the study presented in this chapter. (a) transverse view of the proximal tibia (b) sagittal view of the proximal tibia 101

Figure 5-2. Micro-CT machine set up. (A) Inside view of Zeiss Versa 510 micro-CT machine (B) Schematic representation of a micro-CT imaging system (Created with BioRender.com). 103

Figure 5-3 Histogram depicting the image segmentation threshold for the "Bone" and "non-bone" areas. The threshold was set around the midpoint between the peaks representing "bone" and "non-bone" in the histogram. 103

Figure 5-4: Tibia trabecular bone ROI analysis: For BV/TV calculation. (A). Trabecular ROI region (pink) in sagittal slide of the 3D reconstruction image of proximal tibial plateau (B). Trabecular ROI region in axial slide of the 3D reconstruction. Red shape represent the hand-drawn ROI (C) A stack of manual region growth ROI for calculating BV/TV, with 3D rendering of the BV surface (yellow) and TV surface (blue) (Domander et al., 2021). For Tb.Th and Tb.Sp calculation. (D) Trabecular ROI regions (blue) in sagittal slide of the 3D reconstruction image of proximal tibial plateau (E) Trabecular ROI region in axial slide of the 3D reconstruction. (F) 3D rendering of the BV surface (yellow) and TV surface (blue) 105

Figure 5-5 Precise Sb.P thickness measurement method based on intensity profiles. (A) An example illustrating the process of drawing a vector line (profile line) from the selected point in each zone. The white ellipse highlights the subchondral plate region of interest (ROI). (B) A typical intensity profile obtained from example vector line, showing HU values from tibia cartilage to tibia bone, with P1 and P2 points indicated by vertical dashed yellow lines. The corresponding HU values are indicated by horizontal dashed yellow lines. The distance (in pixel number) between P1 and P2 represents the thickness of the trabecular plate at that specific point. (C) ① Increase stage: Vertical line 1 and vertical line 2 are placed at the start and end of the intensity increase stage, respectively. Line 2 and line 3 are set based on line 1 and line 2, respectively. P1 is determined as the position on the profile line where the HU value equals "50% (GV_{line1} + GV_{Line2})". ② Decrease stage: Vertical line 3 is positioned at the start of the intensity decrease stage in the intensity profile, while line 4 is placed at the end of the decrease stage. P2 is calculated as HU_{P2} = "50% (GV_{line3} + GV_{Line4})" 107

Figure 5-6. A typical cross section CT image (a) was analyzed using different thresholding method in Image J to determine their suitability for trabecular bone segmentation. The techniques analyzed were (b) manual thresholding (31442-65535), (c) Huang method (35549-65535), (d) Otsu method (30905-65535), (e) Default method (29165-65535) (f) Mean method (33808-65535). 110

Figure 5-7 Summary of subchondral plate thickness averaged across all zones (Sb.P) for all groups and both compartments (n = 9 from 3 biological independent rats per group, one-way ANOVA; ns, not significant; *p ≤0.05 ,p < 0.01, ***p<0.001, ****p<0.0001). 111**

Figure 5-8 Subchondral plate thickness (Sb.P) for all groups, zones and compartments (ns, not significant; *p ≤0.05 ,p < 0.01, ***p<0.001, ****p<0.0001). 111**

Figure 5-9. Comparison of BV/TV among groups in each compartment (ns, not significant; *p ≤0.05 ,p < 0.01, ***p<0.001, ****p<0.0001). 113**

Figure 5-10. Comparison of BV/TV among groups: (a) between compartments and (b) between limbs (ns, not significant; *p ≤0.05 ,p < 0.01, ***p<0.001, ****p<0.0001). 114**

Figure 5-11. Comparison of trabecular bone thickness (Tb.Th) among groups in each compartment (ns, not significant; *p ≤0.05 ,p < 0.01, ***p<0.001, ****p<0.0001). 115**

Figure 5-12. Comparison of trabecular thickness (Tb.Th) among groups: (a) between compartments and (b) between limbs (ns, not significant; *p ≤0.05 ,p < 0.01, ***p<0.001, ****p<0.0001) 116**

Figure 5-13. Comparison of trabecular spacing (Tb.Sp) among groups in each compartment (ns, not significant; *p ≤0.05 ,p < 0.01, ***p<0.001, ****p<0.0001) 116**

Figure 5-14. Comparison of of trabecular spacing (Tb.Sp) among groups: (a) between compartments and (b) between limbs (ns, not significant; *p ≤0.05 ,p < 0.01, ***p<0.001, ****p<0.0001) 117**

Figure 5-15. Representative micro-CT images of the tibial plateau: Each row shows the coronal view of the left limb, coronal view of the right limb, and axial view of the left limb. Osteophyte mineralization is indicated by the red arrows. Scale bar = 1000 µm. 118

Figure 5-16: Subchondral bone resorption in the BMP-treated left limb. The figure shows the same location in the image stack from three different views: coronal plane, sagittal plane, and axial plane of the left limb (from left to right). The red arrows indicate the area of subchondral bone resorption. 119

Figure 5-17. A. Three-dimensional (3D) reconstruction of the 30ºTO left limb using Mimics software revealed the site of the osteotomy incision (indicated by the blue arrow) and the tibia-fibula connecting area (indicated by the red arrow). Bone healing displayed a 30º-varus bone remodelling. The axial slices from micro-CT (A.1-4) provide detailed views of the healing stages. (A-3) The osteotomy area showed newly formed woven bone filling the osteotomy incision area. (A-2) Woven bone tissue was undergoing transformation into lamellar bone, with intact cortical bone visible. (A-1) Cortical bone regeneration was progressing, accompanied by the disappearance of woven tissue in the marrow area. (A-4) The tibia-fibula connecting area displayed an intramembranous ossification where woven bone tissue is generated around the old cortical bone and undergone resorption, cortical bone and lamellar bone was widely restored quickly and most of the bone tissue in the marrow space was resorbed B. Sagittal dissection images of the tibia bone in the 30ºTO left limb are presented, with corresponding histological sagittal slices (B.3-4). Toluidine-blue staining revealed the presence of cartilage tissue in the osteotomy incision area (B-3), while it was scarce in the tibia-fibula connecting area (B-4). Scale bar = 500 µm and 100 µm. 120

Figure 5-18. 3D reconstruction using Mimics software, presenting the (A) front view and (B) side view of the 30ºTO right limb. (C 1-4) The axial CT slices obtained from tibia-fibula connecting area provide detailed views of the remodelling status. 121

Figure 5-19. (A) 3D reconstruction of the 0ºTO right limb, (B) sagittal image after CT-reconstruction and (C) a cross section across the tibia-fibula connection area. No evidence of woven bone or active bone remodelling was observed in these regions. 121

Figure 5-20: 3D reconstruction using Image J, presenting the (A) front view, (B) side view, and (C) back view of the 10ºTO left limb, and 30ºTO left limb. The osteotomy incision area (in A) and fibula remodelling area (in C) are indicated with red arrows. 122

Figure 5-21 Representative images from CT scanning sequencing (coronal plane) illustrate the knee alignment of the left limb in the 0ºTO and 30ºTO groups. The varus alignment of the left limb in the 30ºTO group shifts the weight-bearing axis (WBA) from the medial to the lateral compartment. The HKA (Hip-Knee-Ankle) angle, indicated by the red line, represents the angle between the hip-knee line and the knee-ankle line. The weight-bearing axis, marked by the orange line, is the line from the center of the femoral head down to the center of the ankle. 123

Figure 5-22. (a) Segmentation and 3D reconstruction of the joint area from a 0° TO and a 30° TO left limb illustrate joint alignment, viewed anteriorly with the tibia tuberosity facing front and center. The gray-level model is the original CT image; the coloured model has undergone smoothing and hole-filling for better visualization the alignment. (b) The images illustrate the natural contact areas (femur-meniscus touch area) of the two compartments in 0° TO and 30° TO varus alignment, indicated in red. 123

Figure 5-23. Re-stabilization of a rat tibia following 30ºTO osteotomy. 130

Figure 6-1 (A) Spatial gait parameters are shown for the rat hind limbs. Forelimb prints are removed for clarity. (B) Temporal gait parameters are described with a Hildebrand plot for quadrupedal rodent gait. Dashed lines indicate a moment in time in the gait cycle, which is depicted by the rat drawing above each line. One gait cycle is defined from the first foot-strike event (when the heel touches the ground) to the next foot-strike event. Normal alternated footfall pattern in running is from left front (LF) to right hind (RH), to right front (RF), to left hind (LH). 135

Figure 6-2(A) The DigiGait™ system (Mouse Specifics, Inc, Quincy, MA, USA) with the light panel door open to show the high-speed digital camera and two fluorescent lights. (B) A close-up view of the DigiGait™ running chamber under overhead lighting. 137

Figure 6-3: Screen-captured image of the DigiGait™ gait analysis system (a) Image captured from high-speed video, showing the digital black and white measures of gait. (b) Plot of paw area in one gait cycle, indicating the midline distance. (c) Unfiltered gait signals generated for each of the 4 paws and limbs: periodic waveforms representing the stance and swing phases of the stride. The curve represents the identified foot of each limb while in contact with the treadmill. (d) Filtered gait signals (some figures are adapted from DigiGait™ documentation). 138

Figure 6-4: Cross validation of PLS-DA left limb model with different numbers of components. The Q^2, R^2 and accuracy increase as the number of components increases, with Q^2 reaching highest before it plateaus at the model with 5 components (indicated with red star). 141

Figure 6-5 PLS-DA model for discriminatory separation and cross-validation: sham (0ºTO) group and 30ºTO group of left limbs at 4th month and 5th month: a. 3D scores plot of PLS-DA left limb model illustrating separation between two groups. The coloured region displays the 95% confidence region. b. PLS-DA Cross-validation details: the negative Q^2 suggested a significant overlap between the two groups in 4th month, however, 5th month data demonstrates good discrimination quality with clear separation between groups. 144

Figure 6-6. PLS-DA model for discriminatory separation and cross-validation: sham (0ºTO) group, 30ºTO group, and 30ºTO group with treatment of left limb: a. 3D scores plot of PLS-DA left limb model illustrating separation between three groups. The coloured region displays the 95% confidence region. b. PLS-DA Cross-validation details: Q^2 <0.5 indicates the model lack effective predictiveness. 145

Figure 6-7. PLS-DA model for discriminatory separation and cross-validation: sham (0ºTO) group, 30ºTO group, and 30ºTO group with treatment of right limb: a. 3D scores plot of PLS-DA left limb model illustrating separation between three groups. The coloured region displays the 95% confidence region. b. PLS-DA Cross-validation details: Q^2 <0.5 indicates the model lack effective predictiveness. 146

Figure 6-8: PLS-DA model for discriminatory separation between right limb 30ºTO group and treatment group (best quality among all comparison) (a) 2D scores plot of the PLS-DA model illustrating class separation between two groups. (b) Cross validation: the model with 6 components is the optimal model for discriminatory separation. 157

Figure 6-9 PLS-DA model for discriminatory separation and cross-validation: sham (0ºTO) group, 30ºTO group, and 30ºTO group with BMP treatment or with APS treatment a. 3D scores plot of PLS-DA left limb model illustrating class separation between four groups. The coloured region displays the 95% confidence region. b. PLS-DA Cross-validation details: Q^2 <0.5 indicates the model lack effective predictiveness. 157

Figure 6-10: Hierarchical clustering dendrogram of the sample dataset for all groups. The samples are color-coded into four categories, the distance measure between branches indicates the level of dissimilarity between clusters; longer branches suggest greater dissimilarity, meaning the groups are less closely related. 158

Figure 6-11. Hierarchical clustering heatmap of the left limb sample dataset for all groups (using the average value of each variable for each group). The samples are color-coded into four categories, with their classification displayed in the dendrogram. The colour gradient (from blue to red) represents the scaled value of the variables, ranging from low to high. The variables shown are the important variables (VIP > 1) identified by the PLS-DA model, arranged in ascending order of importance. 159

Figure 6-12. Hierarchical clustering heatmap of the right limb sample dataset for all groups (using the average value of each variable for each group). The samples are color-coded into four categories, with their classification displayed in the dendrogram. The colour gradient (from blue to red) represents the

scaled value of the variables, ranging from low to high. The variables shown are the important variables (VIP > 1) identified by the PLS-DA model, arranged in ascending order of importance. 160

Figure 6-13 PLS-DA model for discriminatory separation and cross-validation: BMP treatment group versus APS treatment group a. 2D scores plots of PLS-DA illustrating class separation between two groups for each limb. The coloured region displays the 95% confidence region. The two groups in the left limb are clearly separated, whereas they appear merged in the right limb. b. PLS-DA Cross-validation details: The left limb model demonstrates good quality with clear separation between groups. However, in the right limb model, the two groups lack effective predictiveness with a negative Q^2 value. 161

Figure 7-1. Volcano plot illustrating significant differentially expressed proteins in (a) 30ºTO left knee compared to the sham group left knee and (b) 30ºTO contralateral (right) knee compared to the sham group right knee. Please note that a small portion of data points may extend beyond the axis limits. Upregulated proteins (adjusted p-value< 0.05) are depicted in red, while downregulated proteins (adjusted p-value< 0.05) are indicated in green. Others are shown in black. 180

Figure 8-1 Comprehensive overview of thesis flow and the development of the chronic overload OA model. This figure connects the array of measurement outcomes from each chapter, showing how OA changes and treatments are evaluated. It also illustrates the transition from animal models to clinical relevance. 211

List of tables

Table 1-1. Preclinical *in vivo* OA models. 28

Table 1-2. Quantitative biomechanical analysis and markers in animal models 50

Table 2-1 Tibial Osteotomy animal models presented in the literature. 58

Table 2-2 Analgesia drug dosage table 66

Table 3-1. The density of blood components and the density position of separate gel (normative baseline values) 70

Table 3-2. IL-1RA concentration in PRP and APS collected at the first 12 weeks after surgery (n=4 for week 1, and n=6 for all other time points). 74

Table 4-1. Protocol of paraffin-embedding method for sample processing. 78

Table 4-2. Toluidine blue staining protocol (Schmitz et al., 2010b). 78

Table 4-3. OA cartilage histopathology -- grading methodology, adapted from (Pritzker et al., 2006). 81

Table 4-4. OA cartilage histopathology – stage methodology, adapted from (Pritzker et al., 2006). 82

Table 4-5. OA cartilage histopathology – scoring methodology, adapted from (Pritzker et al., 2006). 83

Table 4-6: Histological section OA grading 90

Table 4-7 Staging result (mean of three zones) of histological sections. 92

Table 4-8: Staging result of histological sections (n=9, mean ±SD) 93

Table 4-9: Score result of the histological sections (Score = grade × stage). 94

Table 6-1 Terminology 135

Table 6-2 Gait feature selection from the PLS-DA model of left limb with different components. The features with variable importance (VIP score > 1.0) in different components are listed and ranked based on their VIP scores, from high to low. The model with 3 components has been validated as the optimal PLS-DA model for discriminatory separation. 147

Table 6-3 Gait feature selection from the PLS-DA model of right limb with different components. The features with variable importance (VIP score > 1.0) in different components are listed and ranked based on their VIP scores, from high to low. The model with 5 components has been validated as the optimal PLS-DA model for discriminatory separation. 148

Table 6-4. All variables with VIP > 1 between three groups for the left and right limbs are coloured (mean ±SE). The variables are grouped into four categories. 151

Table 6-5 A summary of the variables with VIP > 1 in both the left and right limbs (mean ±SE). 151

Table 6-6. Gait feature selection (VIP > 1) in different components from the PLS-DA model for pairwise discriminatory separation between the 30ºTO group, sham group, and treatment group in the left limb. The features are listed and ranked in descending order based on their VIP scores of component 1. 153

Table 6-7: Gait feature selection (VIP > 1) in different components from the PLS-DA model for pairwise discriminatory separation between the 30ºTO group, sham group, and treatment group in the right limb. The features are listed and ranked in descending order based on their VIP scores of component 1. 156

Table 6-8. Gait feature selection from the PLS-DA model for discriminating between the BMP treatment group and the APS treatment group in the left limb. The features with significant variable importance (VIP score > 1.0) in the first component are listed in descending order. 162

Table 7-1. Example of calculation of adjusted p-values.....175

Table 7-2 Summary of the upregulated biological processes in each comparison between 30°TO and 0°TO, for both left and right limbs, presenting the OA condition. The numbers (area 1, area 2) in the figure indicate the comparison where area 1 is compared to area 2, suggesting that the upregulated pathways are enriched in area 1 relative to area 2. Each comparison is detailed in the subsequent results and tables in section 7.4.1. L= left limb, R=right limb, M=medial compartment, L= lateral compartment. ..178

Table 7-3 Summary of the representative upregulated biological processes in each comparison within the BMP-treated group and the APS-treated group, presenting the OA condition. The numbers (area 1, area 2) in the figure indicate the comparison where area 1 is compared to area 2, suggesting that the upregulated pathways are enriched in area 1 relative to area 2. Each comparison is detailed in the subsequent results and tables in section 7.4.2 and section 7.4.3. L= left limb, R=right limb, M=medial compartment, L= lateral compartment.....179

Table 7-4. Differentiated upregulated and down regulated genes (adjusted p-value < 0.05 and fold changes FC>2) when comparing the 30ºTO left knee (OA knee) with the 0ºTO left knee (healthy knee). The bolded genes are the top 10 with the most significant p-values. 181

Table 7-5 Top upregulated pathways in OA cartilage samples (n=6), ranked by the p-value of pathway enrichment when comparing the 30ºTO left knee (OA knee) with the 0ºTO left knee (healthy knee). Pathways exhibiting representative biological processes related to OA, as identified in previous literature, are highlighted in bold. A Log P Value (equivalent to -log10 p-value) greater than 1.3 is considered significant. The "Term" column represents the serial number of specific biological processes or pathways as identified in databases. The "Count" column indicates the number of genes enriched from the input list. The "Gene symbols" column listed the enriched genes. 183

Table 7-6 Differentiated upregulated genes when comparing left medial compartment (BMP-treated OA in overloading condition) with left lateral compartment (BMP treated OA in unloading condition). The bolded genes are the top 10 with the most significant p-values. 184

Table 7-7. Top upregulated pathways in BMP-treated knee in overloading condition (n=3), ranked by the p-value of pathway enrichment when comparing left medial compartment (BMP-treated OA in overloading condition) with left lateral compartment (BMP treated OA in unloading condition). Pathways exhibiting representative biological processes related to OA, as identified in previous literature, are highlighted in red. A Log P Value (equivalent to -log10 p-value) greater than 1.3 is considered significant. The "Term" column represents the serial number of specific biological processes or pathways as identified in databases. The "Count" column indicates the number of genes enriched from the input list. The "Gene symbols" column listed the enriched genes. 186

Table 7-8 Differentiated upregulated genes when comparing left limb (BMP-treated OA) with right limb (healthy). The bolded genes are the top 10 with the most significant p-values. 187

Table 7-9. Top upregulated pathways in BMP-treated knee (n=6), ranked by the p-value of pathway enrichment when comparing left limb (BMP-treated OA) with right limb (healthy). Pathways exhibiting representative biological processes related to OA, as identified in previous literature, are highlighted in red. A Log P Value (equivalent to -log10 p-value) greater than 1.3 is considered significant. The "Term" column represents the serial number of specific biological processes or pathways as identified in databases. The "Count" column indicates the number of genes enriched from the input list. The "Gene symbols" column listed the enriched genes. 188

Table 7-10 Differentiated upregulated genes when comparing left medial compartment (APS-treated OA in overloading condition) with left lateral compartment (APS treated OA in unloading condition). The bolded genes are the top 10 with the most significant p-values. 189

Table 7-11. Top upregulated pathways in APS-treated knee in overloading condition (n=3), ranked by the p-value of pathway enrichment when comparing left medial compartment (APS-treated OA in overloading condition) with left lateral compartment (APS treated OA in unloading condition). Pathways exhibiting representative biological processes related to OA, as identified in previous literature, are highlighted in red. A Log P Value (equivalent to -log10 p-value) greater than 1.3 is considered significant. The "Term" column represents the serial number of specific biological processes or pathways as identified in databases. The "Count" column indicates the number of genes enriched from the input list. The "Gene symbols" column listed the enriched genes. 190

Table 7-12 Differentiated upregulated genes when comparing left limb (APS-treated OA) with right limb (healthy). The bolded genes are the top 10 with the most significant p-values. 191

Table 7-13. Top upregulated pathways in APS-treated knee (n=6), ranked by the p-value of pathway enrichment when comparing left limb (APS-treated OA) with right limb (healthy). Pathways exhibiting representative biological processes related to OA, as identified in previous literature, are highlighted in red. A Log P Value (equivalent to -log10 p-value) greater than 1.3 is considered significant. The "Term" column represents the serial number of specific biological processes or pathways as identified in databases. The "Count" column indicates the number of genes enriched from the input list. The "Gene symbols" column listed the enriched genes. 194

1 Introduction

1.1 Motivation and Objectives

Osteoarthritis (OA) is one of the most common chronic health problems worldwide, causing significant pain and disability, leading to a high burden on health services. It is a multifactorial disease involving various biological and mechanical influences. Knee OA is the most prevalent type of OA and is largely mechanically driven. With the six distinct subdivided OA types clinical classification system that has been recently proposed, the chronic mechanical overloading phenotype is the most common phenotype in the population.

As OA clinical studies are constrained due to the fact that diagnosed patients often represent at advanced stages of the disease leading to an inability to explore the early stages of the condition, *in vivo* animal models are essential for understanding the disease's pathogenesis, and testing the efficacy of different therapeutics before proceeding into clinical trials.

However, there is currently no representative model that closely mimics the natural mechanical condition of the mechanical overloading phenotype of OA. The overuse of post-traumatic osteoarthritis (PTOA) models and chemical injection models, which induce an acute intra-articular inflammatory response to trigger OA, may present distinct etiologies and disease progression.

The tibial malalignment model, induced by an extra-articular surgery (osteotomy), offers a promising approach to present the chronic natural course of primary OA. Therefore, the overall aim of this thesis is to develop a tibial malalignment model of OA and use this to characterize of mechanically-induced OA and evaluate early pharmacological intervention.

1.2 Chapter summary

This introductory chapter provides a comprehensive background on OA, exploring its pathophysiology, aetiology, diagnostic methods, and prospective treatments. Furthermore, it illuminates the role of biomechanics in initiating, propagating, and treating this disease condition.

A thorough review is given on the use of animal models to biomechanical effects in OA pathogenesis, as well as the mechanisms of cartilage and subchondral bone repair in OA progression. Measurement methods related to disease outcome analysis are also presented.

This review leads to the approach taken in this thesis.

A more concise review of literature relevant to subsequent individual chapters are provided within each chapter.

1.3 Osteoarthritis: an overview of the disease

1.3.1 Epidemiology

Osteoarthritis (OA) is a highly prevalent chronic disease that affects the joints contributing significantly to the loss of physical function (Kloppenburg and Berenbaum, 2020). It is characterised by pain due to cartilage disintegration, bone remodelling and inflammation of the synovium. The incidence of any type of OA in 2017 was 10.7%, with a one-year consistent frequency of $6.8/10^3$ adults worldwide (Swain et al., 2020). In the UK, pain associated disability as a result of OA represents a significant burden (22% of the total burden of ill health) in societal and personal costs (Wolf et al., 2019, Versus Arthritis, 2019). Internationally, hip and knee OA is the 11th highest cause of disability (GBD 2017 Disease and Injury Incidence and Prevalence Collaborators, 2018). Knee OA (KOA) is the most prevalent type of OA and is increasing in incidence as obesity and life span increase (Wallace et al., 2017, Hunter and Bierma-Zeinstra, 2019). The latest musculoskeletal calculator (published in 2019) estimated that in England in 2012 18.2% of the population over 45 years old had clinically diagnosed KOA, 1/3 of which was severe (Versus Arthritis, 2019).

1.3.2 Phenotypes

KOA is principally categorised into two main types, primary OA - also known as idiopathic OA - which is characterised by natural cartilage degeneration during ageing as a result of anonymous reasons, and secondary OA which occurs as a result of known medical conditions or risk factors (Altman et al., 1986). However, the heterogeneous pathophysiology of OA challenges the traditional classification of the clinical condition, particularly where the “anonymous” reasons can be documented, such as sprains, fatigue or repetitive high impacts. Therefore, Dell’Isola *et al* subdivided knee OA into six clinical phenotypes based on a qualitative analysis of the existing data from 24 studies: 1) long-lasting pain; 2) up-regulation of inflammatory markers; 3) metabolic disorder (estrogen imbalance, dyslipidemia, diabetes, and obesity); 4) changes in the bone and cartilage homeostasis; 5) altered joint mechanics (medial meniscus overload or varus malalignment) (Figure 1B); and 6) minor joint disease (slight clinical symptoms with chronic progression) (Dell'Isola et al., 2016). The complexity is confounded by these phenotypes not necessarily being discrete, with multiple phenotypes potentially co-existing (Bierma-Zeinstra and van Middelkoop, 2017).

1.3.3 Diagnosis and risk factors

Defining KOA (Figure 1-1A) phenotypes is difficult due to many complex factors, as the degeneration of the joint is affected by a combination of mechanical and biological effects (Sandell and Aigner, 2001b). The hallmarks of KOA are the degeneration of the articular cartilage in the weight-bearing region, structural changes of the surrounding bone, and joint inflammation (Lespasio et al., 2017a) .

Presently, OA is primarily diagnosed based on clinical symptoms, such as injury history and physical examination, with radiographic features serving as a pivotal diagnostic tool (Sinusas, 2012). OA's defining features includes the articular cartilage defects in weight-bearing areas, osteophyte formation, structural modifications in the subchondral bone, and joint inflammation (Vina and Kwoh, 2018a, Lespasio et al., 2017b).

Clinical studies provide important data for correlating the OA diagnostic clinical symptoms (OA pain and disability) with particular tissue pathology, joint structural anatomy and genetical difference. These connections are termed as the "risk factors" for OA (Malfait et al., 2013). Some risk factors may serve as initial triggers for the disease, while others might emerge as secondary causes. These secondary factors influence disease progression and correlate with disease severity. Risk factors include **individual-centred factors** such as age, gender, race, genetic background, metabolic disorder, endocrine, diet, bone density, and **joint-related factors** such as different shapes of bone/joint, muscle weakness, occupation/sports, and injury and joint overloading (Vina and Kwoh, 2018b). The therapeutic modification or preventive actions related to these factors could influence the disease's onset, its progression, or potentially mitigate its severity. Biomechanics stands out as a central theme in joint-associated factors, becoming a significant focal point in much recent KOA research (Glyn-Jones et al., 2015, van Tunen et al., 2016).

Biomechanical factors play an important role in understanding the mechanism of KOA pathogenesis and help to address clinical questions. For example, it is reported that frontal plane knee malalignment has the strongest relation with KOA development (Palazzo et al., 2016). The natural knee alignment is around 1° varus (Cooke et al., 2007a). However, these data are all derived from retrospective studies, which are population-based studies without laboratory experiments to confirm these findings. Moreover, OA is a progressive disease that is usually only diagnosed in patients at an advanced stage (Hayami et al., 2006b). It is important to detect the onset of the disease in OA research. This is key not only for studying the aetiology of the disease, but also would represent a big step towards developing preventative treatment and in diagnosing pre-radiographic OA.

1.4 Biomechanical factors in OA onset

Biomechanical factors of OA herein are defined as joint-related mechanical factors based on anatomy and function (Glyn-Jones et al., 2015, van Tunen et al., 2016).

Anatomical factors include changes in joint morphology and limb alignment (Glyn-Jones et al., 2015), where these can be changes of the shape of the tibia, femur, or patella. The reasons for these changes are not fully known, but are likely to be due to Wolff's law, which describes how bone tissue can be remodelled via osteocytes responding to the local mechanical environment (Chen et al., 2010). These morphological changes can, therefore, be created by joint loading changes, but will also then induce

changes in joint loading and so initiate or accelerate the OA (Neogi et al., 2013). The morphological changes can predict the onset of OA a year earlier than visible radiographic changes (Neogi et al., 2013). Knee malalignment (i.e. varus or valgus alignment) is also a strong risk factor in OA onset and progression (Tanamas et al., 2009) (Figure 1-1B). A population-based longitudinal study in rural China revealed that the proportions of knees with normal, valgus, and varus alignment in the population were 29.9%, 56.5%, and 13.7%, respectively. The prevalence of medial and lateral KOA was 16.0% and 4.3%, respectively. The varus malalignment was linked to an increased prevalence of medial knee OA, while valgus malalignment was associated with a higher prevalence of lateral knee OA (Wang et al., 2018a).Malalignment is defined as a shift from the collinear mechanical alignment of hip, knee and ankle to either a medialised (varus) or lateralised (valgus) loading distribution (Sharma et al., 2001). The alignment changes can be a result of localised morphological changes. In the varus knee, the mechanical axis (from mid femoral head to mid ankle) will pass medial to the centre of the knee. This induces an adduction moment that increases the force on the medial tibiofemoral compartment (Tetsworth and Paley, 1994). The opposite happens in the valgus knee (Tetsworth and Paley, 1994). This loading imbalance contributes to OA progression (Sharma et al., 2001). A 1° deviation of varus alignment out of the natural physiological range increases the medial load by 5% (Schipplein and Andriacchi, 1991b, Halder et al., 2012), and, as such, varus and valgus malalignment is a known independent risk factor in the progression of medial and lateral OA (Tanamas et al., 2009). Of these, varus alignment is more common in the knee OA population and is significantly associated with OA development (Brouwer et al., 2007b).

Functional factors include previous knee injury, poor muscle function, reduced proprioceptive acuity, activities (occupational activity and sports activity), and joint laxity (Glyn-Jones et al., 2015, van Tunen et al., 2016, Bennell et al., 2012, Richmond et al., 2013). Knee injury mainly includes knee ligament ruptures, sprains or meniscal tears (Thomas et al., 2017) (Figure 1-1C-E). These injuries carry a high risk of post-traumatic OA (PTOA) onset compared to uninjured individuals (Thomas et al., 2017). There is some evidence of the high incidence of OA in athletes being mainly due to joint injury (Bennell et al., 2012). Meniscal and anterior cruciate ligament (ACL) injuries each account for one quarter of all knee injuries (Thomas et al., 2017). Ligament injuries can cause changes in joint mechanics, including translation and shear, leading to overload (Figure 1-1E) (Kernozek et al., 2013). Simply, meniscal tears decrease the contact area between cartilaginous surfaces thus increasing contact stresses during load transfer (Figure 1-1D) (Masouros et al., 2008). Muscle weakness (Figure 1-1C), including atherogenic muscle inhibition, was mostly thought to be a secondary factor that results from progression of OA damage, but there is also population-based evidence showing that muscle dysfunction is a primary risk of OA initiation, preceding knee pain and muscle atrophy (Slemenda et al., 1997). Quadriceps weakness specifically is a better predictor of joint pain and joint space narrowing than radiographic evidence (Palmieri-Smith et al., 2010). Impaired knee proprioception refers to a deteriorated accuracy in position

and motion sense, caused by impaired articular mechanoreceptors (Knoop et al., 2011). Reduced proprioceptive accuracy has been found in OA patients and this causes a decrease in knee stabilization and joint movement coordination, both of which are directly related to mechanics, and has a significant association with knee pain (Knoop et al., 2011, van Tunen et al., 2018). These factors are linked in that the loss of muscle strength can be attributed to afferent sensory dysfunction (i.e. impaired proprioception) and the subsequent reduction in efferent neuron stimulation (Slemenda et al., 1997). Although there is currently no robust evidence that proprioceptive changes cause OA onset, it has being proposed as a potential putative OA risk factor (Roos et al., 2011). Activities (including physical activity, occupational activity and sports activity) are controversial factors for knee OA as the cartilage homeostasis relies on moderate mechanical loading but could change to catabolic metabolism in high intensity and long duration abnormal mechanics (Griffin and Guilak, 2005). Occupational activity with heavy lifting, frequent deep knee flexion (squatting and kneeling) and sports activity (at the elite level) with significant impact, twisting, turning and running have a demonstrated higher risk of OA (Richmond et al., 2013). Whereas, there is no supportive evidence that physical activity (moderate sports activity) and recreational sports activity without suffering injury increase the risk of OA (Richmond et al., 2013, Bennell et al., 2012). Some large studies have reported that ice hockey and football (soccer) players, wrestlers and weightlifters have a much higher incidence of OA than endurance sport athletes (Kujala et al., 1994, Tveit et al., 2012). This is suggestive that there is a biomechanical tolerance level in weight-bearing joints (or simply a higher incidence of injury in these sports); this level is not currently known (Thelin et al., 2006). Lastly, joint laxity refers to the loss of joint stability with deficiencies in the primary soft-tissue stabilisers such as the cruciate ligaments, secondary stabilisers such as the capsule, or in knee alignment (van Tunen et al., 2016). Related evidence has shown that patients with medial knee OA have laxity, which is usually in the varus-valgus direction (van Tunen et al., 2018). All of these factors are related to the biomechanics (loading, motion) and in general, alterations in these factors will change the loading on the knee (van Tunen et al., 2016) (Figure 1-1F). Acute changes in loading or long-term overuse loading will subsequently induce the structural, biological and mechanical level changes and present as clinical symptoms. Additionally, these mechanical factors are related to genomic factors. Some reports show that these mechanical factors can lead to altered gene expression, influencing the phenotypic health of chondrocytes in articular cartilage. This results in a loss of the tightly regulated balance of gene expression, leading to a dysregulated state characteristic of the OA disease state (Lee et al., 2005, Bloks et al., 2024) .Although biomechanical factors can be a direct-causative factor in knee OA, they are not independent risk factors in OA development; many other risk factors are associated with these. For example, obesity is an important risk factor for OA; not only does it cause systemic inflammation (Berenbaum et al., 2013), but it also interacts with confounding biomechanical factors such as evidence of decreased regular cyclic physiologic joint loading (lowering the risk factor) and altered gait and increased peak knee force (both increasing the risk factor) (Issa and Griffin, 2012, Aaboe et al., 2011). At the molecular and cellular level, cartilage degradation is generally affected by biological

and mechanical insults (Sandell and Aigner, 2001b) and many risk factors induce OA by combined inflammation and mechanical stress-induced signalling pathway in chondrocyte mechano-transduction (Guilak, 2011). With the recent discovery of mechano-signalling in chondrocytes, the mechanism of biomechanical factors is clearer. It involves the mechanical signal (including abnormal stress, compression, and fluid pressure) exposed to chondrocytes in the cartilage extracellular matrix, and converts these to intracellular signals via mechanical transient receptors (ion channels, integrins) in the surface of chondrocytes (called mechanoreceptors) (Guilak, 2011, Gilbert and Blain, 2018). This suggests that these biomechanical factors might play a critical role in the initiation and progression of OA, independent of the influence of inflammation. Therefore, although there is tantalising information, there is still no consensus in the understanding of the biomechanical factors underlying OA initiation and progression (Hunt et al., 2020, Saxby and Lloyd, 2017, Guilak, 2011). To identify these factors and to address this fundamental gap, preclinical models should be developed that are clinically representative of biomechanically induced OA (McCoy, 2015a, Serra and Soler, 2019, Kuyinu et al., 2016b). This is the focus of part of this PhD.

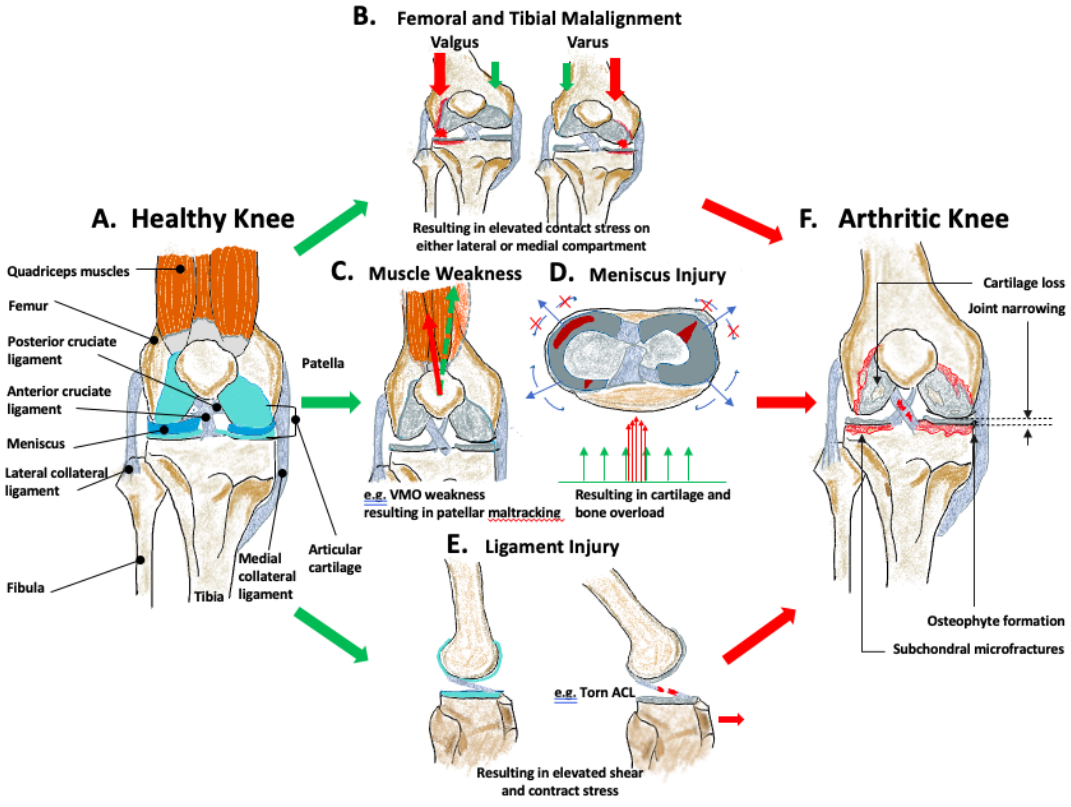

Figure 1-1: Biomechanical factors leading to osteoarthritis (OA). A. represents the healthy knee. B. femoral and tibial malalignment with resulting varus or valgus angulation and medial or lateral joint overload, C. quadriceps muscular weakness leading to muscle imbalance and local joint overload, D. meniscus injury leading to increased contact stress, E. ligament injury leading to changes in the overall knee mechanics. All of these will eventually contribute to increasing the mechanical stress on the healthy knee and induce joint structural changes, including cartilage loss, joint narrowing, osteophyte formation, and subchondral microfractures resulting in, F. arthritic knee.

1.5 Animal models of OA

Experiments to investigate these biomechanical factors are difficult in human studies as the mechanical intervention and direct outcomes are hard to perform and observe independently (Wendler and Wehling, 2010), and the available human tissue diagnosed as OA is not in the early stage (Hayami et al., 2006b). *Ex vivo* joint models cannot truly mimic musculoskeletal mechanics and the arthritic environment. Thus, *in vivo* animal models are important in studying the onset and early stages of this disease, particularly when investigating biomechanical aspects (Kuyinu et al., 2016b). The two main goals of using OA *in vivo* models are 1. to understand the pathology/pathophysiology of the disease, especially in the early stages, and 2. to test the safety and efficacy of different therapeutics developed before entering into clinical trials (Kuyinu et al., 2016b). Recent advances in measurement techniques for *in vivo* animal studies have enabled and improved the analysis of OA and reduced animal usage (Teeple et al., 2013). In the light of recent work on *in vivo* animal models and methodological advances on biomechanical aspects of KOA, the purpose of this PhD is to create a mechanically induced chronic primary OA *in vivo* model, with drug treatments and advanced measurement techniques focusing specifically on biomechanical aspects in the context of the clinical phenotypes.

1.5.1 Classical animal models of OA

As OA is a multifactorial disease driven by genetic, biological, and biomechanical factors (Glyn-Jones et al., 2015), there are several different *in vivo* models that study various distinct features of OA. Each model replicates a unique OA pathogenesis that reflects the specific mechanism of interest as well as the target uses for drug treatment (Cope et al., 2019). Generally, small mammals, including mice, rats, rabbits and guinea pigs, are considered for primary basic research (Serra and Soler, 2019), such as the study of the pathology/pathophysiology of the disease, and assessing the effectiveness of different therapeutics (Kuyinu et al., 2016b). Larger animals are slower to develop the disease, are more expensive, less reproducible and harder to handle (Serra and Soler, 2019), yet can be more relevant to the anatomy, dimensions and biomechanics of human joints (Lampropoulou-Adamidou et al., 2014). Therefore, they are more widely used in translational preclinical studies, where the clinical progression of the disease and treatment are being considered. Of these, the goat is considered to have to closest anatomy to the human (Proffen et al., 2012).

These *in vivo* OA models are characteristically classified as: spontaneous models which include naturally occurring and genetically modified models, and induced models which can be chemically or surgically induced (Table 1-1). In recent years, some non-invasive induced models have been developed as alternatives to surgical models (Poulet, 2016). These OA models are typically categorised in terms of classical primary and secondary OA types. Spontaneous models characterise to a certain extent the natural progression of human primary OA with or without genetic modification. The STR/ort and

C57BL/6 strains of mice are predisposed to developing spontaneous idiopathic OA and exhibit quicker skeletal maturation and aging compared to other genetically distinct strains of mice. Their pathogenic genes might include multiple genes involved in the synthesis and degradation of cartilage ECM (McCoy, 2015b, Glasson, 2007).In contrast, nduced models are developed as a result of replicating specific known risk factors of secondary OA and these models are usually chemically or surgically induced models (McCoy, 2015b). The induced methods stimulate acute inflammation and/or alter the joint mechanics (Serra and Soler, 2019).

The Dunkin Hartley guinea pig is the most commonly used spontaneous model to develop naturally occurring, age-related OA. This has a high incidence and occurs at a reasonably young age compared to humans (Jimenez et al., 1997). It has similar histopathology to the human disease and the histological changes can be observed normally as early as the 3rd month in a guinea pig (Kraus et al., 2010). The *Str/ort* strain of mouse is a spontaneous osteoarthritic model where 85% of all male mice have mild OA lesions in the medial tibial plateau from 10 weeks of age (Mason et al., 2001). Similarly, the rabbit is a spontaneous model where naturally occurring OA can be found in over 50% of rabbits by the 6th year of age (Arzi et al., 2012). Genetically modified models are mainly mice, which are designed to knock down, knockout, knock-in or mutate specific genes to breed a strain that is more susceptible to OA (Little and Hunter, 2013).

The induced methods aim to generate the joint destabilization and increase joint contact force, and/or create an intra-articular inflammation, and so consequently alter cell metabolism and induce an OA lesion (Teeple et al., 2013). Chemically induced models mostly include intra-articular injection of an agent to trigger acute local inflammation, extracellular matrix degradation and chondrocyte apoptosis (Bendele, 2001). The chemical agents generally used in induced animal models of OA are papain (Sukur et al., 2016), quinolone (Rodrigues-Neto et al., 2016), collagenase (Lee et al., 2020), carrageenan (Korotkyi et al., 2019), Freund's adjuvant (Robin, 2017), and sodium mono iodoacetate (MIA) (Adeyemi and Olayaki, 2017) which is the most commonly used. Surgically induced models mainly use intra-articular invasive surgery to generate joint instability or create chondral defects to induce OA. PTOA is the most widely studied secondary OA model and is commonly used to analyse mechanical aspects of OA. At present, the most commonly used surgically induced models are anterior cruciate ligament transection (ACLT) and meniscectomy (Lampropoulou-Adamidou et al., 2014, Ramme et al., 2018). Other models used include collateral ligament transection (Bendele, 2001) other meniscal injury (partial meniscectomy (Ali et al., 2018), medial meniscal tear/transection (Brederson et al., 2018, Pucha et al., 2020, Temp et al., 2020a)， and destabilization of the medial meniscus (Arzi et al., 2012)), chondral/osteochondral defects (McNulty et al., 2012, Figueroa et al., 2014, Mastbergen et al., 2006, Serra et al., 2014, Flanigan et al., 2010), or ovariectomy (oestrogen deficiency causing subchondral osteoblast changes) (Xu et al., 2019). Additionally, a novel non-articular invasive method was raised

again recently, using tibial osteotomy (TO) to induce a varus tibial malalignment and joint mechanical overload (Britzman et al., 2018b). This model is more representative of the human primary overloading OA condition without any inter-articular damage or destabilization of internal joint mechanics (Britzman et al., 2018b).

Although surgical models better mimic the pathogenic mechanisms than chemical models and have a shorter progression period than spontaneous models, they involve aseptic procedures, and the results are highly dependent on surgical skill. This means that ensuring repeatability and minimising variability of these invasive models is difficult. To address these issues, some studies create PTOA by using non-invasive methods through applying an external mechanical load to the relevant joint without disrupting the skin or the joint capsule (Christiansen et al., 2015) through either single-impact injury or repetitive loading (Poulet, 2016). There are four main types of these non-surgically induced model type: (1) intra-articular fracture of the tibial plateau (Lewis et al., 2011, Schenker et al., 2014, Kimmerling et al., 2015); (2) ACL rupture through tibial compression overload (Lockwood et al., 2014, Khorasani et al., 2015); (3) cyclic articular cartilage tibial compression (Melville et al., 2015, Poulet et al., 2011b); and (4) moderate running exercise. Compared to severe surgical PTOA models, these models are more likely to represent real biomechanical conditions in OA development.

Table 1-1. Preclinical *in vivo* OA models.

OA models	**Subcategory**	**Species**	**Model**	**Characteristics**	**Ref.**
Spontaneous	Naturally developing	Guinea pig Rabbit Horse Mouse	Natural wear and tear of the joint.	1. Represents human primary osteoarthritis (OA). 2. Investigate the initial pathogenesis of OA. 3. Long progression time. Small animal has advantage of short time required for maturity.	(Arzi et al., 2012, McDougall et al., 2010, Jimenez et al., 1997, Staines et al., 2017, McIlwraith et al., 2012, Mason et al., 2001)
	Genetically modified	Mouse Rat	Susceptibility due to genetic selection (genes involved in cartilage degradation, inflammatory mediators, chondrocyte apoptosis, and subchondral bone metabolism).	1. Study the effect of specific genetic conditions on the pathogenesis of OA. 2. Help to establish the molecular basis of OA, but low translatability to clinical trials.	(Little and Zaki, 2012b, Miller et al., 2013b, Poulet et al., 2013)
Chemically Induced		Mouse Rat Rabbit Goat	Intra-articular injection of a chemical that induces joint inflammation.	1. Mainly an inflammatory model. 2. It is used to study drugs and responses to pain and inflammation.	(Adeyemi and Olayaki, 2017, Rodrigues-Neto et al., 2016, Lee et al., 2020, Sukur et

OA models	Subcategory	Species	Model	Characteristics	Ref.
				3. Simple and repeatable. 4. Although this produces OA within a short period it does not reproduce the pathophysiological mechanisms.	al., 2016, Cheng et al., 2019, GBD 2017 Disease and Injury Incidence and Prevalence Collaborators, 2018, Laurent et al., 2003)
Surgically Induced	Anterior cruciate ligament transection (ACLT)	Mouse Rat Goat	ACL injury produced by arthrotomy (medial or lateral) or arthroscopy (joint destabilization).	1. Suitable choice for pharmacologic studies. 2. Imitates the cartilage degradation after ACL rupture, but develop OA lesion slowly. 3. Can be combined with meniscectomy to achieve advanced lesions.	(Ramme et al., 2018, Piskin et al., 2007, Kamekura et al., 2005, Hayami et al., 2006b, Jackson et al., 1993)
	Meniscal injury	Mouse Rat Canine Goat	Partial or total meniscectomy; medial meniscal tear / transection (MMT) through transection of the medial collateral ligament (MCL) and medial meniscus leads to abnormal joint load distribution	1. A more severe approach than ACL transection, causing rapid degeneration. 2. Canines are the most widely used.	(Ali et al., 2018, Piskin et al., 2007, Brederson et al., 2018, Knights et al., 2012, Bendele, 2001, Kahn et al., 2016, Pucha et al., 2020, Temp et al., 2020a)
	Destabilization of the medial meniscus (DMM)	Mouse Rat Rabbit	Sectioning of medial meniscotibial ligament causes the DMM and joint load changes.	1. Less invasive and slower disease progression than ACLT. 2. Easier to perform than MMT on small animals like the mouse.	(Glasson et al., 2007, Iijima et al., 2014, Goetz et al., 2017)
	Ovariectomy	Mouse Rat Rabbit Guinea pig Ovine	Estrogen reduction leads to accelerated cartilage erosion.	1. Study the effect of estrogen deficiency on OA pathology progression, and therapeutic intervention. 2. Not recommended in therapeutic trials.	(Xu et al., 2019, Castaneda et al., 2008, Castaneda et al., 2010, Qin et al., 2013, Sniekers et al., 2010, Oestergaard et al., 2006, Dai et al., 2006) (Cake et al., 2005, Kreipke et

OA models	Subcategory	Species	Model	Characteristics	Ref.
					al., 2014, Hoegh-Andersen et al., 2004)
	Chondral/ osteochondral defects	Mouse Rabbit Canine Bovine	Focal chondral lesion are created using arthrotomy which triggers local inflammation that changes the chondrocytes' metabolism. Also changes the biomechanics in area surrounding lesion.	1. Evaluate joint cartilage repair locally, and the healing response to different therapies. 2. Widely used in tissue bioengineering and regeneration medicine with various biomaterials.	(McNulty et al., 2012, Figueroa et al., 2014, Mastbergen et al., 2006, Serra et al., 2014, Flanigan et al., 2010)
	Tibial Osteotomy (TO)	Rat Guinea pig Rabbit Canine	Surgically setting tibial varus (or valgus) malalignment to increase mechanical loading on the medial (or lateral) compartment of the joint	1. Biomechanical method to induce OA via extra-articular surgery, without any internal joint damage. 2. More representative of the human primary overloading OA, dependent on the magnitude of the malalignment	(Britzman et al., 2018b, Wei et al., 1998b) (Reimann, 1973a, Mankin et al., 1981b) (Johnson and Poole, 1988b, Panula et al., 1997a)
Non-invasive (single-impact injury and repetitive loading)	Intra-articular fracture of tibial plateau	Mouse Rat Rabbit Canine	Fix the knee of the animal in 90° position and apply an impact with an indenter to cause a closed fracture in the articular surface of animal lower limb.	1. Study articular cartilage degeneration after higher-energy impact trauma injuries (e.g. frontal vehicle collisions).	(Lewis et al., 2011, Schenker et al., 2014, Kimmerling et al., 2015, Lahm et al., 2005, Rundell et al., 2005, Allen et al., 2020)
	ACL rupture via tibial compression overload	Mouse Rat	An axial load is applied to the calf which is fixed between the upper and lower loading cups, leading to a cranial displacement of the tibia relative to the femur, overloading the ACL and causing it to rupture.	1. Rapidly developing OA process following an acute ACL rupture, a similar mechanism to that of a sports injury. 2. It needs a greater peak force (12N) applied in a short time when compared to the cyclic compression loading model	(Lockwood et al., 2014, Khorasani et al., 2015, Brown et al., 2020)
	Cyclic articular cartilage tibial compression	Mouse Rat	Cyclic axial compressive force (4.5N – 9N) in a similar setup to the tibial compression arrangement, simulating an overloaded	1. Study articular cartilage degeneration induced by chronic overloading. 2. Initiate OA in an adjustable fashion with a peak force	(Melville et al., 2015, Poulet et al., 2011b, Maerz et al., 2015,

OA models	Subcategory	Species	Model	Characteristics	Ref.
			bodyweight, causing high loads across the ankle and knee joints.	below the ACL-rupture threshold. 3. Not representative of the biomechanical loading environment due to muscle contractions and gait	Christiansen et al., 2012)
	Running exercise model	Mouse Rat	Train rodents running on a treadmill or wheels to induce OA.	1. Can be combined with genetic or specific strain rodents susceptible to OA, to shorten the spontaneous process or create more severe OA. 2. Potentially represents the specific type of OA in patients associated with occupational loading and sports activities	(Lapvetelainen et al., 2002, Lapvetelainen et al., 1995)

As described previously, a recent systematic review clacyssified clinical OA to 1. chronic pain related, 2. inflammation related, 3. metabolic syndrome related, 4. bone and cartilage homeostasis-related, 5. mechanical overload related, and 6. minor joint disease related phenotypes (Dell'Isola et al., 2016). Some studies also compared the differences in expression of OA biomarkers and suggested a distinct aetiology and pathophysiology between different OA phenotypes (Little and Hunter, 2013, Wei et al., 2010). However, the traditional classification of OA models above (spontaneous, genetically modified, chemically-induced, surgically-induced) based on different intervention methods leading to OA (Table 1-1) does not clarify how they relate clearly to each pathogenesis and the six distinct OA clinical classifications now used (Dell'Isola et al., 2016). This section summarizes how these animal models relate to the clinical classifications.

Types 1 and 2. Responses to chronic pain and inflammation are usually conducted using chemically induced models, which induce cartilage degeneration based on triggering the inflammatory mechanism rapidly (Serra and Soler, 2019). The MIA method induces widespread chondrocyte death leading to intense pain and is typically used to study OA-associated pain (Pitcher et al., 2016). However, these chemical models cannot be used to study the pathogenic mechanism of OA in humans.

Type 3. The metabolic phenotype of OA is usually characterized by surgical (ovariectomy) models or spontaneous OA models. These models are appropriate to study diabetes, obesity and other metabolic disturbances (estrogen imbalance) that cause OA (Xu et al., 2019).

Type 4. Bone and cartilage homeostasis phenotype presents a OA subgroup with significant changes in cartilage and bone metabolism (Dell'Isola et al., 2016), categorised to strophic (few osteophytes with severe joint space narrowing) and hypertrophic (large osteophytes with little joint space narrowing) subsets (Roemer et al., 2012a). The ACLT surgical model is usually used in studying this phenotype. Bone osteophytes can be rapidly induced in experimental canine OA as early as a few days after ACL surgical induction (Gilbertson, 1975), and the subchondral and trabecular bone remodeling can be observed at around 2 months (Lavigne et al., 2005).

Type 5. The mechanical overloading phenotype which accounts for 12%-22% of OA incidence (Dell'Isola et al., 2016) is usually modelled by surgical disruption of joint biomechanics, such as meniscectomy or ligament transection, causing joint instability. These models can simulate a human injury event: so-called PTOA models (Little and Hunter, 2013). However, as shown in a population study, PTOA comprises only approximately 12% of symptomatic OA (Brown et al., 2006). Therefore, it could be contended that there is an overuse of the PTOA models in representing the chronic overloading OA phenotype.

Type 6. Ageing or minor joint disease phenotypes are best studied by naturally occurring models (Lampropoulou-Adamidou et al., 2014).

The mechanical overloading phenotype itself has been shown to arise from 1) long-term overuse or cyclic small loads or 2) a short-term high load (impact) (Gardiner et al., 2016) and these two are suggested to have distinct pathophysiology progression (Little and Hunter, 2013). For example, a comparative study developed in guinea pigs with or without surgical intervention (ACLT surgery) showed that there are several differences in biomarkers between these two mechanical overload phenotypes (Wei et al., 2010). A later study characterised the subgroups of the mechanical overload phenotype into two: one having severe medial OA and varus malalignment with a high prevalence of injury history (55%), and the other having evidence of lateral OA and valgus alignment with lower body mass index (BMI) (Dell'Isola et al., 2016). Therefore, current PTOA models only model the short impact (injury-history) subgroup, and there should be another type of biomechanically induced OA model which occurs in a relatively idiopathic, non-traumatic and slow-progressive condition to present the "primary" chronic overloading OA (Dell'Isola et al., 2016). The studies more representative of this form of mechanical overloading OA are the non-invasive cyclic overloading model (Poulet et al., 2011a) and the extra-articular TO surgical model (Britzman et al., 2018b). These will be described in more detail in the next section (4.2).

As the PTOA surgical model cannot cover all the mechanical overloading phenotypes, here, a new term is defined, biomechanically induced animal models (biomechanical model for short) to present all the mechanical overloading phenotypes of OA, including the "primary" mechanically induced slow-

progressive OA - chronic overloading OA - which is naturally occurring after long-term lower levels of increased loading (mechanical overuse), and "secondary" PTOA after the acute high impact or trauma. The main mechanism is to alter the joint mechanics based on changing the loading distribution, or creating joint instability or joint defects.

The following section will focus on these biomechanical aspects identified as key in animal models of biomechanical mechanisms in OA development.

1.5.2 Biomechanical aspects on developing POA model

In this section, the recent advances in the development of mechanical overloading models are summarised and it is highlighted that there remains a gap in ensuring that these models sufficiently closely mimic the clinical condition in terms of biomechanical aspects. Two key considerations in studying mechanically driven OA are described: 1. how to develop a mechanical model without inflammatory artefacts and 2. how to induce OA without significant trauma and so enable the detection of changes indicative of early-stage OA.

1.5.2.1 Isolating biomechanical changes from inflammation in post-traumatic OA models

Currently, the key challenge needing to be resolved in PTOA models is how to develop a purely biomechanical model excluding tissue injury and inflammation following the surgery. Certainly, OA is an inflammatory disease; besides the local joint tissue inflammation, OA can also cause a low-grade systemic inflammation associated with metabolic disorders and innate immunity (Berenbaum, 2013, Kyostio-Moore et al., 2011). However, whether mechanics or inflammation is the origin of OA has been controversial for a long time. Recent studies have demonstrated that abnormal mechanical loading can activate mechanoreceptor signalling, which also contributes to inflammation and cartilage degradation (Berenbaum et al., 2013, Guilak, 2011). Thus, where current surgical models of OA can potentially cause inflammation due to the surgery, it is not clear if it is that or the OA that causes the inflammation (Courties et al., 2015). This could potentially result in misleading conclusions on the possible effects of mechanical factors on systemic inflammation and OA progression. Interestingly, one study observed surgical inflammation in the synovium at the first week in the medial meniscal transection (MMT) rat model, but this resolved by week three (Salazar-Noratto et al., 2019c), suggesting that the inflammatory effect might reduce to zero if the study were to progress to later time points.

To mitigate these concerns, a non-invasive biomechanical model would be a suitable method to avoid the risk of unnatural internal joint biomechanics and localised tissue damage-induced inflammation. Such models usually initiate OA through causing a closed insult without disrupting joint function or breaking the skin and joint capsule (Christiansen et al., 2015). The earliest non-invasive model used an indenter to apply a single impact on the knee of the animal, leading to an intra-articular fracture of tibial plateau (Furman et al., 2007). Another traumatic, but non-invasive method is the compression model in

which the animal is positioned with upper and lower loading cups fixed to the calf, and a compressed axial loading is applied to cause the anterior displacement of tibia to overload the ACL to cause its rupture. This model has a similar mechanism as a sports injury and can result in rapid OA development (Christiansen et al., 2012). A comparative study between biomechanical (non-invasive) ACL rupture model with surgical (invasive) ACL transection model showed that these had very different effects on the joint mechanics, supporting the view that the invasive model cannot present the disease process well (Ramme et al., 2018). However, both of these described models produce direct intra-articular tissue damage (ACL rupture, tibial plateau fracture).

To avoid artefacts and further refine the models, the molecular markers of OA could be measured from different fluids by choosing specific biomarkers of cell degeneration and metabolism. The local response can be studied by obtaining biomarkers from the joint synovial fluid, while systemic information representing total body level are usually collected from serum and urine sample (Teeple et al., 2013). In a PTOA study, the RNA sequencing results of synovial fluids between pre-OA (before surgery), OA (after surgery) and sham-operated samples could isolate the driven alterations from an acute response to surgery and inflammation (Kemper et al., 2019). Following signalling pathway analysis, the dysregulation in key biomarkers revealed an acute inflammatory response to surgery, such as in immune response related inflammation and cell homeostasis, while the altered gene expression in the late-stages of OA was largely related to metabolic changes (fatty acid biosynthesis) and catabolic response (proteolysis) (Kemper et al., 2019). The biomarkers analysed from joint synovial fluid can sensitively reflect changes related to early PTOA while other body fluids, such as urine and serum, can be influenced by different diseases or metabolic conditions ongoing inside the body (Teeple et al., 2013). Serum biomarker sensitivity may be increased by adding a mechanical stimulus (such as moderate exercise) to the basic OA model; this may correspond to a later disease stage (Chu et al., 2018, Erhart-Hledik et al., 2012).

1.5.2.2 Developing less-invasive biomechanical models to better present the chronic overload OA phenotype to understand the early stages of OA.

Due to the lack of suitable models, little is known about the pathophysiology of the chronic progression of biomechanically induced OA, especially in the early stage. This is potentially significantly different from current PTOA models as their rapid OA induction is too severe to replicate human OA and the speed of OA progression means that it is hard to detect OA onset. Also, subchondral bone microfractures that are markers of early-stage OA, are hard to observe in current animal models (Ramme et al., 2016). Patients with chronic overloading OA without known major injuries and PTOA patients are also different in other ways such as muscle activation, gait pattern, knee mechanics (Robbins et al., 2019) and radiological characteristics (Swärd et al., 2010). Therefore, in order to address these two mechanically-induced forms of OA, (PTOA and chronic overloading OA), there are two points which

need to be further studied: 1. lessening the invasiveness/trauma for biomechanical models to replicate the early stage of PTOA, and 2. producing a non-traumatic method to study the chronic overloading OA phenotype.

In response to this, there are recent studies that have developed less invasive models with lower controlled single impact to better study the early stage of PTOA. For example, one study investigated a dose-response relationship through using arthroscopy to directly load the canine medial femoral condyle to create a controlled acute injury at multiple different loading levels (Brimmo et al., 2016a). Magnetic resonance imaging (MRI) and symptomatic assessments were used as outcome measures. An 18MPa impact replicates a "physiological" level of impact in daily activities, which is near the threshold (20MPa) for chondrocyte apoptosis; 40MPa causes an "athletic trauma" level, which leads to degenerative changes in animal models; and a 60MPa impact leads to a "severe trauma" level, which is associated with PTOA changes (Brimmo et al., 2016a). The lowest level successfully generates subchondral bone microfractures that closely mimic those found in patients' knees (Brimmo et al., 2016a). More severe soft tissue damage models have nuanced different levels of severity, for example, the destabilization of the medial meniscus (DMM) model is less severe than the surgical ACLT method (Glasson et al., 2007). The DMM model sections the medial meniscotibial ligament to offload the medial meniscus; this produces mid-to moderate OA (on a human OA scale) with subchondral bone defects occurring in 4 weeks (Glasson et al., 2007, Iijima et al., 2014, Culley et al., 2015).

Studies on the chronic overloading OA phenotype focus on developing a less-invasive model by the application of controlled, long-term slowly increased loads on the knee. These studies have utilised methods such as cyclic overloading (Ko et al., 2013), running exercise (Lapvetelainen et al., 2002, Lapvetelainen et al., 1995) and creating different angles of TO (Britzman et al., 2018b).

The cyclic compression loading model is an advanced method of OA induction and is the only model that imposes long-term repetitive small controlled elevated loading. This model fully replicates the non-invasive ACL rupture model, but with a reduced load that maintains ACL integrity (Poulet et al., 2011b). The method produces cartilage and subchondral bone damage: indicators of early-stage OA even with very low loads (Ko et al., 2013). This non-invasive cyclic compression model is one of the most promising models of the chronic OA phenotype model induced through mechanical overuse and has been used as an adjunct to the DMM injury model (Holyoak et al., 2019).

Another potential method for applying mechanical cyclic loads to joints non-invasively is through elevated exercise; this has been developed with treadmill or wheel running (Poulet, 2016). The level of exercise would need to be sufficient to induce or accelerate OA (Poulet, 2016) and has been found to increase the incidence and severity of knee cartilage damage in genetic mice or specific trains with OA susceptibility (Lapvetelainen et al., 2002, Lapvetelainen et al., 1995). These exercise models could enhance spontaneous models by reducing the time taken to induce OA. In addition, as the exercise model

directly represents the specific type of OA patients with frequent occupational activities and sports activities, this model could be further developed to study the effects of activity factors on OA development. However, exercise is not commonly used to induce OA in isolation, but it is considered a confounder and so is assessed in order to differentiate the effects of exercise from exercise plus concurrent OA disease (Frisbie et al., 2008).

TO is another promising biomechanical method to model the chronic overloading model of OA. At present it is the only way to use extraarticular surgery to create OA in an animal model. This has the advantage of a surgically induced method that precisely mimics the OA pathogenic mechanisms and avoids the joint damage of traditional intraarticular surgery. Additionally, it avoids the necessity of fixing the animal in a cycling loading machine for long periods. Clinically, osteotomy has been reported for over 2000 years (Smith et al., 2013b) and is used for treating knee OA to improve pain and function (Brouwer et al., 2014a) by unloading the affected knee compartment. The animal osteotomy models initiate cartilage overload by removing a wedge of bone in the proximal third of tibia, distal to the tibial tubercle (Coventry, 1985b). The transtibial valgus osteotomy model is most generally used, causing the mechanical axis to shift to the lateral compartment of the knee (Panula et al., 1997a). This method has been used to induce OA in dogs (Johnson and Poole, 1988b, Panula et al., 1997a), rabbits (Reimann, 1973a, Mankin et al., 1981b) and guinea pigs (Wei et al., 1998b). Results from these studies have shown various levels of degenerative changes on either the overloaded compartment alone (Mankin et al., 1981b) or on both compartments (Reimann, 1973a). However, the model is not popular and hasn't been well developed. The reasons for this may be the high level of surgical skill required, the cost, and the technical difficulties in keeping a stable osteotomy position during the post-operation rehabilitation (Panula et al., 1997a). A more recent study (Britzman et al., 2018b) has created a 30° varus proximal TO model in healthy rats. This successfully induced OA as measured using biomechanical evaluations, histology and C-telopeptides of type II collagen (CTX-II), a cartilage degradation biomarker. The optimal angles to investigate biomechanical factors in the natural course of OA are not known. Typically 30° malalignment is used in animal models as this causes OA changes within three months, yet clinical malalignment is much smaller than this (Cooke et al., 2007a). Animal biomechanics is significantly different from the human loading due to quadrupedalism and anatomical differences, so it is hard to compare clinical and animal model malalignment angles. Larger malalignments and incisions closer to the joint induce OA more quickly (Schipplein and Andriacchi, 1991b) and even larger angles produce other non-physiological effects such as subluxation (Wei et al., 1998b, Shoji and Insall, 1973b).

In this PhD, a biomechanical model that utilizes TO surgery to create the tibia malignment and induce OA is developed (Chapter 2), thereby eliminating the need for intra-articular surgical interventions. This approach seeks to more accurately represent the biomechanical factor induced chronic overload OA phenotype, particularly focusing on the early stages of the condition. By adopting this model, the aim is

to separate biomechanical effects from inflammatory responses inherent in OA models. Ultimately, this will enhance the understanding of biomechanical triggers in both the initiation and progression of OA.

1.6 Pathophysiology of osteoarthritis

The degenerative joint in OA disease is characterised by the loss of articular cartilage, thickening of subchondral bone, and the formation of osteophytes (Staines et al., 2013). This means the joint defects in OA can happen in both the cartilage (known as chondral defects) or underlying bone (osteochondral defects) (Lydon et al., 2017).

1.6.1 Articular cartilage pathological degeneration and remodelling mechanism in OA

There are two types of cartilage in the synovial joints, hyaline cartilage and fibrocartilage. The articular cartilage is the hyaline cartilage, visible on the surfaces of synovial joints with a glass-like (hyaline) appearance. Hyaline cartilage consists of chondrocytes (matrix producing cells) and the extracellular matrix (ECM). The ECM is a gelatinous material, rich in collagen 10-25%, glycosaminoglycans (GAGs) 5-15%, and water 70-80% (Horkay, 2012). Type II collagen accounts 90-95% of the collagen found in the ECM (Liu et al., 2021). GAG molecules are covalently attached to the protein core, forming the large aggregating proteoglycans (Figure 1-2). In adults, chondrocytes present a minimal anabolic and proliferative pattern, and the collagen fibres in hyaline cartilage persist throughout life with little replacement activity (Liu et al., 2021). The ECM composition varies with the layer changes. From the superficial layer (connected to synovial fluid) to the deep layer (connected to the subchondral bone), both the fibrillar component (collagen) and interstitial fluid (water) is decreases while the ground substance (GAGs) increases. In the deep layer, chondrocytes are becoming hypertrophic and they support the ECM mineralizing process by producing type X collagen. The medial and lateral menisci of the knee joint is fibrocartilage. Its matrix is abundant in densely braided collagen fibers, which makes it particularly strong against pressure. Few chondrocytes are arranged alongside the thick collagen fibers. Compared to hyaline cartilage, fibrocartilage has a significant proportion of type I collagen in addition to type II collagen (Armiento et al., 2019).

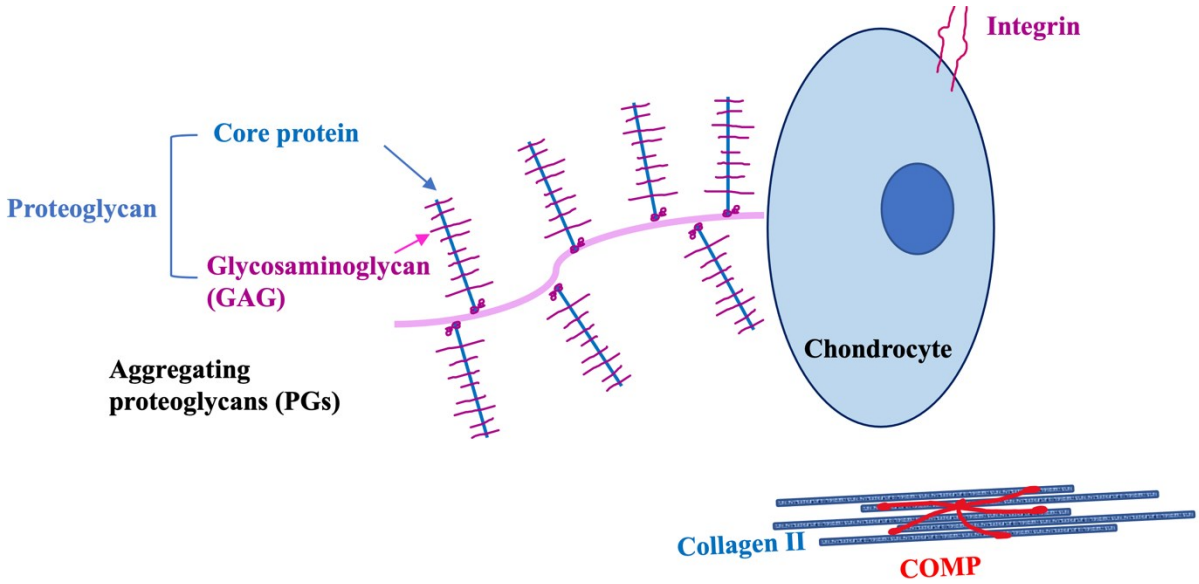

Figure 1-2 **Molecular components in the extracellular matrix (ECM) of articular cartilage.** Articular hyaline cartilage consists of a single cellular component, chondrocyte, embedded in a complex matrix which mainly includes collagen II and the large aggregating proteoglycans (PGs). PGs have a protein core to which glycosaminoglycan molecules are covalently attached. Cartilage oligomeric matrix protein (COMP), functions as a molecular bridge by binding collagen II fibrils11. Integrin is the receptor of mechanical stress, causing stress-induced signalling directly.

On a cellular and molecular level, mature healthy cartilage chondrocytes maintain a metabolic balance between matrix component synthesis and degradation. **Catabolic stimuli**, such as mechanical insults (including impact loads and joint injuries) and biological insults (like degradation products, inflammatory cytokines, and oxidative stress) (Loeser et al., 2016), or **anabolic stimuli** (such as non-destructive cyclic compression) can provoke chondrocyte reactions, activating biosynthesis and metabolism (Sandell and Aigner, 2001a) (Figure 1-3). This disrupts the balance. Catabolic factors enhance the production of matrix-degrading proteinases and proinflammatory cytokines from chondrocytes, while decreasing the production of matrix components and proteinase inhibitors. This cascade perpetuates cartilage degradation (Goldring and Otero, 2011). Growth and differentiation factors in cartilage metabolism, typically viewed as positive cartilage homeostasis regulators, usually stimulate chondrocyte anabolic activity and hinder catabolic activity. The most understood **anabolic factors** are Insulin-like growth factor-1 (IGF-1), TGF-β/bone morphogenetic protein (BMP) families, prostaglandin E2 (PgE2), and COMP (Goldring et al., 2017). **Catabolic cytokines** primarily include pro-inflammatory mediators like interleukin IL-1, IL-6, IL-8, IL-11 (Kokebie et al., 2011), and IL-1β (Svala et al., 2015). Furthermore, chondrocytes produce several proteolytic enzymes in latent forms that activate outside the cells in activation cascades. These include collagenases 1, 2, and 3 (MMP-1, -8, and -13); gelatinases (MMP-2 and -9); stromelysin-1 (MMP-3); membrane type 1 (MT1)-MMP (MMP-14);

and aggrecanases (ADAMTS-4 and ADAMTS-5) which specifically degrade cartilage matrix native collagens and proteoglycans (Miller et al., 2013a).

The underlying mechanism of the above molecular expression involves the activation of **intracellular signalling pathways** by various insults that regulate gene transcription in chondrocytes (Figure 1-3). For example, mechanical impact can result in local cartilage defects and the release of cartilage matrix products, which can directly activate stress-induced signaling via integrins and other receptor-mediated events in chondrocytes (Firestein et al., 2016). Indirectly, this mechanical stress also stimulates the synovial membrane, leading to the activation of macrophages and inflammatory cells such as T cells, which produce IL-1β and TNF-α, further activating some of the same signaling pathways (Blasioli and Kaplan, 2014). The major pathways involve signal transduction by stress-activated protein kinases (JNKs), p38 kinases, NF-κB, PI3K, and JAK/STAT signaling, causing aberrant expression of catabolic genes such as Interleukins, COX-2, MMPs, and ADAMTS. These genes are directly involved in early-stage cartilage repair and the degradation of type II collagen and aggrecans in the cartilage matrix (Goldring, 2012). In contrast, moderate dynamic compression (10%-20% strain amplitude) has anabolic effects, which can interfere with inflammation and inhibit the pro-catabolic response of cartilage to mechanical injury, and inhibit TNF-α, and IL-6 by blocking the associated signalling pathways (Zhang et al., 2014). Upregulated aggrecan and collagen synthesis (Li et al., 2013d) and downregulated Akt-dependent pathways (Niehoff et al., 2008) contribute to this effect. In summary, the disruption of chondrocyte gene expression equilibrium ultimately causes the initiation of cartilage degradation.

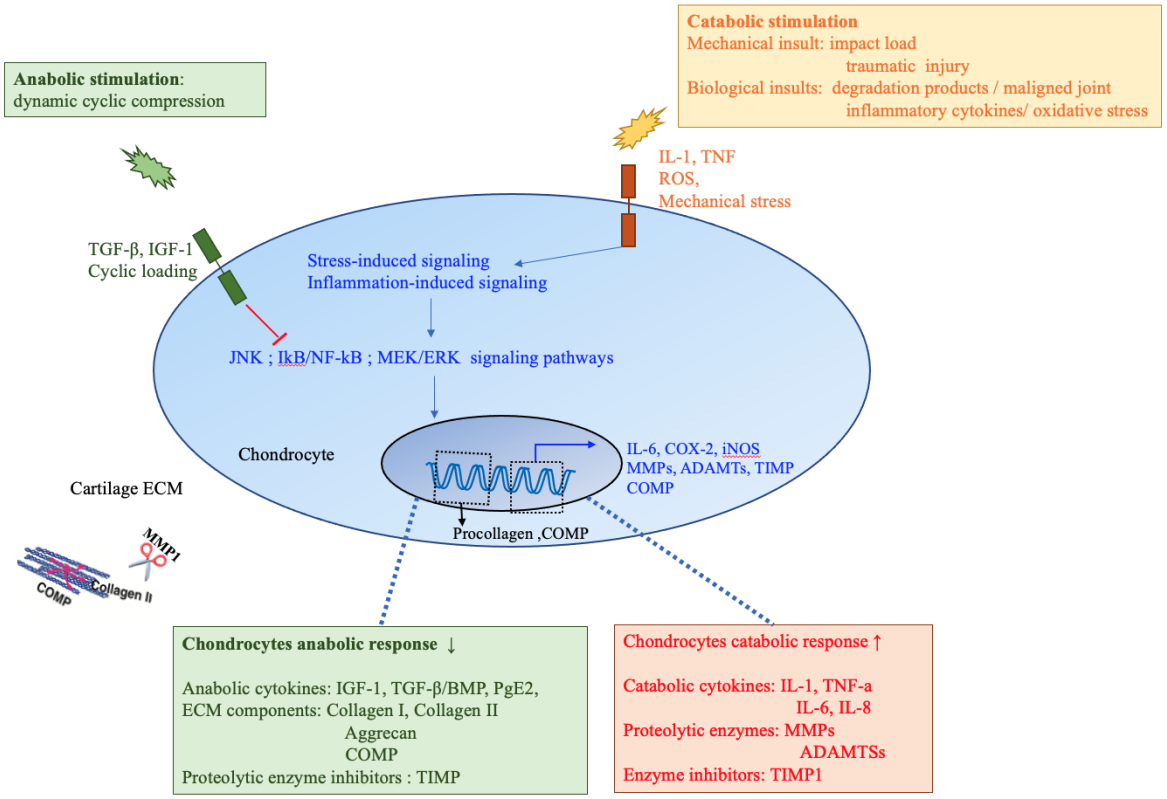

Figure 1-3 Schematic representation of various insults causing intracellular signalling pathways that regulate the level of molecular expression in chondrocytes.

Histologically, cartilage in OA is characterized by co-existing states of articular cartilage degradation and remodelling in the joint centre, and new osteophyte cartilage formation at the joint margins (Scharstuhl et al., 2002). For the cartilage degradation process, the proteoglycan (PTG) loss in the cartilage surface is the early event in the process, later stage is the cartilage fibrillation (cartilage repair) and clefts formation in the cartilage, the end stage is the erosion shown in the articular cartilage (Scharstuhl et al., 2002). Articular cartilage has a limited ability to self-repair (intrinsic healing capacity) when it is damaged. This is due to the low cells and high matrix to cell ratio in the content, and no direct blood supply and nerves in the articular cartilage environment. In some cases, a repair tissue is produced, but the repaired cartilage is fibrocartilage, which has inferior mechanical properties (e.g. less resilience) compared to hyaline cartilage.

Cartilage remodelling is a continuous process which includes cartilage degradation and cartilage regeneration (Li and Xu, 2015). Compared to the active bone adaptive remodelling process (described in section 1.6.2) , the mature articular cartilage and extracellular matrix, in general, is considered in a relatively quiescent condition (Li and Xu, 2015). For instance, collagen in mature cartilage has a slow turnover rate, taking 117 days for half of the collagen molecules in the cartilage to be degraded and replaced with new collagen molecules (Verzijl et al., 2000). But in OA, the cartilage remodelling can

be reactivated, both in non-calcified cartilage (articular cartilage) and calcified cartilage (located between articular cartilage and subchondral bone) (Wang et al., 2022). The cartilage in OA progressive disease reflects a failed cartilage remodelling (Brew et al., 2010). Recent evidence suggests that the cartilage repair might be a reactivation of the transient chondrocyte phenotype, which was in permanent phenotype in the healthy cartilage. This ectopic initiation plays a role in the OA development (Pitsillides and Beier, 2011).

Another mark of this pathologic remodelling is the presence of vascularisation in articular and meniscal cartilage. This vascular infiltration, coupled with nerve growth, is a key onset change in OA and potential pain source in OA (Ashraf et al., 2011b). This process stems from vascular channels—housing osteoclasts, osteoblasts, and blood vessels—extending from the subchondral bone, through calcified cartilage, into the cartilage's non-calcified layers during OA. As these channels get invaded by blood vessels, the surrounding cartilage undergoes ossification. While typical chondrocytes release anti-angiogenic elements, osteoarthritic cartilage changes, like the loss of proteoglycans, might weaken this protective mechanism. Simultaneously, chondrocytes in osteoarthritic cartilage amplify pro-angiogenic factors like VEGF, promoting osteochondral angiogenesis (Franses et al., 2010).

Osteophyte formation is also a characteristic of cartilage repair in OA patients (Xu et al., 2017). The complex process is still unclear to date. Some insights are that the cellular differentiation programme within osteophyte formation undergoes both the cartilage repair process and the fracture callus formation process in the endochondral ossification (Gelse et al., 2003, van der Kraan and van den Berg, 2007). Osteophytic chondrocytes originate from mesenchymal stem cells that reside in the periosteum. The mesenchymal cells are aggregated and committed to differentiate to cartilage cells (chondrogenic differentiation) for cartilage repairing, then the chondrocytes stop proliferating and becoming hypertrophic chondrocytes. Then the endochondral ossification happens, the hypertrophic chondrocytes secrete collagen, matrix metalloproteinase and vascular endothelial growth factor, to supporting angiogenesis and ECM calcification (Xu et al., 2017, Gelse et al., 2012b).

1.6.2 Subchondral bone defects and remodelling mechanism in OA

The subchondral bone, which describes the bone components situated below the calcified cartilage, also plays a crucial role in initiating and progressing OA (Castañeda et al., 2012). It can be divided into two unique anatomical divisions: the subchondral bone plate and the subchondral trabecular bone (Goldring and Goldring, 2010, Madry et al., 2010). When normal subchondral bone undergoes non-physiological strain due to the risk factors, it sparks a pathological cascade, resulting in OA changes in subchondral bone and the surrounding tissues. In early-stage OA, the subchondral plate becomes thinner and more porous, concurrent with initial cartilage degeneration. The subchondral trabecular bone also degrades, exhibiting increased separation and thinner trabeculae. Concurrently, microdamage manifests in both the calcified cartilage and subchondral bone, persisting throughout the entire pathological phase (Li et

al., 2013a) (Figure 1-4). In late-stage OA, both the calcified cartilage and subchondral plate thicken, with ongoing damage to the non-calcified cartilage. The subchondral trabecular bone becomes sclerotic, potentially a biomechanical adaptation in response to the widespread cysts and microdamage in the subchondral bone. However, this compromises the biomechanical structural integrity of the subchondral bone (Li et al., 2013a) (Figure 1-4) .

At the cellular and molecular levels, subchondral bone consists of cellular components and the extracellular matric. Cellular components are osteoblasts which synthesize the unmineralized extracellular matrix (known as osteoid), which eventually becomes mineralized bone; osteocytes: as the osteoid mineralizes, osteoblasts become trapped within lamellae in lacunae, maturing into osteocytes; and osteoclasts which resorb bone by releasing H+ ions and lysosomal enzymes. The extracellular matrix (ECM) comprises collagen fibres and related proteins, with type I collagen fibre as its primary component. At the onset of OA, mechanical forces such as pressure, shear, and elongation alter the properties of subchondral bone (Day et al., 2001b, Hayami et al., 2006b). These forces have a profound impact on the biological behaviour of cells in bone, triggering mechanotransduction cascades that result in tissue remodelling (Jones et al., 1995).

In OA subchondral bone, there's an increase in the populations of osteoclasts (for subchondral bone resorption) and osteoblasts (for subchondral bone remodelling). The overproduction of osteoclasts increased the expression of cathepsin K (CTSK), an essential enzyme expressed by osteoclasts for bone resorption (Soki et al., 2018). At the beginning of OA, the increased subchondral bone resorption, and the formation of extensive lacuna, leads to the release of growth factors such as BMPs, TGFβ (previously embedded in the bone ECM) into the subchondral bone marrow (Zhu et al., 2021). Subsequent activities of these factors contribute to angiogenesis, nerve innervation, and the recruitment of MSCs and osteoprogenitors. The increased osteoblast presence in the subchondral bone leads to elevated production of IL-6, IL-8, MMP-13, IGF-1, osteopontin, osteocalcin, TGF-β1, type I collagen, ALP, VEGF, and RANKL (also known as osteoclast differentiation factor). In contrast, the production of osteoprotegerin (OPG) is reduced compared to normal osteoblasts. This increased production induces the cascade of downstream events, including sclerosis, osteoclastogenesis, and angiogenesis (Wei and Bai, 2016). Although the overproduction of osteoid (synthesized by osteoblasts) leads to an increase in bone volume and density, it also results in reduced calcium binding to collagen fibers, thereby making the mineralization level insufficient. This abnormal mineralization is because of the overproduction of the homotrimeric (α1) 3 form of type I collagen by osteoblasts, which has less affinity with calcium than the (α1) 2 form of type I collagen (Gabusi et al., 2012). This unmineralized, immature bone results in the excessive osteoids and bone cysts in OA. The diminished material rigidity in the subchondral bone might increase cartilage degeneration during joint loading (Bianco et al., 2018, Li and Aspden, 1997).

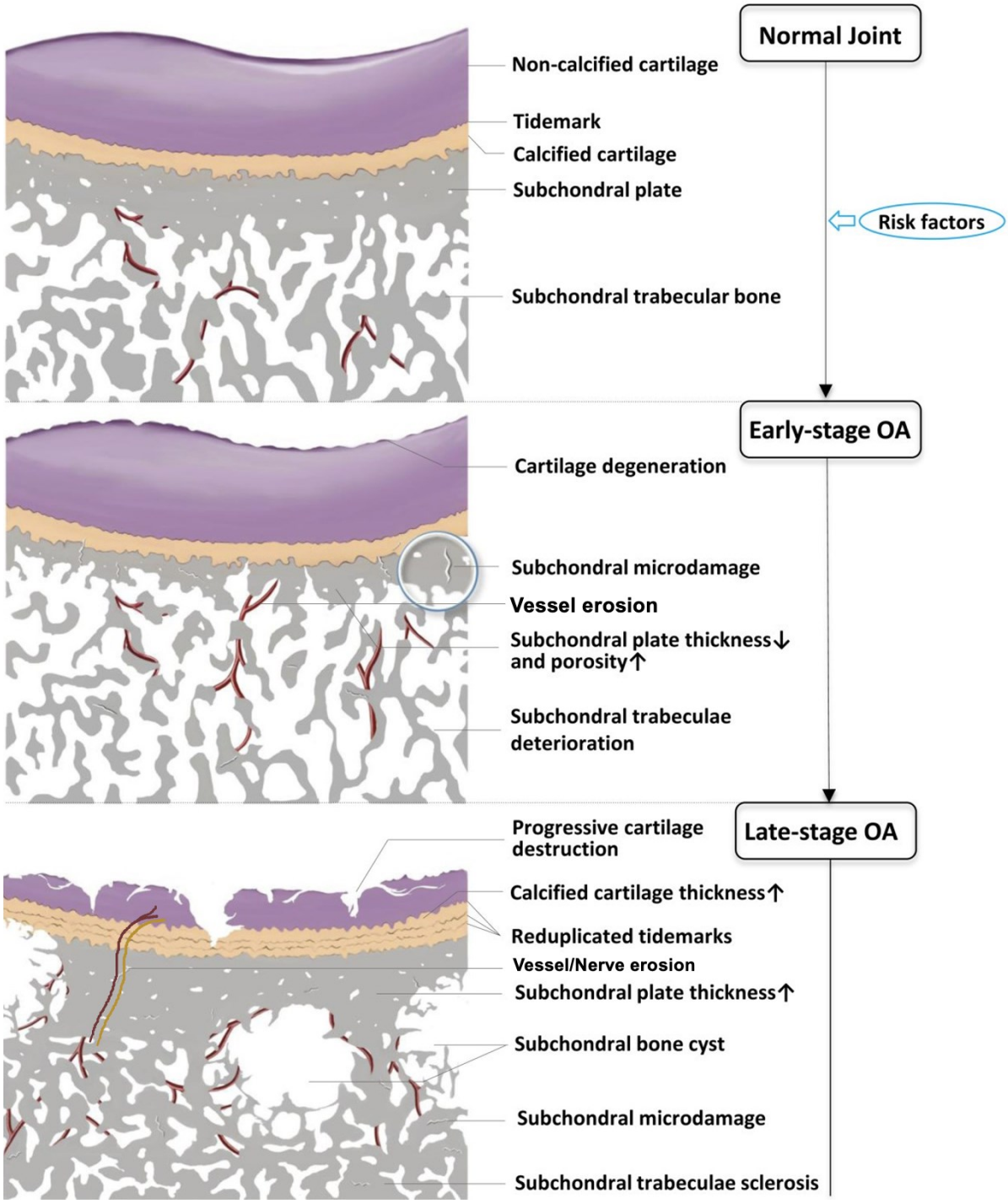

Figure 1-4 Hypothetical model of early and late-stage OA pathogenesis. Adapted from 'Subchondral bone in osteoarthritis: insight into risk factors and microstructural changes,' by Li et al., 2013. Available at https://doi.org/10.1186/ar4405.

The minor osteochondral defects have the ability to heal via recruiting bone marrow-derived stromal/stem cells present in the bone marrow to the damaged area. The pathological repair mechanism

of subchondral bone is based on the endochondral ossification mechanism of bone formation process. Bone formation (osteogenesis) is a conversion (transformation) process of a pre-exciting mesenchymal tissue into bone tissue. This includes two major conversion models: intramembranous ossification and endochondral ossification. The mechanism of osteochondral defect repair in OA is endochondral ossification. In this transformation, the aggregated mesenchymal cells differentiate into cartilage tissue, which is later replaced by bone. In other words, this is an indirect transformation process where a cartilage intermediate is formed and ultimately replaced by bone cells (Horton, 2003). The skeletal components of the vertebral column, pelvis, and limbs initially develop as cartilage and subsequently ossify into bone. Another transformation model (intramembranous ossification) is a direct conversion of mesenchymal tissue into bone where the process occurs mainly in the skull bone. In addition, mature bone architecture (without defects) can also remain in an adaptive remodeling process, which is related to the mechanical usage (Lanyon, 1996). Increased bone mass results from vigorous exercise, whereas disuse and inactivity lead to its reduction (Courteix et al., 1998, Zerwekh et al., 1998). Reports suggest that during bone remodelling, osteoclasts and osteoblasts work together to balance bone mass. This coupling of bone formation to bone resorption renews around 25% of trabecular bone volume annually (Huiskes et al., 2000, Frost, 1988, Rodan, 1991).

At the cellular level, the endochondral ossification process in subchondral bone defects relating to OA pathology can be described in an order of chondrocytes proliferating, becoming hypertrophic, and mineralizing (Figure 1-5): 1. Mesenchymal cells are aggregated and committed to differentiate to cartilage cells, inducing by transcription factors, (such as Paired Box 1 (Pax1) and scleraxis) to active cartilage-specific genes. 2. The committed mesenchyme cells are condensed and differentiate into chondrocytes. Chondrocytes divide rapidly to form a cartilaginous model of the bone, and secret cartilage extracellular matrix. N-cadherin and Sox-9 gene plays important role in this step. 3. The chondrocytes stop proliferating and the chondrocytes in the centre of the shaft becoming hypertrophic chondrocytes, and getting apoptosis. They mineralize their extracellular matrix by secreting more collagen X and more fibronectin into the ECM to induce calcium carbonate. 4. The chondrocytes' death allows blood vessels to enter, and the space becomes bone marrow. A group of cells surrounding the cartilage model differentiate into osteoblasts. Blood vessels bring in osteoblasts and begin producing bone matrix over the partially degraded cartilage. Similarly, the secondary ossification centre forms as the same steps with the vessels enter into the ends of bones. Finally, all cartilage is replaced by bone, with the cartilage tissue serving as a blueprint for the bone that develops (Horton, 2003).

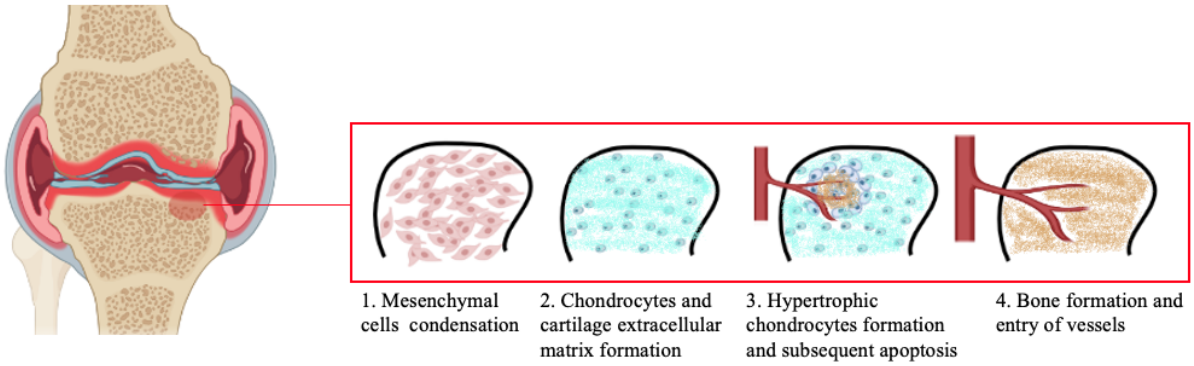

Figure 1-5 Schematic diagram of endochondral ossification (created with BioRender.com)

Therefore, the action of OA degeneration process can be summed up as both cartilage and subchondral bone physiological regulation and pathologic remodelling. Mechanical effects are now seen as essential factors in understanding the physiopathological mechanisms of OA (Stoltz et al., 2018).

Building on the cartilage and subchondral bone repair mechanisms in OA pathophysiology introduced above, the subsequent chapters of this thesis will investigate the contribution of mechanical stress to OA pathophysiology in a rodent model, utilizing histopathological, imaging, biomechanical, and molecular analyses.

1.7 OA treatment

OA treatment is mainly classified into conservative treatments which include pharmacologic, mechanical and physical treatment; and surgical treatment. Traditional approaches have mainly focused on utilizing medications known for their effectiveness in relieving inflammation and pain associated with OA, such as nonsteroidal anti-inflammatory drugs (NSAIDs), corticosteroids, or hyaluronic acid (HA) injections. Although these treatments provide temporary pain relief, they do not specifically target the underlying mechanisms responsible for OA progression (Brzusek and Petron, 2008, Filardo et al., 2016).

Increasing understanding of the molecular mechanisms involved in OA progression has grown hope for the potential use of targeted biologic agents in its treatment. As described in Section 1.6, OA stems from the cartilage (and subchondral bone) defects and progressive degradation cycle (an imbalance of catabolic and anabolic factors), driven by pro-inflammatory cytokines like interleukin-1β (IL-1β) and tumor necrosis factor-alpha (TNFα) (Goldring et al., 2008, Goldring, 2006). Certain growth factors such as BMP-7 exhibit protective effects against cartilage degeneration and have been noted in several clinical studies (Chubinskaya et al., 2007, Hunter et al., 2010a). There have been attempts to utilize

individual recombinant biologic agents, such as anti-IL-1β (Goldring, 2001, Malemud, 2010) anti-TNFα (Ohtori et al., 2015) IL-1Ra (Ohtori et al., 2015) BMP-7 (Hunter et al., 2010a), as OA treatments to interrupt the degenerative cycle and improve cartilage repair. However, the outcomes of clinical trials have generally been disappointing thus far. Animal experiments showed that numerous factors could aggravate osteophyte formation when these factors improves cartilage repair, such as bone morphogenetic protein 2 (BMP2), transforming growth factor beta (TGF-β), and Alarming S100A8/A9. (Xu et al., 2017).

This disappointment may stem from the complexity of the signaling pathways and differentiation mechanisms involved in articular cartilage formation. Maintaining artificial chondrogenesis in a stable, permanent cellular phenotype, as seen in healthy articular cartilage, is challenging. The cartilaginous tissue produced during cartilage repair typically only represents a transient stage in the process of bone formation. The main outcomes after biologics treatment are still hypertrophic chondrocytes and mechanically inferior collagen I/II fibrocartilage (Armiento et al., 2019). The challenges of cartilage repair in regenerative medicine limit the therapeutic methods (such as BMPs) currently available for OA treatment.

Due to this complexity and lack of clear mechanism of OA disease progression and cartilage repair, cell therapies have emerged as promising treatments. These avoid the limitations of biologic agents, which are typically restricted to targeting a specific molecular at a time. One approach is to boost the number of chondrocytes by stimulating bone marrow to encourage endogenous cell migration into the defect or by directly implanting mesenchymal stromal/stem cells (MSCs) (McIntyre et al., 2018). However, as therapies involving MSCs are mostly at the research level and the process of isolating them from bone marrow is complex, clinical trials in MSCs to date have largely been low-powered safety studies, often lacking a control group, resulting in high risk of bias and absence of high-level evidence (Pas et al., 2017).

Alternatively, cell therapies derived from a patient's own peripheral blood, such as autologous platelet-rich plasma (PRP) and the novel Autologous Protein Solution (APS) cell therapies, have gained widespread clinical use in the United States for treating knee OA. The use of APS is a promising new field. APS contains concentrated anti-degeneration cytokines that inhibit OA progression and have shown positive effects on OA (Vedi and Woodell-May, 2020). Interleukin-1 receptor antagonist (IL-1ra), as well as soluble forms of cell receptors for IL-1 and TNFα (sIL-1RII and sTNF-R), are present in high concentrations in APS. The presence of white blood cells (WBCs) can stimulate the production of these cytokines (King et al., 2021). However, the complexity of OA and a lack of understanding of its basic mechanisms, coupled with a shortage of comparable studies and both methodological and intrinsic limitations in these treatments, make the efficacy of this APS therapy challenging to critically appraise. Therefore, further investigation is required to clarify the effectiveness and underlying mechanism of APS therapy.

On the other hand, the idea that the progression of OA results from or is driven by mechanical factors has led to the widespread clinical used of mechanical treatment for OA. The core of the biomechanical-based method involves altering knee joint overloading or realigning the weight-bearing line (WBL) through conservative intervention or surgery to mitigate pain and delay disease progression. Physical approaches are commonly used in early-stage OA or for prevention, including footwear modifications (Hinman et al., 2008, Erhart et al., 2008), knee braces (Gaasbeek et al., 2007), and strengthening of the lateral hamstring muscle (Rutherford et al., 2010, Reeves and Bowling, 2011). For patients whose symptoms cannot be controlled by these means, surgical intervention is an option. Total knee arthroplasty and unicompartmental knee arthroplasty have been successful operations for primary and secondary OA. High tibial osteotomy (HTO) is more suited for younger patients without severe cartilage destruction, preserving a good range of motion in the knee and permitting demanding activities (Takeuchi et al., 2010). Thus, in addition to biomechanical factors playing a key role in OA initiation and progression, biomechanical-based treatments also present a promising avenue for halting OA progression. In this thesis, biomechanical-based treatments are considered as a way of inducing the OA, but the focus on treatment is biologics (Chapter 3).

1.8 Measures of disease outcome

There are three key diagnostic tools for biomechanically induced OA: biochemical, biomechanical and imaging markers to measure the biological, functional and structural changes during OA development (Andriacchi, 2012). Typically, microscopic tools (biochemical) are usually used in small animals, and macroscopic tools (biomechanical and imaging) are used in large animals and humans but have not been well studied to date (Kuyinu et al., 2016b). Characterizing biomechanical models and outcomes relies on measuring biomechanical factors, but biomechanical changes are very subtle in animal models, in particular in rodents due to their size and quadrupedalism, and a single mechanical factor might respond to both mechanical and inflammatory stimuli and cause multiple marker changes. These reasons hinder the early detection and characterization of this mechanically driven disease in animal models. Therefore, advanced diagnostic tools are needed for animal models in order to improve the understanding of this disease.

1.8.1 Histological measurement tools

Histologically, OA covers a group of joint diseases characterized by chondrocyte death, proliferation, and the regeneration/repair and degradation of cartilage matrix (Pritzker, 2003). Although OA can be categorized into various subsets based on aetiology, the symptoms and imaging findings in clinical diagnosis exhibit similar characteristics in advanced stages of OA. Histopathological assessment serves as a valuable tool for identifying advanced-stage OA and distinguishing differential features between subgroups (Pritzker et al., 2006).

Currently, histopathology remains the gold standard for cartilage evaluation and OA diagnosis in animal models. Safranin-O staining is the classic way to assess cartilage loss by staining the proteoglycan content of cartilage (Rutgers et al., 2010b). However, the differences between *in vivo* OA models make it challenging to standardize measurements. Studies that aim to correlate cartilage degradation, bone remodelling, and biomechanics with OA development and progression will require extra healthy groups for baseline data if there is not an accepted scoring system for comparison with the diseased group. In order to standardize measurement in OA research, Mankin et al. (1971) developed the Histological-Histochemical Grading System (HHGS), which considers cellular, staining, and structural changes in OA progression. However, issues such as poor reproducibility, standardized assessment, inter-observer variations, and limited investigation of early and intermittent OA stages were later identified as issues with the Mankin scoring system.

Subsequently, the Osteoarthritis Research Society International (OARSI) system was established as an alternative scoring system, adhering to the five cardinal principles of an ideal cartilage histopathology system: simplicity, utility, scalability, extendibility, and comparability (Pritzker et al., 2006, Rutgers et al., 2010a). This system is widely used for assessing OA in both human and animal models. OARSI has developed a species-specific histopathology grading system for OA animal models, focusing on changes in cartilage, synovial membrane, and subchondral bone, based on an extensive literature review (Aigner et al., 2010). This initiative aimed to promote consensus in scoring criteria across OA animal studies, however, the differences in induction methods may limit their relevance to naturally occurring OA in humans (as discussed in this chapter). The OARSI scoring system for human OA studies has seen further improvement in the 2015 OARSI recommendations for clinical trials, which updated the previous measures of OA baseline characteristics, including periarticular sites of structural changes (e.g., synovial membrane, subchondral bone), biochemical markers of inflammatory and metabolic mediators, patient physical function, and patient global status (McAlindon et al., 2015). Therefore, the development of the OA scoring system reflects researchers' increasingly comprehensive understanding of OA. In this thesis, Chapter 0 will discuss the histological results from the OA model established herein, validating the model for OA occurrence and establishing it as the gold standard for assessing OA states in this work. These results will be used in subsequent chapters to correlate OA states with the subchondral bone changes observed in micro-CT (Chapter 0), alterations in gait patterns (Chapter 6), and serum proteomic changes (Chapter 0).

1.8.2 Imaging measurement tools

Radiography stands as the classic gold standard and the most widely used way of OA imaging in the clinic and research (Roemer et al., 2014a, Kuyinu et al., 2016b). The key structural hallmarks in radiographs are joint space narrowing, osteophyte formation and subchondral sclerosis (Roos et al., 2011). Although there is a lack of sensitivity and not all joint structures can be identified, joint structural

pathology (joint space narrowing (JSN)) detected using X-ray is still the current golden standard in the clinical assessment of OA progression and the efficacy of therapies in FDA guidance (1999) (Roemer et al., 2014a).

Advanced non-invasive 3D imaging methods accelerate OA research as they non-destructively enable the assessment of the early state of OA to directly image cartilage and subchondral microstructure changes and synovitis. MRI is applicable for early diagnosis and prediction of OA because of its ability to visualise cartilage, subchondral bone marrow lesions (BMLs), synovium, menisci, and ligament, and quantify glycosaminoglycan in the cartilage (Wang et al., 2018b, Link et al., 2017b, Brimmo et al., 2016a). MRI techniques have been used experimentally in large animals (swine (Unger et al., 2018)) to small rodents (McErlain et al., 2012)) to characterise OA pathophysiology (Głodek et al., 2016), including the ability to obtain markers from machine learning approaches to predict cartilage lesion progression (Pedoia et al., 2017).

Microscopic computed tomography (Micro-CT) is another powerful 3D imaging technique for non-invasive joint structural evaluation, such as subchondral trabecular bone defects, healing and remodelling and has been used for early stage subchondral change quantification in rodents (Botter et al., 2006b). Enhancements include the use of contrast agents (Stewart et al., 2013), and novel segmentation to assess mineralised joint microstructural changes as a result of OA in rats (Ramme et al., 2017) .

Recent research has highlighted that changes in subchondral tissues - including subchondral trabecular bone deterioration, subchondral microdamage, and subchondral plate thickness - are potentially new structural markers in the early-stage of knee OA. Interestingly, these changes seem to come prior to the damage in the cartilage layer (Day et al., 2001b, Hayami et al., 2006b, Li et al., 2013c). MRI is adept at detecting BMLs associated with microdamage in the subchondral trabecular bone, as evident in micro-CT scans (Felson et al., 2001b). A dog model study that found that subchondral bone marrow oedema might be the earliest detectable sign of OA onset (Libicher et al., 2005b). This theory received partial validation from a matched case-control study in humans that found that subchondral bone lesions have the highest probability of predicting radiographic OA, when comparing with multiple other early-stage features such as cartilage or meniscal damage (Roemer et al., 2015). In this thesis, imaging tool Micro CT, will be used in Chapter 0 to characterize subchondral trabecular bone defects, remodelling during OA onset, progression, and post-treatment phases.

1.8.3 Gait analysis and quantitative biomechanical markers

Apart from the measurement tools described above, mechanical factors in biomechanically induced OA are receiving more attention because of their significant influence on joint loading with both experimental and computational tools being used. The changes in joint biomechanics and gait are mainly due to pain avoidance and joint dysfunction (e.g. joint degradation changes) (Johnson and Waugh, 1979).

Gait analysis, a biomechanical research method rooted in the principles of mechanics, processing methods, and an understanding of anatomy and physiology, provides a framework for studying walking function (Cappozzo, 1984, Whittle, 1993). Diseases affecting bones, nerves, and muscles can hinder walking ability. Hence, contrasting normal and abnormal human gaits is instrumental in studying diseases, as seen in severe knee OA patients (Sagawa Jr et al., 2013), after-stroke patients (Carmo et al., 2012a) and arthroplasty patients (Sander et al., 2012a).

Two types of analysis have been used to assess the joint function, static weight-bearing and dynamic gait analysis. In the standing state, it is easy to measure the functional loading on the two compartments of the knee. The medial side of the knee usually bears 60% of the force while the lateral side transmits 40% loading approximately (Kettelkamp and Chao, 1972). However, in the walking state, there is also an adduction moment that can increase the loading on the medial side; this varies between the different gaits (Johnson and Waugh, 1979). Thus, quantification of dynamic loading is more important. To obtain these measurements, it is necessary to digitize the state of the person's walking process. This analysis method is called gait analysis.

Gait analysis technology, using motion analysis, force analysis, and musculoskeletal dynamics, allows for the experimental quantification of mechanical factors, yielding insights into internal tissue loading (Eftaxiopoulou et al., 2014b, Cleather and Bull, 2011, Howard et al., 2000). Although gait analysis and biomechanical markers have been widely used in human studies (Whittle, 2014, Hamai et al., 2009, Heiden et al., 2009, Yakhdani et al., 2010), characterising animal mechanical behaviour is challenging. (Sagawa et al., 2013, Carmo et al., 2012b, Sander et al., 2012b). Despite these challenges, rodent gait models (Table 1-2) have been successfully developed and have been used for rheumatoid arthritis (Berryman et al., 2009b) and neuropathic pain behaviour research. Although these tools have not been widely applied in OA (Poulet et al., 2014a, Poulet et al., 2014b), they can provide a rich suite of biomechanical biomarkers (Table 1-2).

Table 1-2. Quantitative biomechanical analysis and markers in animal models

Analysis method	**Technique**	**Description**	**Key values/variables**	**Derived values**	**Ref**
Spatiotemporal	DigiGait; CatWalk	Space-Time changes during a gait cycle. Expressed in terms of the percentage of the gait cycle	stride length step length step width foot splay characterization of the paw print stance time stride time	Limb duty factor = stance time/stride time Gait symmetry = (right stride time-left stride time)/stride time Limb phase= (left fore foot strike time-left hind foot strike time)/ stride time	(Lakes and Allen, 2016, Vrinten and Hamers, 2003b, Eftaxiopoulou et al., 2014b, Allen et al., 2012, Jacobs et al., 2014, Jacobs et al., 2017)

			swing time stride time	Gait Compensation （shift to contralateral limb to protect injured limb）	
Kinetic (dynamic)	Fixed static force plate	The forces of motion due to physical (contact) and remote (gravity) interaction with the outside world	Ground reaction forces (GFR) that can be separated into three components: vertical forces (out of the floor), braking-propulsion forces (horizontal shear), mediolateral forces (lateral shear) Body segment accelerations, masses, and moments of inertia	Peak vertical force (largest vertical force achieved) and vertical impulse(product of force and time) Peak braking force and braking impulse Peak propulsive force and propulsive impulse 1st peak mediolateral force, 2nd peak mediolateral time and mediolateral impulse Intersegmental forces and moments, e.g. Knee flexion moment (KFM); knee adduction moment (KAM) Peak KFM KAM impulse Ratio of KAM and KFM	(Howard et al., 2000, Allen et al., 2012, Vilensky et al., 1994, Maly et al., 2015, Erhart-Hledik et al., 2015, Kean et al., 2011, Jacobs et al., 2017)
Kinematic	3D Optical motion tracking systems with reflective markers (e.g. Vicon) 3D biplanar video analysis	The measurement of three degrees of freedom (DOF) of rotation motion of all the joints, as well as three DOFs of translation for some joints	toe-off angle (propulsion angle); toe clearance angle foot clearance angle (limb position during swing) touch down angle knee flexion angle knee abduction/adduction angle femoral rotation angle sagittal plane (2D) joint range of motion (ROM) angles: knee ROM, ankle ROM, hip ROM	Coupled vector angle = knee adduction angle/flexion angle Swing velocity = stride length / swing time Peak angles during stance and swing phase Angular velocity patterns (characterised by peak flexion and extension velocities during swing phase)	(Eftaxiopoulou et al., 2014b, Lakes and Allen, 2016, Allen et al., 2012, Vilensky et al., 1994, Pereira et al., 2006, Zeng et al., 2017, Agrawal et al., 2019)
Computational musculoskeletal (Msk) modelling	Rigid body dynamic analysis combined with muscle modelling, e.g. OpenSim.	Virtually recreate the mechanical function of musculoskeletal tissue to quantify internal loads	Musculoskeletal geometry Gait kinematics data Gait kinetic data (external force: GRF) Body segment parameters	individual muscle forces individual joint contact forces	(Delp et al., 2007, Johnson et al., 2008, Britzman et al., 2018b)

			Muscle anatomy		
Computational finite element modelling	Stress analysis using software, e.g. MarcMENTAT, Ansys, Abaqus	Imaging to obtain geometry. Msk modelling to define boundary conditions. Software to quantify tissue and structural response in terms of stresses, strains and deformations.	Bone geometry of the knee Cartilage geometry after staining Muscle forces from msk modelling Joint contact forces from msk modelling	Localised cartilage, bone, ligament and menisci stresses and strains	(Zanjani-Pour et al., 2020a, Das Neves Borges et al., 2014, McErlain et al., 2011)

Gait analysis has been used in clinical assessment of osteoarthritis. Mobility impairment (disability) and pain are the primary symptom for OA patients. Knee flexion moment (KFM) and knee adduction moment (KAM) have been shown in clinical OA studies as surrogate measures of joint loading that are associated with cartilage thickness (Agrawal et al., 2019, Maly et al., 2015, Erhart-Hledik et al., 2015). KAM is more significantly correlated with severe OA, while peak KFM has a greater effect in the early-stages of OA (Erhart-Hledik et al., 2015, Zeng et al., 2017). Also, it is observed that OA knees have significantly reduced joint range of motion (ROM) (Zeng et al., 2017). Other derived measures such as KAM impulse and coupled vector angle have been shown to be associated with joint loading and structural severity of OA (Kean et al., 2011, Agrawal et al., 2019). These mechanics markers have been used in human OA gait analysis and are often applied in preclinical animal studies. For example, dynamic changes in ground reaction force (GFR) and gait asymmetry can be observed as early as one week post- surgery in the rat MMT model (Jacobs et al., 2017). Higher peak KAM and medial knee joint contact force and decreased peak flexion and extension velocities in the swing phase of gait have also been observed in studies (Britzman et al., 2018b, Vilensky et al., 1994). Gait compensation has also been found to be a biomechanical marker in a rat OA model (Allen et al., 2012). Combining spatiotemporal, kinematic and dynamic gait analysis can measure more subtle gait changes (Eftaxiopoulou et al., 2014b) and, when combined with musculoskeletal modelling (Britzman et al., 2018b, Johnson et al., 2008) and computational finite element modelling, this can lead to tissue-specific analysis of local biomechanical overload. This has been applied extensively in humans (Zanjani-Pour et al., 2020a) and presents potential in preclinical rodent models of chronic overload OA.

This thesis presents the spatiotemporal analysis method to identify OA gait markers and validate these markers as effective measures for OA severity and treatment assessment in this chronic overload OA model (Chapter 6).

1.8.4 Biochemical markers

Biochemical markers serve as essential tools in the investigative, prognostic, early-diagnostic, and therapeutic efficacy evaluation of OA, specifically concerning joint tissue (cartilage and subchondral bone) degeneration and remodeling (Rousseau and Delmas, 2007).

Most interest in developing OA markers focuses on those specific to cartilage degradation events. These events involve the disrupted metabolic balance between the synthesis and degradation of primary cartilage components, primarily concerning Type II collagen synthesis and degradation. These cartilage metabolic activities can be measured through several molecules and some of these molecules have been verified as markers for cartilage degeneration (Murphy and Lee, 2005). For increased collagen synthesis (cartilage repair) process (predominantly in the early OA stage), the most researched markers include Procollagen II N-terminal propeptide (PIIANP) (Shinmei et al., 1993), Cartilage Oligomeric Matrix Protein (COMP), and latexin. Type II collagen and COMP have become the most commonly chosen early indicators in animal research (Legrand et al., 2017, Appleton et al., 2007, Orhan et al., 2021). Markers for collagen degradation include entities such as Coll2-1 and C-terminal telopeptide of type II collagen (CTX-II). CTX-II has become the most acknowledged biomarker in both human (Meulenbelt et al., 2006b) and animal studies (Duclos et al., 2010b, Legrand et al., 2017). It often acts as a stand-in for histological assessments (Legrand et al., 2017). Additionally, evaluating the presence and quantity of degradative enzymes can indicate the cartilage tissue's catabolic state. Enzymes involved in the degradation process, such as matrix metalloproteinases (MMP-13 and -3), and aggrecanases (ADAMTS-4 and -5) are also noteworthy. From the perspective of consistent inflammation and mechanical stress on chondrocytes, Interleukin-6 (IL-6), interleukin-1β (IL-1β), tumour necrosis factor-alpha (TNF-α), and Coll2-1NO2 (indicative of oxidative stress), play vital roles (Legrand et al., 2017, Appleton et al., 2007, Orhan et al., 2021).

In evaluating OA through bone markers, researchers are expanding upon existing bone markers in assessing bone metabolic and turnover activities. This turnover is a continual process aimed at removing defective bone and replacing it with newly synthesized material (Chapurlat and Confavreux, 2016). These markers primarily fall into three categories: 1. Markers linked to the regulation of osteoblast differentiation and bone formation: this category includes bone morphogenetic proteins (BMP-2, BMP-7) (Ma et al., 2020), receptor activator of nuclear factor kappa-B ligand (RANKL) /RANK/osteoprotegerin (OPG) system (Walsh and Choi, 2014), periostin (POSTN) (Chapurlat et al., 2000), fibulin-3, and Fibronectin (FN1). 2. Markers indicative of osteoclastogenesis, bone sclerosis and bone resorption: these include type I procollagen (PINP) (Chapurlat and Confavreux, 2016), Sclerostin (Krishnan et al., 2006), and WNT1 inducible signaling pathway protein 1 (Krishnan et al., 2006)) (Chapurlat and Confavreux, 2016). 3. Enzymes degrading ECM in bone tissue: Type I collagen is the major component of the ECM in bone, the degradation of which can be tracked by Cathepsin K, a crucial catalytic enzymes expressed by osteoclasts (Chapurlat, 2014). These bone markers are emerging

as potential new OA markers. These bone markers offer insights into the relative differentiation of the metabolic activity of subchondral bone and trabecular bone to compare with the traditional joint structural changes from imaging (Chapurlat and Confavreux, 2016).

Despite the comprehensive range of available markers, the field still lacks a universally accepted gold standard biochemical marker (Table 1-2) (Parra-Torres et al., 2014a, de Sousa et al., 2017b). The pursuit for the identification of specific biomarkers of biomechanically induced OA still continues (Roemer et al., 2014a). More recently, advanced high-throughput methods and proteomics techniques have facilitated the discovery of new OA biomarkers in both human and animal studies. In this thesis (Chapter 0), a semi-quantitative proteomics method will be used to characterize proteomic profile changes during OA onset, progression, and post-treatment, in rat serum and articular cartilage within the OA model, attempting to discover biomarkers.

In summary, the aim of this thesis is to develop a tibial malalignment model of OA and use this to characterize mechanically-induced OA and evaluate early pharmacological intervention. The specific aims are to:

- Establish a tibial malalignment-induced OA model to create a model of chronic primary OA resulting from natural chronic overloading, with varying levels of severity (Chapter 2);
- Characterize the OA joint changes in this model and the effect of the pharmacological interventions (Chapter 3) through histopathology (Chapter 4), radiographic structural changes (Chapter 5), gait patterns (Chapter 6), and proteomic changes (Chapter 7).

2 Surgical model development

2.1 Summary

This chapter details the methodologies used to develop the model of malalignment induced OA in rats. The dissection result confirmed the successful induction of varus tibial malignment at a specified level, five months post the tibial osteotomy surgery.

2.2 Introduction

High tibial osteotomy (HTO) is a surgical method to move the loading from one compartment of the knee to another, by changing the mechanical axis (Figure 2-1). This has been used to *treat* (offload one compartment) OA as well as *induce* (overload one compartment) OA.

2.2.1 Clinical use of high tibial osteotomy

In clinical practice, the concept of osteotomy for treating limb varus and valgus deformities has existed for over 2000 years (Smith et al., 2013a). More recently, it has also been utilized for treating knee OA to improve pain and function (Brouwer et al., 2014b). However, the emergence of successful knee arthroplasty surgery has led to a relative neglect of osteotomy (Rönn et al., 2011, Amendola and Panarella, 2005). Nevertheless, suboptimal outcomes of arthroplasty in young and active individuals have sparked a resurgence of interest in osteotomy surgery (Flecher et al., 2006). Although osteotomy principles and operative techniques exist, standardization has yet to be achieved. Upper tibial osteotomy is the most commonly used technique in clinical settings, as the osteotomy through the cancellous bone of the metaphysis allows for faster healing and correction closer to the actual deformity (Coventry, 1985a). Furthermore, an upper and more proximal osteotomy can be easily converted to a total knee replacement (TKR) in the future (Smith et al., 2013a).

Currently, HTO has become a widely recognized treatment option for medial compartment OA of the knee, particularly for younger, active patients who are in the early stages of OA and want to return to a high level of activity (Herman and Giffin, 2016, Santoso and Wu, 2017). Patients receiving HTO can benefit from natural joint preservation, without the need for additional intra-articular surgery, and physical loading being almost completely unaffected (Figure 2-1). This leads to the model idea that HTO could also be used to investigate early OA without intra-articular intervention in an animal model.

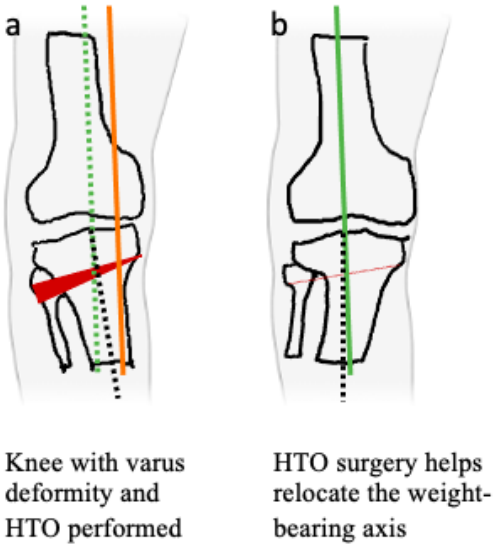

Figure 2-1. High tibial osteotomy for knee osteoarthritis pain in active people: (a) in a varus knee, the load-bearing axis (mechanical axis, green line) goes through the medial compartment (orange line); HTO surgery is the removal of the bone indicated in red. (b) HTO realigns the weight-bearing axis of the lower limb towards the lateral compartment thereby decreasing contact pressures and loading transmission on the medial compartment and correcting the varus deformity. In some cases even where there is low varus deformity, HTO can still be used to offload the medial compartment.

2.2.2 TO used in animal model

In an opposite sense, osteotomy has been developed as a method for *inducing* OA in dogs, rabbits, and pigs over the past 30 years (Table 2-1). However, this model has not been widely spread and well developed. This is likely attributed to technical surgical complexity as well as cost. Also, there are technical challenges in maintaining a stable osteotomy position during post-operative movement (Panula et al., 1997b). The osteotomy model removes a specific wedge of bone in the proximal third of the tibia, distal to the tibial tubercle (Coventry, 1985a). This then shifts the mechanical axis during gait to overload the healthy part of the knee. Among the various osteotomy models, the transtibial valgus osteotomy model is the most commonly utilized, leading to a mechanical axis shift toward the lateral compartment of the knee (Panula et al., 1997b). By making a larger angle and positioning the incision closer to the joint, greater loading changes can be induced in the knee joint, resulting in a more rapid induction process of OA (Schipplein and Andriacchi, 1991a). While neutral mechanical alignment in humans ranges from 0° to 2° varus (Cooke et al., 2007b), most studies opt for a 30° malalignment in the osteotomy model, a more severe angle than typical clinical malalignment. Researchers use this severe malalignment as it facilitates the development of rapid OA changes in approximately 3 months, enabling cost-effective biological studies. This is also the standard induction time utilized for most other surgically induced animal models of OA.

2.2.3 Literature reviews of reported TO animal models

Among the various osteotomy models, the transtibial valgus osteotomy model is commonly used (Table 2-1). Reimann (1973b) conducted the first reported attempt of an osteotomy model on rabbits using a 30º medially arched incision in the proximal tibial area (1973b) . Histological examination after 10-12 weeks revealed clear degenerative changes in the cartilage of the lateral tibial and femoral condyles (Reimann, 1973b). Subsequently, Mankin et al. (1981a) performed a 20º proximal tibial osteotomy on rabbits and observed that the histological grading indicated 2.4 times greater overload in the lateral compartment compared to the medial compartment. In dog osteotomy models, Johnson and Poole (1988a) removed a 7mm wedge of bone (to create an average of 30º valgus) to induce proximal tibial osteotomy. Histological evidence demonstrated the production of degenerative lesions in both the lateral and medial compartments of the operated leg and the control leg. A later study shows that this 30º valgus proximal tibial osteotomy in dogs was a slow progressive OA model, capable of detecting early-stage changes (such as cartilage fibrillation) after 7 months using Mankin's grading system (Panula et al., 1997b). A guinea pig osteotomy model was created using a mid-diaphyseal femoral osteotomy to create a 30º valgus malalignment. Justification for cutting the bone at this level included the suggestion that this procedure avoids surgical intervention near the metaphysis, which may impact the epiphyseal bone but results in less pronounced and slower changes in the knee compared to the conventional proximal tibial osteotomy. After 3 months, histological evidence revealed decreased fibrillation and subchondral bone thickness medially, and increased thickness laterally (Wei et al., 1998a).

Apart from older research papers dating back two decades ago, there have been relatively few recent studies that specifically investigate osteotomy models, particularly in small animals. A recent study introduced a 30º varus proximal tibial osteotomy model in healthy rats, successfully inducing OA. This model was assessed using biomechanical evaluation (gait analysis) and measurement of the cartilage degradation biomarker CTX-II. The authors proposed that this model better represents idiopathic OA in humans compared to other intraarticular techniques (Britzman et al., 2018a).

Table 2-1 Tibial Osteotomy animal models presented in the literature.

Year	species	Surgical method	Main findings	Ref.
1973	Rabbit	30º valgus proximal tibial osteotomy	Histologically, evident initial degenerative changes were observed in the cartilage of the lateral tibial and femoral condyles.	(Reimann, 1973b)
1991	Rabbit	20º valgus proximal tibial osteotomy	OA changes in the overloaded lateral compartment present a 2.4-fold greater magnitude compared to the medial compartment.	(Mankin et al., 1981a)
1988	Dog	Remove 7mm wedge of bone to cause proximal tibial osteotomy (a mean of valgus 30º)	The osteotomy model is capable of inducing degenerative changes in cartilage.	(Johnson and Poole, 1988a)
1997	Dog	30º valgus proximal tibial osteotomy	The osteotomy model present slow-progressive form of OA.	(Panula et al., 1997b)
1998	Guinea Pig	30º mid-diaphyseal femoral valgus osteotomy	The femoral osteotomy model induces a less severe and slower knee changes compared to the conventional tibial osteotomy. In the early stages of OA, bone changes become more prominent than cartilage alterations. There is a decrease in cartilage failure medially and an increase laterally.	(Wei et al., 1998a).
2018	Rat	30º varus proximal tibial osteotomy	Tibia osteotomy induces cartilage degeneration on healthy rodents	(Britzman et al., 2018a)

2.2.4 The chosen model to induce OA

Although valgus deformity was commonly chosen in previous studies to induce OA lesions, this project used the varus malalignment model for two main reasons. Firstly, varus malalignment in humans has a higher associated risk of OA compared to valgus malalignment (Brouwer et al., 2007a, Sharma et al., 2010). In the natural alignment of the knee joint, the medial compartment bears approximately 55%-70% of the load (Schipplein and Andriacchi, 1991a). As a result, the cartilage on the medial side is more

susceptible to degeneration. The natural progression of OA in a guinea pig study also demonstrated that OA initially developed in the medial central part and progressed towards the lateral and peripheral areas (Wei et al., 1998a). The second reason is related to the surgical procedure's complexity and potential complications. The varus model allows for the incision to be made from the inner side of the tibia, distal to the tibial tubercle. This approach helps minimize the risk of common peroneal nerve injury (Saragaglia et al., 2011).

2.3 Materials and Methods

2.3.1 Experimental groups and research design

This study was approved by Home Office (UK) and Central Biomedical Service of Imperial College London (PPL Number: PD51CDDA3), and follows the 3Rs principle as stipulated by the *Animals (Scientific Procedures) Act 1986*, which regulates the utilization of animals for research purposes in the UK.

In order to minimize the unnecessary use of animals, a power analysis was conducted prior to the study to determine the minimum required sample size for each group. The study by Britzman et al (2018a) provided quantification of the serum biomarker (CTX-II) in a rat model of OA induced by a 30º osteotomy. The standard deviation and mean value of CTX-II serum levels at week 10 in the Sham and 30º osteotomy groups were used for the power analysis. Both G Power Software (Faul et al., 2009) and Piface software indicated that a minimum of 3 animals per group was necessary to achieve 90% power in detecting significant differences at a significance level of 0.05.

Histology scores, knee joint contact force, and ground reaction force at week 10 from Britzman et al.'s article were also used for power analysis. The results consistently indicated that a minimum of 3 animals per group would yield over 90% power in detecting significant differences at the 0.05 level of significance. Considering that there are 7 groups in total in the study in this thesis (described later on), the power analysis suggests a total sample size of 21 rats.

However, it is important to account for potential attrition (or death) of animals, which is expected to be a maximum of 18.2% and primarily occurs within the first 2 week after surgery (Britzman et al., 2018a). According to (Britzman et al., 2018a), at the end of the first 2 weeks, 4 rats were culled due to sub-optimal osteotomies or surgical complications. Therefore, the formula by Charan and Kantharia (2013) was used to calculate the corrected sample size in this study:

$$\text{Corrected sample size} = \text{Sample size} / (1 - [\% \text{ attrition}/100]),$$

leading to a corrected sample size in this study of 26 rats.

In summary, the power analysis determined that a minimum sample size of three rats per group was required for this study. Taking into account the potential surgical complications leading to the culling

of rats from the groups, the study was started with a total of 26 rats divided into seven groups. This allocation ensured that each group would have a minimum of three rats available for data collection at the outset.

A total of 26 Sprague Dawley (SD) rats (Charles River Laboratories, Portage, MI, USA), aged 14 weeks and weighing approximately 400 g at the initiation of the experiments, were used for this study. The animals were housed in ventilated innovate cages, accommodating three animals per cage, and were provided with sawdust bedding. The housing environment maintained a controlled temperature and humidity, with a regular 12-hour light/dark cycle. Animals were allowed to move freely in cages and provided free access to food and water. Prior to their inclusion in the 20-week study, the animals underwent a one-week acclimation period.

Animals were randomly assigned to 3 groups. A tibia osteotomy surgery was performed in the right proximal tibia and fixed with either a 30º, 10º or 0º plate. A group of 10 rats received a 30º tibia osteotomy (Group 1); 10 rats received a 10º tibia osteotomy (Group 2), and the other 6 rats underwent sham surgery, a 0° osteotomy (Group 3) (Figure 2-2). Several rats were excluded from the study due to wound breakdown following the surgery, and thus were not included in the subsequent analyses. Based on a previous study, the onset of osteoarthritis (OA) in this model initiated at approximately 10 weeks after surgery (Britzman et al., 2018a). Hence, early pharmacological intervention was initiated at 2 weeks prior to the expected OA onset (at week 8) to prevent OA. Within the 10º tibia osteotomy group and the 30º tibia osteotomy group, one-third of the rats (n=3) were intra-articularly injected with 50 µl of APS into the knee joint on the operated leg, while another one-third were injected with BMP-7 (Figure 2-2) (see Chapter 3 for description of the choice of intervention). Gait analysis and blood collection were conducted pre-operatively and monthly thereafter. The collected blood samples were analysed using liquid chromatography-tandem mass spectrometry (LC-MS; see Chapter 7). At week 20, after sacrificing the rats, micro-CT imaging (Chapter 5) and cartilage sections (Chapter 4) were obtained. Figure 2-2 illustrates the number of rats and the timepoints for intervention and assessments. Due to various reasons (surgery complications, treadmill performance, image quality etc.), only n=3 for each group had all complete data (gait, imaging, and proteomics) at the end and were taken into account in the final result. The cartilage loss was assessed using Toluidine-blue staining, which served as the standard for determining the onset of OA. Subchondral bone measurements using micro-CT, proteomics analysis from serum samples, and gait analysis (see Chapter 6) was performed to establish a biochemical and biomechanical profile for characterizing the onset and progression of OA.

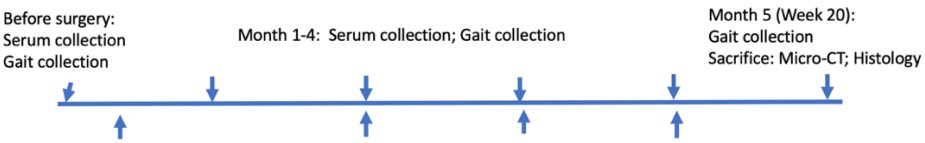

Groups	Sham (n=3)	10°TO (n=6)	30° TO (n=9)
No treatment	3	3	3
BMP-7	0	3	3
APS	0	0	3

Figure 2-2. Experimental groups and the timepoints of intervention (BMP-7, APS) and assessments

Young male mice only were used in this study due to the differences in susceptibility to OA joint damage between sexes and ages. Scientists are increasingly recognizing the importance of sex, like age, as a biological variable in the pathogenesis of joint damage (Malfait and Miller, 2020, Boyan et al., 2013). A recent study investigating sex and age interactions in the rat MIA model found that MIA induced more pronounced deficits in older rats, particularly in aged females (Ro et al., 2019). Conversely, another study using the C57BL/6J mice MMT model found that MMT caused more severe cartilage damage in young males than in females (Temp et al., 2020b). Additionally, older rats exhibit more pronounced differences between males and females. Therefore, in order to use a limited number of rats, a single sex was chosen to mitigate heterogeneity. For future studies, both sexes and various age stages need to be considered.

2.3.2 Operative procedure

2.3.2.1 Animal husbandry and pre-surgery care

26 healthy male Sprague-Dawley rats (12 weeks old, 400g) were used in this study. The animals were placed in quarantine for 1 week. To familiarize them, the researcher handled each animal for a period of 10 minutes twice daily for seven days.

2.3.2.2 Pre-surgery care

Animals were offered untreated jelly for 2 days prior to surgery to acclimatise them to Buprenorphine jelly in the surgery. Animals were kept in groups of 3 in 1500cm^2 individually ventilated.

2.3.2.3 Osteotomy surgery

This surgical method is based on the work of Britzman (Britzman, 2017) with some improvements. The surgeries were performed by the PhD student (Leah Xu) and a collaborator, Dr Ibidumo Igah. The following steps outline the surgical procedure and are shown in Figure 2-3:

1. Prior to commencing the surgery, all equipment was autoclaved to ensure sterility. The procedure was performed by a surgeon (conducting the surgery,I.I or L.X) and a surgical assistant (assisting the surgery, maintaining aseptic techniques and monitoring anaesthesia, vital signs, and animal well-being, Olivier Dubois). Strict sterile protocols were adhered to.

2. After confirming the availability of all equipment, the surgical area was separated from the recovery area to maintain a sterile surgical field throughout the procedure. The surgeon prepared the surgical site by using sterile drapes to cover unprepared parts of the animal and adjacent surfaces to prevent contamination. Sterile instruments were placed in an instrument tray or on a sterile surface. The multisaw and drill were placed in their sterile drapes, ready for use by the surgeon.

3. During the surgery, the animal was anesthetized in an inhalation chamber using 5% Isoflurane in O^2. Subsequently, the animal was placed on a heating pad in the non-sterile area, and anaesthesia was maintained using an inhalation mask with 2% Isoflurane. A subcutaneous injection of 0.05 mg/kg buprenorphine was administered after induction and before the surgery began. Additionally, 2 mg/kg of bupivacaine was injected subcutaneously along the incision site after suturing. Cornea ointment was applied to protect the eyes.

Analgesia and antibiotics were administered for the following 10 days: 0.3 mg/kg Buprenorphine was given orally (mixed with jelly), and 5 mg/kg Baytrill was administered via drinking water after the surgery.

The pedal withdrawal reflex, assessed by pinching the tail and the metacarpal region of the hind foot, was tested after the induction of anaesthesia. The absence of a pedal withdrawal response served as the primary method for assessing the depth of anaesthesia. The respiratory rate (60-80 breaths/min) and body temperature, measured using a rectal thermometer (35.8-37.5°C), were included in the overall evaluation of vital signs during surgery. If any two parameters were outside the acceptable range and did not improve with supportive measures, euthanasia was considered. The decision was made by two individuals (surgeon and assistant) after assessing the animal.

4. Throughout the procedure, any animals with unstable vital signs were provided with appropriate analgesia or other supportive measures, and consultations with the Named Veterinary Surgeon (NVS) were conducted. If symptoms persisted, euthanasia was performed under Schedule 1. The respiratory rate (60-80 breaths/min) and body temperature from the rectal thermometer (35-37.5°C) were continuously monitored during surgery. Euthanasia was considered if any two of these parameters were outside the acceptable range and did not improve despite supportive measures; the decision was made by the surgeon and assistant.

5. The animal's fur was clipped liberally around the left leg, removing the bulk of the dirt and then cleaned using dilute povidone applied to sterile gauze. The animal, heat pad and inhalation mask were then moved to the surgical table and final skin cleansing performed. At this point, the surgeon performed

a standard ‘gown-up’ procedure. After gowning up, the surgeon was deemed to be sterile and care was taken to avoid touching any non-sterile items. The assistant monitored the anesthesia. If any non-sterilise items were touched, then the surgeon changed into a new sterile pair of gloves before continuing. At this point a final check was made that the animal was adequately anesthetized by checking the pedal withdrawal response.

6. Once the animal was prepared, a skin incision was made on the left leg, just lateral to the tibia, running from the anterior of the ankle to just anterior of the knee joint. Referring to the surgical procedure from previous animal models and clinical experience in humans, a longitudinal incision was made from the tuberosity, extending downward along the tibial shaft. This exposed the upper ¾ of the medial side and the upper ⅓ of the lateral side of the tibia. Blunt dissection techniques were used to expose the tibia, taking care to avoid excess tissue trauma and muscle damage.

A surgical plate (3.5mm broad, 1mm thick, 25mm length, 5-hole) was inserted against the lateral side of the tibia, aligning the top edge as anterior on the tibia as possible. Three holes were drilled (using a 1.1mm drill) through the top hole of the plate and through the tibia. A short sized screw (6mm) was used to secure the plate in place, acting as a guide for the osteotomy. Using the middle of the plate as a guide, a surgical saw was used to cut halfway through the tibia perpendicular to the bone, running from the medial to lateral side. A second cut was made approximately 10mm below the first cut, at an angle of 10° or 30°, approaching the first cut. Slowly and sequentially advancing with the saw, both cuts were joined until they met, resulting in the removal of a triangular section of bone. The osteotomy cut was performed 1.5 cm below the tibial plateau (0.5 cm below the patellar tendon), distal to the tibial tuberosity (Figure 2-3). This surgical technique was optimized through extensive practice in cadavers.

7. At this point, the two sections of the tibia should have been aligned, ensuring a smooth osteotomy cut and an appropriate angle. If necessary, the bone surfaces were smoothed or adjusted using a saw or file, however every effort was made to ensure that this was not required as it could lead to unnecessary tissue trauma.

8. The plate was then removed from the animal, and a pre-bent plate with an angle of 10° or 30° degrees was implanted from the lateral side. The plate was bent to the exact alignment before the surgery by a technician using 3D-printed 10° or 30° moulds in the mechanical workshop. Once the bent plate was reattached to the bone using the pre-drilled holes, and the two halves of the tibia were positioned to conform to the plate, a hole was drilled through the bottommost hole on the plate, and a screw was inserted to hold it in place. As the rat tibial bone is not straight, a straight plate cannot fit the bone perfectly. Efforts were made to position the top edge of the plate as proximal to the tibial plateau as possible. The bottom hole was not pre-drilled. Ultimately, this resulted in the tibia being placed in a varus position of approximately 10° or 30°.

9. The remaining hole was then drilled, and screws were placed through all the holes as previously described. All screws (1.5mm thread, 6mm-12cm length depending on the size of the rat) were tightened to ensure stable plate fixation without penetrating too deeply into the muscle. The length of the screws was maintained to cross both cortices.

10. Sterile saline was used to clean any excess blood. The muscle was closed using a tagging suture with 6.0 Vicryl. The skin was closed using an intradermal suture (continuous pattern) with 4-0 Ethibond Excel. Skin closure was reinforced with glue after the nylon 4-0 nonabsorbable suture. The fascia was left open to minimize the risk of compartment syndrome. Subcutaneous administration of bupivacaine was performed at the end of the surgery after suturing.

11. The isoflurane was then gradually reduced while maintaining oxygen flow, allowing the animal to regain consciousness on oxygen. Rehydration was performed through subcutaneous injection of saline. Subsequently, the rat was placed in a heat box set at 30°C for post-surgery recovery, which typically took around 30 minutes. The animals were revived from anaesthesia, observed during the recovery period, and then returned to their housing.

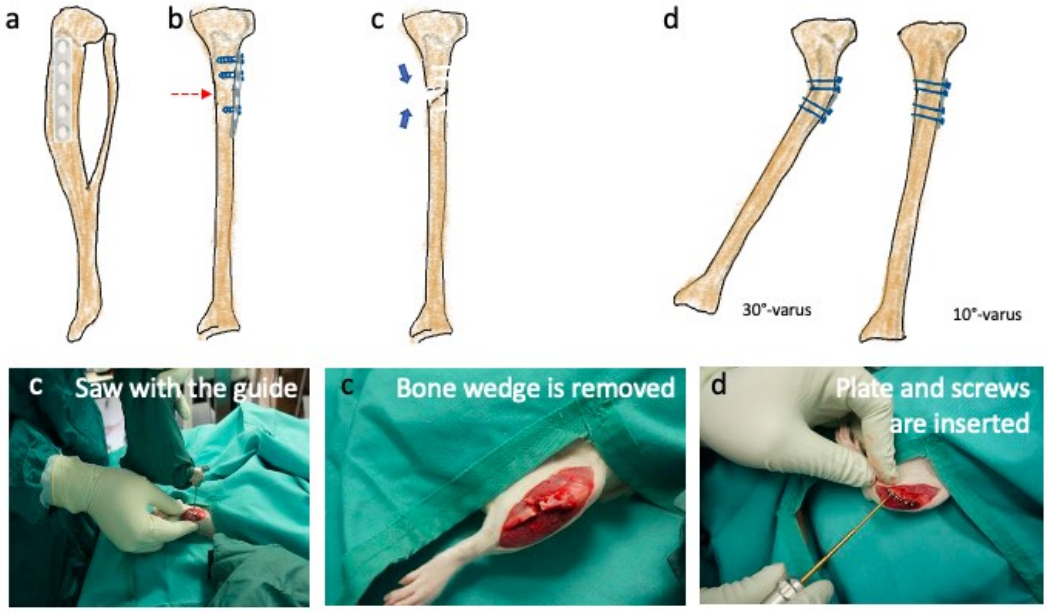

Figure 2-3. Tibial osteotomy surgery using photographs by (Britzman, 2017). (a) A surgical plate is inserted against the lateral side of the tibia (lateral view), aligning the top edge as anterior on the tibia as possible. (b) Three holes are drilled through the top holes of the plate and through the tibia, acting as a guide for the osteotomy. (c) Using the middle of the plate as a guide, the tibia is cut from the medial side by saw and a 10° or 30° wedge is removed. (d) The five-hole plate is inserted into the lateral side of the tibia, thereafter 4 screws are inserted.

2.3.2.4 Sham surgery

Sham surgeries were performed to create animals with an osteotomy angle of 0°, following a similar approach outlined for the osteotomy procedure.

1. The animal was prepared and the tibia is exposed as described earlier. The plate was then attached by aligning it with the tibia and drilling through all four holes before securing it with screws.

2. The surgical saw was used to create an incision approximately 50% of the way through the bone, ensuring that the medullary cavity was breached to simulate a fracture healing response similar to that of the osteotomies. After this step, the animals were closed up using the same techniques as before and allowed to recover in the same manner.

2.3.2.5 Post-surgery care

Post-operative analgesics and antibiotics were given for a period of 10 days, and then as needed based on the animal's condition. The animals were housed individually following the surgery for a period of 10 days. Daily pain scoring and post-operative scoring using the official Animal Welfare Score Sheet for Rodents (PPL28018) was conducted to monitor the well-being of the animals. Buprenorphine was administered orally three times per day (every 8 hours) for the first 3 days, and the frequency was reduced to twice daily (every 12 hours) in some cases based on pain scoring assessments. Baytrill was provided in the drinking water, with water bottles being refreshed once daily, both during and after surgery for 10 days. If the animal required re-suturing, Baytrill was administered subcutaneously instead.

The post-operative scoring and monitoring were conducted in three stages:

1. During the first four days after the operation (day 0 - day 3), the animals were checked three times a day (every 8 hours) in their accommodation. Food and water were placed at the bottom of the cage for easy access in case of limited mobility.

2. From day 4 to day 10, the animals were checked twice daily (every 12 hours) in their accommodation for an additional week.

3. From day 10 to day 15, the animals were checked daily thereafter.

Upon complete healing of the osteotomy, a welfare score of between 3 and 9 would require consultation with the NVS and/or NACWO, and analgesia would be administered accordingly. Animals with scores exceeding 9 (endpoint) would be euthanized using Schedule 1 methods.

After the designated period (after day 15), the animals were returned to their original caging for group housing starting from day 16. They were kept in groups of 3 in individually ventilated cages with a floor area of 1500cm^2 throughout the study.

Table 2-2 Analgesia drug dosage table

Analgesia / Drug	Dose (mg/kg)	Route of administration	Frequency	Duration
Buprenorphine (analgaesia)	0.05mg/kg	Subcutaneous injection	Once	On the day of surgery (pre-surgery after induction)
Baytrill (antibiotics)	5mg/kg	Subcutaneous injection	Once	On the day of surgery (pre-surgery after induction)
Bupivacaine (analgaesia)	2mg/kg	Subcutaneous injection	Once	On the day of surgery (end of the surgery after suture); Use locally in surgical incision area
Buprenorphine	0.3mg/kg	Oral (mixed with jelly)	Three times/day	10 days after surgery
Baytril	10mg/kg/24 hours	Oral (Drinking Water)	Refresh water bottles once daily	10 days after surgery
Or Baytril	10mg/kg	Subcutaneous injection	Once	5 days after re-suture

2.3.2.6 Humane end points

In the event that any animal displayed signs of respiratory distress, a 20% weight loss, or symptoms of hypocalcaemia, it would be euthanized using a Schedule 1 method such as overdose of CO_2 or intraperitoneal pentobarbital.

After the osteotomy had healed, if an animal exhibited two or more of the following clinical signs: piloerection, pallor, ocular or nasal discharge, or diarrhoea, appropriate analgesia or other supportive measures were provided, and the NVS was consulted. If the symptoms persisted for more than one working day, the animal would be euthanized using a Schedule 1 method.

Animals showing signs of hypocalcaemia would be immediately euthanized using a Schedule 1 method, such as exposure to a rising concentration of CO_2 or intraperitoneal injection of Pentobarbital.

2.4 Results

The tibial malignment was assessed after the rat was sacrificed at week 20 through visual (and photographic) inspection of the plate and tibia. The plate angle was remeasured using a goniometer. The results indicate that the plate was able to maintain a consistent angle throughout the experimental period. This finding implies that the plate and screws successfully provide stable fixation for bone remodelling at a specific angle. Examples of photographic assessment are provided in Figure 2-4. Notably, the degree of misalignment is more pronounced in the 30º TO group in comparison to the 10º TO group.

Figure 2-4. Photographs of dissected tibiae for the 0º TO, 10º TO, and 30º TO groups.

The following chapter describes the methodology used for early treatment of OA in this animal model.

3 Interventions to prevent OA

3.1 Summary

The aim of this chapter is to outline the methodologies underlying the selection of the OA therapies (BMP and APS), including the workflow for preparing these biological interventions. These treatments were selected to potentially prevent the onset of OA in the developed model (Chapter 2).

An ELISA assay was utilised to verify the successful preparation of APS, revealing concentrations similar to those found in previous human studies. This affirms that APS can be successfully prepared from each individual rat across the entire duration of the study.

3.2 Introduction

The background for this chapter has been reviewed in Chapter 1, Section 1.7. The following introduction elaborates on autologous cell therapy which is the most promising biological method of OA treatment currently in clinical investigation.

Autologous platelet-rich plasma (PRP) is the most studied autologous biologics therapy for OA, where the platelet contains an abundance of growth factors and cytokines that are critical in soft tissue healing and bone mineralization (Sampson et al., 2010). However, the efficacy of autologous PRP for OA remains uncertain due to a lack of robust clinical trials and inconsistencies in preparation (Chahla et al., 2017). Additionally, confusion arises from different preclinical studies' results, due to the biological complexity of the therapy (Jones et al., 2019). As a result, PRP does not have FDA approval for OA treatment (Beitzel et al., 2015)

A more recent cell therapy approach involves the use of Autologous Protein Solution (APS), which is derived from a patient's own blood and contains concentrated anti-degeneration cytokines. APS shows positive effects on OA and is currently under Phase III clinical trial(Vedi and Woodell-May, 2020). APS presents a more defined composition compared to PRP, with its main molecules confirmed to target the molecular mechanisms of OA.

APS is rich in white blood cells (WBCs) and anti-inflammatory cytokines. High concentrations of Interleukin-1 receptor antagonist (IL-1ra), as well as soluble forms of cell receptors for IL-1 and TNFα (sIL-1RII and sTNF-R), are found in APS (O'Shaughnessey et al., 2014a); the presence of leukocytes can stimulate the production of these cytokines (King et al., 2021). Both IL-1ra and sTNF-R can inhibit the IL-1β and TNFα inflammatory signalling cascade present in OA (Cominelli and Pizarro, 1997, Van Zee et al., 1992). These cytokines persist in APS and can be released from WBCs.

In ex-vivo cell culture studies (O'Shaughnessey et al., 2011) and cartilage culture studies (Matuska et al., 2013), APS has well demonstrated its ability to block the IL-1β signal and TNFα signal, reduce the

inflammatory cytokines and MMPs release, and promote the chondrocyte proliferation. However, there are very limited number of in-vivo studies to validate the benefits of APS treatment. An athymic rat study confirmed that a human blood-based APS derived APS Kit (NCT02262364) can decrease collagen and cartilage degeneration (King et al., 2017). Some larger animal studies, such as canine (Wanstrath et al., 2016) and horse (Bertone et al., 2014) found reduced pain and lameness scores and increased weight-bearing after APS injection (Wanstrath et al., 2016). Similarly, two human feasibility studies demonstrated the improvement in pain, function, and stiffness score within 6 month after one dose treatment (Vedi and Woodell-May, 2020, Kon et al., 2018).

The above in-vivo studies either illustrate functional improvement in large animals (or humans), or affect change in the OA mechanism using human APS in a small animal. However, there has not yet been a study to determine whether APS can actually alter the OA disease progression *in vivo* . Therefore, the first aim of this interventional study related to APS is to assess the effects of rodent's autologous APS injection on preventing OA initiation in an established model of tibia malignment-induced OA (Chapter 2). The results are reported in subsequent chapters; this chapter focused on the methodology. The second aim is to evaluate the histological cartilage degradation, gait scores and cytokine levels in response to APS treatment; these are reported in later chapters. For a comparative analysis of cell therapy efficacy, this study also employs individual recombinant biological agents, BMP-7, as another OA treatment method. Although BMP-7, a growth factor, has been noted to exhibit protective effects against degenerative cycles and enhance cartilage repair in several preclinical studies (Chubinskaya et al., 2007, Hunter et al., 2010a), the clinical trials are very few, and the results regarding its effectiveness in disease progression are not very promising (Hunter et al., 2010b) and mostly unpublished thus far (NCT01111045, NCT01133613) (Jones et al., 2019).

3.3 Materials and methods

3.3.1 Blood fraction

In this section, the process of isolating the buffy coat (which includes WBC and anti-inflammatory cytokines) from whole blood is detailed.

For APS therapies, it is crucial to include both the cells and cytokines as the desired product. Due to WBC's larger size compared to sub-visible particulates (cytokines), a filtration step based on molecular size to isolate the desired product, commonly used in cell therapy production processes, is not feasible. This is because the particulates would be removed along with the cells (Figure 3-1).

Separation of blood components is achieved based on their different densities. A density gradient separation method is performed using density media (separation gel) and centrifugation to separate blood components based on their different densities. Compared to using centrifugation alone, this approach enhances the resolution of separation for various cellular fractions (Figure 3-1).

Polyester gel is commonly utilized for blood separation in clinical laboratory testing. With its intermediate density (1.04 g/cm^3), the gel physically forms a gel barrier between the liquid phase (density < 1.04 g/cm^3) and the cells (density >1.04 g/cm^3) (Table 3-1).

To retain WBCs in the desired phase, a separation gel with a higher density (1.077 g/cm^3) is chosen. The blood cells separate in the following order (Table 3-1): 1.a top layer consists of plasma; 2. an opaque, white buffy coat layer composed of mononuclear WBCs (T cells, B cells, NK cells, dendritic cells and monocytes), a fraction of polymorphonuclear WBCs (granulocytes like neutrophils and eosinophils); 3. a gel barrier (lymphoprep); and 4. a bottom layer of erythrocytes (Portillo et al., 2021) (Figure 3-1).

Table 3-1. The density of blood components and the density position of separate gel (normative baseline values)

Layer (after centrifuge)	**Components**	**Density g/ml**	**Cell size**	**Particulates weight**
Upper layer	Normal Serum	1.023 (Fatás et al., 2008)	No cell	e.g. IgM 950 kDa, ~ 1 mg/mL in serum (Dati et al., 1996)
	Normal Plasma	1.025 (Fatás et al., 2008)	No cell	e.g. Fibrinogen 340 kDa protein (Leeman et al., 2018)
Buffy Coat	Platelets	<1.08	1.7 ± 0.1 μm in diameter	e.g. Platelet Factor 429 kDa
	WBC	~1.08 (Norouzi et al., 2017)	12 – 17 μm in diameter.	e.g. IGF-1 21.8 kDa
Separate Gel	polyester gel	1.04	--	--
	lymphoprep	1.077	--	--
Bottom layer	RBC	1.11	6 – 8 μm in diameter.	e.g. Hemoglobin 64 kDa (Handin et al., 2003)

3.3.2 Workflow for the Preparation of APS Injections

Since the current commercial kit is not suitable for small animals, the APS was prepared using basic laboratory equipment. This approach involved a blood separation step followed by an APS concentration step.

First, 1 ml of peripheral blood was collected from each rat using an anticoagulated tube. The anticoagulated blood was diluted 1:1 with normal saline.

Then, the anticoagulated diluted blood was transferred to a new tube containing 1 mL of Lymphoprep density gradient medium （Stemcell technologies, Canada） (Figure 3-1a). Care was taken during this step to prevent blood from breaking through the Lymphoprep layer. This can avoid red blood cell contamination after centrifugation. To achieve this, the tube was laid relatively flat, the pipettor was set to a slow speed, and the 2 ml of diluted peripheral blood was slowly overlaid onto the Lymphoprep layer by tilting the tube and allowing the blood to flow down the tube wall.

Next, the blood was processed through gradient centrifugation. The centrifugation was performed at 20°C for 20 minutes at 800g with no brake. Figure 3-1b is a visual representation of the blood component layers after centrifugation.

The upper 1/3 plasma layer was removed slowly and discarded. The lower 2/3 of the plasma layer was collected as the PRP sample. The buffy coat was gently collected and placed into a concentrator (Amicon centrifugal Filter, Amicon, US) (Figure 3-1c). The concentrator was then centrifuged at 20°C for 20 minutes at 14,000g, producing the concentrated APS (~100µl) for injection (Figure 3-1b).

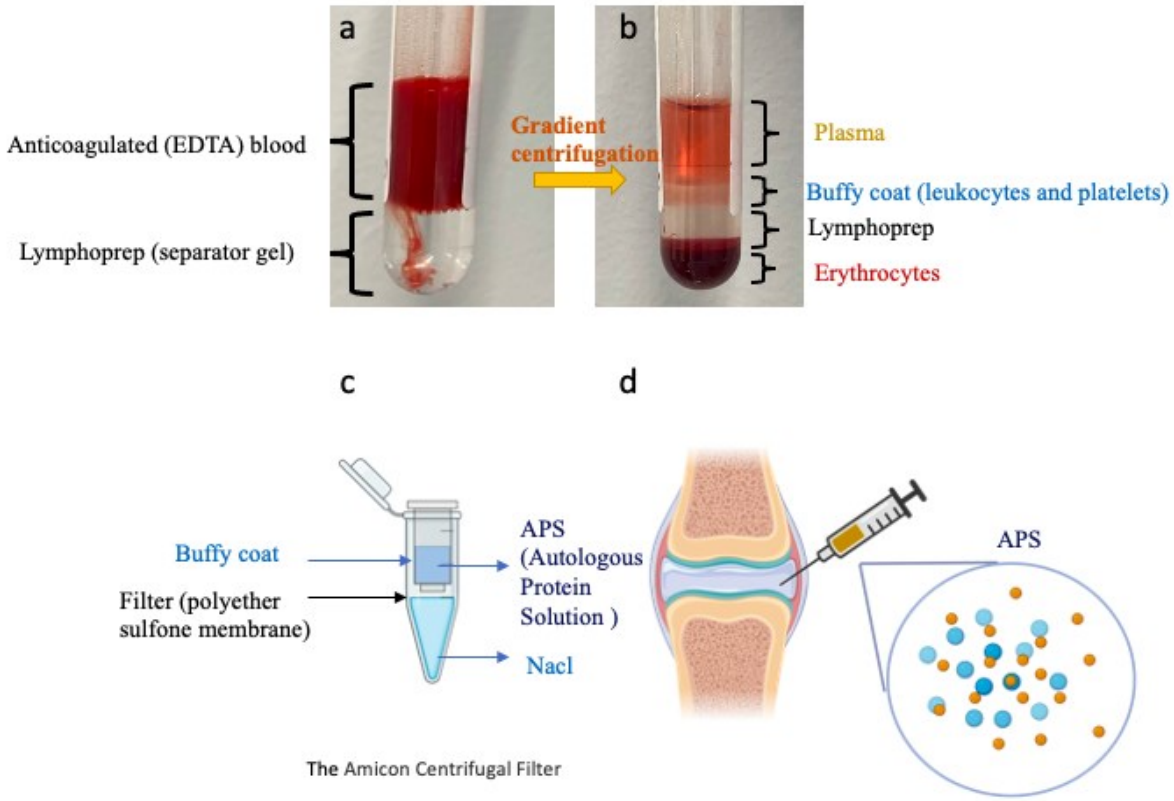

Figure 3-1. Workflow for the Preparation of APS Injections (a, b) Blood separation step: Images showing the different blood layers obtained from the density gradient centrifugation before and after spinning. (c) APS concentration step: Schematic illustrating the use of Amicon for APS concentration. (d) Schematic of the intra-articular injection process (Created with BioRender.com）.

3.3.3 Intra-articular injection procedure

Early pharmacological intervention involving BMP-7 and APS treatment commenced 2 weeks prior to the onset of OA (at week 8) and continued with a monthly (every 4 weeks) administration schedule. The decision on the injection timepoint stems from a previous study conducted by our group using this model. That research found that serum CTX-II levels (an early-stage OA marker) began increasing from week 6 and showed a significant difference at the week 10 timepoint between the 30º TO and sham surgery groups. This suggests that the onset of OA occurs around week 10 (Britzman et al., 2018a). In this research, for the 10º /30º TO surgery group, 1/3 rats received the intra-articular injection of 50 µl recombinant human BMP-7 (Proteintech, US) into the knee joint of the operated leg under anaesthesia. Similarly, one-third of the rats were injected with 50 µl of APS under anaesthesia. APS was administered immediately after concentrated from rat circulating blood from blood sampling.

The detailed procedure for the intra-articular injection is as follows: the tibia and femur were bent to 45º flexion and the surgeon palpated the patellar tendon. Next, a 26-gauge needle was inserted approximately 3 mm next to the lateral margin of the patellar tendon. Following verification of no soft-tissue resistance, the compound was injected directly into the articular cavity.

3.3.4 APS concentration quantitation via ELISA

The ELISA technique was used to quantitatively measure the concentration of IL-1ra, the main component and primary functional content of APS for the treatment of OA. The quantitative measurement of IL-1ra concentration was conducted on the serum sample from the 10°TO (n=3) and 30°TO (n=3) surgery groups without treatment, using the Mouse IL-1ra ELISA Kit (Invitrogen, US). The procedure of Elisa is as follows:

1. Collect serum sample by centrifugation at 3000 rpm, 4ºC for 10 minutes from whole blood.
2. Dilute the sample 50× with dilution buffer.
3. Pipette standards, quality controls, dilution buffer (as blank), and duplicate samples into appropriate wells of the ELISA plate.
4. Add the same volume of IL-1ra biotin-labeled antibody to each well.
5. After incubation and washing steps, add the same volume of streptavidin-HRP conjugate and substrate solution to each well, respectively.
6. Finally, measure the absorbance readings using a single microplate reader (Bio-Rad 550) set to 450 nm.

3.4 Result

ELISA analyses (Figure 3-2a) revealed significantly higher concentrations of the anti-inflammatory cytokine IL-1ra in APS compared to PRP, both before (week 0 – healthy rats baseline) and after surgery (week 1). To further verify the preparation of APS in a broader range beyond healthy rats, an investigation into IL-1ra concentrations across the subsequent 12 weeks post-surgery was undertaken (Figure 3-2b) using the 10°TO (n=3) and 30°TO (n=3) surgery groups without treatment. Data from only 4 rats (2 from the 10°TO group and 2 from the 30°TO group) at week 1 were collected because the animals actively resisted just after surgery. At other time points, data were collected from all 6 animals. The results revealed that IL-1ra concentrations did not decrease in pre-OA rats compared to the normal baseline (W0). This observation is consistent with findings from a prior clinical study, which revealed an inclination towards increased anti-inflammatory cytokines compared to inflammatory cytokines in OA patients' APS sample (O'Shaughnessey et al., 2014b). This study supported that APS can be successfully prepared across a broad range of OA individuals.

The average concentration and standard deviation of IL-1ra in APS (Table 3-2) are comparable to those reported in a previous study that utilized the Autologous Protein Solution Kit (Zimmer Biomet Biologics, Warsaw, IN) to obtain APS from human donors (currently under investigation in the USA) (King et al., 2017). Notably, the IL-1ra concentration in APS surpasses the normative baseline values (681 pg/ml) observed in whole blood samples.

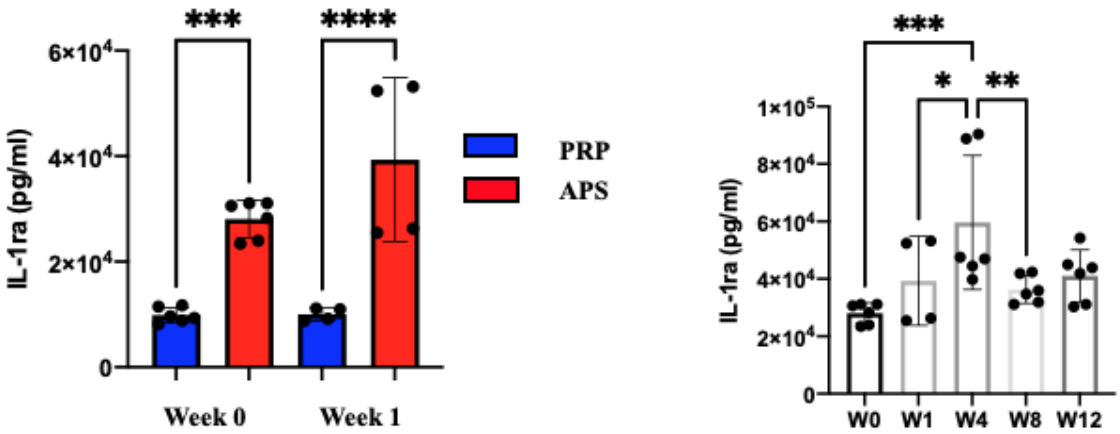

Figure 3-2. (a) The comparison of IL-1RA concentration in PRP and APS collected at week 0 (before surgery) and week 1 (after surgery). (b) The concentration of IL-1RA in APS during the first 12 weeks after surgery (n=4 for week 1, and n=6 for all other time points).

Cytokine IL-1ra	**PRP (W0)**	**PRP (W1)**	**APS (W0)**	**APS (W1)**	**APS (W4)**	**APS (W8)**	**APS (W12)**
Average (pg/ml)	9856.547	10005.01	28080.28	39326.1	59641.09	37828.01	41053.014

Standard deviation	1441.107	1217.967	3548.849	15545.59	23347.62	4838.669	9063.760
Range (pg/ml)	8835-11729	8750-10962	28290–31098	25486-53170	39798-90355	31864-42363	30331-54202

Table 3-2. IL-1RA concentration in PRP and APS collected at the first 12 weeks after surgery (n=4 for week 1, and n=6 for all other time points).

In summary, this chapter has shown that APS can be successfully prepared using the methodology described, revealing concentrations similar to those found in previous human studies. The following chapters report on the full characterisation of the rat model of OA and the effect of the therapeutic intervention using histopathology, micro-CT, gait analysis and proteomics.

4 Histopathology analysis of assessing cartilage changes in OA

4.1 Summary

This chapter presents the histological analysis characterising changes in cartilage following the onset of OA in the model presented in Chapter 2 and subsequent BMP and APS treatments described in Chapter 3. It elaborates on the histopathology scoring of articular cartilage, the gold-standard method for diagnosing and assessing the occurrence and severity of OA in this study. Distinct characteristics were observed in the cartilage analysis of each group in the medial compartment of the left limb. Early-stage OA was noted in the 10ºTO group, progressive (intermediate stage) OA was observed in the 30ºTO group, local repair was seen in the BMP group characterised by hypertrophic differentiation, and OA was fully prevented in the APS-treated group. The histology gold-standard result was also utilised for correlation analysis with the underlying subchondral bone changes observed in micro-CT (Chapter 0), alterations in gait (Chapter 0) and serum changes (Chapter 6).

4.2 Introduction

The background of this chapter has been extensively reviewed in Chapter 1, Section 1.3. The introduction here builds upon the concepts discussed in that section to provide context for this chapter.

Histologically, OA involves a group of joint diseases marked by chondrocyte death, proliferation, and the simultaneous regeneration/repair and degradation of the cartilage matrix (Pritzker, 2003). Establishing standard measurements is challenging due to variations in the etiology and induction methods used across different models. Although histology struggles to distinguish differential features between subgroups, it can provide a general diagnostic standard for the disease, especially since OA frequently displays similar characteristics in its advanced stages (Pritzker et al., 2006). At present, histopathology remains the gold standard for cartilage evaluation and OA diagnosis in animal models, with Safranin-O staining typically used to assess cartilage loss (Pritzker et al., 2006).

In this study, the most commonly used and standardized OA histopathological system developed by the OARSI working group in 2006 (Pritzker et al., 2006) is used. This system is applicable to both human and animal models and is based on the five cardinal principles of an ideal cartilage histopathology system: simplicity, utility, scalability, extendibility, and comparability. The system was chosen because it fulfilled the requirement for accurate histology measurements and focused solely on the results of the histology section, excluding macroscopic appearances and functional assessments, which are difficult and complex to obtain from animal models. The OARSI standard incorporates principles derived from cancer pathology and grades OA based on the depth of the cartilage lesion involvement and the extent of the affected cartilage area (for more details, refer to Section 4.3.3) (Pritzker et al., 2006).

4.3 Material and methods

4.3.1 Sample processing

Isolation of the knee

Animals were euthanized using a Schedule 1 method at week 20. Specifically, 1 ml of Pentobarbital was injected intraperitoneally to induce an overdose of anaesthesia (Schedule 1 method), followed by severing the femoral artery to confirm death.

After the rats were sacrificed, soft tissue was carefully dissected from the femur and tibia. The patella tendon and quadriceps tendon were cut using a surgical scalpel, allowing the removal of the patella from the joint. Sequentially, the lateral collateral ligament, medial collateral ligament, anterior cruciate ligament, and posterior cruciate ligament were cut, facilitating the separation of the femur and tibia without disturbing the tibial articular cartilage of the joint. A small amount (5mg) of the tibial surface cartilage from each limb, including the medial and lateral compartments, was harvested and snap-frozen for proteomics analysis (Chapter 7).

Fixation

Approximately 10mm from the joint, the femur was cut using a bone cutter. The whole tibia and feet were preserved for complete micro-CT imaging. The tibia and feet were immediately placed in a 100ml plastic container filled with 10% (wt/vol) neutral buffered formalin (NBF) from Sigma-Aldrich, St. Louis, MO. The formalin-containing sample was placed on a gentle roller to ensure proper fixation, with the formalin solution being changed daily.

After 48 hours of fixation in formalin, the metal plate used for bone fixation was easily removed. The post-operative plate angle were remeasured using a goniometer. The whole tibia was then placed in a conical 50ml tube in a vertical position, ensuring consistent orientation and alignment for subsequent scanning. A small amount of formalin was added to the bottom of the tube to maintain sample hydration during scanning.

Decalcification

Following the 48-hour fixation in 10% neutral buffered formalin prior to micro-CT scanning, the tibia was cut through the lesser trochanter (approximately 10mm from the joint) and demineralized in 10% formic acid (Sigma-Aldrich) for 21 days. Using a smaller section of tissue allows the decalcifier to penetrate the joint quickly. The formic acid solution was changed daily for two weeks. After one week, the sample was easily halved along the medio-lateral axis, cutting across both compartments to ensure complete decalcification (Figure 4-1a). Both the front and posterior parts of the sample were then placed back into the same container with 10% formic acid for another week.

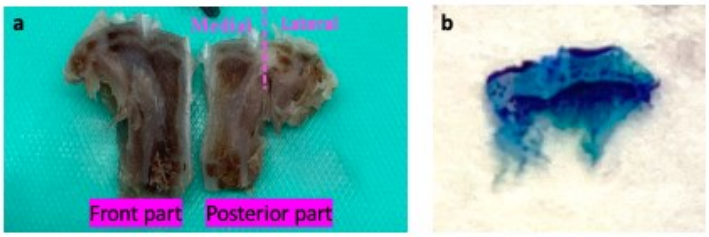

Figure 4-1: a. Histology sample preparation: the proximal tibia sample is halved across both compartments, b. Whole view of the slice after Toluidine-blue staining.

Dehydration （paraffin-embedding）

The sample was sequentially transferred through a series of ethanol dilutions for dehydration, including 70% ethanol (1 hour), 80% ethanol (1 hour), 90% ethanol (1 hour), and 100% ethanol (2 hours). Following ethanol dehydration, the samples were cleared using Histo-Clear II (National Diagnostics, Atlanta, US) for 2 hours.

Next, the samples were processed in a paraffin bath and placed in a vacuum oven for two days. This step is crucial as the vacuum helps the paraffin penetrate the entire sample. After two days, the samples were embedded in paraffin wax and kept at 4°C overnight. The paraffin blocks (samples) were then serially sectioned at 100 µm intervals into 5 µm-thick sections for staining (Table 4-1).

The paraffin-embedding method was used for sample processing, as it can effectively maintain the integrity of both the tissue and subcellular structures, and it allows for long-term preservation of the tissue at room temperature.

Table 4-1. Protocol of paraffin-embedding method for sample processing.

Staining procedure (Solutions)	**Duration**
10 % neutral buffered formalin	48 hours
10% Formic acid	21 days
70% ethanol	1 hour
80% ethanol	1 hour
90% ethanol	1 hour
100% ethanol	2 hour
Histo-Clear II	2 hour
Paraffin bath (vacuum oven)	48 hours
Paraffin wax embedding	4°C overnight

4.3.2 Toluidine blue staining protocol

Toluidine blue staining is a widely accepted histological procedure commonly used to evaluate cartilage loss by staining the proteoglycan content (Rutgers et al., 2010a) (Figure 4-1b). Additionally, it is utilized for assessing the chondrogenic differentiation of cells and evaluating the maturity and quality of cartilaginous tissue (Bergholt et al., 2019). Toluidine blue is a cationic dye that exhibits an affinity for the sulfur present in cartilage, making it a suitable choice for staining proteoglycans. In this model, toluidine blue staining was used to assess cartilage degeneration and to evaluate the chondrogenic differentiation (chondrogenesis) during bone healing and remodelling.

During toluidine blue staining, hyaline articular cartilage exhibits distinct coloration patterns. Cell nuclei are stained blue, cytoplasm appears light blue, and the extracellular matrix takes on shades of pink or purple (Schmitz et al., 2010a). This metachromatic staining effect occurs due to interactions between the cationic dye and the anionic polymerized intermolecular bonds, resulting in shifts in spectral properties (Sylven, 1954). The staining protocol utilized in this study is outlined in Table 4-2.

Table 4-2. Toluidine blue staining protocol (Schmitz et al., 2010b).

Staining procedure (Solution)	Duration (min)
Histo-Clear II	4
Histo-Clear II	4
Histo-Clear II	4
100% Alcohol	1
95% Alcohol	1
95% Alcohol	1
Tap water rinse	1
0.04% Toluidine blue	5
Tap water rinse	1
Warm air dry	9
Histo-Clear II	1

4.3.3 Histopathology scoring of articular cartilage.

The joints were sectioned in the frontal plane, resulting in two halves that were embedded in a paraffin block. The halves were placed horizontally with the cut surface facing down to ensure optimal sectioning orientation. After embedding, the samples were placed on ice for 2 hours to allow the paraffin to fully solidify. From each knee, the paraffin blocks were then serially sectioned at 100 µm intervals into three 5 µm-thick sections for staining. By following this procedure, 3 samples from the central region of each joint, specifically covering the central weight-bearing area were obtained. The region was chosen as it represents the primary weight-bearing area where degenerative changes are most pronounced (Strassle et al., 2010).

Once stained, the cartilage degeneration scoring is performed on the three slides from the central region of each joint. Next, cartilage degeneration of each section was assessed by standardized OA histopathological system from OARSI guidelines (Pritzker et al., 2006). Finally, the values of each rat joint in each compartment is averaged as the score from the three sections.

The key pathological parameters of degeneration included cartilage loss, which includes extracellular matrix loss and chondrocyte death/loss. Extracellular matrix loss is characterized by the depletion of proteoglycans (e.g., aggrecan) visible as a loss of staining colour, as well as collagen matrix fibrillation observed in histological images. Chondrocyte death is indicated by cellular disarray, including clustering, hypercellularity, and hypocellularity (Thomas et al., 2007).

OA grading method:

The grading of OA severity (Figure 4-2) (Table 4-3) is based on the depth of progression of OA into the cartilage. This grading index serves as an indicator of the disease's severity and biological progression, under the assumption that deeper involvement of the cartilage signifies a more advanced and progressed state of the disease. The grade assigned is determined by identifying the most advanced grade observed within the cartilage, irrespective of its horizontal extent. The assessing procedure was conducted in a blinded manner, with the evaluator unaware of the group of each slide.

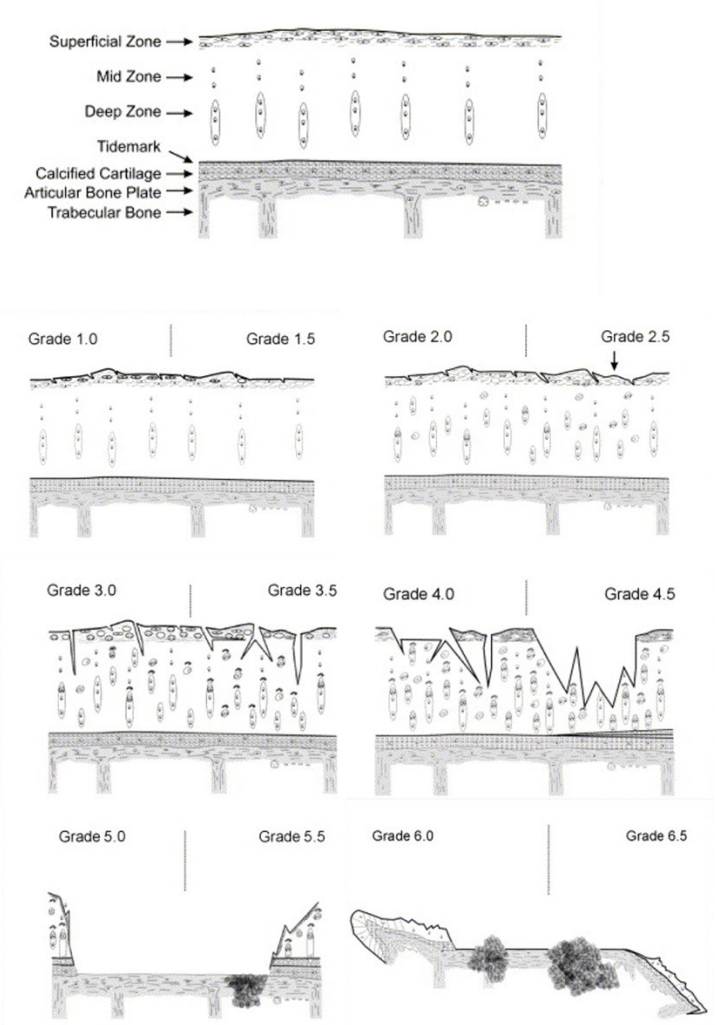

Figure 4-2. OA cartilage histopathology -- grading methodology, adapted from (Pritzker et al., 2006).

Table 4-3. OA cartilage histopathology -- grading methodology, adapted from (Pritzker et al., 2006).

Grade (key feature)	Associated criteria (tissue reaction)
Grade 0: surface intact, cartilage morphology intact	Matrix: normal architecture Cells: intact, appropriate orientation
Grade 1: surface intact	Only superficial zone are affected Matrix: superficial zone intact but uneven, focal superficial fibrillation , foal superficial condensation Chondrocytes: death, proliferation (clusters), hypertrophy
Grade 2: surface discontinuity	Damage extending from superficial zone to the superficial zone–mid zone. Matrix: Focally fibrillation, increased or decreased matrix staining Chondrocytes: death, proliferation (clusters), hypertrophy
Grade 3. vertical fissures (clefts)	Fissures extending download into the mid zone Matrix: fibrillation, fissures vertically extend into mid zone Chondrocytes: death, proliferation (clusters), hypertrophy mostly adjacent to fissures.
Grade 4: erosion	Cartilage matrix loss in superficial layer (in earliest stage) and in mid layer surround fissures domain (later stage).
Grade 5: denudation	Cartilage and matrix: fibrocartilage and mineralized cartilage kept within unmineralized cartilage denuded Bone: microfracture and repair in the bone surface
Grade 6: deformation	Extensive articular contour deformation. Fibrocartilaginous articular surfaces, Bone remodelling (microfracture, fibrocartilaginous and osseous repair), marginal and central osteophytes

OA staging method:

The staging of OA is determined by the horizontal extent of the affected cartilage area (volume) within one side of a joint compartment, regardless of the underlying grade. This staging approach is more sensitive in detecting early or mild stages of OA compared to grade scoring (Pritzker et al., 2006). Therefore, many animal studies use this staging method to assess OA independently (Thomas et al., 2007).

Following the OARSI guidelines, the entire medial/lateral tibial cartilage plateau was devided into three zones of equal width: zone 1 (outer edge of the joint), zone 2 (central plateau), and zone 3 (inner edge adjacent to the central cruciate ligament) (Figure 4-3). The final value for each section is calculated by averaging the scores of the three zones.

The staging of cartilage degeneration in each zone ranges from 0 (no degeneration) to 5 (severe degeneration) according to the criteria described in Table 4-4.

Table 4-4. OA cartilage histopathology – stage methodology, adapted from (Pritzker et al., 2006).

Stage	% cartilage involvement (surface, area, volume)
0	No degeneration
1	Minimal degeneration: < 10% affected
2	Mild degeneration: 10-25% affected
3	Moderate degeneration: 26-50% affected
4	Marker degeneration: 50% affected

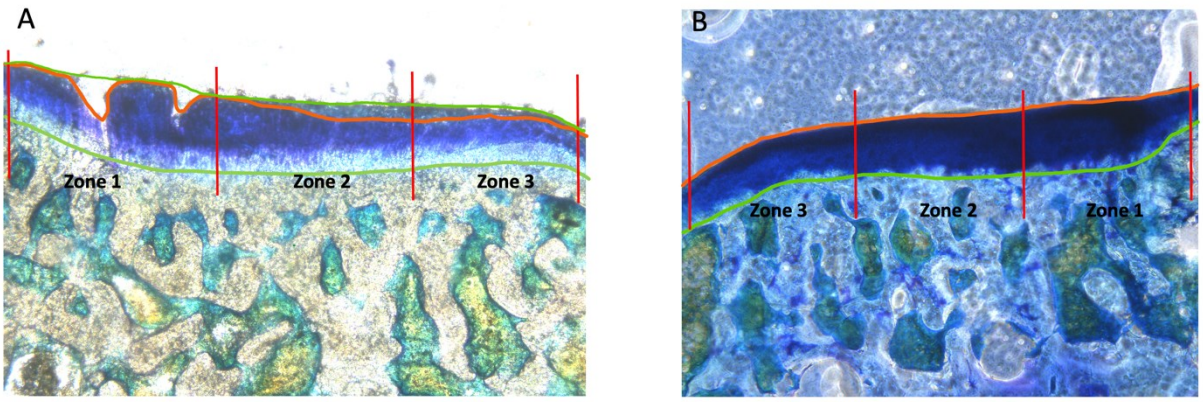

Figure 4-3. Histological section evaluation of one joint compartment of the rat with 30ºTO surgery (An example section is from the lateral compartment of a left leg A and right leg B in 30ºTO group). As shown, the entire cartilage is indicated by green tracing, and the cartilage lesion area is delineated by orange tracing. The tibial plateau is divided into three zones equally (marked by red vertical lines), with outer zone 3, central zone 2 and inner zone 1.

OA score

After integrating the grade and stage assessments, the final OA score was obtained (Table 4-5), which represents a comprehensive evaluation of the severity and extent of OA.

The OA score is a composite index that combines the grade and stage of the disease. It is calculated using the formula: score = grade x stage, resulting in a range of 0-24 (Table 4-5). This scoring method offers a comprehensive evaluation by assigning equal weight to both the severity (grade) and extent (stage) of OA (Pritzker et al., 2006).

Table 4-5. OA cartilage histopathology – scoring methodology, adapted from (Pritzker et al., 2006).

	Stage 1	Stage 2	Stage 3	Stage 4
Grade 1	1	2	3	4
Grade 2	2	4	6	8
Grade 3	3	6	9	12
Grade 4	4	8	12	16
Grade 5	5	10	15	20
Grade 6	6	12	18	24

Score = grade × stage.

4.3.4 Statistical analysis

To evaluate changes in histology scores between different OA conditions (osteotomy groups and treatment groups), statistical significance was tested. Levene's test was used to test the equality of variances between groups. For groups with equal variances, a one-way analysis of variance (ANOVA) with Tukey's multiple comparisons post-test was used. GraphPad Prism software (Version 9.4.0, Dotmatics, 2022) was used for all statistical analysis. For groups with variances that were significantly different ($P<0.05$), the Kruskal-Wallis test with Dunn's multiple comparisons test was applied.. Results were considered statistically significant if the p value was ≤ 0.05. Data are reported as means ± standard deviations (SDs).

4.4 Results

4.4.1 Characterizing cartilage changes

The general cartilage morphology changes in different compartments between the various groups were compared. The analysis focused on variations in surface integrity, matrix staining, thickness, and the presence of fissures as described in Table 4-3 and Table 4-4. The histological scoring results are summarised in Table 4-9 and described in prose below.

In the left limb medial compartment (Figure 4-2A) distinct characteristics were observed in the cartilage analysis of each group. The 0ºTO (sham) group exhibited a healthy cartilage state, with an intact surface and a homogenous matrix architecture. In the 10ºTO group, the cartilage surface remained intact but displayed unevenness. Staining loss in the matrix was evident, along with focal superficial fibrillation and condensation. This can be regard as in an **early-OA stage**. In the 30ºTO group, vertical fissures were observed, extending from the surface into the middle or deep zone of the cartilage. This was accompanied by a layered staining pattern, with increased or decreased matrix staining. Additionally, there was cartilage matrix loss in the superficial layer and around the fissure domain in the mid-layer. Osteophytes were also observed in both the marginal and central sites of this group. This indicates that the cartilage damage has entered a more **progressive OA stage**. Following treatment with BMP in the 10ºTO group, there was an increase in matrix staining. In the 30ºTO group with BMP treatment, the cartilage thickness increased focally, particularly in the middle zone, which is the central weight-bearing zone, resulting in an uneven

surface. However, the 30ºTO group with APS treatment displayed a uniformly increased cartilage thickness with an intact and even surface.

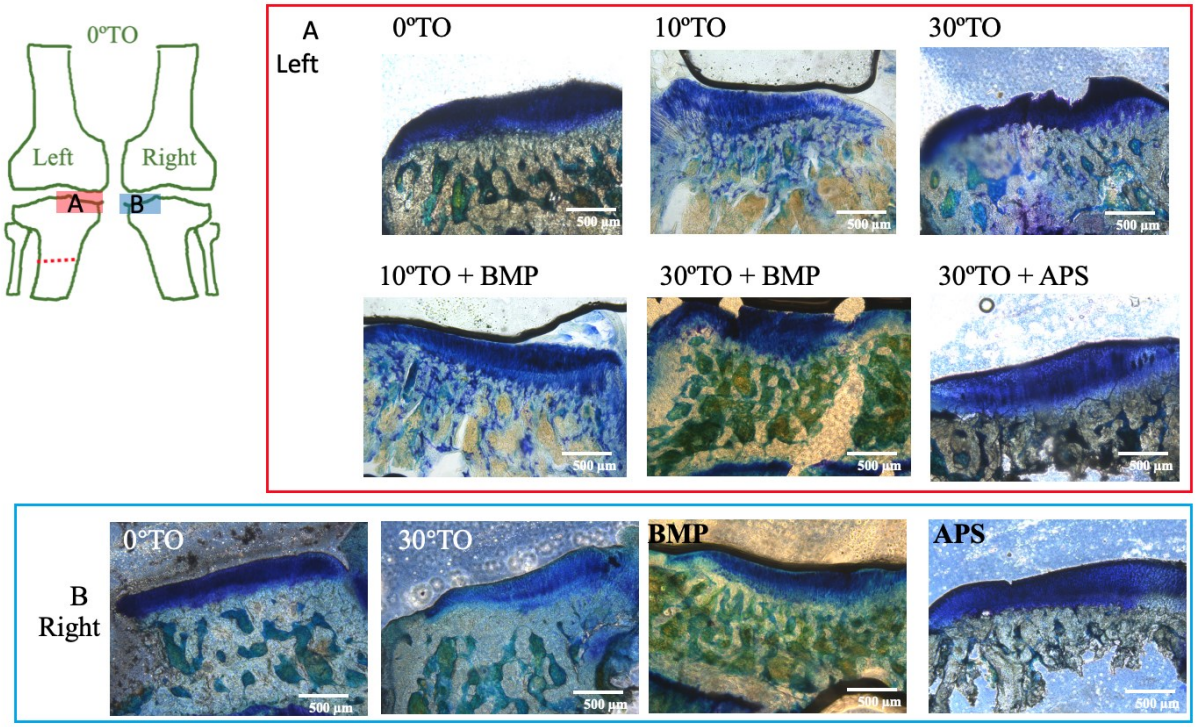

Figure 4-4: Toluidine-blue stained sections of representative left limb medial compartments from each experimental group at 5X objective magnification, scale bars = 500 µm. The cartilage of the (A) 0ºTO (sham) group, 10ºTO group, 30ºTO group, 10ºTO group with BMP treatment, 10ºTO group with BMP treatment, 30ºTO group with APS treatment, (B) Right limb medial compartment.

Moving to the cartilage of the left limb lateral compartment, a relatively even pattern was observed. Staining loss and vertical fissures were only observed in the 30ºTO groups (Figure 4-5). Regarding the right contralateral limb, the cartilage remained intact in all groups, except for the medial compartment of 30ºTO group, which exhibited evident staining loss, considering as early-OA stage (Figure 4-2B). The presence of OA in the right contralateral limb is an interesting finding that is discussed more thoroughly in the micro-CT imaging analysis (Chapter 5) and gait analysis (Chapter 6).

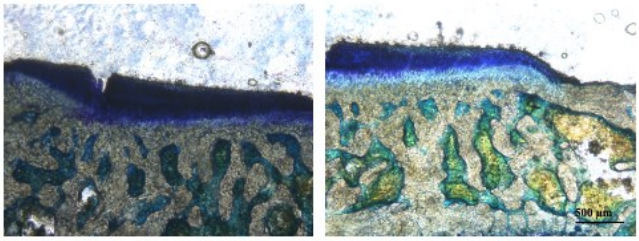

Figure 4-5: Toluidine-blue stained sections of representative left limb lateral compartments from 30ºTO group at 5X objective magnification, bars = 500 µm.

In the previous analysis, the cartilage surface and matrix changes between different groups at low magnifications were described. Moving forward, higher magnifications were used to observe significant differences, including chondrocyte appearance.

At a higher magnification (Figure 4-6 Columns A and B), the **healthy cartilage** exhibits chondrocytes with a homogeneous proteoglycan-rich matrix throughout the entire cartilage. In contrast, the **OA cartilage** shows a layered pattern. The superficial layer of the OA cartilage displays decreased matrix staining, indicating proteoglycan loss, while the middle layer shows increased staining, suggesting chondrocyte hypertrophy. At even higher magnification (Columns C and D), the middle layer shows a columnar arrangement characterized by increased fibrocartilage. Notably, the superficial layer of the OA lesion cartilage exhibits large hypertrophic chondrocytes resulting from chondrocyte differentiation. Furthermore, **BMP treatment group** enlarges the chondrocytes across all layers (superficial, middle, and deepest) compared to the untreated OA cartilage and APS treatment cartilage.

In general, the matrix of **healthy hyaline cartilage (**Figure 4-6 0ºTO**)** displayed a homogeneous ellipsoid structure, with a clear ground substance indicating consistent thickness of the hyaline cartilage and articular calcified cartilage. A thin, tightly organized tidemark was visible. Chondrocytes were consistent in appearance, present within lacunae in an iso-genous group, and perichondrium was present.

In the superficial zone, chondrocytes appeared flattened and elongated, and collagen fibres were parallel to the articular surface, tightly packed in a dense arrangement. In the middle zone, chondrocytes took on a rounded shape and were small in size. They were surrounded by collagen fibres with a random orientation and a looser arrangement. In the deep zone, chondrocytes displayed an ellipsoid morphology, and the collagen fibres aligned themselves perpendicularly to the subchondral bone surface (Ge et al., 2006).

In contrast, observations of the **OA cartilage** (Figure 4-6, 30ºTO-BMP, 30ºTO-APS) revealed different characteristics. The cartilage tissue in OA, particularly during the cartilage repair stage, exhibited abnormal hypertrophic differentiation of chondrocytes (Ge et al., 2006). Generally, the cartilage was focally thickened, and the tidemark was either interrupted or indiscernible, either partially or completely. The organization of chondrocytes was irregular and clustered, with oversized chondrocytes displaying

hypertrophy and signs of cell death, presented as increased or decreased matrix staining in middle zone. Furthermore, vertical fissures (clefts) were observed, extending into the deep zone of the cartilage.

In higher magnification (Figure 4-6 30ºTO BMP, 30ºTO APS, Column C&D), **the superficial layer** exhibited a stain loss and surface loss, and showed fibrocartilaginous articular surfaces with surface discontinuity. Fibrillation in the superficial zone could extend focally into the middle zone. Superficial matrix condensation was also observed. **In the middle zone**, chondrocytes were rounded and larger in size, arranged in distinctive columnar patterns parallel to the longitudinal axis of the bone. Matrix fibrillation extended vertically downward into the deep zone. Densely layered collagen fibers and more flattened, organized cell rows were observed. Collagen fibers within the matrix were regularly arranged, and chondrocytes were parallel to the collagen fibers and present in lacunae. Hypertrophic chondrocytes in this zone exhibited more pronounced nuclei with a higher averaged nucleus/cytoplasm ratio, and the cytoplasm displayed characteristic knot-like condensations. Deposition of dense extracellular matrix indicated a fibrosis process. Toluidine blue stain infiltration into chondrocyte lacunae and small voids (cavities) between chondrocytes were also observed. **In the deep zone**, hypertrophic chondrocytes experienced a significant increase in cell volume before being replaced by trabecular bone, as indicated by the arrows pointing to the hypertrophic chondrocytes. Furthermore, **BMP treatment** enlarges the chondrocytes across all layers (superficial, middle, and deepest) compared to the untreated OA cartilage and APS treatment cartilage.

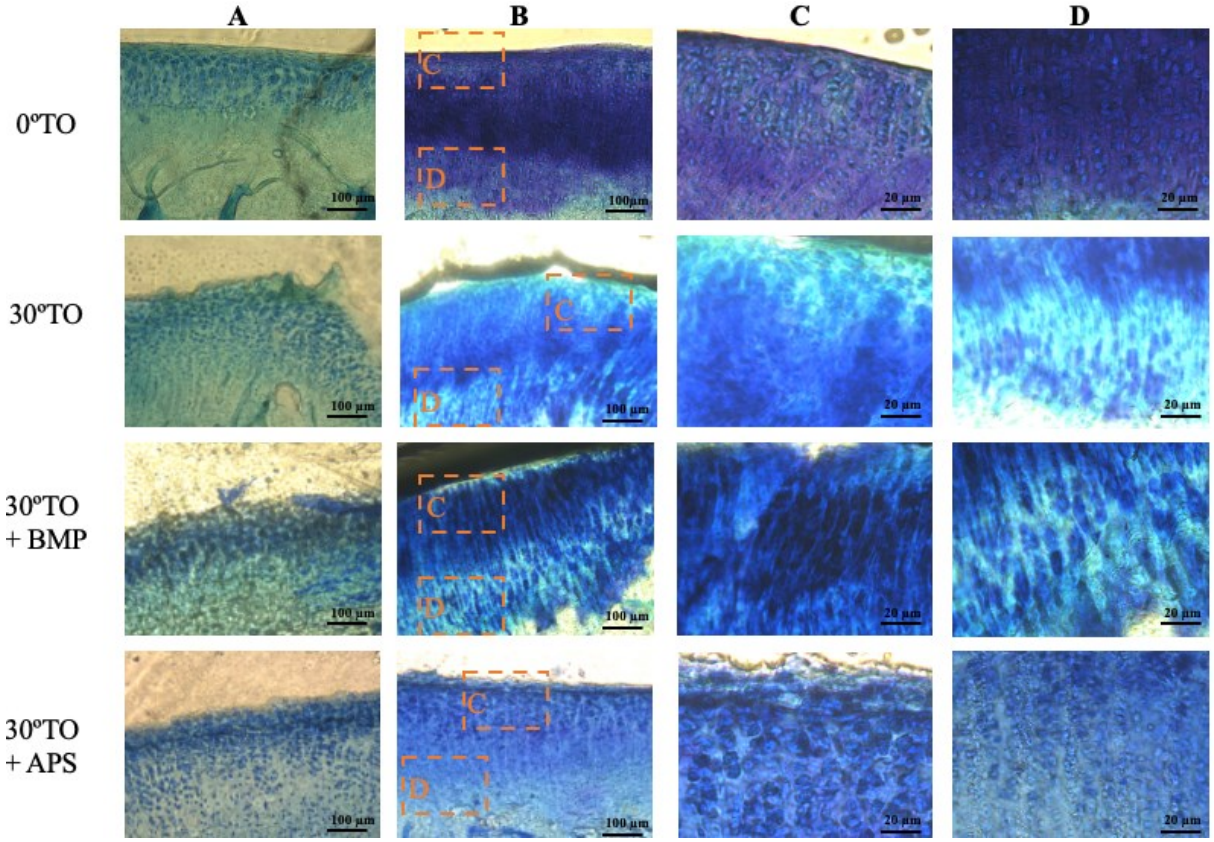

Figure 4-6 (Column A,B) Representative Toluidine-blue stained sections of left limb medial compartment from each experimental group at 5X objective. The boxed area in column B is further magnified (20× objective) in Column C,D. Scales bar: 100 µm (A, B), 20 µm (B, D). Columns A and B display sections from the same group, but the depth of the stain are different due to variations between different staining rounds.

The clear cellular changes between 0ºTO, 30ºTO, 30ºTOBMP groups observed in different layers are depicted in Figure 4-7.

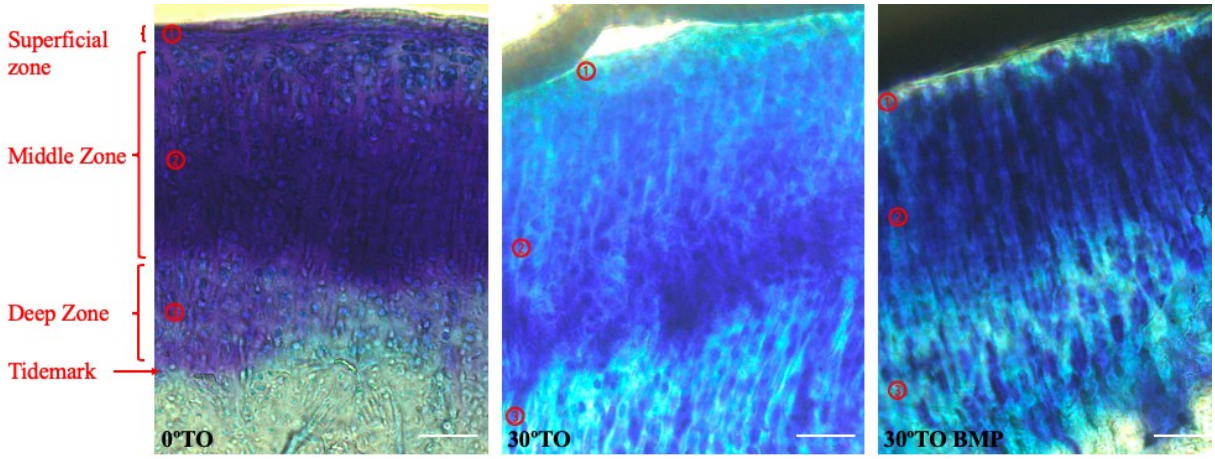

Figure 4-7 Representative sections of left limb medial compartment from 0ºTO, 30ºTO, 30ºTO + BMP group at 20X objective in the same scale (bar = 20µm). The cartilage zones are indicated. This highlights the hypertrophic and fibrosis process observed in cartilage of both the 30ºTO and 30ºTO + BMP groups.

4.4.2 Macroscopic changes and chondrophytes

The macroscopic appearance of the tibia cartilage (with meniscus) was documented during the dissection, prior to tissue fixation and is shown in the 0ºTO (sham) group, the cartilage tissue appeared smooth with a shiny pink watery appearance (Figure 4-8). The 10ºTO group showed no significant changes to the 0°TO group. However, in the 30ºTO group, noticeable alterations were observed on the cartilage surface, including an opaque appearance, rough surface, and wearing in the central weight-bearing area. Following treatment, the cartilage appeared thicker, and the repaired cartilage in the weight-bearing area showed signs of improvement. However, the repaired cartilage did not fully resemble the original healthy cartilage. It exhibited a stiffer and harder (fibrocartilaginous repair) texture and displayed a yellow colour similar to osseous tissue.

Interestingly, there were chondrophytes in the medial posterior margin of the operated limb in the 30ºTO, 30ºTO-BMP treatment, and 30ºTO-APS treatment groups. These chondrophytes appeared as prominent protrusions around the cartilage margin, exhibiting characteristics between cartilage and bone (fibrocartilaginous and osseous tissue). In the 30ºTO -BMP treatment group, the chondrocyte size was significantly increased compared to the 30ºTO no treatment group. In contrast, in the 30ºTO-APS treatment group, the chondrocyte size appeared smaller compared to the 30ºTO no treatment group, and

the chondrophytes felt much softer compared to the BMP-treated group. Chondrophyte formation represents a non-calcified osteophyte precursor, signifying a transitional stage between cartilage repair and endochondral ossification.

However, no chondrophytes were observed in the 10ºTO and 10ºTO-BMP groups, indicating that a higher malalignment angle of 30 degrees is necessary to stimulate chondrocyte formation, which plays a role in joint stabilization. Additionally, the size of chondrophytes was observed to increase with BMP treatment (Figure 4-8)..

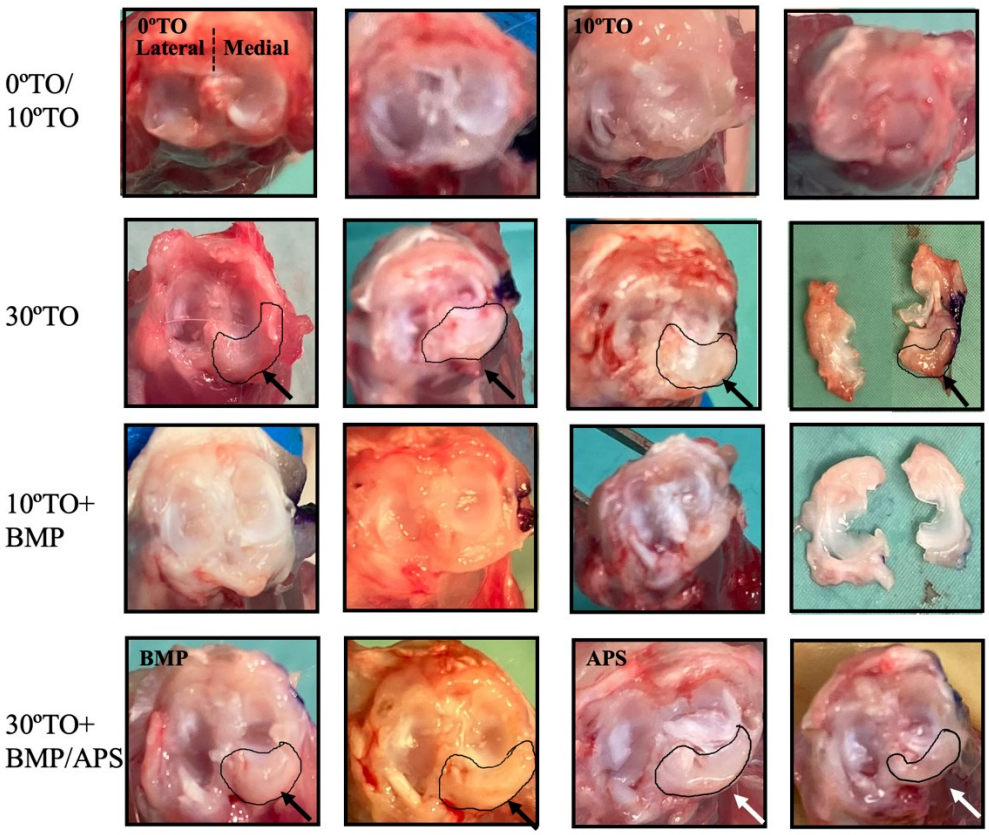

Figure 4-8 Macroscopic changes in the articular cartilage of rats in each group. The arrows indicate a clear chondrophyte in the posterior side of the medial compartment.

4.4.3 Histological section evolution

In this section, the histopathology score, adapted from the OARSI guidelines (Pritzker et al., 2006), is presented to diagnose the occurrence of OA and assess its severity . As previously mentioned, each experimental group represents a specific disease condition (0ºTO, 10ºTO, 30ºTO, 30ºTO + BMP, 30ºTO + APS) and contains 3 biologically independent rats. From each limb of every rat, 3 samples were taken from the central region of each joint, specifically covering the central weight-bearing area. Thus, there are 9 sections (slices) for histological scoring in each experimental group, totalling 54 slices. The

assessment of each slice includes the grading result of OA (Table 4-6), the staging result of OA (Table 4-8), and the overall OA score (Table 4-9).

The histological grading result using the methodology from Table 4-3 is presented in Table 4-6. The data indicate equal variances between groups ($P>0.05$). The one-way ANOVA results show that the mean values (grades) of the 6 experimental groups are significantly different ($P<0.0001$), suggesting that tibia malalignment and treatments significantly affect cartilage healthy grades. The cartilage in the 0ºTO group appears healthy, while the 30ºTO group exhibits a more advanced and progressive state (Grade 3.94, $P<0.0001$) of the disease compared to the 10ºTO group (Grade 1.89, $P <0.0001$). Although BMP treatment results in a significant decrease in grade (Grade 2.06, $P<0.0001$) compared to the 30ºTO (OA) group, it is still significantly different from the 0ºTO (healthy) group ($P<0.0001$). This grade value is based on identifying the most advanced grade observed within the cartilage in terms of vertical extent. This indicates that BMP treatment can repair some small superficial lesions but has limited efficacy in repairing deep lesions. In contrast, APS treatment (Grade 0.33, $P>0.05$ compared to the 0ºTO health group) demonstrates excellent repair of deep lesions.

Table 4-6: Histological section OA grading

Histological feature (Grade)	0ºTO rat medial (n=9)	10ºTO rat medial (n=9)	30ºTO rat medial (n=9)	10ºTO rat+ BMP medial (n=9)	30ºTO rat+ BMP medial (n=9)	30ºTO rat+ APS medial (n=9)
Sample 1 Section 1	0	1	4.5	1	2	0
Sample 1 section 2	0	1.5	4	0	2	0
Sample 1 section 3	0	2	3	1.5	2.5	0
Sample 2 Section 1	0	2.5	3.5	0	1	1
Sample 2 section 2	0	3	4	1	1.5	0
Sample 2 section 3	0	2.5	4.5	1	2.5	1
Sample 3 Section 1	0	1	4	0	2.5	0
Sample 3 section 2	0	1.5	4	0	2.5	1
Sample 3 section 3	0	2	4	1	2	0
Mean of 9 sections (mean ±SD)	**0.00(0)**	**1.89(0.66)**	**3.94(0.44)**	**0.61(0.57)**	**2.06(0.50)**	**0.33(0.47)**

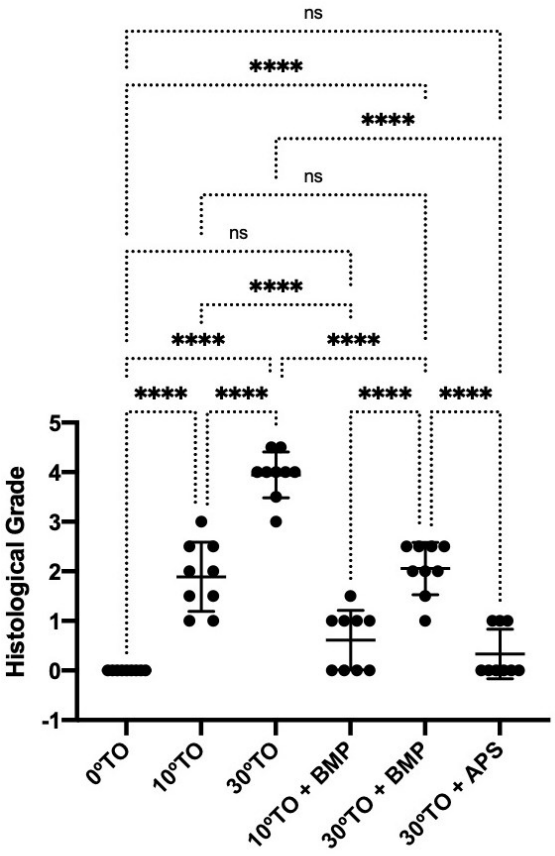

Figure 4-9 Comparison of the histological OA grade among groups in left medial compartment (n = 9 from 3 biological independent rats per group, one-way ANOVA; ns, not significant; *p ≤0.05 ,**p < 0.01, ***p<0.001, ****p<0.0001)

Furthermore, **the staging results** using the method described in Table 4-4 and presented in Table 4-8 and Figure 4-10 reveal that the affected cartilage area (Stage 2.60) is effectively repaired in terms of horizontal extent after both BMP 7 (Stage 0.93, p<0.001) and APS (Stage 0.53, p<0.0001) treatments. These findings, both grade and stage results, highlight the differential effects of BMP and APS treatments on the grading and staging of OA. APS shows superior outcomes in repairing deep lesions and improving the horizontal extent of cartilage repair.

Table 4-7 Staging result (mean of three zones) of histological sections.

Histological feature (Stage)	0ºTO rat medial (n=9)	10ºTO rat medial (n=9)	30ºTO rat medial (n=9)	10ºTO rat+ BMP medial (n=9)	30ºTO rat+ BMP medial (n=9)	30ºTO rat+ APS medial (n=9)
Sample 1 Section 1	0.27	0.70	2.00	0.50	0.93	0.50
Sample 1 section 2	0.23	0.53	2.07	0.47	0.93	0.60
Sample 1 section 3	0.20	0.67	2.13	0.47	0.97	0.50
Sample 2 Section 1	0.30	0.63	2.03	0.50	0.90	0.53
Sample 2 section 2	0.20	0.63	2.07	0.50	1.00	0.50
Sample 2 section 3	0.23	0.70	2.10	0.50	0.93	0.57
Sample 3 Section 1	0.23	0.60	2.03	0.47	0.90	0.50
Sample 3 section 2	0.23	0.60	2.07	0.50	1.00	0.57
Sample 3 section 3	0.27	0.70	2.07	0.47	0.93	0.57
Mean of 9 sections (mean ±SD)	**0.23 (0.03)**	**0.63 (0.06)**	**2.6 (0.04)**	**0.45(0.02)**	**0.93(0.04)**	**0.53(0.04)**

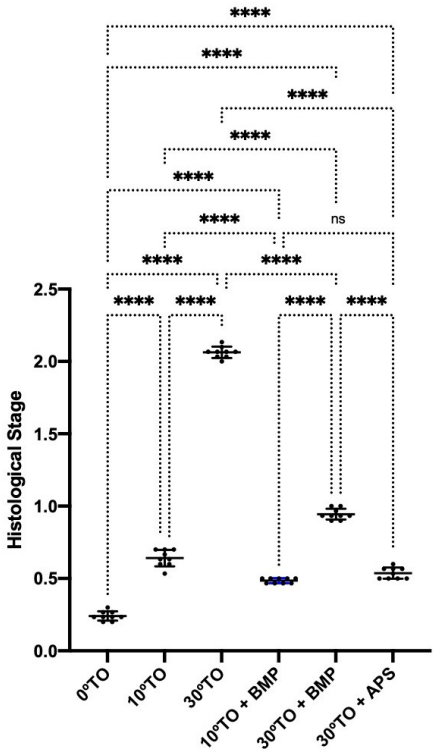

Figure 4-10 Comparison of the histological OA stage among groups in left medial compartment (n = 9 from 3 biologically independent rats per group, one-way ANOVA; ns, not significant; *p ≤0.05 ,**p < 0.01, ***p<0.001, ****p<0.0001)

Next, Table 4-8 and Figure 4-12 list the detailed stage results corresponding to each zone of every group. Interestingly, this evaluation of horizontal extent (stage score in each zone) reveals that the inner and outer zones are consistently the most severely affected zones in all groups (P<0.0001 compared to 0ºTO health group) compared to the middle zone (central loading area). The OA stage in the middle zone has

returned to the baseline after BMP/APS treatment (P>0.5 compared to the 0ºTO health group), as illustrated in Figure 4-11.

Table 4-8: Staging result of histological sections (n=9, mean ±SD)

Histological feature (stage)	0ºTO rat medial	10ºTO rat medial	30ºTO rat medial	10ºTO rat+ BMP medial	30ºTO rat+ BMP medial	30ºTO rat+ APS medial
Zone 1 (inner)	0 (0)	0.6 (0.09)	2.6 (0.08)	0.4(0.08)	1(0.08)	0.6(0.06)
Zone 2 (middle)	0.5 (0.08)	0.5 (0.07)	1.6 (0.08)	0.4(0.08)	0.6(0.08)	0.4(0.07)
Zone 3 (outer)	0.2(0.08)	0.8 (0.10)	2 (0.08)	0.6(0.07)	1.2(0.08)	0.6(0.09)
3-Zone average	**0.23 (0.03)**	**0.63 (0.06)**	**2.6 (0.04)**	**0.45(0.02)**	**0.93(0.04)**	**0.53(0.04)**

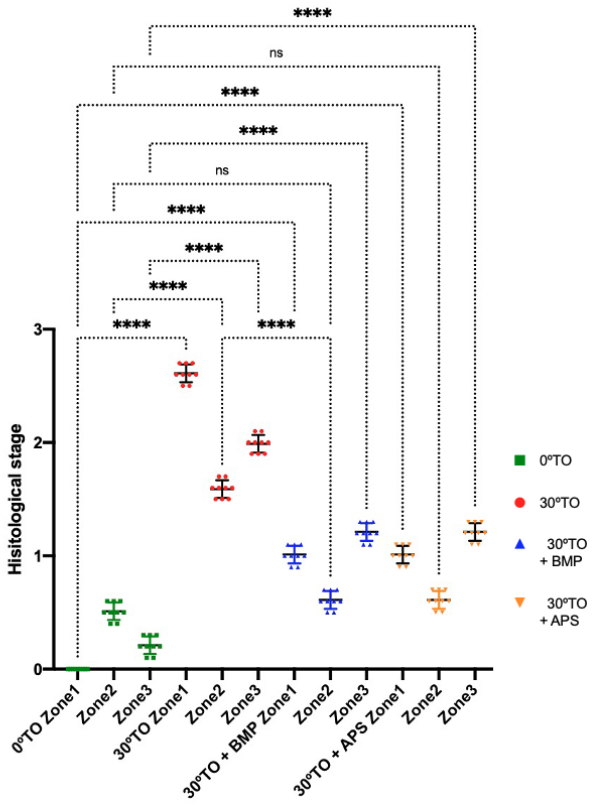

Figure 4-11 Comparison of the OA staging between 0ºTO, 30ºTO, 30ºTO + BMP, and 30ºTO + APS in corresponding zones (n = 9 from 3 biologically independent rats per group, one-way ANOVA; ns, not significant; *p ≤0.05 ,**p < 0.01, ***p<0.001, ****p<0.0001).

The overall score analysis, as outlined in Table 4-5 and with results presented in Table 4-9 and Figure 4-12, reveals the presence of OA in the 10ºTO, 30ºTO, and 30ºTO + BMP groups (score >1). In contrast, the 0ºTO (score 0), 10ºTO + BMP (score 0.3), and 30ºTO + APS (score 0.19) groups indicate a healthier state of cartilage with minimal degenerative changes. To compare statistical significance between groups, the Kruskal-Wallis test with Dunn's multiple comparisons test was used, due to the significantly

different variances between groups (P<0.05). Notably, the 30ºTO group (score = 8.1) showed significantly (P<0.0001) more severe OA when compared to the 0ºTO group (score=0). While BMP treatment (score 1.90) doesn't significantly prevent OA (P>0.5 compared to 0ºTO group), it does slow down its progression (score reduced from 8.1 to 1.90), as also evidenced by histological observations (Figure 4-2). Conversely, APS treatment (score 0.19) has a markedly superior efficacy (P<0.0001 compared to 30ºTO group) in deescalating OA compared to BMP, which is comparable to a healthy state (P>0.5 compared to 30ºTO group). These findings highlight the potential of APS treatment in mitigating the severity of OA and promoting cartilage health.

Table 4-9: Score result of the histological sections (Score = grade × stage).

Histological feature (score)	0ºTO rat medial (n=9)	10ºTO rat medial (n=9)	30ºTO rat medial (n=9)	10ºTO rat+ BMP medial (n=9)	30ºTO rat+ BMP medial (n=9)	30ºTO rat+ APS medial (n=9)
Sample 1 Section 1	0.00	0.70	9.00	0.50	1.87	0.00
Sample 1 section 2	0.00	0.80	8.27	0.00	1.87	0.00
Sample 1 section 3	0.00	1.33	6.40	0.70	2.42	0.00
Sample 2 Section 1	0.00	1.58	7.12	0.00	0.90	0.53
Sample 2 section 2	0.00	1.90	8.27	0.50	1.50	0.00
Sample 2 section 3	0.00	1.75	9.45	0.50	2.33	0.57
Sample 3 Section 1	0.00	0.60	8.13	0.00	2.25	0.00
Sample 3 section 2	0.00	0.90	8.27	0.00	2.50	0.57
Sample 3 section 3	0.00	1.40	8.27	0.47	1.87	0.00
Mean of 3 rats (mean ±SD)	0.0 (0.0)	1.2 (0.46)	8.1(0.21)	0.30(0.13)	1.9(0.33)	0.19(0.18)
Mean of 9 sections (mean ±SD)	0.0 (0.0)	1.2 (0.48)	8.1 (0.91)	0.30 (0.29)	1.9 (0.51)	0.19 (0.29)

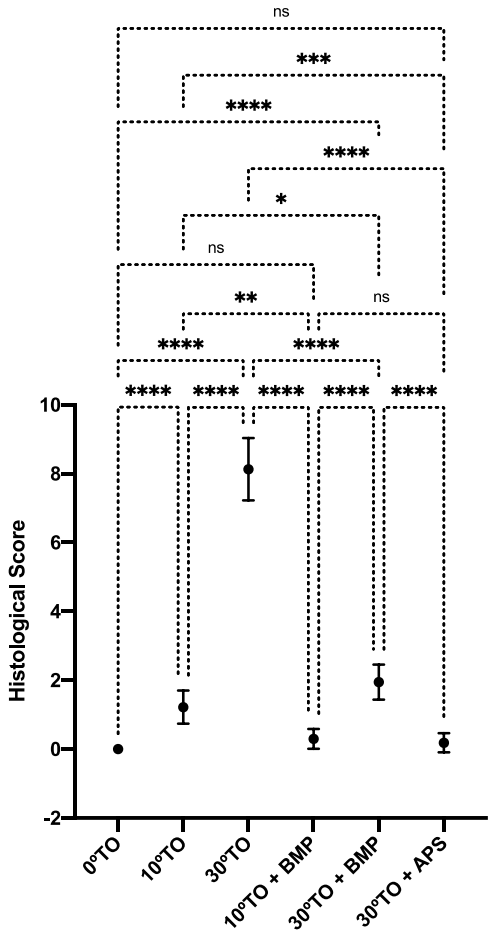

Figure 4-12. Comparison of the average histological OA score among groups in left medial compartment (n = 9 from 3 biological independent rats per group, one-way ANOVA; ns, not significant; *p ≤0.05 ,**p < 0.01, ***p<0.001, ****p<0.0001)

4.5 Discussion

4.5.1 Cartilage degeneration in OA

In this study, a comprehensive histopathology scoring system adapted from the OARSI guidelines was used to evaluate the severity and extent of OA in a surgically inducted tibial malalignment rat model. The findings demonstrated that OA occurs in this surgically induced model, that OA progression is more severe the greater the tibial malalignment and that the OA primarily affected the medial compartment of the operated joint. The results also show that there were different treatment effects with APS and BMP with APS treatment demonstrating greater proximity to healthy cartilage and BMP treatment displaying similarities to the repair stage of hypertrophic differentiation. Figure 4-13 provides a schematic to illustrates these observed changes.

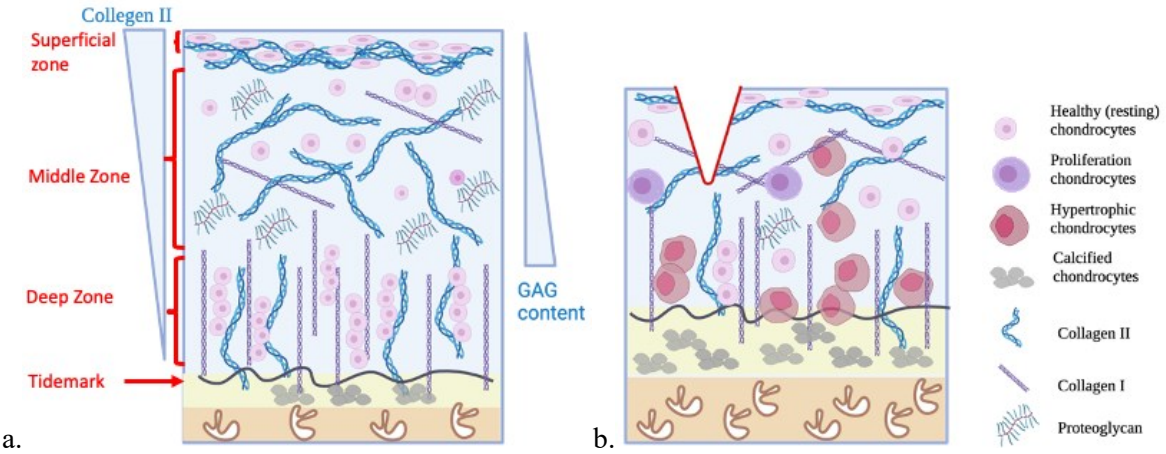

Figure 4-13. Schematic of healthy and OA cartilage structure (chondrocytes and collagen fibres). (a) the normal 'stable' articular chondrocytes in healthy articular cartilage; (b) the 'transient' phenotype cartilage in OA. In the cartilage from OA joint, there is chondrocyte hypertrophy and matrix mineralisation. In the deepest zone of cartilage. The calcified cartilage zone is increased.

Healthy cartilage demonstrated a homogeneous proteoglycan-rich matrix throughout all layers and exhibited strong Toluidine blue staining. In contrast, OA cartilage (include osteophytic cartilage, chondrophytes) displayed a layered pattern, with reduced Toluidine blue staining in the superficial layer, indicating proteoglycan loss. Previous studies have shown that this layer is primarily composed of type I collagen, suggesting the presence of **fibrocartilaginous tissue** during cartilage repair (Gelse et al., 2012a). In the bottom half of OA cartilage, the organization of chondrocytes was irregular and clustered, with oversized chondrocytes displaying hypertrophy and signs of cell death, presented as increased (or decreased) matrix staining and proteoglycan content. The observations of **hypertrophic and fibrocartilaginous tissue** in OA cartilage align with existing evidence that chondrocytes undergo a shift towards hypertrophic and fibrocartilaginous changes during OA progression, contributing to the destruction of articular cartilage tissues (Ji et al., 2019). Hypertrophic chondrocytes have the ability to differentiate into osteoblasts or secrete cytokines that promote cartilage calcification (Kurenkova et al., 2022). Additionally, it has been demonstrated that mechanical forces exerted on chondrocytes can induce morphological changes, as evidenced by more prominently pronounced nuclear and a typical polygonal morphology observed under scanning electron microscopy (SEM) in human chondrocytes in vitro (Beckmann et al., 2014).

Upon examining the higher magnifications (Figure 4-7) of OA cartilage and healthy cartilage, significant differences were observed in the bottom layers of OA cartilage, particularly in the 30ºTO and 30ºTO BMP groups. Notably, large hypertrophic chondrocytes (from chondrocyte differentiation) were observed in the osteophytic cartilage and OA lesion cartilage but were absent in intact articular cartilage. This observation corresponds with the finding that OA cartilage (both centre cartilage lesion and osteophyte cartilage) lacks a tide mark or a continuous subchondral bone plate beneath the articular

cartilage and instead exhibits uneven bone trabeculae. This suggests the action of osseous tissue in forming bone trabeculae in the deepest zones of OA and osteophytic cartilage.

Interestingly, the findings deviated from initial expectations, as hypertrophic-like changes were anticipated to be limited to the deepest layers of articular cartilage above the calcified cartilage, and would be organized similarly to the growth plate with a resting zone, proliferating zone and hypertrophic zone (Nilsson et al., 2007). However, oversized chondrocytes were observed throughout various layers of the cartilage, even appearing in the superficial layer. This need further investigation, such as immunohistochemistry, to determine if these chondrocytes are indeed hypertrophic. Therefore, the study could not definitively confirm if hypertrophic-like chondrocytes drive the calcification process in the deepest cartilage layer of OA.

Literature reports have presented conflicting findings regarding the distribution of large hypertrophic chondrocytes in OA cartilage and osteophytic cartilage, with some studies suggesting they are limited to the bottom layers (Gelse et al., 2003, Aigner et al., 1995), while others indicate their absence in the overlying hyaline zone. Some studies propose that OA degeneration begins in the deepest layer of cartilage near the subchondral bone plate (Gelse et al., 2003, Aigner et al., 1995, Gelse et al., 2012b). In contrast, other studies have found there are no significant variations in chondrocyte size between deeper and more superficial regions of the articular cartilage (Bush and Hall, 2003). And a positive correlation has been observed between the severity of cartilage damage in human OA and an increase in chondrocyte size and hypertrophic markers compared to healthy cartilage (Gratal et al., 2019). Hypertrophic cartilage markers, such as Col X and MMP-13, have been found to exhibit a uniform distribution throughout the tissues (Gratal et al., 2019). This **diffused hypertrophic pattern** reflect the differences between cartilage degeneration in the OA process and the physiological process of endochondral ossification, potentially contributing to functional changes in OA cartilage.

Overall, the results in this chapter provide valuable insights into the histopathological features of OA cartilage, highlighting the presence of hypertrophic and fibrocartilaginous tissue. To gain further insight into OA progression, it is necessary to identify specific markers and signal pathways (in Chapter 7) that can differentiate hyaline cartilage chondrocytes from fibrocartilage cells and hypertrophic chondrocytes.

4.5.2 Chondrocyte hypertrophic process and chondrocyte formation during cartilage repair

Microscope results revealed that, in the 30ºTO -BMP treatment group, chondrocyte size significantly increased compared to both the 30ºTO no-treatment group and the 30ºTO -APS treatment group. It is hypothesized that BMP treatment in OA can help cartilage repair but also enhance chondrophyte formation. These chondrophytes appear as prominent protrusions around the cartilage margin, exhibiting characteristics intermediate between cartilage and bone (fibrocartilaginous and osseous tissue).

To understand why the BMP group had larger and stiffer chondrophytes, a literature review was undertaken. It is well-known that osteophyte formation is facilitated by BMPs, which belong to the TGF-ß superfamily and are crucial for morphogenesis, skeletal development, and bone formation (van der Kraan and van den Berg, 2007) (Balemans and Van Hul, 2002). For example, BMP7 is a well-known bone-inducing factor for bone formation and embryonal cell differentiation. BMP8B, homologous to BMP-7, was also found to have significantly higher expression in osteophytic chondrocytes (Ying et al., 2001). In contrast, BMPs are suppressed in articular cartilage (permanent cartilage), with high expression of GREM1, a BMP antagonist (Fajardo et al., 2009, Davidson et al., 2007) (Tardif et al., 2004). GREM1 is reported to bind and block the activity of BMP-2, -4, and -7, especially at the intracellular level (Merino et al., 1999). However, GREM1 is not detected in osteophyte cartilage (Gelse et al., 2012b), suggesting an opposite pattern regarding the regulation of BMPs on articular cartilage and osteophyte.

Healthy cartilage and osteophytes represent distinct phenotypes, with significant differences in molecular mechanisms between these two cartilaginous tissues (Gelse et al., 2012b, Xu et al., 2017). The chondrocytes in healthy cartilage are in a a postmitotic status and retain this stable phenotype for a period of many decades. In contrast, the chondrocytes in osteophytes are in an active status, including anabolic and catabolic process. It is a transient stage towards bone formation. The cellular differentiation programme involved in forming the chondrophytes is more similar to the formation of growth plate and fracture soft callus, following the processes of chondrocyte hypertrophy and endochondral ossification process (Gelse et al., 2012b).

However, chondrophyte formation does not necessarily reflect a typical transient chondrocyte phenotype. The process leading up to endochondral ossification is prolonged in osteophytic cartilage. In the fracture callus, it is a fast process that the chondrocytes becoming hypertrophic chondrocytes (pro-apoptotic status), and terminally replacing by mineralized tissue. However, within chondrophytes, the chondrocyte hypertrophic and mineralization processes develops more gradually, spanning months or even years (Gelse et al., 2012b). Therefore, osteophytic cartilage exhibits both transient and non-hypertrophic characteristics.

In the histology results, it is observed that the hypertrophic chondrocytes were primarily focally located in the deep layer of chondrophyte cartilage, while the upper half of cartilage retained most features of articular cartilage. Previous molecular studies have also demonstrated that most chondrocytes in the chondrophyte cartilage have not yet differentiated to the hypertrophic status (Gelse et al., 2003) (Gelse et al., 2012b).While type X collagen, a marker of chondrocyte hypertrophy and terminal differentiation, is only positive in the deepest chondrophytes cartilage, the upregulation of COL10A1in osteophytic cartilage is not significant, indicating the transient nature of osteophytic cartilage(Gelse et al., 2003) (Gelse et al., 2012b) .

There is controversy in this field, as some studies have reported no significant upregulation of type X collagen expression in late-stage OA (Brew et al., 2010). This suggests that, besides fibrillated cartilage which has undergone terminal differentiation (hypertrophic process, produce collagen X and apoptosis) and thus do not have high collagen X expression in the late stage of OA, a significant portion of intact viable cartilage in late-stage OA may not undergo the common pathogenic mechanism involving chondrocyte hypertrophy (Brew et al., 2010). Therefore, chondrocyte hypertrophy may not be a universal pathogenic mechanism in OA, and alternative approaches to reinitiating matrix production in non-hypertrophic chondrocytes should be explored.

Inhibition of chondrocyte hypertrophy and its transition into osteophytes can be achieved through various means. Mechanically, osteophytes serve as a compensation mechanism for joint stabilization in response to varus gait. At the molecular level, the mechanisms have not been fully understood but the BMP injection may contribute to osteophyte formation as a side effect.

These findings introduce a novel concept in the treatment of cartilage repair and OA, focusing on stabilizing the permanent chondrocyte phenotype and preventing their hypertrophic process (terminal differentiation) rather than only using pro-chondrogenic anabolic factors (chondrocyte proliferation). Antagonistic and inhibitory factors of the BMP and Wnt pathways (from Chapter 7), may help maintain the permanent chondrocyte phenotype and prevent osteophyte formation.

To date, the mechanisms that enable the articular chondrocyte to keep in this permanent phenotype has not been fully understand. The cartilaginous cap of mature osteophytes can be further studied as a prototype for cartilage repair tissue, and can further contribute to the understanding of the control of chondrogenesis (Gelse et al., 2012b). Comparative studies between transient cartilage repair tissue chondrocytes (seen in cartilage repair and fracture callus process), osteophytes (an intermediate stage), and permanent chondrocytes (seen in health articular cartilage) will provide valuable insights into the control of chondrogenesis and contribute to the advancement of OA treatment strategies.

In summary, this chapter has shown histological evidence of a dose-response relationship in OA development to the angulation of a tibial osteotomy on a rat model of OA. APS and BMP can be used to treat the OA, with different effects. Specifically, APS treatment closely aligns with the characteristics of healthy cartilage, whereas BMP treatment resembled the repair phase of cartilage's hypertrophic and fibrocartilaginous differentiation. The following chapter will investigate the subchondral changes in the developed OA model.

5 Micro CT imaging in characterising OA subchondral bone changes

5.1 Summary

This chapter aims to use Micro CT analysis to characterise changes in subchondral bone following the onset of OA and the administration of BMP and APS treatment. Distinct characteristics were observed between each group in both limbs. As the severity of OA increased, there was an observation of subchondral bone absorption and remodelling, as well as osteophyte formation, to accommodate the mechanical imbalance caused by malalignment. This was accompanied by an increase in subchondral bone plate thickness, a decrease in trabecular bone volume fraction (BV/TV), a reduction in trabecular bone thickness, and a decrease in space. The BMP treatment group was observed to be more active in repairing this remodelling back to normal, albeit stimulating osteophyte formation. The results also show tibial bone remodelling stemming from malalignment.

5.2 Introduction

Radiography is the classic golden standard and the most widely used way of OA imaging in the clinic and research (Roemer et al., 2014b, Kuyinu et al., 2016a). Although there is a lack of sensitivity and not all joint structures can be visualised, the detection of joint space narrowing (JSN) by X-ray is still the main criterion used in the assessment of OA progression and therapies (Roemer et al., 2014b). Additionally, knee malalignment identified in full-leg radiographs is an important indicator of disease progression and treatment outcomes (Hinman et al., 2006). However, the limitations of radiography are obvious and include: a two-dimensional (shadow) imaging of three-dimensional variables and the use of ionising radiation. With the reduction of the cost and widespread adoption of other technologies, MRI and CT (and micro-CT) based OA studies have become more common (Roemer et al., 2014b).

As described in Chapter 1, Section 1.4 and Section 1.6.2, OA is mechanically characterized by an imbalance between the breakdown and repair of cartilage and subchondral bone. While most OA studies have focused on cartilage changes, fewer have addressed the changes in bone. Recent studies have shown that in the early phases of OA, bone changes are more pronounced and occur earlier than those in cartilage (Wei et al., 1998a). These bone changes, including both the subchondral bone in the joint area and the entire tibia on a larger scale, are subject to physiological regulation, as well as pathologic healing and remodelling in response to mechanical abnormality stimulation (Huiskes et al., 2000). Microdamage in subchondral tissues has recently been identified as a novel structural marker in the early stages of knee OA, occurring prior to damage in the cartilage layer (Day et al., 2001a, Hayami et al., 2006a). Moreover, some researchers suggest that the presence of osteophytes, a proliferative change observable in CT scans, may serve as an early indicator for predicting OA development, even before conventional radiographic diagnoses (such as joint space narrowing) are possible (Katsuragi et al., 2015).

To enhance its application in detecting the initial stages of OA, micro-CT has recently been utilized to quantify subchondral changes in rodent models (Botter et al., 2006a). The parameters of subchondral bone commonly reported include subchondral plate thickness, trabecular bone volume, trabecular spacing and thickness (Figure 5-1) (Moodie et al., 2011, Das Neves Borges et al., 2017, Ping et al., 2021, Li et al., 2013b, Christiansen, 2016, Mohan et al., 2011). Studies also indicate that increases in osteophyte size are strongly associated with severe cartilage defects and subchondral sclerosis (Boegard, 1998, Roemer et al., 2012b). In addition, previous studies also utilized finite element (FE) analysis to investigate the effects of tibia malignments on the localised loading (stress and strains distribution) of tibia platform (Inoue et al., 2016, Martay et al., 2018, Nie et al., 2021). (Kiapour et al., 2014).The aim of the work presented in this chapter is to use micro-CT images to assess the subchondral bone structural changes, osteophytes formation and whole-tibia anatomical changes in OA within the animal model presented previously and to use FE simulation to validate the changes in whole-limb bone remodelling that occur due to alterations in loading patterns established via tibia osteotomy surgery in this OA animal model. The study hypothesizes that malalignment-induced osteoarthritis influences the CT-measured parameters related to the distribution and arrangement of subchondral bone, and subsequently induces large-scale whole-limb anatomical changes, which include alterations in tibia morphology and joint alignment.

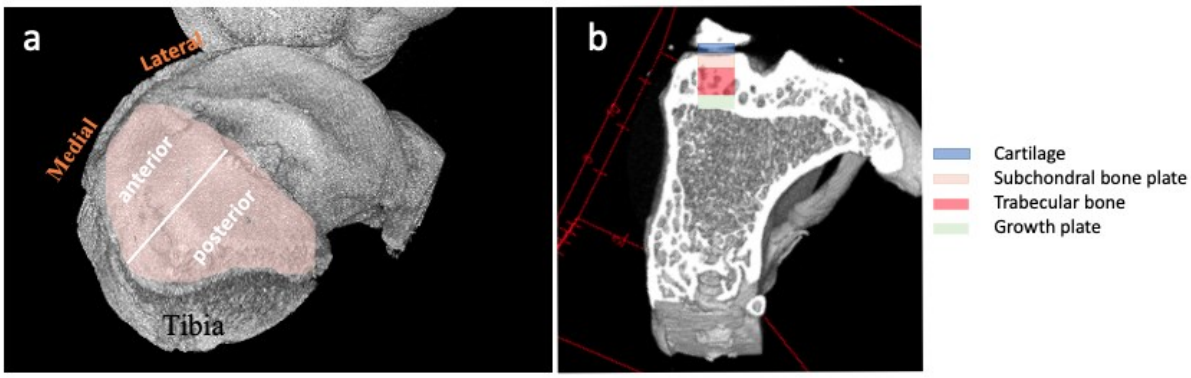

Figure 5-1. Outline of the CT-measured regions in the study presented in this chapter. (a) transverse view of the proximal tibia (b) sagittal view of the proximal tibia

5.3 Material and methods

5.3.1 Micro-CT imaging protocol

As described in the methods in Chapter 3, the tibiae were carefully dissected from the femurs, removing all the soft tissues, menisci and capsules. After the lower limb (tibia and feet) was fixed for 48 hours in formalin, the whole lower limb was moved to a conical 50ml tube and placed in a consistently aligned and oriented vertical position. The tube contained a small amount of formalin to help maintain sample hydration during scanning.

The scan protocol included a rough scan of the whole limb and a separate detailed scan of the knee (Figure 5-2).

The higher resolution scan can provide greater separation of the two grey level peaks (Figure 5-3), which affects the segmentation of the trabecular structure within the bone tissue. Generally, the measurement error increases with the decrease of the ratio of objective size to voxel size, therefore for accurate morphologic measurement the ratio is recommended to be as high as possible (Christiansen, 2016). In the subchondral bone measurement, it is suggested that the voxel size should be less than half of the structure thickness (trabecular bone thickness). Previous studies suggested the voxel sizes need to achieve between 6–20μm on mouse trabecular bone measures (Christiansen, 2016). They tested the trabecular measurement result and found that they do not vary significantly when the voxel size is within the range of 6-20μm, but has obvious errors with greater voxel sizes of 30μm (Christiansen, 2016). Consequently, it is challenging to detect the subchondral bone changes between healthy and diseased individuals. After referencing several studies related to the micro-CT imaging of rat subchondral bone (Verdelis et al., 2011, Kim et al., 2021), the pixel size was set at 9.90μm in the study, which presents the smallest achievable pixel size under the given protocol setting. In this study, the Zeiss Versa-510 microCT system (Figure 5-2) was employed for the CT scanning. The source energy was set at 70.07 kV voltages, with a power of 6. A complete rotation of 360º was performed to capture the entire section of the proximal tibia. Each sample required an average scan time of approximately 42 minutes, encompassing 801 projections. The exposure time was set at 3 seconds to optimize image quality and minimize potential artifacts.

This technique utilized a micro-CT with a field of view (FOV) of 20272μm wide × 20272μm high, along with a pixel size of 9.90μm. Similarly, for the whole tibia view, CT scanning was applied in a FOV of 49686μm wide × 49686μm high, with a pixel size of 24.26μm.

Micro-CT volumes were calibrated using Hounsfield units (HU), a standard scale for measuring the density of materials in CT scans. Before each sample scan, water and air were scanned for calibration, setting HU values at 0 for water and -1000 for air. This step ensured consistent analysis and interpretation across all scans.

Following each scan, a stack of 2300 cross-sections was reconstructed, with an interslice distance of 1 pixel (9.9μm or 24.26μm). The reconstructed images were standardized to a resolution of 1500 × 1500 pixels, with a pixel size of 9.9μm or 24.26μm, depending on the specific view, as described above. These images were stored as 8-bit representations, with 256 grey levels, facilitating further processing and analysis of the volumetric data.

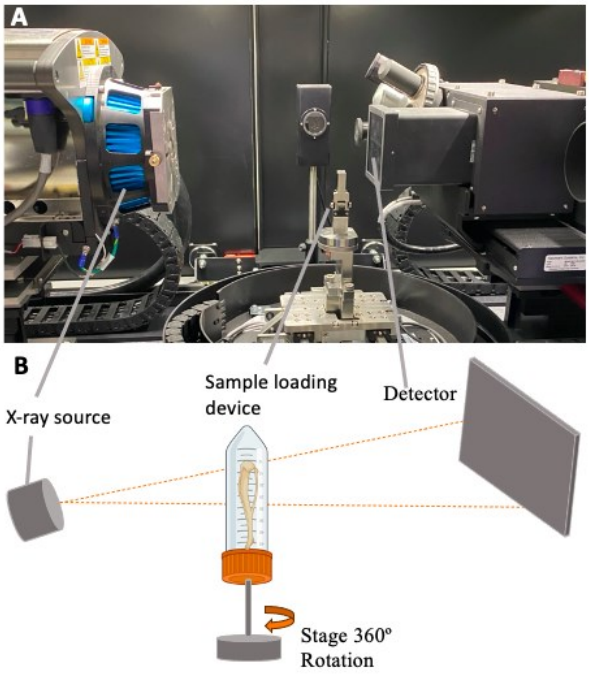

Figure 5-2. Micro-CT machine set up. (A) Inside view of Zeiss Versa 510 micro-CT machine (B) Schematic representation of a micro-CT imaging system (Created with BioRender.com).

5.3.2 Micro-CT image analysis

5.3.2.1 Trabecular bone measures

Step 1. Thresholding

The first step involved segmenting the images into 'bone' and 'non-bone' based on the HU histogram (Figure 5-3), resulting in a binarized image. Two methods were tested for determining the segmentation threshold in image analysis, manual thresholding and "auto threshold" algorithms.

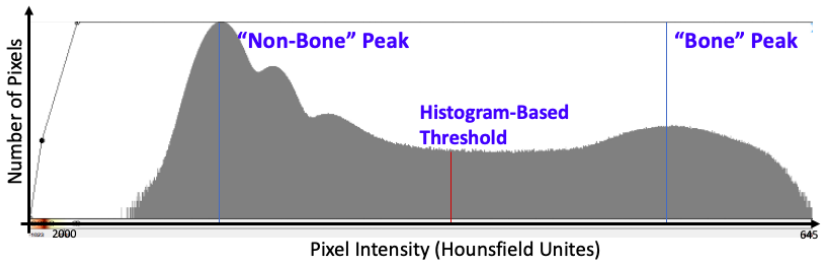

Figure 5-3 Histogram depicting the image segmentation threshold for the "Bone" and "non-bone" areas. The threshold was set around the midpoint between the peaks representing "bone" and "non-bone" in the histogram.

The first method involved manual determination of a threshold value (or range), which was manually set to separate the foreground (trabecular bone) pixels from the background (non-bone areas, such as air, tissue, or bone marrow) through thresholding. This threshold was then uniformly applied to all images within the stack. In Image J, manual adjustment of the threshold is possible. Following micro-CT

scanning reconstruction, a stack of 16-bit RGB images is obtained. Grayscale colours range from 0 to 255. By choosing a threshold value, such as 100, pixels with values below 100 become part of the background, while pixels equal to or above 100 become part of the foreground. It is common to select a threshold that separates the peaks in the histogram (Figure 5-3). The second method utilized an automatic threshold determination approach and each slice of the stacks was individually segmented using this method. Image J offers various auto-thresholding methods for the separation of bone and background. In this study, Otsu's method (Otsu, 1979) was chosen for segmentation after comparing different auto-thresholding methods (shown in the results below). The algorithm assumes a threshold "t" to separate pixels into two classes (background and foreground), aiming to find the optimal threshold value where the within-class variance (weighted variance) between the two classes is minimized. The key of the auto-thresholding process in Image J is to iterate through all possible values and automatically measure the within-class variance.

Step 2. Segmentation

In the binarized images, the regions of interest (ROI) for the trabecular bone in the tibia lateral and medial compartments were manually drawn separately (Figure 5-4B). These ROIs were demarcated from where the condyle was flattened (a feature that will be discussed later; from below the subchondral plate) or where bone content was less than 90% and extending distally towards the growth plate interface (Figure 5-4A) (Das Neves Borges et al., 2014). Approximately 120 slices per joint were used for analysis, The segmented ROIs of the trabecular bone were analysed using the 3D algorithms in BoneJ (Domander et al., 2021), a plugin in ImageJ software. This resulted in the calculation of various structural parameters of the trabecular bone, including the bone volume fraction (BV/TV), trabecular thickness (Tb.Th) and trabecular spacing (Tb.Sp).

The bone volume fraction (BV/TV) represents the volume of mineralized bone per unit volume of the sample (Figure 5-4C). The bone volume (BV) was determined by summing the voxels within the identified bone threshold range, providing a three-dimensional measurement of the segmented bone. The total volume (TV) refers to the total number of voxels in the image, encompassing both bone and non-bone regions.

When using BoneJ to calculate the bone fraction (BV/TV), a modified method was used here (Figure 5-4 A-C) in which manual selection of the ROI region was used, starting from the image where bone content was less the 90% (BV/TV < 90%). This ensures that the entire area, including both the centre and periphery, is included in the analysis. The traditional method (Figure 5-4D-F), on the other hand, involves drawing a rectangular ROI that fits within the sample as much as possible and is then cropped accordingly, leaving the cropped images from the ROI region completely filled with trabeculae (Figure 5-4E). In this thesis, enlarging the ROI region through manual selection was conducted, because: 1) the trabecular bone (TB) stacks are not perfectly cylindrical - the size of the ROI region largely depends on

the bone's size in the top slice; and 2) manual ROI selection accommodates the variability of BV/TV in different zones of the cartilage. A small rectangular ROI cannot fully represent the overall condition of the bone. The issue of the rectangular ROI selection method in BoneJ's auto-calculation was highlighted previously study (Moodie et al., 2011).

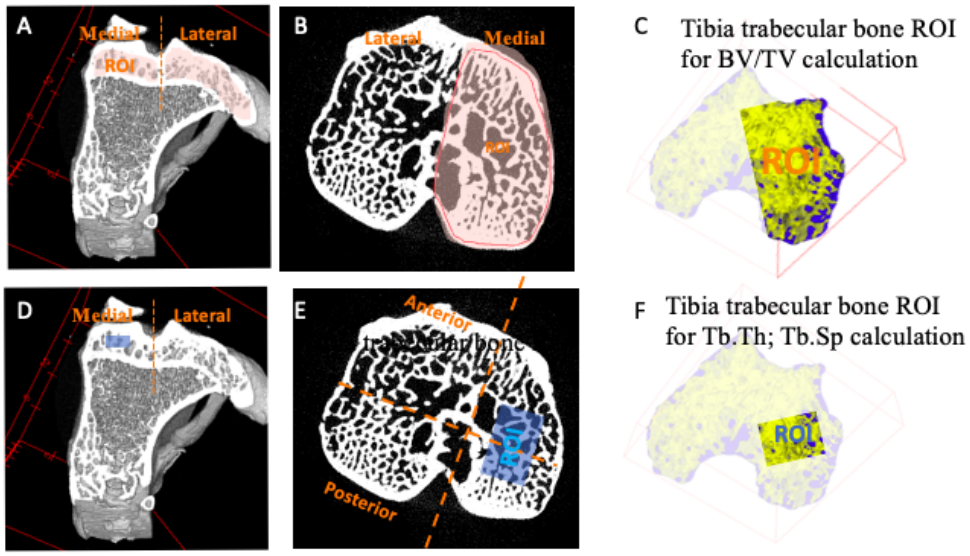

Figure 5-4: Tibia trabecular bone ROI analysis: **For BV/TV calculation.** (A). Trabecular ROI region (pink) in sagittal slide of the 3D reconstruction image of proximal tibial plateau (B). Trabecular ROI region in axial slide of the 3D reconstruction. Red shape represent the hand-drawn ROI (C) A stack of manual region growth ROI for calculating BV/TV, with 3D rendering of the BV surface (yellow) and TV surface (blue) (Domander et al., 2021). **For Tb.Th and Tb.Sp calculation.** (D) Trabecular ROI regions (blue) in sagittal slide of the 3D reconstruction image of proximal tibial plateau (E) Trabecular ROI region in axial slide of the 3D reconstruction. (F) 3D rendering of the BV surface (yellow) and TV surface (blue)

Step 3. Calculating BV/TV

(1) In the previous segmentation step (Figure 5-4 A-C), the ROI region was manually selected for each image using the region-growing method, extending from the sharp top (small ROI) to the cylindrical bottom (large ROI). In the calculation step, the volume of the sample is calculated from the HU of each pixel. The HU values of the foreground (bone) and the background (total ROI region volume) were calculated separately, leading to the percentage of bone volume in total volume. The detailed steps performed in ImageJ are as follows: After applying the "Otsu method" threshold to each image, the bone area was identified in several images within the stack (Figure 5-4 C). The region growth segmentation method was utilized to segment the entire stack of images iteratively.

(2) The ROI area of each image was then measured, using “macro” plugin to automatically measure the area in every image of the stack. The macro code specifies the number of slices, running the

"measure" function accordingly. The area values of the ROI region were summed in each image and multiplied by the pixel spacing (1.5µm). This yielded the total volume (TV), which represents the sum of the selected ROI areas.

(3) For calculating the bone volume (BV), a similar method was used but by selecting the "limited threshold" option. This involved summing the pixels above the threshold and multiplying them by the pixel spacing.

Step 4. Calculating Tb.Th and Tb.Sp

Following the previous steps, a re-segmentation of the image stack was performed to a smaller rectangular ROI (central loading area of each tibial compartment) in order to calculate the trabecular properties (Figure 5-4 D-E). To improve the uniformity of the results, the last 15 images starting from the 3rd image from the growth plate (to totally exclude the growth plate) were selected from all stacks. This selection criterion was applied consistently across the entire dataset.

Trabecular thickness (Tb.Th) and trabecular spacing (Tb.Sp) are both three-dimensional measures used to assess the average diameter of the trabecular bone and the bone marrow cavities, respectively. In this study, these measurements were calculated using the local sphere fitting algorithm implemented in BoneJ (Dougherty and Kunzelmann, 2007).

5.3.2.2 Subchondral plate thickness measures

The **Subchondral bone plate (**Sb.P) was subsequently selected from the point where the bone condyle was visible in the central part of each compartment. This selection extended to the point where the trabecular bone appeared or when the bone content dropped to 90%. In previous methods, thickness was usually calculated based on the number of consecutive slices and the thickness of each slice using Image J. However, in this study, the thickness was directly measured using the Mimics software, employing the 4-point measurement method. This method involves a precise anatomical analysis by calculating the distance between two surfaces based on selecting four specific points (two from each surface) along a region of interest (based on HU profiling) on the selected image (Figure 5-5). The thickness was calculated as the mean distance between two surfaces after Mimics reconstruction.

To measure the subchondral bone thickness of the medial and lateral tibial compartments, the longitudinal sections were selected around the insertion of the posterior cruciate ligament. Similar to the histological scoring, the entire medial/lateral tibial plateau was divided into three zones of equal width: zone 1 (outer edge of the joint), zone 2 (central plateau), and zone 3 (inner edge adjacent to the central cruciate ligament). The subchondral bone thickness was determined by averaging the measurements obtained from the middle three zones.

For the medial tibial compartment, the subchondral plate thickness was determined by separately measuring the longitudinal distance of the coloured sections in each of the three zones. Additionally, proliferative changes in the marginal zone were designated as osteophytes, which are not included in the plate thickness measurement.

To determine the two surfaces of the subchondral bone plate, the surface was identified corresponding to the cartilage-Sb.P interface, and the Sb.P- trabecular bone (Tb.B) interface. The segmentation method relies on the HU (or grey values, GV) threshold profile, facilitated by the Mimics software. The measurement script operates as follows (Figure 5-5).

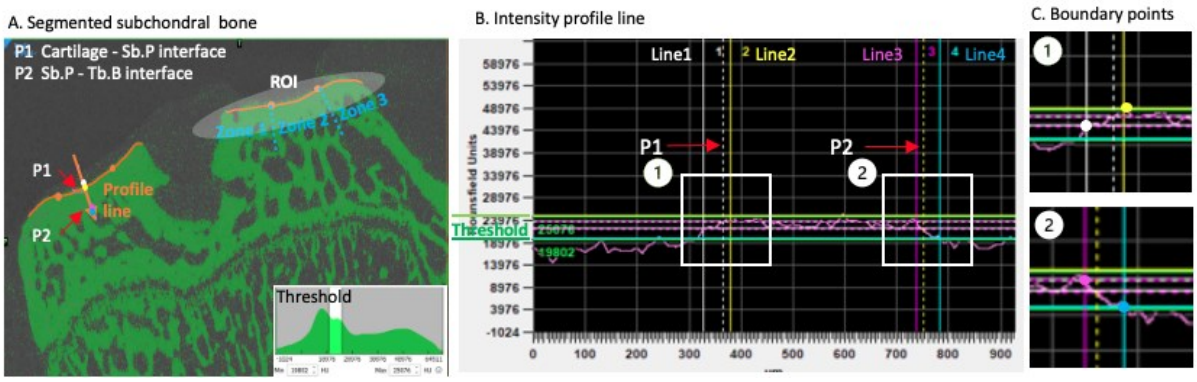

Figure 5-5 Precise Sb.P thickness measurement method based on intensity profiles. (A) An example illustrating the process of drawing a vector line (profile line) from the selected point in each zone. The white ellipse highlights the subchondral plate region of interest (ROI). (B) A typical intensity profile obtained from example vector line, showing HU values from tibia cartilage to tibia bone, with P1 and P2 points indicated by vertical dashed yellow lines. The corresponding HU values are indicated by horizontal dashed yellow lines. The distance (in pixel number) between P1 and P2 represents the thickness of the trabecular plate at that specific point. (C) ① Increase stage: Vertical line 1 and vertical line 2 are placed at the start and end of the intensity increase stage, respectively. Line 2 and line 3 are set based on line 1 and line 2, respectively. P1 is determined as the position on the profile line where the HU value equals "50% ($GV_{line1} + GV_{Line2}$)". ② Decrease stage: Vertical line 3 is positioned at the start of the intensity decrease stage in the intensity profile, while line 4 is placed at the end of the decrease stage. P2 is calculated as HU_{P2} = "50% ($GV_{line3} + GV_{Line4}$)".

The subchondral bone plate (Sb.P) thickness was determined using a vector approach. Each point on the upper surface of the Sb.P corresponds to a point on the Sb.P-Tb.B surface. In previous human studies, such as the work by Liukkonen et al. (2017), the minimum Euclidean distances method was employed to identify the closest point. A vector line was created from each point on the Sb.P upper surface, and the interaction point with the Sb.P-Tb.B surface was considered the closest point. This approach relied on calculating the Euclidean distances between the endpoints of the Sb.P segmentation. For each selected point on the Sb.P surface, perpendicular tangents were generated, terminating at the Sb.P-Tb interface.

In this study, instead of generating perpendicular tangents, the vector line was generated by repeating the distance measurement for one point several times. The minimum value obtained from the vector line of each point was considered the thickness for that specific point. In other words, for each point on the upper surface, the closest point on the lower surface was identified by drawing multiple lines from the upper point to the lower surface and selecting the minimum distance. The minimal distance between these two points represented the thickness at that specific point.

To reduce measurement error, three points on the cartilage surface were marked for each zone. The thickness of each zone was estimated by calculating the average length of these three vector lines. Measurements were taken on three non-consecutive slices from one joint, and the average of the thickness values from these three slices was considered the final thickness measurement for that particular zone of the cartilage.

5.3.2.3 3D reconstruction

To obtain the 3D reconstruction model, Materialise Mimics® (version 10.01, Materialise NV, Leuven, Belgium) was used to create 3D solid models, and subdivided them into discrete elements in STL format. These elements were subsequently exported to Geomagic Wrap® (Raindrop Geomagic, Inc., Morrisville, NC) for hole filling and model smoothing, and to SolidWorks (version 2023, Dassault Systèmes, Vélizy-Villacoublay, France) for assembly. The femur-meniscus contact area was selected using collision detection tool in SolidWorks to pinpoint the areas where two elements touch.

For the segmentation of the meniscus, a degree of estimation and simplification of the meniscus contour was used due to insufficient detail about the meniscus structure in the micro-CT images (Zanjani-Pour et al., 2020b). Illustrating the geometry of the meniscus was based on the calcified portions (front area) of menisci (Figure 5-22), which are typical anatomical features in rodent and were segmented from the micro-CT scan. The other cartilage area of menisci, not clear visible in the micro-CT scans, were reconstructed by filling the gap between the between the calcified menisci and the external surface of the tibia and femoral element.

5.3.3 Statistical analysis

In the statistical analysis, each dataset (n=3) from the different groups (described in Chapter 2: 0ºTO, 10ºTO, 30ºTO, 30ºTO BMP, 30ºTO APS) was analysed for each parameter (BV/TV, Tb.Th, Tb.Sp, Sb.P).

Firstly, normality tests were conducted using the Shapiro-Wilk test, considering the small sample size. The results indicated that the datasets for each variable conformed to a normal distribution ($P > 0.05$). Secondly, Levene's test was performed to assess the equality of variance between two groups for each parameter. A significance level of $F > 0.05$ indicated that the datasets of the two groups had equal variances.

Following the confirmation of normality and equality of variance, an ordinary one-way ANOVA was utilized to compare the mean values between each group. For post-hoc analysis, Fisher's LSD (Least Significant Difference) test was used with a 95% confidence interval. Individual p-values (P) were obtained for each parameter (BV/TV, Tb.Th, Tb.Sp, Sb.P) from each comparison, with a significance level of $P < 0.05$ considered statistically significant. The results are presented as the mean and standard deviation (SD).

5.4 Result

5.4.1 Thresholding method comparison and selection

The first part of the results section is the evaluation of thresholding algorithms to identify the most effective method for segmenting trabecular bone in the CT dataset. A representative image was selected for this purpose, and the auto-threshold values generated by each method were recorded. When these images were mathematically compared to those obtained using a manual threshold (threshold range: 31442-65535), it was found that the Otsu auto-threshold method most closely matched the original image (Figure 5-6a) and the manually segmented image (Figure 5-6b), accurately representing trabecular bone physiology. As a result, the Otsu method was chosen for all subsequent subchondral bone measurements in this study. An important aspect of the Otsu auto-thresholding method is its ability to determine an optimal threshold for each image individually, leading to greater stability in the calculated results of trabecular bone parameters within the same group of animals. This was in contrast to manually adjusted thresholds, which showed variations even under identical technical settings between two scans. Due to these differences, the study did not maintain a consistent manually adjusted threshold value for all images. Instead, the Otsu threshold was applied to each image, ensuring optimal segmentation for each case.

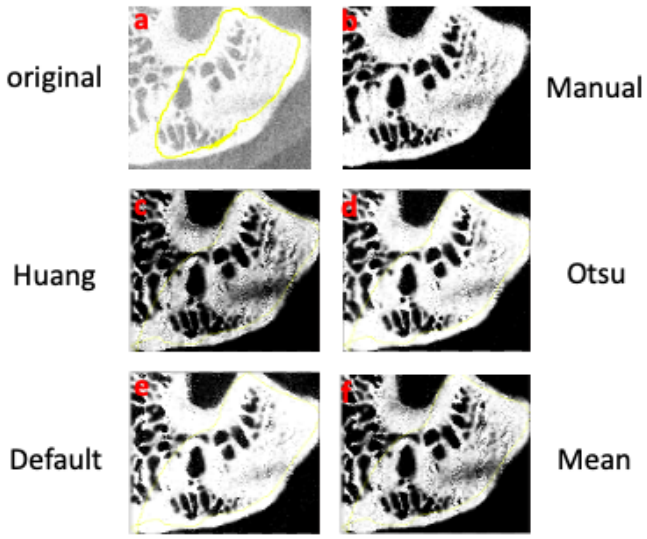

Figure 5-6. A typical cross section CT image (a) was analyzed using different thresholding method in Image J to determine their suitability for trabecular bone segmentation. The techniques analyzed were (b) manual thresholding (31442-65535), (c) Huang method (35549-65535), (d) Otsu method (30905-65535), (e) Default method (29165-65535) (f) Mean method (33808-65535).

5.4.2 Detection of subchondral plate changes by micro-CT

There was an increase in subchondral plate thickness in the 30ºTO-induced OA group medial compartment (Figure 5-7). The thickness recovered to a level similar to the 0ºTO health group following BMP treatment, but APS treatment did not yield the same result. The outer zone demonstrated the highest sensitivity to different OA conditions, with both compartments of the surgical limb showing significant changes (Figure 5-8).

An overall similar trend was observed in the left two compartments and the right medial compartment (Figure 5-8). Following the malalignment surgery, there was an increase in subchondral plate thickness in 30ºTO group. However, after BMP treatment, the thickness decreased and returned to a level similar to the health group (0ºTO). In contrast, APS treatment did not significantly reduce the thickness compared to the 30ºTO group.

In the medial compartment of the left limb, the Z1 (outer) zone exhibited the most significant changes. Both the BMP-treated group and APS-treated group showed a significant decrease in thickness compared to the 30ºTO group. These findings align with the finite element analysis (in chapter 5.4.6), which indicated that the margin area of the medial compartment experienced the largest loading changes. Similarly, in the lateral compartment, the outer zone (Z1) also showed the most significant changes between groups (Figure 5-8).

Additionally, in the healthy left knee, it is observed that both the outer and inner zones had lower values compared to the middle zone. However, in the 30ºTO group, the values of outer and inner zones increased beyond those of the middle zone. This finding aligns with the histology results, where the cartilage in the middle zone exhibited the most significant repair response, aimed at protecting the central loading area. Consequently, the outer and inner areas displayed higher scores of cartilage defects, leading to an increase in subchondral bone plate thickness in these two zones.

For the right medial compartment, significant changes were observed in all three zones: Z1 (outer), Z2 (middle), and Z3 (inner), when comparing all groups. In the right lateral compartment, significant changes were observed in the outer zone (Z1) between all groups.

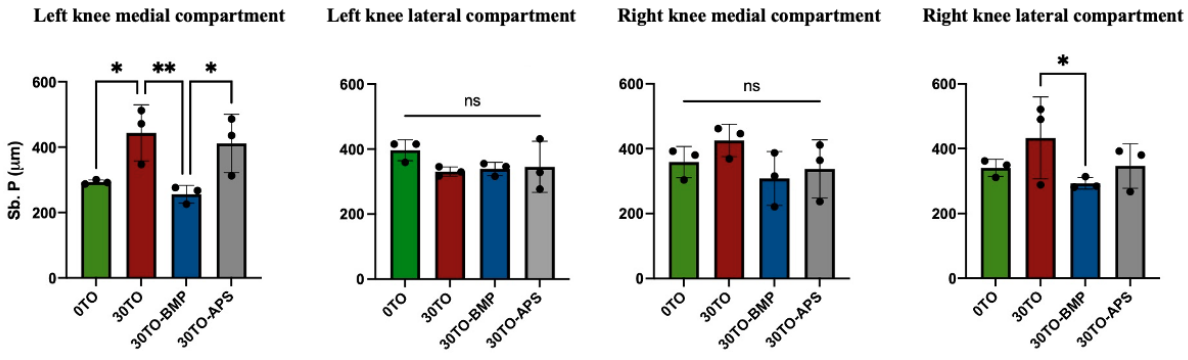

Figure 5-7 Summary of subchondral plate thickness averaged across all zones (Sb.P) for all groups and both compartments (n = 9 from 3 biological independent rats per group, one-way ANOVA; ns, not significant; *p ≤0.05 ,**p < 0.01, ***p<0.001, ****p<0.0001).

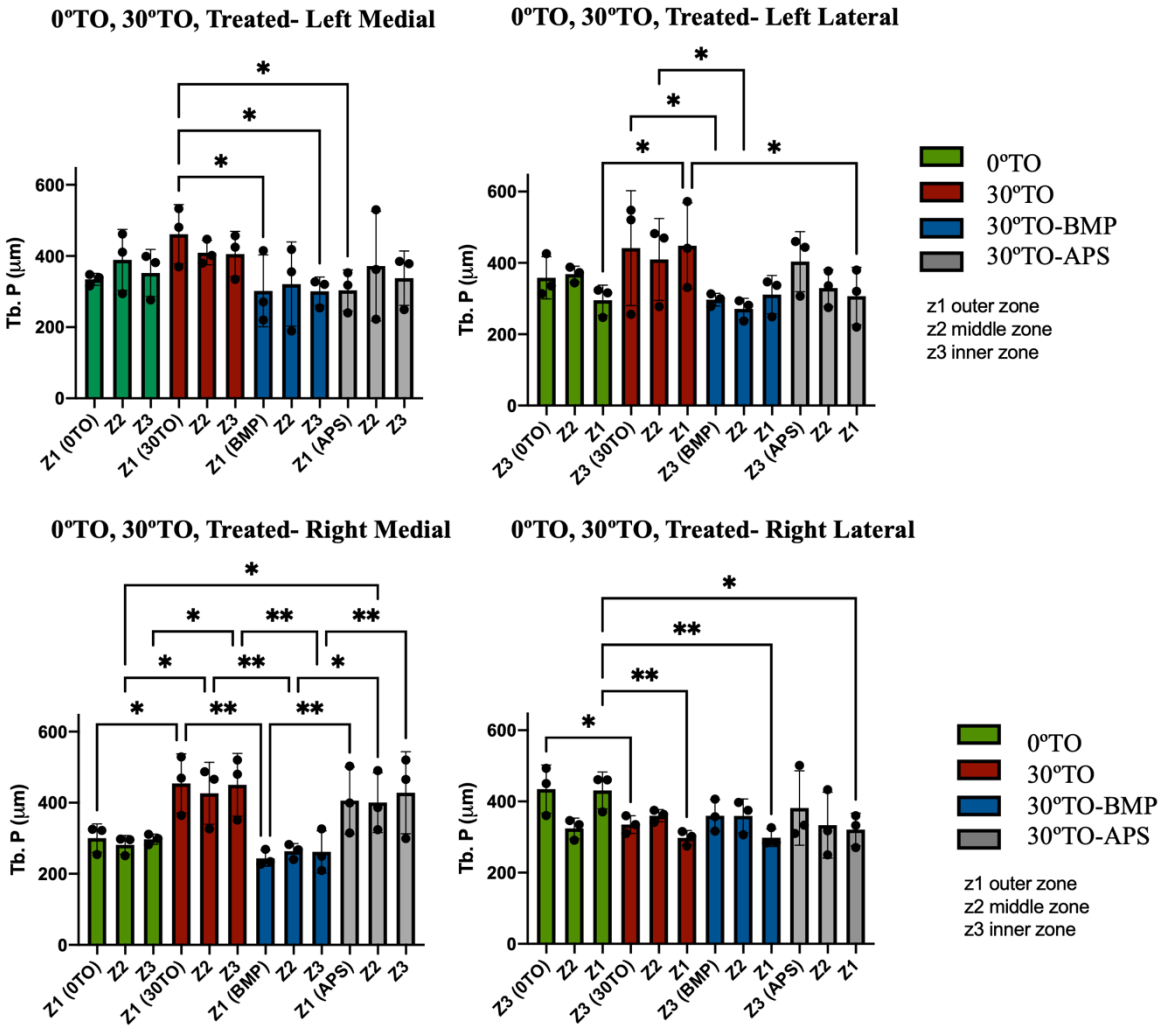

Figure 5-8 Subchondral plate thickness (Sb.P) for all groups, zones and compartments (ns, not significant; *p ≤0.05 ,**p < 0.01, ***p<0.001, ****p<0.0001).

5.4.3 Detection of trabecular bone changes by micro-CT

Bone volume fraction (BV/TV) as a critical measurement for subchondral bone changes, with a decrease in bone volume noted in tibial malalignment-induced OA groups (10ºTO and 30ºTO) and a partial recovery in the BMP-treated group (30ºTO-BMP), though not to healthy (0ºTO) levels (Figure 5-9). APS-treated group didn't show significant recovery.

Trabecular thickness (Tb.Th) increased in the 10ºTO group's medial compartments but decreased in the 30ºTO group, with BMP treatment promoting recovery to healthy levels; lateral compartment thickness remained unchanged across groups (Figure 5-11). APS-treated group didn't show significant changes.

Trabecular spacing (Tb.Sp) followed similar patterns, with the BMP treatment group showing notable improvement, even surpassing healthy group levels in the lateral compartments (Figure 5-13).

Trabecular bone volume

The analysis of bone volume fraction (BV/TV) revealed it to be the most significant differentiating measurement for subchondral bone. The following changes are observed:

There was a consistent trend across all four compartments, with a decrease in bone volume in the tibia malalingment-induced OA group (10 TO and 30ºTO groups), followed by an increase in the treated groups (30ºTO-BMP group and APS-treated group). However, the bone volume did not return to the level observed in the healthy (0ºTO) group.

After malaignment surgery, in the medial compartment of the left limb, the 10ºTO group did not exhibit a significant decrease in bone volume, while the 30ºTO group showed a significant decrease compared to the 10ºTO group. This funding suggest that the medial compartment undergoes a strong subchondral bone remodelling under 10ºTO malaignment loading, overloading (raise to 30º malignment) can potentially cause OA (bone absorption). However, in the other three compartments, the 10ºTO group showed a more pronounced decrease and approached the level of the 30ºTO group (Figure 5-9).

Following treatment, the BMP treatment group (both 10ºTO and 30ºTO) showed a significant increase in bone volume. The 10ºTO BMP treatment group exhibited a significant increase in all four compartments, reaching a level similar to the sham group. Similarly, the 30ºTO BMP treatment group also showed a noticeable increase. However, the APS treatment group either remained at the same level as the no-treatment group or only showed a slight increase.

Among the four compartments, the lateral compartment of the left knee exhibited the most significant changes between the 0ºTO, 30ºTO, and 30ºTO-BMP treatment groups. There is a significant decrese in lateral compartment in 10/30ºTO group, compared to not significant decrease in medial compartment. Moreover, the BMP injections, as treatments for OA, have the potential to promote bone volume incurese.

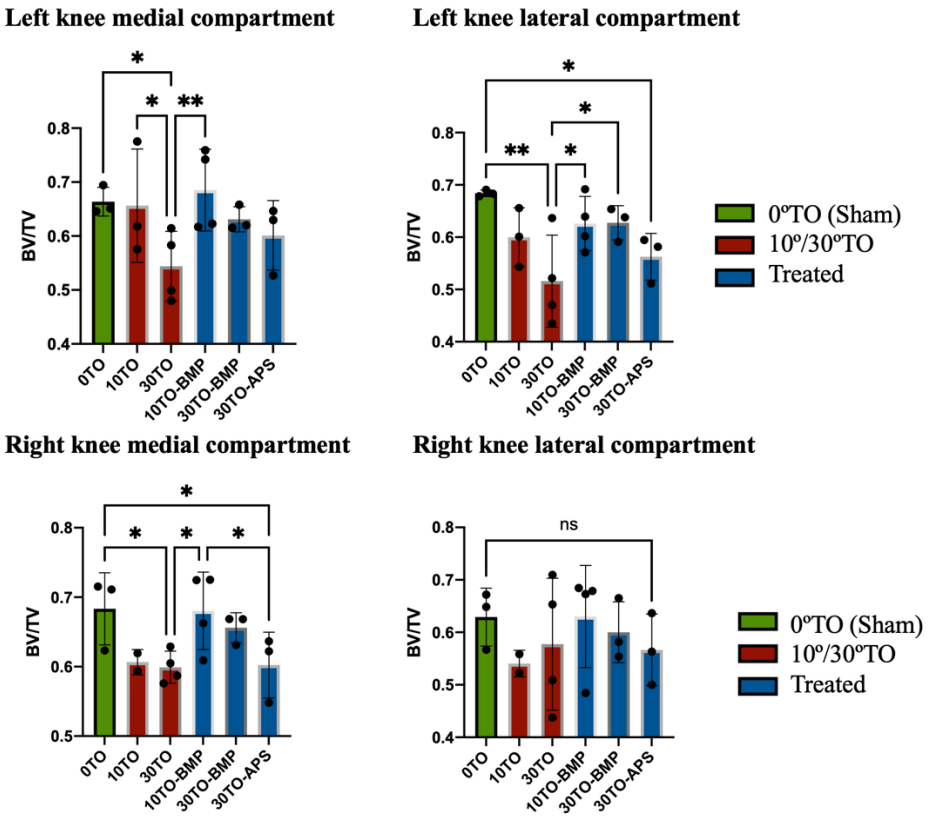

Figure 5-9. Comparison of BV/TV among groups in each compartment (ns, not significant; *p ≤0.05 ,**p < 0.01, ***p<0.001, ****p<0.0001).

Nextthe measurements from both the medial and lateral compartments are combined and the data from both limbs are considered. The following differences are observed:

For comaparing medial and lateral comparemnt between groups, the medial compartment commonly had lower bone volume than the lateral compartment in the health group (0ºTO). However, in tibia malignancy-induced OA, the lateral side exhibited a more significant decrease, resulting in higher bone volume in the medial compartment compared to the lateral compartment (Figure 5-10).

For comparingt the left and right limb, the bone volume in the left limb was consistently lower than that in the right limb. BMP treatment led to an increase in bone volume but did not alter this relationship.

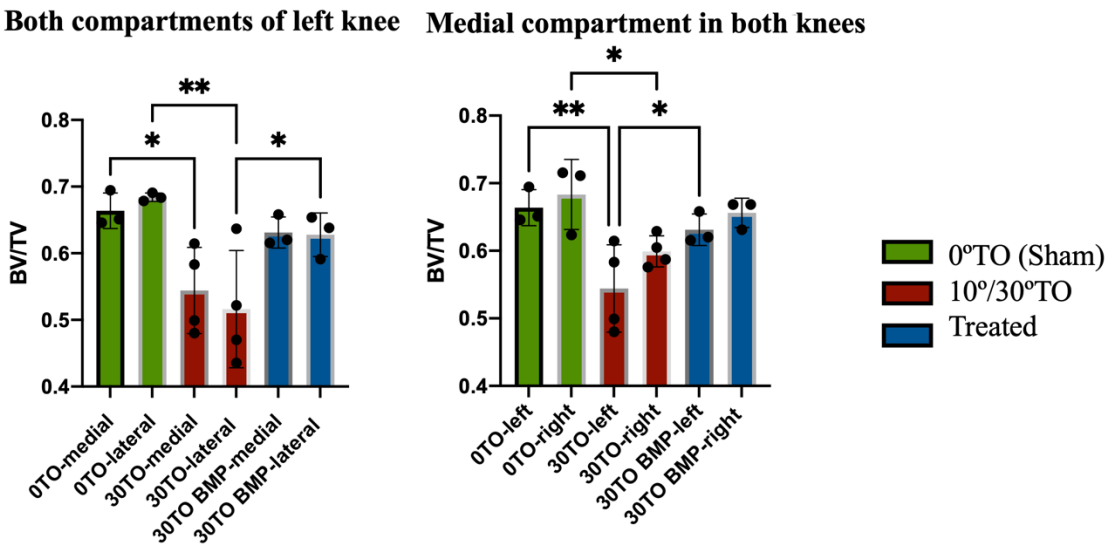

Figure 5-10. Comparison of BV/TV among groups: (a) between compartments and (b) between limbs (ns, not significant; *p ≤0.05 ,**p < 0.01, ***p<0.001, ****p<0.0001).

Trabecular bone thickness

Next, the trabecular bone thickness (Tb.Th) among groups was analyzed within each compartment. In the medial compartment of both the right and left knees, similar trends were observed. Trabecular bone thickness had an increase in the 10 TO group, but a decrease in the 30 TO group. Following BMP treatment, there was a significant increase in trabecular bone thickness, almost restoring it to the level observed in the sham surgery group. However, APS treatment did not significantly contribute to the increase in bone thickness. Conversely, the lateral compartment in both knees did not show significant differences in trabecular bone thickness among the groups (Figure 5-11).

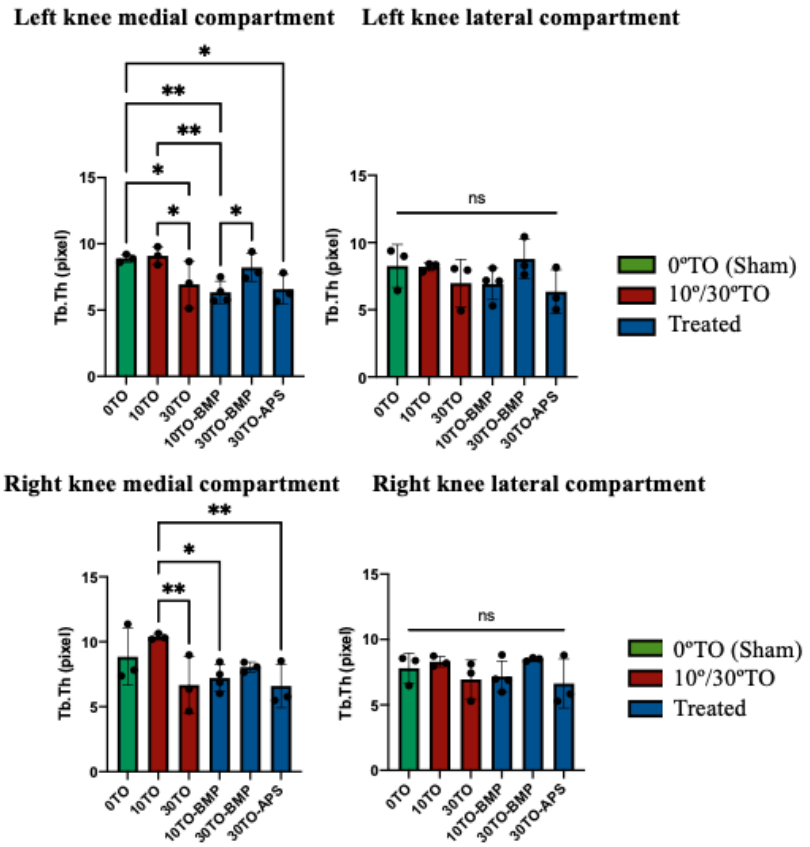

Figure 5-11. Comparison of trabecular bone thickness (Tb.Th) among groups in each compartment (ns, not significant; *p ≤0.05 ,**p < 0.01, ***p<0.001, ****p<0.0001).

In order to further analyze the data, the measurements from the medial and lateral compartments were combined and the measurements between the left and right limbs were combined (Figure 5-12). Although no statitistically significant changes were observed, consistent trends wereobserved. For both compartments, the 30°TO group showed a decrease in trabecular bone thickness, and after BMP treatment, there was a subsequent increase. Similarly, for both limbs, the 30°TO group showed a decrease in trabecular bone thickness, followed by an increase after BMP treatment.

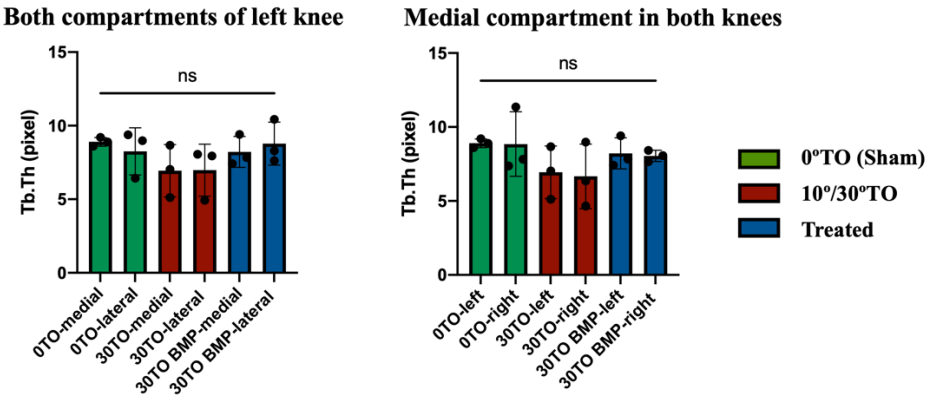

Figure 5-12. Comparison of trabecular thickness (Tb.Th) among groups: (a) between compartments and (b) between limbs (ns, not significant; *p ≤0.05 ,**p < 0.01, ***p<0.001, ****p<0.0001)

Trabecular Spacing

Finally, the study proceeded to analyze trabecular spacing (Tb.Sp) among groups within each compartment. The analysis of trabecular spacing revealed a similar trend (but more significant) compared to the trabecular thickness measurements (Figure 5-13) (Figure 5-14). In both the medial and lateral compartments of the left limb, the 10ºTO group showed an increase in trabecular spacing, while the 30ºTO group showed a decrease. Following treatment, the BMP group exhibited a significant increase in trabecular spacing, nearly reaching the levels observed in the healthy control group (0ºTO group). Notably, in the lateral compartment, the BMP group even exhibited higher spacing than the health group. However, the APS group did not show substantial changes in spacing and remained at a similar level as the 30ºTO (non-treated) group.

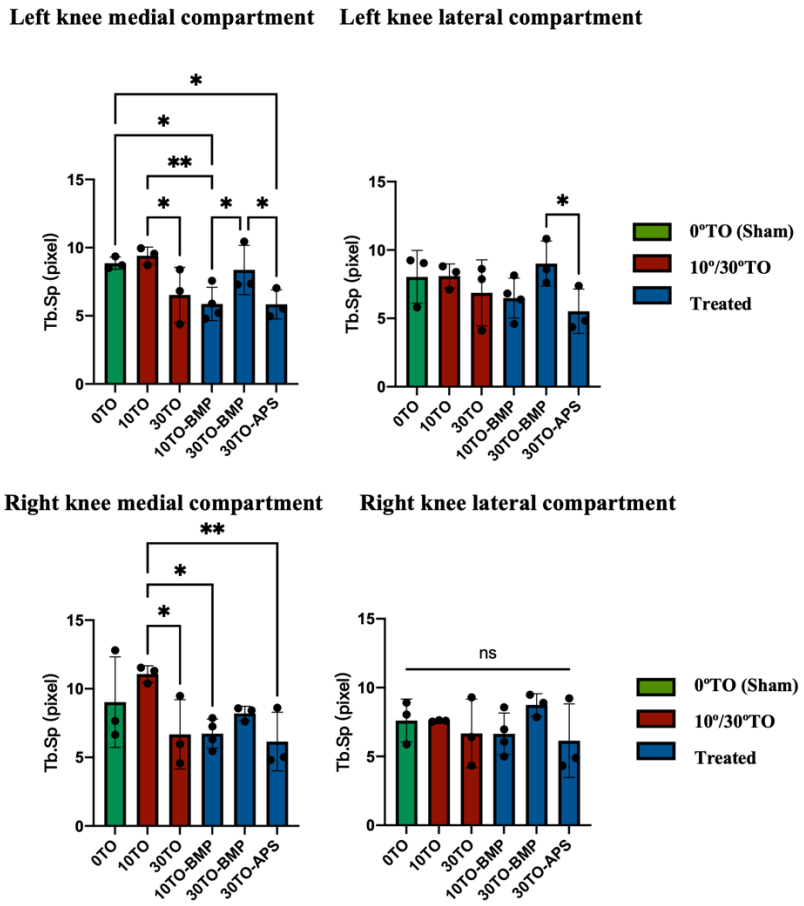

Figure 5-13. Comparison of trabecular spacing (Tb.Sp) among groups in each compartment (ns, not significant; *p ≤0.05 ,**p < 0.01, ***p<0.001, ****p<0.0001)

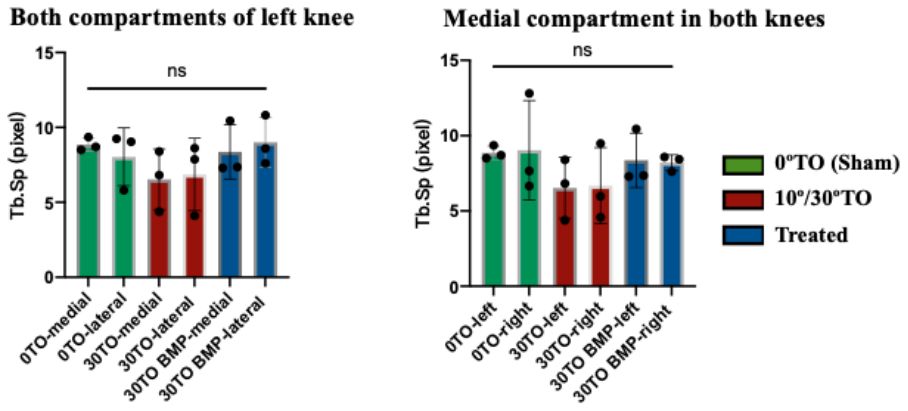

Figure 5-14. Comparison of of trabecular spacing (Tb.Sp) among groups: (a) between compartments and (b) between limbs (ns, not significant; *p ≤0.05 ,**p < 0.01, ***p<0.001, ****p<0.0001)

5.4.4 Osteophytes

Osteophytes were absent in the 0ºTO (sham-operated) and 10ºTO (early OA) groups, and notably appeared in the left (surgery) joint of the 30ºTO group, specifically in the medial compartment and at the margins of the subchondral bone. Osteophyte size decreased after APS treatment, particularly in areas adjacent to the joint space, whereas BMP treatment did not yield a similar reduction (Figure 5-15). In the 10ºTO-BMP group, following BMP treatment, small osteophytes were observed, even though they were not present in the 10ºTO early OA group. The APS treatment appeared to have a positive effect on reducing osteophyte formation in the treated joints.

Osteophytes typically appear as bony protrusions or lumps at the margins of the subchondral bone in areas of high mechanical stress, particularly in the medial side of the joint close to the periosteum. This observation aligns with the results obtained in section 5.4.2, where the outer zone of the medial compartment displayed the most significant increase in subchondral bone thickness, indicating the highest mechanical stress in this area.

In the 30ºTO BMP group, although there was not a significant decrease in osteophyte size, the position of the osteophytes was observed to be near the growth plate, which differed from the group without treatment. Interestingly, with bone remodelling occurring in the loading side (medial compartment), there is also bone absorption in the unloading side, specifically in the lateral compartment in the posterior area (Figure 5-16).

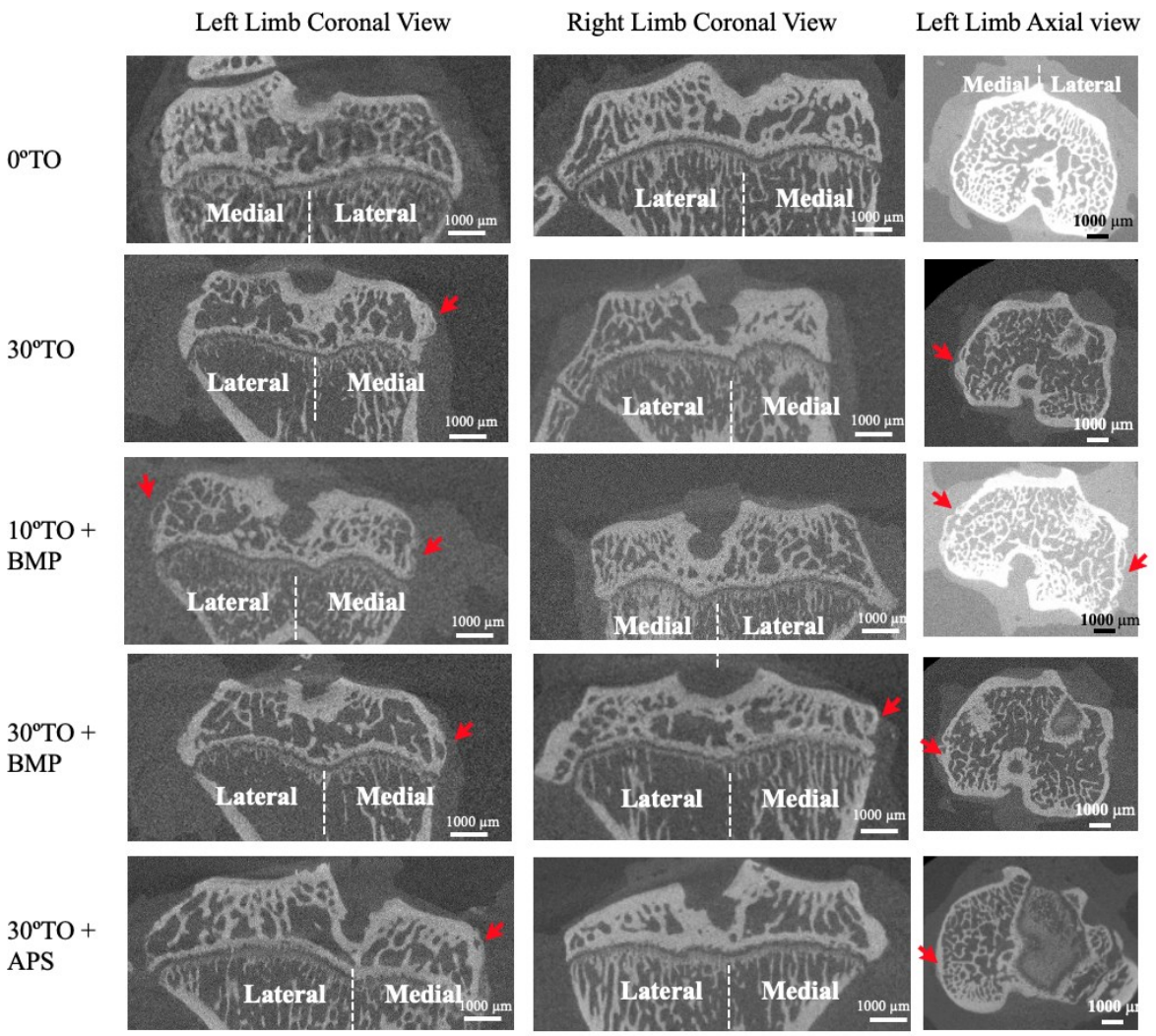

Figure 5-15. Representative micro-CT images of the tibial plateau: Each row shows the coronal view of the left limb, coronal view of the right limb, and axial view of the left limb. Osteophyte mineralization is indicated by the red arrows. Scale bar = 1000 µm.

Bone remodelling was prominent in the loaded side (medial compartment), while significant bone absorption was observed in the unloaded side, particularly in the lateral compartment's posterior area (Figure 5-16).

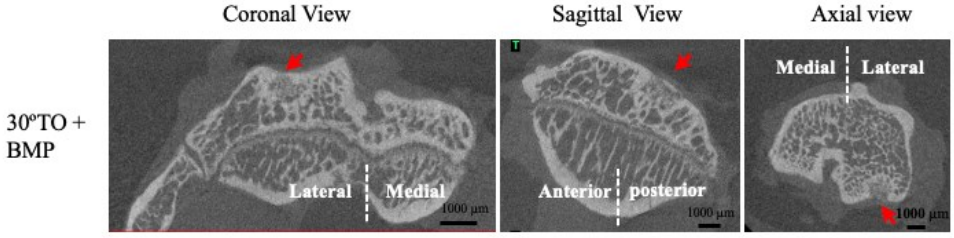

Figure 5-16: Subchondral bone resorption in the BMP-treated left limb. The figure shows the same location in the image stack from three different views: coronal plane, sagittal plane, and axial plane of the left limb (from left to right). The red arrows indicate the area of subchondral bone resorption.

5.4.5 Bone remodelling

Bone remodelling was visible in both the surgically treated (left) tibia and the non-surgical (right) tibia. The left tibia displayed incomplete bone healing (endochondral ossification) at the osteotomy incision, and rapid bone adaptive remodelling (intramembranous ossification) in the tibia-fibula connecting area (Figure 5-17). In the right limb, bone adaptive remodelling (intramembranous ossification) was also observed, as a compensatory response to the loading changes (varus malalignment) in the left limb (Figure 5-18).

In the 0ºTO (sham) group, the osteotomy incision showed complete bony union, indicating successful healing. However, in the 30º-surgery group, which included the 30ºTO group, 30ºTO-BMP group, and 30ºTO APS groups, the osteotomy incision displayed an incomplete bony union with ongoing ossification (Figure 5-17). There were no significant differences observed among these three groups (with or without treatment) in terms of healing progress.

Within the osteotomy incision area, distinct stages of bone healing were observed. In the lower area (Figure 5-17 image 3), the newly formed bone tissue consisted of a network of woven bone and cartilage, indicating active bone formation. Moving upward, in the slightly upper area (Figure 5-17, image 2), bone healing was slightly more advanced as it had not been subjected to traumatic damage. In this region, there was an increase in the amount of bone tissue in the cortical region, and a greater presence of lamellar bone. Additionally, a significant portion of the bone tissue within the marrow space had undergone resorption. In the uppermost area (Figure 5-17, image 1), woven bone tissue was being replaced by lamellar bone, and the cortical bone had been widely restored. Most of the bone tissue within the marrow space had been resorbed, indicating a complete endochondral ossification.

In the tibia-fibula connecting area, no cartilage tissue was observed. Woven bone tissue was present around the old cortical bone (Figure 5-17, image 4), but it was gradually replaced by cortical and lamellar bone. Most of the bone tissue within the marrow space had undergone resorption. This region primarily exhibited intramembranous ossification, as seen in the intact cortical bone.

Interestingly, in the right limb, where no surgical procedures were performed but varus malalignment was present as a compensatory response to the loading changes in the left limb, strong bone remodelling with intramembranous ossification were observed. The cortical bone in the right limb was significantly thicker, and in some sections, woven bone tissue was observed and filled the cortical bone (Figure 5-18, image 4). The cortical bone had been extensively restored, replacing the woven bone (Figure 5-18, image 2). In contrary, 3D reconstruction of the healthy right limb from the 0ºTO group shown the smooth

cortical bone and absence of woven bone without active bone remodelling (Figure 5-19). The marrow space appeared clear, indicating a stable bone structure.

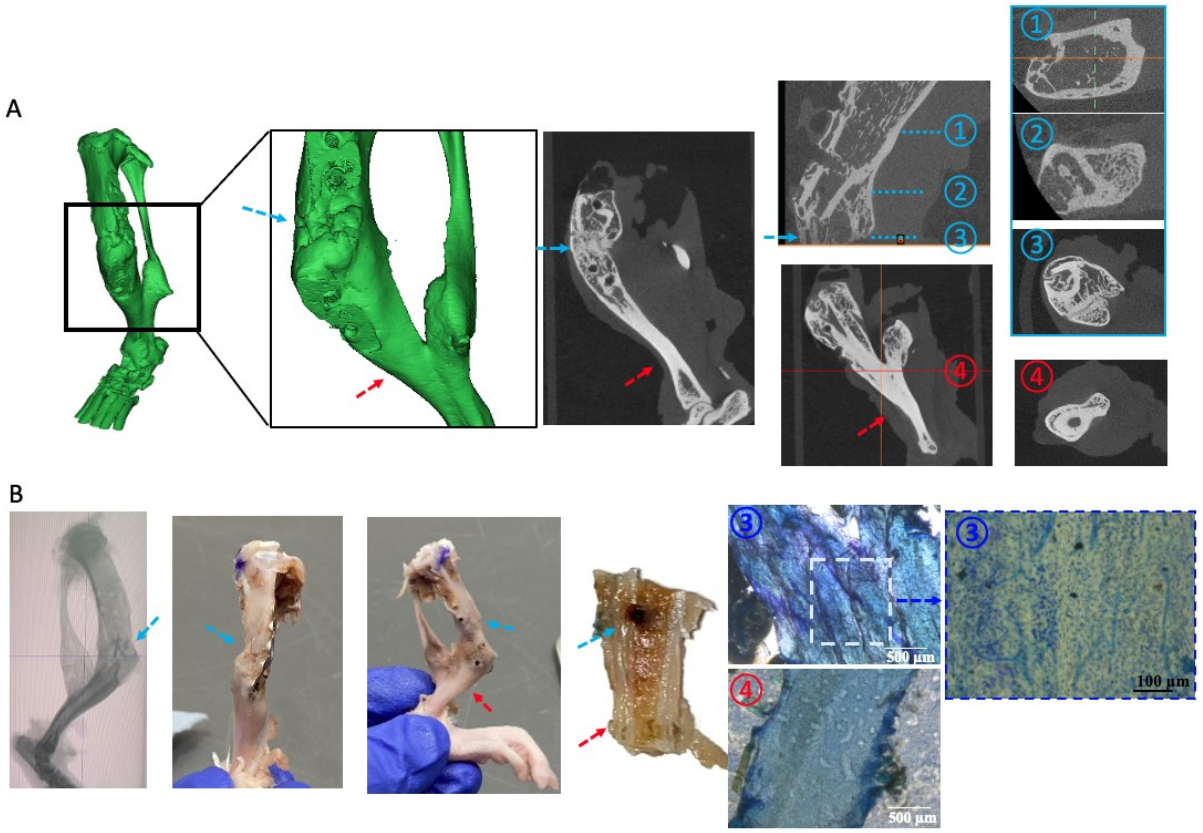

Figure 5-17. **A**. Three-dimensional (3D) reconstruction of the 30ºTO left limb using Mimics software revealed the site of the osteotomy incision (indicated by the blue arrow) and the tibia-fibula connecting area (indicated by the red arrow). Bone healing displayed a 30º-varus bone remodelling. The axial slices from micro-CT (A.1-4) provide detailed views of the healing stages. (A-3) The osteotomy area showed newly formed woven bone filling the osteotomy incision area. (A-2) Woven bone tissue was undergoing transformation into lamellar bone, with intact cortical bone visible. (A-1) Cortical bone regeneration was progressing, accompanied by the disappearance of woven tissue in the marrow area. (A-4) The tibia-fibula connecting area displayed an intramembranous ossification where woven bone tissue is generated around the old cortical bone and undergone resorption, cortical bone and lamellar bone was widely restored quickly and most of the bone tissue in the marrow space was resorbed **B.** Sagittal dissection images of the tibia bone in the 30ºTO left limb are presented, with corresponding histological sagittal slices (B.3-4). Toluidine-blue staining revealed the presence of cartilage tissue in the osteotomy incision area (B-3), while it was scarce in the tibia-fibula connecting area (B-4). Scale bar = 500 µm and 100 µm.

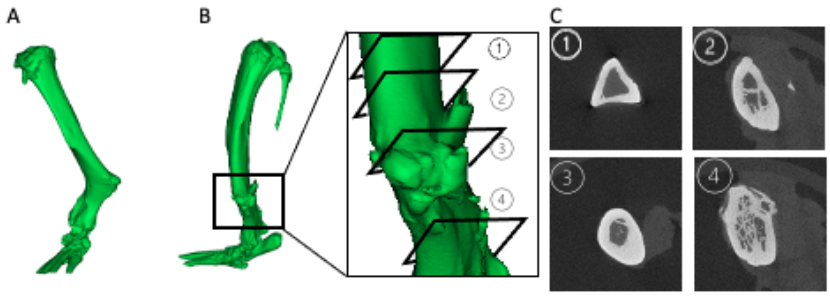

Figure 5-18. 3D reconstruction using Mimics software, presenting the (A) front view and (B) side view of the 30ºTO right limb. (C 1-4) The axial CT slices obtained from tibia-fibula connecting area provide detailed views of the remodelling status.

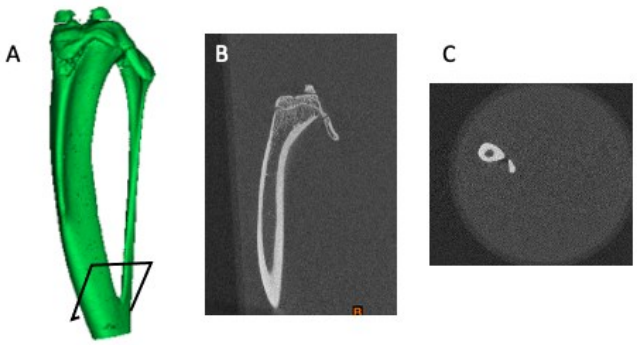

Figure 5-19. (A) 3D reconstruction of the 0ºTO right limb, (B) sagittal image after CT-reconstruction and (C) a cross section across the tibia-fibula connection area. No evidence of woven bone or active bone remodelling was observed in these regions.

The subsequent analysis involved the comparison of bone remodelling between groups based on the 3D reconstruction modelling of each rat. The observations of the osteotomy incision site indicate that the bone is healing with a 30º-varus or 10º-varus remodelling, as illustrated in Figure 5-20A. Interestingly, the bone also demonstrates a growth-forward remodelling from the area beneath the edge of the bone plate incision area, suggesting that the plate-bone connection site is a stress concentration area. In addition, a notable increase in the thickness of the cortical bone were observed, alongside an active remodelling procedure in the distal fibula. It was apparent that the 30º-varus remodelling model exhibited stronger responses than the 10º-varus remodelling model (Figure 5-20 B).

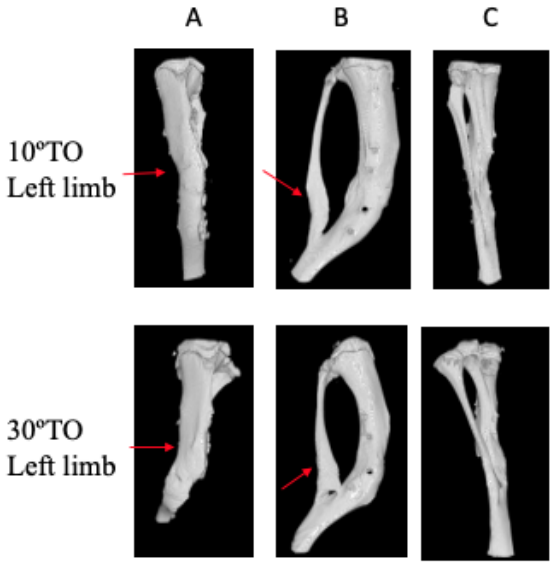

Figure 5-20: 3D reconstruction using Image J, presenting the (A) front view, (B) side view, and (C) back view of the 10ºTO left limb, and 30ºTO left limb. The osteotomy incision area (in A) and fibula remodelling area (in C) are indicated with red arrows.

Next, the Hip-Knee-Ankle (HKA) angle is used to assess the overall alignment of the lower limb. In the micro-CT image (Figure 5-21a), the HKA angle in the 0ºTO group is around 180º, indicating that the weight-bearing axis passes straight through the hip, knee, and ankle. This alignment is considered ideal for the even distribution of weight and joint health. In the 30ºTO limb (Figure 5-21b), an angle less than 180º is indicative of varus alignment. This HKA angle directly reflects how the weight-bearing axis passes through the knee joint, causing the load-bearing axis to shift to the medial compartment of the knee (Martay et al., 2018). Therefore, in the 30ºTO group, the weight-bearing axis deviates from the centre, shifting to the medial compartment. Consequently, increased loading is transmitted through the medial compartment, creating overloading conditions there.

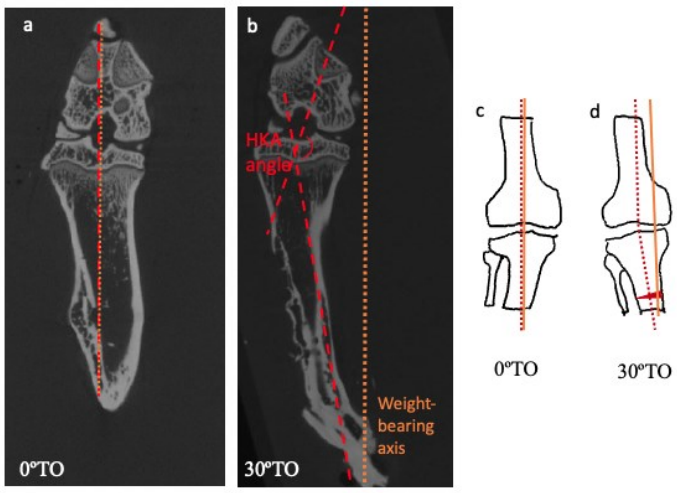

Figure 5-21 Representative images from CT scanning sequencing (coronal plane) illustrate the knee alignment of the left limb in the 0ºTO and 30ºTO groups. The varus alignment of the left limb in the 30ºTO group shifts the weight-bearing axis (WBA) from the medial to the lateral compartment. The HKA (Hip-Knee-Ankle) angle, indicated by the red line, represents the angle between the hip-knee line and the knee-ankle line. The weight-bearing axis, marked by the orange line, is the line from the center of the femoral head down to the center of the ankle.

To obtain detailed information on knee alignment and the shift in loading, the femur, tibia, and meniscus from a 0° TO and a 30° TO left limb left limb were segmented and then processed with 3D reconstruction (Figure 5-22). Figure 5-22a illustrates that the 30° TO left limb exhibits abnormal joint alignment compared to the 0° TO limb. Figure 5-22b highlights the joint contact area (femur-meniscus touch area) resulting from segmentation, demonstrating that the natural contact areas of the two compartments become unevenly distributed in varus alignment. The load is transferred through the meniscus to the cartilage; therefore, illustrating the contact area shift on the meniscus is a surrogate of what is occurring at the cartilage level. Consequently, in the 30° TO left limb, there is a medial, outward, and posterior shift, as well as an increase in the femorotibial cartilage surface contact area.

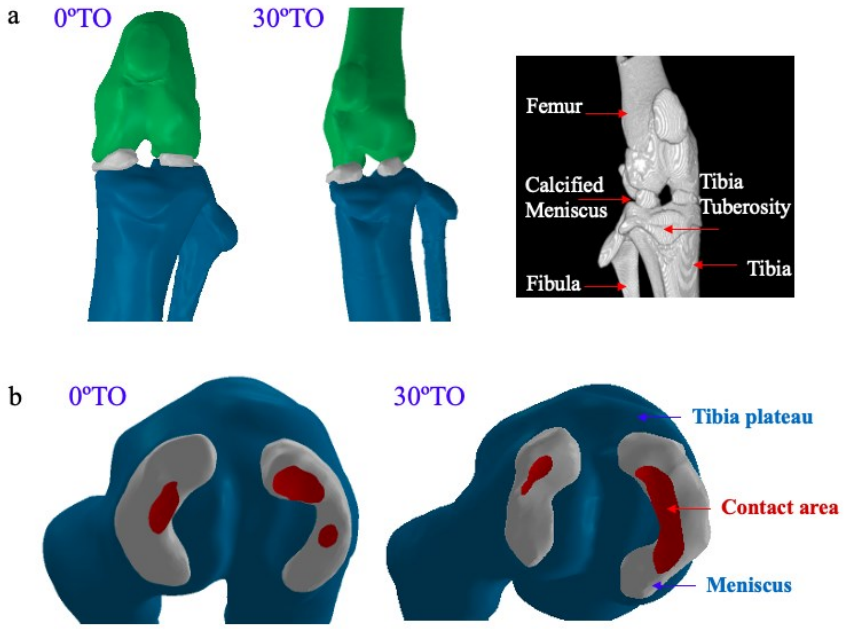

Figure 5-22. (a) Segmentation and 3D reconstruction of the joint area from a 0° TO and a 30° TO left limb illustrate joint alignment, viewed anteriorly with the tibia tuberosity facing front and center. The gray-level model is the original CT image; the coloured model has undergone smoothing and hole-filling for better visualization the alignment. (b) The images illustrate the natural contact areas (femur-meniscus touch area) of the two compartments in 0° TO and 30° TO varus alignment, indicated in red.

5.5 Discussion

This chapter presents findings on subchondral and tibial bone remodelling in a tibia osteotomy (TO)-induced OA model, capturing the early-stage (10ºTO group) and progressive stage (30ºTO group) of OA, and the stages following pharmacological treatment (10ºTO BMP group, 30ºTO BMP group, and 30ºTO APS group). The results confirm that mechanical abnormalities, such as tibia malalignment-induced OA, can trigger subchondral bone remodelling. This includes changes like increased trabecular plate thickness and reductions in trabecular bone volume, spacing, and thickness, which vary according to the severity of OA. Furthermore, mechanical factor-induced remodelling in OA can be reversed or mitigated by early pharmacological intervention, with BMP treatment proving more effective than APS (refer to result 5.4.2, 5.4.3 and 5.4.4). Additionally, adaptive bone remodelling is active in both the surgically treated (left) and non-surgical (right) tibia in response to tibia malalignment (varus) conditions (refer to result 5.4.5).

The discussion does not address other factors that are known to be associated with OA, such as gait changes. This forms the main part of the following chapter and will be discussed in Section 6.4.3.

The discussion here will compare the results with other studies and further explore the biomechanical aspects of subchondral bone changes, osteophyte formation, and bone remodelling during the initiation and development of OA.

5.5.1 The biomechanical aspects of subchondral bone changes

In this chapter, a series of subchondral bone changes can be primarily explained through mechanical interactions. The 30º alignment increases loading in the medial compartment, leading to cartilage loss in the medial compartment of the operated leg, as presented in Chapter 4. This, in turn, increases the mechanical loads in the subchondral bone. To accommodate these new mechanical requirements, the system modifies bone mass and distribution via bone resorption or remodelling. Generally, an increase is observed in subchondral bone plate thickness, a decrease in trabecular bone volume fraction (BV/TV), a decrease in trabecular bone thickness, and a decrease in space. This mechanical imbalance ultimately leads to the formation of osteophytes in the periphery of the medial compartment.

Mechanical forces, including pressure, shear, or elongation, are now known to influence cellular metabolism and potentially tigger bone remodelling (Stoltz et al., 2018). The results show that malalignment-induced osteoarthritis affects all measured parameters: subchondral plate thickness, trabecular bone volume, trabecular spacing and thickness. These alterations in the distribution and arrangement of subchondral bone, primarily in the left medial compartment.

Firstly, subchondral plate thickness is a consistent differentiating marker (Figure 5-8), particularly noting the sensitivity of outer zone changes in indicating the initiation of OA and alterations in loading. Following malalignment surgery, an increase is observed in subchondral plate thickness, which

decreased after BMP treatment. This aligns with results from previous studies. For instance, in a DMM model, the DMM-affected limb showed an increased subchondral plate thickness compared to the contralateral limb at 8 weeks (Moodie et al., 2011). Another DMM model reported increased medial plate thickness from 4 weeks post-surgery, continuing up to 20 weeks (Das Neves Borges et al., 2017). And in the contralateral joint, there is also observed the significant plate thickening in the medial compartment, but no changes in the lateral side of the contralateral joint (Das Neves Borges et al., 2017), this aligns with the results from the right (no-surgery) limb in this thesis. This observed structural changes in the contralateral limb probably occur due to changes in gait, it is discussed more thoroughly in gait analysis chapter 6.4.3.

Secondly, bone volume fraction (BV/TV) proved to be the most significant differentiating measurement for subchondral bone (Figure 5-9). A decrease was observed in the 10ºTO and 30ºTO groups, followed by an increase in treated groups. This aligns with results from previous studies. In the DMM model, an increased thickness of the medial subchondral bone plate was reported, leading to a decrease in trabecular bone volume in the medial compartment (Das Neves Borges et al., 2017), and decreased BV/TV compared to the contralateral limb at 8 weeks (Moodie et al., 2011). In the anterior cruciate ligament transection and partial medial meniscectomy (ACLX) model, the volumetric bone mineral density (vBMD) in the ACLX-affected limb decreased from 4 months post-surgery (McErlain et al., 2008). Furthermore, the treatment with Raloxifene, a TGF-b1 inhibitor, has been shown to increase bone mineral density (BMD) and bone volume fraction (BV/TV) in an ACLT-induced OA model (Ping et al., 2021). Interestingly, when comparing the four compartments of both limbs in the study (Figure 5-9), the lateral compartment of the left knee, rather than the medial compartment, showed the most significant changes in both the OA and BMP treatment groups. This finding suggests that not only overloading but also off-loading in the lateral compartment can contribute to OA and a decrease in bone volume (bone resorption). Contrasting with the overloading condition in the medial compartment, off-loading in the lateral compartment does not facilitate bone remodeling (such as an increase in bone volume for balance). This led to a marked decrease in the lateral compartment in the 10/30ºTO groups, unlike the less significant decrease in the medial compartment. Furthermore, BMP injections, used as a treatment for OA, appear to have the potential to promote an increase in bone volume (bone remodeling).

Thirdly, it is found that trabecular spacing (Tb.Sp) and trabecular thickness (Tb.Th) differentiated between the 10ºTO and 30ºTO group, indicating a balance between remodelling and resorption in response to tibia-femur alignment changes (Figure 5-11, Figure 5-13). The 10ºTO group, which represents an early stage of OA, exhibited increased thickness and spacing, suggesting ongoing bone remodelling. In contrast, the 30ºTO group, representing a more intermediate stage of OA, showed decreased thickness, indicating a predominance of bone resorption. These findings diverge from the existing literature, which generally describes thinner trabeculae and increased spacing in the early stage of OA, progressing to thicker trabeculae and localized decreased spacing in sclerotic areas in late-stage

OA (Li et al., 2013b). The effects of biologic interventions on trabecular bone adaptive remodelling were also evident in the study. The BMP treatment group exhibited increased Tb.Th and Tb.Sp, indicating a potential remodelling effect. In contrast, the APS treatment group showed minimal changes in trabecular bone structure, suggesting a limited impact on remodelling. Similarly, this result does not align with a previous study that reported reduced trabecular spacing with Raloxifene treatment in an ACLT-induced OA model (Ping et al., 2021).

The variability in trabecular bone measurements (Tb.Th and Tb.Sp) observed in the study may be attributed to several factors. Firstly, the subtle nature of these measurements makes them highly dependent on voxel size in the scan settings and the selection of regions of interest (ROIs) during image processing. This variability makes it challenging to directly compare quantitative results across different studies or imaging machines (Christiansen, 2016). Furthermore, the specific OA model used in the study may have contributed to the observed differences. The tibial osteotomy (TO) model represents a mild long-term overloading condition, where OA is induced through pure force distribution changes in the two compartments. In contrast, models such as the anterior cruciate ligament transection (ACLT) and destabilized medial meniscus (DMM) models induce OA through severe joint destabilization, potentially bypassing the early stage of OA progression. The late stage of OA is characterized by subchondral bone sclerosis and the presence of widespread cysts, leading to thicker trabeculae and localized decreased spacing in the affected areas, which aligns with the results in these ACLT and DMM models.

Similarly, the rapid osteoarthritic induction and significant inflammation associated with chemical-induced models result in much quicker subchondral bone changes compared to biomechanical models, and the damage can quickly involve the contralateral compartment in the same knee. For example, in a low iodoacetate-induced rat model, significant decreases in trabecular BV/TV were observed at two weeks (early stage of OA), followed by an increase (not statistically significant) at six (intermediate stage) and ten weeks (advanced or late stage), particularly in the medial compartment. The subchondral plate thickness exhibited significant increases at two weeks (medial compartment) and six weeks (both compartments), but no significant difference at ten weeks. These models also displayed subchondral bone sclerosis, cysts, and osteophytes at ten weeks (Mohan et al., 2011).

5.5.2 The biomechanical aspects of osteophyte formation

The presence of osteophytes is indicative of joint remodelling and attempts at stabilizing the affected joint. The formation of osteophytes indicates that the cartilage damage moves into a degenerative, progressive, and irreversible stage. The underlying role of osteophytes in OA is unclear to date; early osteophytes stabilize the joint, but with increasing size, they restricts motion and become a source of pain. Therefore, it is controversial orthopaedic surgery, of whether or not to remove proximal tibial osteophytes during joint surgeries (Overley and Beideman, 2015, Jeon et al., 2015). Currently, there are

no specific medications or surgical methods available to prevent or invert the osteophyte formation (Xu et al., 2017) .

In this study, there was significant osteophyte development in the medial compartment and at the margins of the subchondral bone in groups with 30º tibial osteotomy (TO), both with and without bone morphogenetic protein (BMP) treatment. Therefore, malalignment appears to stimulate osteophyte formation, with BMP administration potentially enhancing this growth. Interestingly, in the 10ºTO group, BMP stimulation may contribute to osteophyte growth, possibly serving to stabilize the malaligned knee prior to the progression towards a more severe OA stage. In addition, a marked decrease in the size of osteophytes with APS treatment is observed, suggesting a potential therapeutic intervention to manage osteophyte development.

These findings corroborate with existing research. For instance, Moodie et al. (Moodie et al., 2011) reported bone loss on the posterior portion of the medial plateau in a destabilization of the medial meniscus (DMM) model. Interestingly, moderate treadmill exercise was shown to alleviate cartilage degeneration, reverse subchondral bone damage, and inhibit osteophyte growth, whereas intense exercise exhibited little effect on OA progression (Iijima et al., 2017).

Another interesting aspect of the findings is that BMP treatment, often used for OA treatment and enhancing cartilage repair, may stimulate osteophyte growth. Previous research suggests that osteophytes during OA emerge from the periosteum's mesenchymal stem cells, initiated by the stimulation of transforming growth factor-beta (TGF-β) (an endogenous factor, originates from within the body) (De Bari et al., 2001). Accordingly, in the study, the osteophytes (without treatment) were primarily located in the joint's medial and lateral sides, adjacent to the periosteum.

The study also discovered that osteophytes in BMP-treated groups were situated closer to the growth plate, a distinctive pattern compared to the untreated group. This aligns with prior studies where BMP-2-induced osteophytes develop faster than those derived from mesenchymal stem cells. This may be because cells in the growth plate region are already differentiated into cartilaginous tissue, requiring less time to transform into osteophytes (Blaney Davidson et al., 2007). BMPs appear to play a crucial role in the endochondral ossification process (the later stage of osteochondral ossification), while TGF-b is seemingly more involved in the initial phase, where MSCs differentiate into osteophytic cartilage (Blaney Davidson et al., 2007).

Lastly, the dualistic status in OA joints, characterized by coexisting articular cartilage degradation and new osteophytic cartilage formation, complicates the use of biological treatments. For instance, in experimental OA, the administration of TGF-β inhibitors exhibited a dualistic effect: it significantly reduced the size of osteophytes but exacerbated cartilage degradation (Scharstuhl et al., 2002). BMP could potentially exhibit a similar dualistic role in OA. While it may enhance chondrogenesis and cartilage repair in early-stage OA, it might also contribute significantly to osteophytic cartilage

development in later stages. Despite BMP's efficacious performance in subchondral bone repair, the dualistic role of BMP necessitates careful consideration of dosage and duration in treatment strategies.

Autologous Protein Solution (APS), on the other hand, presents a promising alternative for OA treatment. It showed an impressive treatment effect in the study, addressing both cartilage degradation and new osteophytic cartilage formation. The use of APS could potentially circumvent the dualistic role of BMP, providing a more balanced approach to OA management. GREM1, a BMP-antagonist found in high concentrations in healthy articular cartilage, might also be a potential therapeutic agent for inhibiting BMP-induced osteophyte formation (Gelse et al., 2012b). However, a limitation of this section is that it could not quantitatively measure the osteophyte volume changes using current imaging methods because the osteophyte has a similar grey level to the bone, making it difficult to distinguish the interface between the two.

5.5.3 The biomechanical aspect of loading with OA initiation

The analysis of histological staging (Chapter 4, Figure 4-13) revealed that the most severe impact of OA was observed in the inner and outer zones, rather than the central zone (central loading area) which was initially expected. Despite bearing the highest contact forces, the central area displayed the most active cartilage repair response, as evidenced by increased cartilage thickness and lower OA scores with histology. In contrast, the outer zone, which was less frequently loaded but underwent significant loading changes due to limb varus, showed severe cartilage defects and increased subchondral bone thickness (Chapter 5, section 5.4.2). These findings suggest that OA cartilage defects may not directly result from increased contact forces, but rather from sudden changes in mechanical loading, particularly in areas less adapted to such stresses. This aligns with studies suggesting that OA changes are caused not by high contact forces, but by changes in joint kinematics (Andriacchi et al., 2004). When the load-bearing regions of the cartilage moves to less frequently loaded areas, it causes mechanical damage to the cartilage and raises the coefficient of friction. The subsequent increase in coefficient of friction contributes to accelerated OA progression in the high loaded regions (Carter et al., 2004).

The findings prompt a re-evaluation of the factors contributing to the initiation of OA. Specifically, it is questioned whether high mechanical loads directly cause OA or if loading pattern changes (such as unloading, loading region shift, joint kinematics changes) play a more significant role. Current mechanobiological understanding from computational simulations suggests that cartilage growth and ossification are inhibited under physiological loading conditions, by the local application of intermittent hydrostatic compressive stress.

However, excessive shear or tensile strains in cartilage lead to mechanical failure of the fibrous matrix (Carter and Wong, 2003). As a result, the cartilage environment is sustained by intermittent fluid pressure, while mild tension or shear stimulates subchondral bone growth and ossification processes from the subchondral bone growth front area (bone-cartilage contact area) (Carter and Wong, 1988).

Therefore a recent study about the mechanobiology mechanism of OA onset, the unloading, blunt impact, mechanical abnormalities (such as frictional shear stress) and other mechanically related factors (such as joint kinematics) are considered crucial in the onset and progression of OA, while overloading force is not considered an independent mechanical stimulus (Carter et al., 2004). This understanding helps explain the occurrence of chondrocytes (precursor state of osteophytes) and their differentiation (such as endochondral ossification) process (Chapter 4, Section 4.5.2). This notion supports the hypothesis that the onset and progression of OA in this study might occur by mechanical factors (1) decreased loading, which activates the subchondral growth front by reducing fluid pressure, and (2) mechanical abnormalities that intensify surface wear during joint articulation.

This understanding helps explain the differentiation directions of chondrocytes towards cartilage repair or form chondrophytes (and osteophytes). When the destruction of articular cartilage occurs, multipotent cells (multipotent mesenchymal tissue) originating from the subchondral marrow spaces become exposed and propose to differentiate into bone. However, in regions of the joint that experience high mechanical loads, the repetitive cyclic pressure generated during movement redirects the differentiation process towards the chondrogenic pathways (or fabric cartilage formation) (Loboa et al., 2003). Meanwhile, at the edges of the joint, endochondral ossification and bone formation are persistence by hydrostatic pressure, resulting in the formation of osteophytes (Carter and Beaupre, 2001).

5.5.4 The biomechanical aspect of loading with bone remodelling

The bone remodelling of the osteotomy incision area and the tibia-fibular connection (high stress area) was observed in histology and micro CT scans (Figure 5-17). The osteotomy incision area underwent endochondral ossification, and cartilage tissue was noticeable in the histology sections. This finding is consistent with the fracture callus observed in other group's fracture models (Estai et al., 2011). However, the tibia-fibular connection area showed signs of intramembranous ossification - an adaptive bone remodelling process that led to rapid rebuilding (thickening) of the cortical bone without the fracture callus step. These findings highlight the dynamic process of bone healing and remodelling in response to surgical interventions and loading changes. Further study of this model can be used to understand the mechanisms underlying bone repair and adaptation. Generally, firm fixated fracture is characterized solely by intramembranous ossification, whereas both intramembranous and endochondral ossification occur in this model (the osteotomy incision area) due to the instability of the tibia after osteotomy, even though the fracture was fixed by the plate (Liukkonen et al., 2017). This makes the osteotomy model a good representative for studying bone remodelling processes, as previous bone healing models struggled to replicate endochondral ossification because these models used bone drill holes to simulate bone defects, which resembled firmly fixed fractures (Liukkonen et al., 2017).

Furthermore, an increased thickness of the cortical bone and a strong remodelling process in the distal fibula are observed. Such remodelling activity can be attributed to an increase in bending and torsional

forces following malalignment surgery, indicating that the bone is actively remodelling to regain stability (Figure 5-21). These findings suggest that the tibial osteotomy, resulting in a fracture, is causing rotational instability in the lower limb, with the fibula undergoing remodelling to restore rotational stability and balance. An intact fibula provides more torsional stability in a rat tibia osteotomy model, aiding bone healing post-tibia osteotomy (Shefelbine et al., 2005). In the lower limb of a rat, both the tibia and fibula contribute to some degree of rotational stability. The fracture of the tibia can cause rotational instability in the lower limb and delay bone healing by reducing bone callus strength, which cause the fibula to remodel and provide additional rotational stability (Grundnes and Reikerås, 1993). Moreover, a larger malignment angle can increase shear forces, leading to medial femoral subluxation from the tibia and joint unloading (Wei et al., 1998a, Shoji and Insall, 1973a). These results indicate a need for further computational finite element (FE) modelling to focus on the stress changes in the bone remodelling areas.

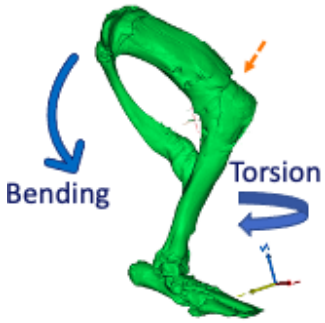

Figure 5-23. Re-stabilization of a rat tibia following 30ºTO osteotomy.

From the results in Section 5.4.5, it is concluded that abnormal loading, both in terms of force and changes in the contact area, occurs in this bone remodelling and OA initiation process. Figure 5-21 confirms that the 30ºTO left limb is in a varus alignment condition, with the weight-bearing axis shifting from the center to the medial compartment. Consequently, increased loading is transmitted through the medial compartment, creating overloading conditions there, while the lateral compartment experiences unloading. This aligns with findings reported in other tibial osteotomy studies (Martay et al., 2018, Shoji and Insall, 1973a). This scenario, considered the initial state for the OA process, could lead to changes in the loading distribution between the two compartments and subsequent responses in cartilage and subchondral bone.

Furthermore, the 3D reconstruction of the OA joint, including the femur, tibia, and meniscus, revealed a change in the contact area in the 30ºTO left limb (Figure 5-22b). The contact area, or the cartilage compression area, is where the cartilage layers of the femur and tibia endure compressive forces from the adjacent bones. As the medial side bears more weight and pressure, the medial cartilage area is subjected to increased stress. This is suggested by the result (Figure 5-22b) that shows an enlarged contact area in the medial cartilage, as the cartilage needs to disperse these extra pressures over a broader

area. Thus, the findings indicate an increase and shift in the contact area to the outer and posterior area of the medial compartment, aligning with dissection observations (in Chapter 4) where chondrophytes were observed in the medial posterior compartment of the left limb. This evidence underscores the reliability of the experimental models and confirms that the *in vivo* osteotomy method in this study effectively replicates the varus condition as a precursor for OA development.

This study posits that the bone remodelling observed in the in-vivo model may not be merely a simplistic repair process of the fracture (osteotomy incision), but rather one influenced by stress and strain conditions that potentially enhance the structure and physical properties of the tissue, notably in the sub-plate area and the tibia-fibular connection area. This concept is known as adaptive bone remodelling. This idea was articulated by Wolff, who proposed that "every change in the form and function of a bone is followed by certain definitive changes in its internal architecture" (Cowin, 1986). Wilhelm Roux (1895) defined the concept of functional adaptation as quantitative autoregulation controlled by functional stimuli. Currently, most bone remodelling studies are still primarily focused on computational and mathematical levels, but the model used in this study validates this concept *in vivo*. This is consistent with a previous study in a mature sheep model following the removal of the ulna. Despite the wear on the proximal radius being double that on the distal side, the majority of new bone, in the 50 weeks following the ulnar osteotomy, was predominantly deposited on the distal periosteal surface of the radius bone, likely due to higher mechanical loading (Stoltz et al., 2018).

5.5.5 Conclusion

In conclusion, this chapter has shed light on the subchondral and tibial bone adaptive remodelling activities in the TO-induced OA model. The key findings demonstrate that changes in bone structure are directly influenced by the loading environment during the initiation and progression of OA. Notably, alterations in subchondral bone plate thickness, trabecular architecture, and osteophyte formation, especially after biological interventions, underscore the potential for targeted treatments in OA management. These insights lay the groundwork for future research to further elucidate OA mechanisms, develop early diagnostic tools, and optimize therapeutic strategies.

6 Gait analysis in characterising OA functional changes

6.1 Summary

This chapter explores the effectiveness of using gait analysis to detect the condition of OA, building on the foundational histological (Chapter 0) and imaging (Chapter 0) evaluations that identify and assess OA in this biomechanical animal model. The established discriminatory models and identified specific gait features in this chapter are capable of achieving clear distinctions and predictive capabilities among normal gait, OA-affected gait, and post-treatment gait. As a result, this gait analysis method proves to be a valid tool for detecting the progression and alleviation of OA within a biomechanical OA model. Notably, Paw Area at Peak Stance (related to weight support) and Maximum Change in Area over Time (Max dA/dT) (related to gait coordination) stand out as the pivotal and consistent measurements among all evaluated gait features. Changes in gait patterns are likely linked to joint cartilage degradation and structural alterations, as evidenced by micro-CT and histology findings, though their effectiveness in detecting early-stage OA is limited. The discussion highlights the challenges in correlation between gait analysis with micro-scale results and translating findings from animal models to human conditions.

6.1.1 Gait analysis in preclinical rat model

Although human gait analysis has been widely studied for several decades, the application of rodent gait analysis to preclinical studies has only begun relatively recently. A rodent gait model has been utilized in some studies involving rheumatoid arthritis and pain (Berryman et al., 2009a, Poulet et al., 2014a, Lakes and Allen, 2016), but its application in osteoarthritis (OA) research remains less common.

As described in Chapter 1, Section 1.8.3, gait analysis has been used in assessing human OA. Conversely, detecting gait alterations in OA rodents presents significant challenges due to factors such as the redistribution of loading across three other limbs instead of one, and the rapid change in gait sequence (Ferland et al., 2011b). These factors have curtailed the comprehensive application of rodent gait analysis in preclinical pain and arthritis studies.

Despite these challenges, the study of rodent gait may be pivotal in OA research. Its importance is growing as gait analysis is increasingly recognized as a vital non-invasive tool for evaluating the severity of OA and the efficacy of various therapies in a clinical setting, particularly in the context of the role of mechanics in OA. Given that rodent models are the most commonly used preclinical OA models, it becomes important to understand rodent gait in the context of OA assessment and the testing of novel therapeutic approaches. Additionally, it is crucial to acknowledge that while rodent quadrupedal gait patterns differ from human bipedal patterns, the principles underlying gait analysis In OA assessment is analogous–- an altered gait pattern due to change in mechanics, pain avoidance and joint dysfunction (e.g. joint degradation changes).

Presently, the trend in translational studies involving gait analysis exhibits a “scale down” approach. Advanced technologies and measurement techniques are first developed for human subjects, then adapted for larger animals, such as horses and dogs, and finally scaled down for application in rodents. This diverges from the classical path of translational studies in OA, which typically commence with the exploration of disease mechanisms or the testing of new therapies in preclinical small animal (rodents) models, followed by upscaling to larger animal models and ultimately, clinical studies. The preference for the “scale down” approach is driven by the ease of detecting disease-induced gait changes and compensations in humans and larger animals, as opposed to rodents, who have evolved to conceal their gait deficiencies due to their status as prey animals (Lakes and Allen, 2016).

The next stage in gait research is to harness gait analysis not only for “backward" validation—identifying gait change patterns already established in clinical OA patients (Mogil, 2009) — but also for “forward” validation, including the study of joint biomechanics and its role as a measurement in the drug development process. Gait analysis holds promise for illuminating two key aspects of OA: the initiation and progression states of OA disease, and the structural joint damage-related and pain-related gait changes associated with the disease. These potential avenues underscore the need for a renewed focus on the application of gait analysis in rodent models as part of OA research. Accordingly, this study is dedicated to exploring the application of gait analysis in the OA animal model, assessing its effectiveness in distinguishing among healthy, OA-effected, and post-treatment states, as well as examining its correlation with structural joint changes and pain avoidance.

6.1.2 Spatiotemporal characterization

The gait analysis method commonly includes three components: kinematics analysis, kinetics analysis and spatiotemporal analysis. Compared to the difficulty of kinematics and kinetics measurements, which requires the use of reflective markers pasted to the skin surface while walking, current rodent gait analyses are typically limited to spatiotemporal patterns, because of its simple technical procedure and less equipment needed. CatWalk (Noldus, Netherlands) (Vrinten and Hamers, 2003a) and DigiGait (Mouse Specific, USA) (Lakes and Allen, 2016) are two commonly used systems designed for small animal gait studies.

The spatiotemporal gait parameters are a set of measurements to reflect the time-space changes during a gait cycle. It can also be regarded as a kind of kinematics data because it also focuses on recording the time and space changes of limb movement (Lakes and Allen, 2016). The gait cycle is typically divided into a stance phase and swing phase. Stance period includes one time point (starting landing) and four states (Pre-load-bearing, mid-stance, end-stance, early swing). The swing phase includes 3 states (early swing, mid swing, and end swing). Each gait cycle during walking contains a series of typical foot posture transfers (heel strike → contralateral toe-off → heel off → opposite heel strike → toes off → heel strike) (Figure 6-1) (Kharb et al., 2011).

The spatiotemporal gait parameters are further separated into spatial parameters and temporal parameters. The spatial parameters include stride length, paw area, paw length, step width, stride length, spatial gait symmetry and temporal gait symmetry (Eftaxiopoulou et al., 2014a). Temporal parameters usually include stance times, swing time and stride time (Eftaxiopoulou et al., 2014a). Generally, the data are expressed in terms of the percentage of this phase compared to the whole gait cycle (cycle%), or sometimes expressed in seconds (s).

Rodent quadrupedal gait can be described in similar spatio-temporal gait parameters as for human gait. These parameters describe how an animal's paws move in both space and time, including stride length, step length, stride length asymmetry, and step width (Figure 6-1). Different from human gait, compensatory gait patterns are more subtle and important when understanding the rodent gait; a change in a single gait parameter does not tell the full biomechanical story of rodent gait. Therefore, in rodent gait analysis, there are a number of combinatory measures that are not independent but provide important information on gait symmetry for quadrupedal gait. The derived parameters are: distance and angle between paws, orientation and area of different footprints. They can also be analysed in Digigait and are defined in Table 6-1 (Lakes and Allen, 2016), which is what is used in this thesis.

Overall, the objective of the work presented in this chapter is to use a set of gait features for discriminating between normal gait, OA-affected gait, and OA-affected gait following pharmacological intervention. Additionally, this work seeks to elucidate the correlation between changes in gait features and joint structural damage, as evidenced by micro-CT (Chapter 0) and histology results (Chapter 0). The gait discrimination models, along with the identified gait features, are prepared to serve as measurement tools for assessing the gait disturbances and progressive stage OA, and monitoring the effectiveness of treatments in rodent OA models in future studies.

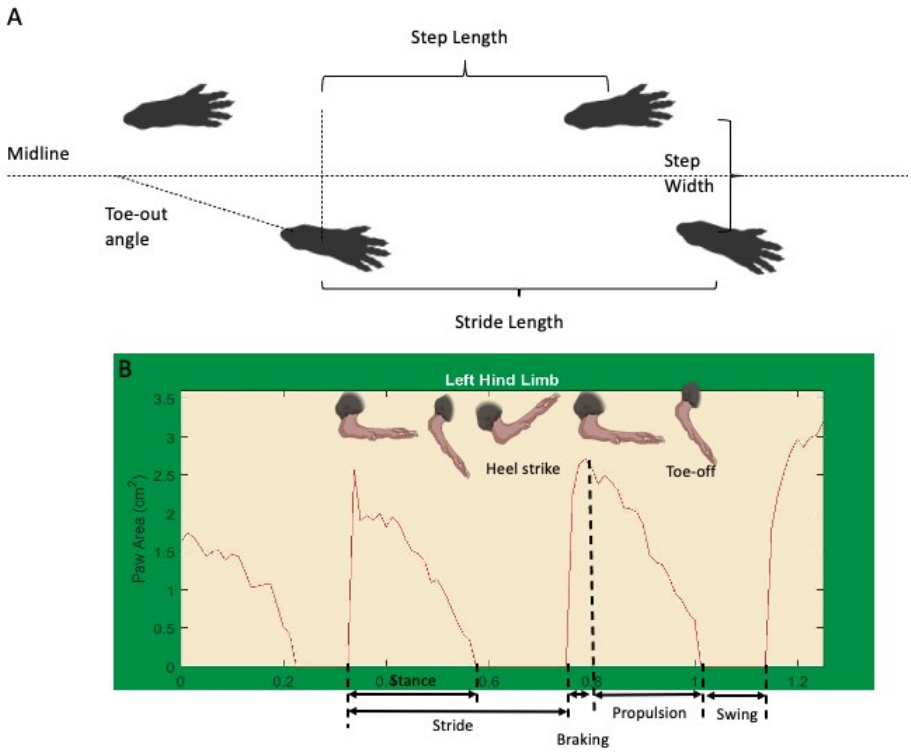

Figure 6-1 (A) Spatial gait parameters are shown for the rat hind limbs. Forelimb prints are removed for clarity. (B) Temporal gait parameters are described with a Hildebrand plot for quadrupedal rodent gait. Dashed lines indicate a moment in time in the gait cycle, which is depicted by the rat drawing above each line. One gait cycle is defined from the first foot-strike event (when the heel touches the ground) to the next foot-strike event. Normal alternated footfall pattern in running is from left front (LF) to right hind (RH), to right front (RF), to left hind (LH).

Table 6-1 Terminology

Term	Definition
Spatial	Relating to positions in space
Temporal	Relating to time
Kinetic	Relating to the forces associated with motion
Kinematic	Relating to motion
Swing Time	Time duration when there is no paw contact with belt
Stance Time	Time duration when the paw contact with belt. Equal to the sum of braking time and propulsion time.

Term	Definition
Stride Time	Time duration of one complete stride for one paw. Equal to the sum of stance time and swing time.
Brake Time	Time duration when initial paw contact to maximum paw contact, just after the swing phase
Propulsion Time	Time duration when maximum paw contact to just before the swing phase
% Brake Stance	Percentage of the braking phase in stance phase
Paw Angle	The angle formed between the paw and the long axis of the animal's direction of motion.
Paw Area at Peak Stance	The area captured by the camera at the time corresponding to peak stance
Paw Area Variability at Peak Stance	The standard deviation of the paw area for a set of strides recorded
Gait Symmetry	Ratio of forelimb stepping frequency to hind limb stepping frequency.
MAX dA/dt	Maximal rate of change of paw area in contact with the treadmill belt during the braking time.
Sciatic Functional Index (SFI)	An equation based on multiple linear regression analysis was developed to assess functional recovery after sciatic nerve injury. The equation includes factors such as paw width, paw length for each hind limb, and the distance between the 2nd and 4th toes.
Tibial Functional Index (TFI)	Using a similar derivation as described above. Evaluate the functional recovery after Tibial or peroneal nerve injury.
Stride Width Variability (SLVar)	The standard deviation of the stride width for the set of strides recorded.

6.2 Materials and methods

6.2.1 Digigait imaging system

In the study, rat gait was recorded using a DigiGait™ Imaging system (Mouse Specifics Inc., Boston, MA). Gait analysis was performed the day before the surgery (as described in Chapter 2) and once every 2 weeks starting from week 6 post-surgery.

In the DigiGait™ Imaging system hardware consists of a high-speed video camera capable of capturing 147 frames per second and a transparent treadmill. The rat was placed on the treadmill, and as it moved, the video camera, mounted inside the treadmill chassis beneath the transparent belt, captures the paw print (Figure 6-2). Illumination was provided by three fluorescent lights, two inside the chassis and one overhead, which illuminated the treadmill area.

The speed of the treadmill belt is adjustable, ranging from 0 to 99.9 cm/s. For this experiment, a data collection speed of 20 cm/s was used, as it allowed the animals to run steadily for a sufficient duration and is commonly used in the literature (refs).

Figure 6-2(A) The DigiGait™ system (Mouse Specifics, Inc, Quincy, MA, USA) with the light panel door open to show the high-speed digital camera and two fluorescent lights. (B) A close-up view of the DigiGait™ running chamber under overhead lighting.

6.2.2 Digigait data processing system

Digigait software generates “digital paw prints” and software identifies the stance duration of a limb (when the paw is in contact with the walking surface) and the swing duration (when the paw is not in contact with the walking surface). Stance is further subdivided into breaking duration (when the paw contact area increase over time) and propulsion duration (when the paw contact area decreases over

time). The vectors associated with each paw area generates a set of periodic waveforms that describe the movement of the four limbs (Dorman et al., 2014). Frame by frame, the software determines the area and the direction of each pixel of each paw and identifies coordinates in space (x, y) and time (t). The paw area is plotted as shown in Figure 6-3.

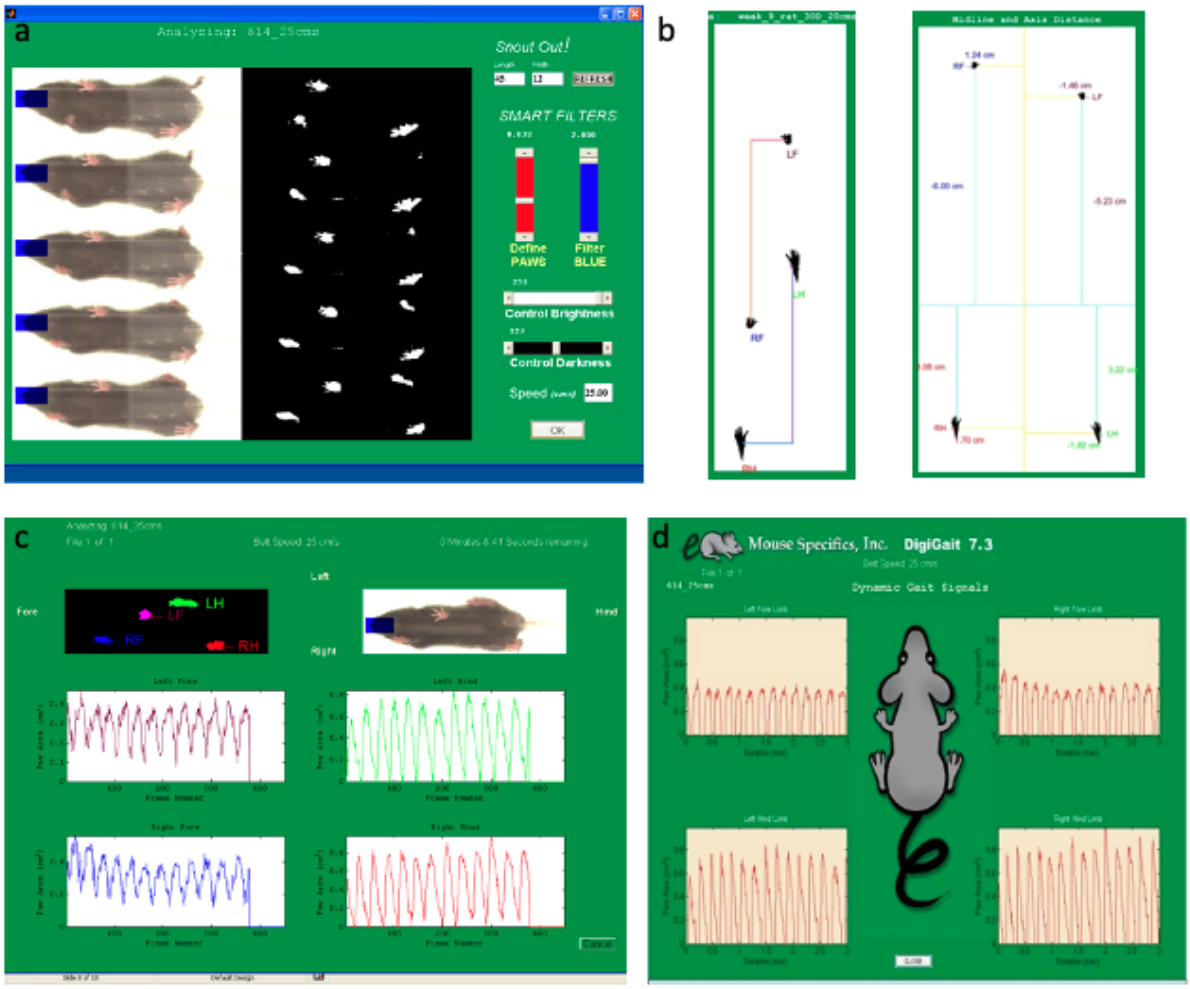

Figure 6-3: Screen-captured image of the DigiGait™ gait analysis system (a) Image captured from high-speed video, showing the digital black and white measures of gait. (b) Plot of paw area in one gait cycle, indicating the midline distance. (c) Unfiltered gait signals generated for each of the 4 paws and limbs: periodic waveforms representing the stance and swing phases of the stride. The curve represents the identified foot of each limb while in contact with the treadmill. (d) Filtered gait signals (some figures are adapted from DigiGait™ documentation).

For analysis purposes, each video was clipped to 3 seconds, including a minimum of 4 consecutive strides. The data were normalized to 100% of the gait cycle, which is defined from the first foot-strike event (when the heel touches the ground) to the next foot-strike event (Figure 6-1).

Once all the images were processed, the gait signals for each paw were filtered and presented, starting with the left hind paw. Additional filtering can be applied to the signals using the "correct" or "connect" command to adjust the swing/stance detection, where the software recognized the paw is on/off the treadmill when it is off/on. And the "delete" function can be used to remove any abnormalities in the

signal. The final filtered gait signal is shown in Figure 6-3. Measures are then calculated for over 50 gait variables.

These measures include more than 50 spatiotemporal parameters that reflect the time-space changes during a gait cycle. They include spatial parameters such as stride length, paw area, paw length, step width, and spatial gait symmetry, as well as temporal parameters such as stance times, swing time, and stride time. These measures were compared with the baseline data collected in sham groups to assess any OA-induced changes.

6.2.3 *In vivo* data collection

A few days before the surgery, the animals were placed on the treadmill twice for 5 minutes each time and allowed to move freely to acclimatise to the environment. To avoid cross-contamination of scents, the walkway was wiped down with an ethanol spray between animals. The animals were trained to walk/run on the treadmill, starting from a speed of 10 cm/s and gradually increasing to 20 cm/s. This training process was repeated twice daily until the animals consistently ran on the treadmill, indicating their readiness for data collection. Small food rewards were given at the end of each training session as a reinforcement.

From week 4, the rats were individually allowed to walk on the treadmill at a low speed of 5 m/min for 10 minutes per day and gradually increasing to 20 cm/s. To effectively enlarge the sample size for subsequent machine-based discriminant analysis, the gait data collection used the Bootstrap method. This approach involved randomly selecting one rat from each group and repeating the process 20 times in one month, (5 mins/rat) for a further 5 months (week 4-20, post-surgery). The selection was completely randomized for each group, and ensured that each rat was recorded at least once at each timepoint. Consequently, there were 20 raw data samples for each group at each timepoint, with each sample providing a dataset containing 50 gait spatiotemporal features (also referred to as parameters or variables in the following results).

6.2.4 Statistical methods

Multivariate discrimination analysis was used in this study to characterize the discriminatory features between study groups and identify gait markers.

Determining the optimal PLS-DA model:

Partial least-squares discrimination analysis (PLS-DA) is a supervised method used to analyse the characteristics that can discriminate between groups based on both dataset differences and the original group classification described previously in the thesis (0ºTO (sham) group, 30ºTO group, and 30ºTO group with treatment).

The PLS-DA models examine the relationship between gait datasets and a categorical variable, y, which indicates the group of each sample in the study (e.g., sham group, 30ºTO group, treatment group). If a statistically significant discrimination between the two groups (classes) is found, the model parameters can be interpreted for their discriminatory power.

The goal of the PLS-DA model is to predict the categorical variable values of unknown samples. The categorical variable y is represented as a vector, with values of -1 and 1 indicating class membership. -1 represents the control class, while 1 represents the case class. The classification procedure applies a threshold, where samples above the threshold are assigned to the disease class, while samples below the threshold are assigned to the sham class (Szymańska et al., 2012).

In PLS-DA, each **component** represents a linear combination of the original features and captures the maximum covariance between the predictor and response variables. The PLS-DA model with one component captures the most significant separation between the classes. Adding a second component may capture more remaining variance but may not improve the classification performance. Therefore, increasing the number of components can make the model more complex and capture more subtle patterns in the data, but it may also overfit the data, leading to poorer performance on new data.

This can be explained using the term "accuracy." **Accuracy** measures how well the PLS-DA model predicts the class labels of new samples, accuracy above 0.7 is generally considered acceptable. The accuracy of the model can vary depending on the number of components used to build the model. When using only one component, the model may not capture all the variations in the data, resulting in lower accuracy. Adding more components can increase the accuracy, but there is a point where too many components can result in overfitting, leading to a decrease in accuracy on new, unseen data. Therefore, the optimal number of components is the one that achieves the highest accuracy while avoiding overfitting.

The **optimal number of components** can be determined by cross-validation (CV), where the data is split into training and testing sets, and the accuracy of the model is evaluated on the testing set. Q^2 assesses the model's predictive capability through cross-validation, which is generally considered indicative of good predictive power when it is above 0.5, though 0.5 is not an absolute threshold for more complex models. During each CV iteration, the predicted data is compared to the actual data, and the sum of squared errors is calculated. This prediction error is then totalled across all samples, resulting in the Predicted Residual Sum of Squares (PRESS). Q^2 is calculated as 1 minus the ratio of PRESS to the sum of squares. The coefficient of determination, R^2, measures the model's ability to capture the data's variance, with a higher R^2 (close to 1) indicating a better fit by the PLS-DA model. A low PRESS (high R^2) and high Q^2 indicate effective predictions, while a negative Q^2 suggests either a lack of predictiveness or an overfitted model, where the model performs well on the training set but poorly on the testing set (Szymańska et al., 2012).

Ideally, the selection of components should aim for the highest R^2 and Q^2 values. However, achieving both simultaneously is often impractical. Therefore, the stability and growth trend of Q^2 should be given priority, as low Q^2 can indicate overfitting, especially when R^2 is significantly higher. This study selects the number of components at the point where Q^2 no longer shows significant increases (indicating the highest Q^2 before it plateaus) as optimal (Figure 6-4). Adding more components beyond this point does not significantly enhance the model's predictive capability.

In the context of three-group discrimination (Section 6.3.1.1), the PLS-DA model failed to demonstrate sufficient predictive capability ($Q^2 < 0.5$). To address this, PLS-DA was applied separately to each pair of groups, simplifying the discrimination process. This approach successfully yielded PLS-DA models with improved predictiveness ($Q^2 > 0.5$) for this pairwise group separations (Section 6.3.1.2). This step is particularly important in scenarios involving three-group discrimination, which presents inherent complexity over two-group scenarios, mainly due to increased variability in the data. Furthermore, potential indistinctness or overlapping characteristics between the third group and the other two add further challenges to simultaneous discrimination among three groups.

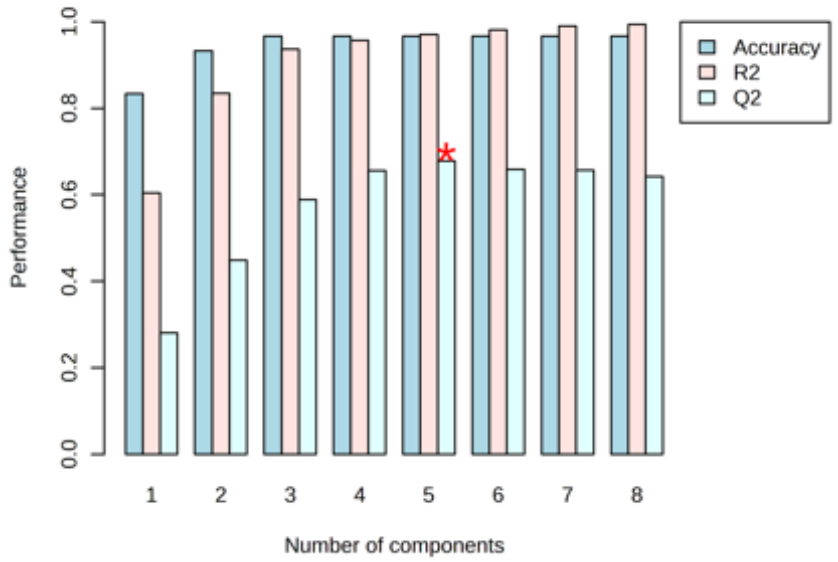

Figure 6-4: Cross validation of PLS-DA left limb model with different numbers of components. The Q^2, R^2 and accuracy increase as the number of components increases, with Q^2 reaching highest before it plateaus at the model with 5 components (indicated with red star).

Identifying the most important features (variables):

The weights of the original features in each component can be used to rank the importance of the features. **Variable Importance in Projection** (VIP), also known as discriminatory power, is a feature importance metric that measures the contribution of each feature to the response variable. Features with higher VIP

values (larger weights) (also refers to important variables, contributory variables or discriminatory variables in the following results) indicate that the feature has stronger explanatory power for the model and are considered more important in separating the classes. In PLS-DA, the first component usually captures the most significant variance, while the second component captures the most significant variance not captured by the first component. A variable's VIP value might be lower in the second component compared to the first component, indicating a smaller weight of variables on the second component. Therefore, once the optimal number of components is selected, the features are selected with VIP values greater than 1 for each component as important features. It is important to highlight that even if the overall predictive performance of the model is insufficient (indicated by a low Q^2 value), variables with a VIP value greater than 1 remain significant. They contribute substantially to explaining the variability among groups and the correlation between these variables (X) and the response variable (Y), thereby discriminating between groups.

To identify variables with consistently high discriminatory power across different models, this study compared the loadings of the same variables in two models (left and right limbs). This comparison was based on the models' similarity (same variables and conditions) to ensure the comparison's validity. **Loadings**, which are qualitative values indicating the contribution of variables to each component, were chosen for comparison instead of VIP scores. This choice was made because VIP scores reflect the significance of variables across the entire model and all components, which precludes direct comparison between models. Variables with high loadings (large positive or large negative values) on a component are considered important for that component. This study focus on comparing the magnitude of the loading in first component. A variable's larger loading value on the first component indicates its dominant role in discriminating data points.

Hierarchical Clustering. Given the low quality of the PLS-DA model (low Q^2 value) in discriminating among four groups, this study opted to use all variables for clustering analysis to simply visualize the distance (close or far) between groups when the model is too complex and the groups overlap in the PLS-DA model.

The Hierarchical Clustering algorithm clusters samples by constructing a hierarchically nested cluster tree (dendrogram). It is an unsupervised learning method that aims to group data points based on certain measures of similarity (such as Euclidean distance), unlike PLS-DA, which is used to predict the categories of the response variable based on the relationships between variables. Clustering is not used to identify markers for predictive functionality. It serves as a method in this study to measure the distance between groups, especially when the PLS-DA plot does not clearly separate them. Instead, PLS-DA is the primary method applied in this study for building predictive models and selecting variables.

6.3 Results

Multivariate discrimination analysis (PLS-DA) was utilized in this study to characterize the discriminatory features between the study groups. The results indicated that the PLS-DA model can effectively discriminate between the OA-affected gait (30ºTO group) and healthy gait (sham group) in both limbs, but it was unable to accurately classify treated gait (treatment group) versus OA-affected gait in the left limb, and treated gait versus normal gait in the right limb (Section 6.3.1 and Section 6.4.2). This suggests that gait in the left limb did not fully revert to normal after treatment, in contrast to the right (contralateral) limb. This finding is consistent with micro-CT and histology results, but not as sensitive as other measurements for differentiating the 10ºTO (early-stage OA).

Several gait features with high discriminatory power (VIP>1) for separating three groups were identified (Section 6.3.1.2). The results show that both the left and right limbs have discriminatory variables in the gait coordination features category (such as Max dA/dT, paw placement positioning, midline distance) and paw features category (such as paw area at peak stance, paw width variability), with more pronounced differences observed in the right limb. This indicates compensatory changes in weight distribution and support in quadrupeds. Moreover, the left (injured) limb also has additional important variables in spatial features, while the right limb contributes more in temporal features, Among these, the most important (contributory) variables are Paw Area at Peak Stance and Max dA/dT, that consistently showed substantial contribution across all discrimination models for both limbs.

Furthermore, there is a differentiation between the two treatment groups. The treated groups are in the same branch as the healthy group, with the APS group being closer to the sham group than the BMP group. This proximity suggests that APS treatment may be more effective than BMP, particularly in recovering gait coordination features.

6.3.1 Discrimination analysis between sham group, 30ºTO group, and treatment group

6.3.1.1 PLS-DA model construction and cross validation

Initially, preliminary pairwise separation using PLS-DA was performed at each time point between the surgery (10ºTO and 30ºTO) groups and sham groups. The results demonstrated that the 30ºTO group (indicative of progressive-stage OA) could be effectively distinguished from the sham groups at the final 5-month time point, with satisfactory accuracy and R^2 values for group differentiation (Figure 6-5). However, the 10ºTO group (early-stage OA) could not be differentiated from the sham group throughout the 5-month period. Consequently, only data related to the 30ºTO group at the 5-month time point were considered for further analyses. The treatment groups (BMP treatment and APS treatment) were combined into a single treated gait group for analysis purposes (detailed in section 6.3.3).

a

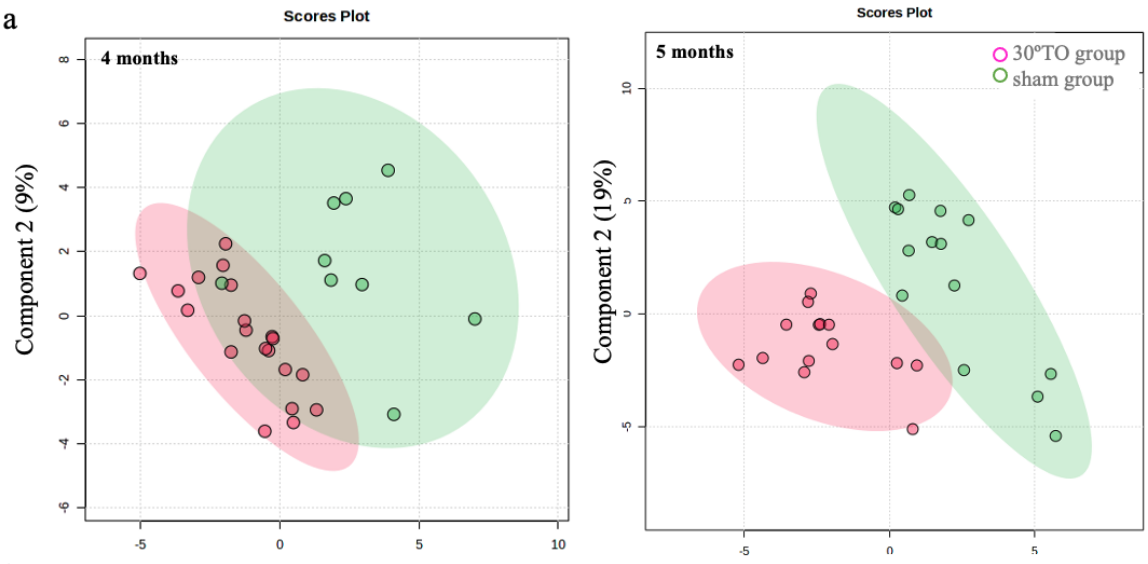

b

4 months

Measure	1 comps	2 comps	3 comps	4 comps	5 comps	6 comps	7 comps	8 comps
Accuracy	0.8	0.8	0.8	0.8	0.72667	0.76	0.76	0.76
R^2	0.47691	0.70372	0.75766	0.7968	0.83502	0.88348	0.91716	0.93742
Q^2	0.033803	**0.11433**	-0.060052	-0.25236	-0.60709	-0.90769	-1.1427	-1.2723

5 months

Measure	1 comps	2 comps	3 comps	4 comps	5 comps
Accuracy	0.83333	0.93333	0.96667	0.96667	0.96667
R^2	0.6045	0.83425	0.93676	0.95672	0.97115
Q^2	0.28065	0.44908	0.58853	0.656	**0.67818**

Figure 6-5 PLS-DA model for discriminatory separation and cross-validation: sham (0°TO) group and 30°TO group of left limbs at **4th month and 5th month**: a. 3D scores plot of PLS-DA left limb model illustrating separation between two groups. The coloured region displays the 95% confidence region. b. PLS-DA Cross-validation details: the negative Q^2 suggested a significant overlap between the two groups in 4th month, however, 5th month data demonstrates good discrimination quality with clear separation between groups.

Subsequently, the three-group discrimination analysis was conducted among the sham group (healthy gait), the 30°TO group (OA-affected gait), and the 30°TO-treatment group (treated gait). The statistical results indicated that the overall predictive performance of the PLS-DA model for both the left limb (Figure 6-6a) or right limb (Figure 6-7a) was suboptimal for predictiveness ($Q^2 < 0.5$). Nonetheless, the models' satisfactory accuracy and R^2 values suggest that they are capable of differentiating between groups based on the existing data. Thus, variables with significant variable importance (VIP > 1) remain significantly contributory towards explaining the discrimination between groups. Cross-validation indicated that the model with 3 components (Figure 6-6b) is the optimal model for separating the groups of the left limb, and 5 components (Figure 6-7b) for the right limb. The gait features (variables) of each component with VIP value over than 1 are listed in Table 6-2 and Table 6-3. It is observed that the number of important features (VIP > 1) in the right limb is half of that in the left limb, indicating that the feature weights tend to be more concentrated in the model for the right limb.

a

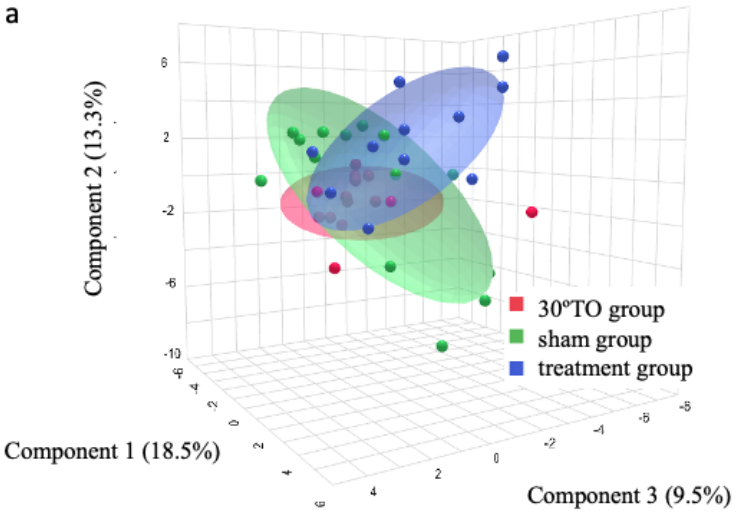

b

Measure	1 comps	2 comps	3 comps	4 comps	5 comps
Accuracy	0.40595	0.63452	0.73254	0.75754	0.75119
R^2	0.5127	0.75106	0.80453	0.84238	0.86714
Q^2	0.19557	0.36755	**0.47126**	0.40701	0.32678

Figure 6-6. PLS-DA model for discriminatory separation and cross-validation: sham (0ºTO) group, 30ºTO group, and 30ºTO group with treatment of **left limb**: a. 3D scores plot of PLS-DA left limb model illustrating separation between three groups. The coloured region displays the 95% confidence region. b. PLS-DA Cross-validation details: Q^2 <0.5 indicates the model lack effective predictiveness.

a

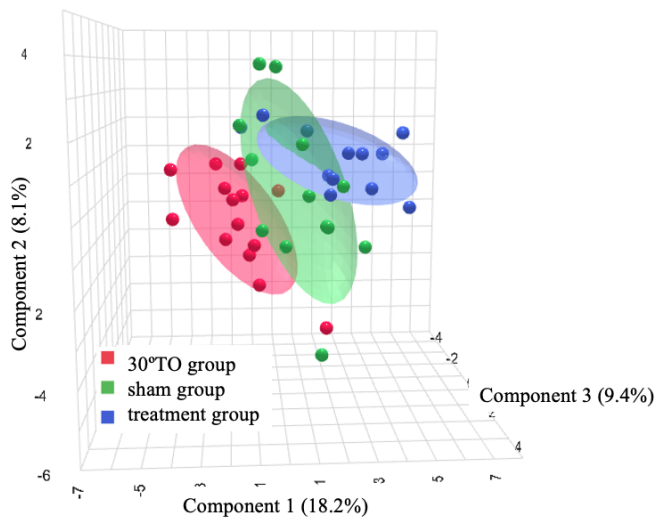

b

Measure	1 comps	2 comps	3 comps	4 comps	5 comps
Accuracy	0.54405	0.57183	0.72976	0.67262	0.64762
R^2	0.48328	0.70509	0.77483	0.8406	0.85746
Q^2	0.24643	0.2693	0.30986	0.39997	**0.44568**

Figure 6-7. PLS-DA model for discriminatory separation and cross-validation: sham (0ºTO) group, 30ºTO group, and 30ºTO group with treatment of **right limb**: a. 3D scores plot of PLS-DA left limb model illustrating separation between three groups. The coloured region displays the 95% confidence region. b. PLS-DA Cross-validation details: Q^2 <0.5 indicates the model lack effective predictiveness.

	Comp. 1 VIP score	Comp. 2 VIP score	Comp. 3 VIP score
Paw Area Variability at Peak Stance in sq. cm (cm^2)	2.1183	1.756	1.6993
Paw Area Variability (cm^2)	2.1183	1.756	1.6993
PawPlacementPositioning[PPP] (cm)	1.9701	1.6554	1.6011
fore limb stance width (cm)	1.9471	1.7781	1.7352
Step Angle (deg)	1.6848	1.4407	1.4523
paw area CV (CV%)	1.6669	1.3821	1.3915
Paw Length Variability (cm)	1.6133	1.3508	1.3422
Paw Area at Peak Stance in sq. cm (cm^2)	1.4897	1.2767	1.2602
Paw Area (cm^2)	1.4897	1.2767	1.2602
PawAngle (deg)	1.3248	1.4845	1.4361
Paw Angle Variability (deg)	1.2569	1.1069	1.1057
SLVar (cm)	1.2435	1.0606	1.043
MAX dA/dT (cm^2/s)	1.2259	1.116	1.1168
Stride Length CV (CV%)	1.1685	0.9883	0.96574
Stride Frequency (step/s)	1.1601	1.007	1.0087
Swing Duration CV (CV%)	1.0959	0.9093	0.90759
Midline Distance (cm)	1.085	0.99388	1.0752
Absolute PawAngle (deg)	0.98839	0.9696	0.97179
Paw Width Variability (cm)	0.91451	1.002	1.0066
Paw Length (cm)	0.87019	1.0355	1.0016
%PropelStride (%)	0.85555	1.183	1.144

Table 6-2 Gait feature selection from the PLS-DA model of **left limb** with different components. The features with variable importance (VIP score > 1.0) in different components are listed and ranked based on their VIP scores, from high to low. The model with 3 components has been validated as the optimal PLS-DA model for discriminatory separation.

	Comp. 1 VIP score	Comp. 2 VIP score	Comp. 3 VIP score	Comp. 4 VIP score	Comp. 5 VIP score
Paw Area at Peak Stance in sq. cm (cm^2)	2.0988	1.7754	1.6954	1.6669	1.6516
Paw Area (cm^2)	2.0988	1.7754	1.6954	1.6669	1.6516
MAX dA/dT (cm^2/s)	2.0593	1.7139	1.6464	1.6313	1.6158
Paw Width Variability (cm)	1.6272	1.4868	1.4274	1.3983	1.3881
Paw Length (cm)	1.5208	1.2948	1.3285	1.4199	1.4143
%PropelStride (%)	1.4755	1.3348	1.3012	1.2516	1.2401
Brake (s)	1.3496	1.1464	1.1048	1.1497	1.1437
%PropelStance (%)	1.3436	1.1947	1.1419	1.1624	1.1545
%BrakeStance (%)	1.3436	1.1947	1.1419	1.1624	1.1545
%BrakeStride (%)	1.2619	1.0861	1.039	1.0837	1.0788
Swing (s)	1.2269	1.0696	1.0423	1.0015	0.99661
Paw Width (cm)	1.1396	0.98228	1.06	1.0204	1.0116
Axis Distance (cm)	1.1395	1.1272	1.1186	1.0817	1.0746
Midline Distance (cm)	1.1312	1.138	1.0904	1.0604	1.0638
Ataxia Coefficient	1.1166	1.0645	1.0769	1.0358	1.0463
Stance/Swing	1.1023	0.97412	1.0359	0.99505	0.99359
%SwingStride (%)	1.0469	0.97503	0.98317	0.94879	0.94437
%StanceStride (%)	1.0469	0.97503	0.98317	0.94879	0.94437

Table 6-3 Gait feature selection from the PLS-DA model of **right limb** with different components. The features with variable importance (VIP score > 1.0) in different components are listed and ranked based on their VIP scores, from high to low. The model with 5 components has been validated as the optimal PLS-DA model for discriminatory separation.

6.3.1.2 Feature selections in PLS-DA models across three groups

Subsequently, the study summarizes the gait features (variables) with significant variable importance (VIP score > 1.0) in Table 6-4, comparing between three groups (sham, 30ºTO, and treated groups) in the left and right limbs separately, based on Table 6-2 and Table 6-3. In the results, Table 6-4, categorizes these features into four categories: spatial features, temporal features, gait coordination features, and paw features (indicating weight support). The results show that both the left and right limbs have differentiating features (VIP>1) in the gait coordination features category (such as Max dA/dT, paw placement positioning, midline distance) and paw features (such as Paw area at Peak stance, Paw width variability), while the left (injured) limb also has more contributory features in spatial features, but the right limb contribute more in temporal features. Additionally, gait alterations were found not only in the hindlimbs but also in similar changes in paw position (decreased stance width) in the left (injured) forelimb, indicating changes in weight distribution and support in quadrupeds.

The summary table (Table 6-4) also lists the **mean values** of each feature in each group for each limb, for comparison of the trends in each limb, particularly how the parameters changed after surgery and

subsequently after treatment. The variables in the right limbs show a more consistent trend, where the contributory variables increased (or decreased) in rats with OA (30ºTO group), but post-treatment, there was a reversal in these variables towards healthy levels, remaining marginally higher (or lower) than the healthy group. There was a clear increase in swing time, an increase in the percentage of time spent in the brake phase during stance (%BrakeStance), and a decrease in the percentage of time spent in the propel phase (%PropelStance) after treatment in the right limb. However, these classical temporal features do not show high importance (VIP <1.0) in the left limb.

		Left Limb			Right Limb		
	Parameters	**Sham**	**30°TO**	**treatment**	**Sham**	**30°TO**	**treatment**
Temporal features	Swing (s)	0.18 ± 0.02	0.17 ± 0.01	0.21 ± 0.02	0.15 ± 0.01	0.13 ± 0.01	0.16 ± 0.01
	%SwingStride (%)	27.06 ± 2.66	25.77 ± 1.54	29.55 ± 2.13	22.51 ± 1.59	19.12 ± 0.98	22.89 ± 1.84
	%BrakeStride (%)	8.04 ± 1.29	6.06 ± 1.01	7.49 ± 1.74	4.01 ± 0.35	4.64 ± 0.48	6.68 ± 0.85
	%PropelStride (%)	64.91 ± 3.35	68.13 ± 1.47	62.94 ± 2.71	73.46 ± 1.57	76.24 ± 1.40	70.44 ± 1.60
	%StanceStride (%)	72.94 ± 2.66	74.23 ± 1.54	70.45 ± 2.13	77.49 ± 1.59	80.88 ± 0.98	77.11 ± 1.84
	%BrakeStance (%)	11.52 ± 2.05	8.06 ± 1.32	10.74 ± 2.43	5.19 ± 0.46	5.82 ± 0.68	8.55 ± 1.00
	%PropelStance (%)	88.48 ± 2.05	91.94 ± 1.32	89.26 ± 2.43	94.81 ± 0.46	94.18 ± 0.68	91.45 ± 1.00
	Stance/Swing	3.21 ± 0.42	3.01 ± 0.17	2.57 ± 0.25	3.69 ± 0.30	4.39 ± 0.23	3.63 ± 0.31
	Stride Frequency (step/s)	1.54 ± 0.03	1.54 ± 0.04	1.42 ± 0.05	1.58 ± 0.04	1.53 ± 0.03	1.51 ± 0.04
	Swing Duration CV (CV%)	16.73 ± 3.85	25.06 ± 4.67	15.40 ± 1.73	15.51 ± 2.42	16.77 ± 2.48	21.28 ± 5.31
Spatial features	Absolute PawAngle (deg)	9.15 ± 1.96	4.81 ± 1.57	8.88 ± 1.80	4.89 ± 0.63	4.06 ± 0.84	4.50 ± 1.05
	Paw Angle Variability (deg)	7.37 ± 1.10	6.72 ± 0.77	3.77 ± 0.74	7.24 ± 1.00	6.29 ± 0.88	8.18 ± 0.73
	StepAngle (deg)	66.32 ± 1.36	66.77 ± 2.30	56.85 ± 2.86			
	SLVar (cm)	0.84 ± 0.24	1.08 ± 0.16	1.86 ± 0.30	1.48 ± 0.30	1.43 ± 0.25	0.90 ± 0.18
	Stride Length CV (CV%)	6.32 ± 1.74	8.02 ± 1.18	13.33 ± 2.27	11.50 ± 2.47	10.56 ± 1.84	6.30 ± 1.25
Gait Coordination	MAX dA/dT (cm^2/s)	329.24 ± 36.83	490.29 ± 24.00	388.39 ± 39.72	480.24 ± 15.58	649.12 ± 29.31	485.55 ± 32.22
		0.41 ± 0.17	0.81 ± 0.15	0.01 ± 0.14	0.30 ± 0.09	0.53 ± 0.11	0.58 ± 0.11
	Paw Placement Positioning [PPP] (cm)	0.12 ± 0.04	0.17 ± 0.03	0.25 ± 0.05	0.22 ± 0.06	0.24 ± 0.05	0.11 ± 0.02
	Midline Distance (cm)	0.68 ± 0.32	0.47 ± 0.19	1.20 ± 0.32	-0.01 ± 0.16	-0.20 ± 0.14	0.26 ± 0.19
	Axis Distance (cm)	-1.87 ± 0.04	-1.85 ± 0.10	-1.84 ± 0.14	1.57 ± 0.07	1.42 ± 0.09	1.69 ± 0.13
Weight support/ paw features	Paw Width (cm)	120.07 ± 7.75	122.14 ± 4.18	128.50 ± 4.00	2.38 ± 0.05	2.74 ± 0.06	2.53 ± 0.10
	Paw Length (cm)	4.26 ± 0.31	5.07 ± 0.14	4.58 ± 0.27	4.96 ± 0.14	5.62 ± 0.14	5.03 ± 0.16
	Paw Length Variability (cm)	0.51 ± 0.10	0.83 ± 0.10	0.42 ± 0.10	0.51 ± 0.08	0.59 ± 0.07	0.67 ± 0.10
	Paw Width Variability (cm)	0.17 ± 0.03	0.22 ± 0.02	0.17 ± 0.02	0.25 ± 0.03	0.16 ± 0.02	0.28 ± 0.03
	Paw Area (cm^2)	4.13 ± 0.33	5.86 ± 0.23	4.62 ± 0.40	5.64 ± 0.17	7.57 ± 0.32	5.81 ± 0.29
	Paw Area at Peak Stance in sq. cm (cm^2)	4.13 ± 0.33	5.86 ± 0.23	4.62 ± 0.40	5.64 ± 0.17	7.57 ± 0.32	5.81 ± 0.29
	Paw Area Variability at Peak Stance in sq. cm (cm^2)	0.41 ± 0.07	0.98 ± 0.10	0.48 ± 0.07	0.65 ± 0.11	0.79 ± 0.10	0.76 ± 0.12
	Paw Area Variability (cm^2)	0.41 ± 0.07	0.98 ± 0.10	0.48 ± 0.07	0.65 ± 0.11	0.79 ± 0.10	0.76 ± 0.12
	paw area CV (%)	9.62 ± 1.30	16.42 ± 1.32	10.70 ± 1.31	12.53 ± 2.05	10.82 ± 1.40	13.98 ± 2.37
	paw angle (deg)	6.40 ± 2.70	1.91 ± 1.99	-7.10 ± 2.41	2.66 ± 1.45	0.46 ± 1.40	2.78 ± 1.50
	fore limb stance width (cm)	2.44 ± 0.13	1.83 ± 0.25	2.76 ± 0.11	2.44 ± 0.13	1.83 ± 0.25	2.76 ± 0.11

Table 6-4. All variables with VIP > 1 between three groups for the left and right limbs are coloured (mean ±SE). The variables are grouped into four categories.

To identify which variables consistently make a large contribution to the component across different models (left and right limb models) and to observe whether their relative importance changes under different conditions (left and right limb models), the analysis then proceeds to compare the **loadings** of the same variables in the models between the left and right limbs (Table 6-5). It was found that the right limb (contralateral non-surgery hind limb) shows slightly higher loadings for the same variables compared to the left limb. This suggests better performance of the differentiated variables in the right limb and the importance of compensation gait measurement in rodent gait analysis.

	Left Limb				Right Limb			
Parameters	Mean of Sham	Mean of 30ºTO	Mean of treatment	Loadings	Mean of Sham	Mean of 30ºTO	Mean of treatment	Loadings
%PropelStride (%)	64.91 ± 3.35	68.13 ± 1.47	62.94 ± 2.71	-0.25	73.46 ± 1.57	76.24 ± 1.40	70.44 ± 1.60	-0.27
Paw Area at Peak Stance in sq. cm (cm^2)	4.13 ± 0.33	5.86 ± 0.23	4.62 ± 0.40	-0.24	5.64 ± 0.17	7.57 ± 0.32	5.81 ± 0.29	-0.26
MAX dA/dT (cm^2/s)	329.24 ± 36.83	490.29 ± 24.00	388.39 ± 39.72	-0.23	480.24 ± 15.58	649.12 ± 29.31	485.55 ± 32.22	-0.28
Midline Distance (cm)	0.68 ± 0.32	0.47 ± 0.19	1.20 ± 0.32	0.20	-0.01 ± 0.16	-0.20 ± 0.14	0.26 ± 0.19	0.24
Paw Length (cm)	4.26 ± 0.31	5.07 ± 0.14	4.58 ± 0.27	-0.24	4.96 ± 0.14	5.62 ± 0.14	5.03 ± 0.16	-0.25
Paw Width Variability (cm)	0.17 ± 0.03	0.22 ± 0.02	0.17 ± 0.02	-0.15	0.25 ± 0.03	0.16 ± 0.02	0.28 ± 0.03	0.16
Paw Area (cm^2)	4.13 ± 0.33	5.86 ± 0.23	4.62 ± 0.40	-0.25	5.64 ± 0.17	7.57 ± 0.32	5.81 ± 0.29	-0.26

Table 6-5 A summary of the variables with VIP > 1 in both the left and right limbs (mean ±SE).

Finally, the study identified the most important (contributory) features for discriminating gait patterns in this animal model. The analysis gives priority to variables with the highest VIP scores, considering these to have the most substantial contribution to the discriminatory model (Table 6-2 and Table 6-3). The biological relevance of the variables is also taken into account. Furthermore, the features needed to be important variables in both limbs, displaying a clear trend post-OA induction and subsequent treatment (Table 6-5). Paw Area at Peak Stance and MAX dA/dT are selected as the top features.

Paw Area at Peak Stance and Max dA/dT emerged as the two most significant and consistent (low SE) measurements among all three group discriminations (Section 6.3.1.1) and later two-group discriminations (Section 6.3.1.3) in both the left and right limbs. The study observed a consistent increase in both Paw Area at Peak Stance and Max dA/dT in each limb after the OA induction, followed by a decrease after treatment.

6.3.2 Discrimination analysis of 30ºTO group with other groups

Given the overall insufficient predictive performance of the three-group separations (low Q^2 value) (Section 6.3.1), this approach can be applied for selecting important gait features but is not suitable for constructing a discrimination model with predictive capability. To investigate the potential for developing a more powerful PLS-DA model with high predictive capability, which could subsequently act as a diagnostic tool in future animal studies, two-group PLS-DA analyses were performed for each limb. These analyses aimed to discriminate between each pair of the three groups separately (sham group, 30ºTO group, and 30ºTO treatment group).

6.3.2.1 Discrimination analysis in left limb between groups

PLS-DA analyses for the left limb were conducted to discriminate between each pair of the three groups separately: the sham group (normal gait), the 30ºTO group (OA-affected gait), and the 30ºTO treatment group (treated gait). First, the PLS-DA model clearly separated the 30ºTO group from the sham group, with cross-validation showing that the model with 5 components was the optimal model for discrimination and prediction (Q^2=0.67818). From each of the 5 components, features with VIP values greater than 1 were selected as important features in (Table 6-6).

Next, PLS-DA effectively discriminate treatment group from the sham group. Cross-validation indicated that the model with 2 components was the optimal model (Q^2=0.53), therefore the important features (VIP score > 1.0) in 2 components are listed in Table 6-6. However, the model could not accurately distinguish between the treated gait and the OA-affected gait (30ºTO group) in the left limb (Q^2 =0.43), suggesting that the gait did not fully revert to normal following treatment Table 6-6.

The important (contributory) variables for discriminating between normal gait and OA-affected gait, as well as normal gait and treated gait, remain the paw features (especially paw area at peak stance) and coordinate features (max dA/dT), which also shown significant contributions across the three-group discrimination model. Yet, in the model comparing sham group with treatment group, the top contributory variables differ, with more variables related to spatial features such as paw angle, and gait coordination, such as tibia functional index (TFI), sciatic functional index (SFI), and Ataxia coefficient, ranking higher (providing more contribution) in the discrimination model (Table 6-6).

30°TO group vs sham group (Q^2 =0.68)	VIP scores (Comp.1)	Sham group vs treatment group (Q^2 =0.43)	VIP scores (Comp.1)	30°TO group vs treatment group (Q^2 =0.53)	VIP scores (Comp.1)
Paw Area Variability at Peak Stance (cm^2)	2.3347	PawAngle (deg)	2.0882	Paw Area Variability at Peak Stance in sq. cm (cm^2)	2.5456
Paw Area Variability (cm^2)	2.3347	fore limb weight support (%)	1.9294	Paw Area Variability (cm^2)	2.5456
Paw Area at Peak Stance in sq. cm (cm^2)	2.1833	StepAngle (deg)	1.8726	paw area CV (CV%)	2.173
Paw Area (cm^2)	2.1833	SLVar (cm)	1.6679	Paw Area at Peak Stance in sq. cm (cm^2)	1.9602
paw area CV (CV%)	1.9905	Paw Angle Variability (deg)	1.6449	Paw Area (cm^2)	1.9602
MAX dA/dT (cm^2/s)	1.988	Stride Length CV (CV%)	1.5732	MAX dA/dT (cm^2/s)	1.8
MIN dA/dT (cm^2/s)	1.4965	TFI (real#)	1.5441	Paw Length Variability	1.4356
Paw Length (cm)	1.4571	SFI (real#)	1.5387	MIN dA/dT (cm^2/s)	1.3846
Paw Length Variability (cm)	1.3732	MIN dA/dT (cm^2/s)	1.4585	fore limb stance width (cm)	1.3755
fore limb stance width (cm)	1.3187	Ataxia Coefficient	1.4126	PawPlacementPositioning[PPP] (cm)	1.365
Paw Drag	1.1617	Overlap Distance (cm)	1.3782	Paw Drag (cm)	1.3309
Paw Placement Positioning [PPP] (cm)	1.1164	Stride Frequency (step/s)	1.3363	Paw Length (cm)	1.2186
Absolute PawAngle (deg)	1.094	Step Angle CV (CV%)	1.3358	Absolute PawAngle (deg)	1.0431
TFI	0.96646	Gait Symmetry	1.3301	Swing Duration CV (CV%)	1.0429
SFI	0.95803	Paw Drag	1.3292		
		PawPlacementPositioning[PPP] (cm)	1.2162		
		fore limb stance width (cm)	1.1935		
		Stride (s)	1.1097		
		StrideLength (cm)	1.1015		
		AFI	1.0469		

Table 6-6. Gait feature selection (VIP > 1) in different components from the PLS-DA model for pairwise discriminatory separation between the 30°TO group, sham group, and treatment group in the left limb. The features are listed and ranked in descending order based on their VIP scores of component 1.

6.3.2.2 Discrimination analysis in right limb between groups

Additionally, PLS-DA analyses for the right limb were conducted to discriminate between each pair of the three groups separately: the sham group (normal gait), the 30°TO group (OA-affected gait), and the 30°TO treatment group (treated gait).

For the right limb, the PLS-DA model effective discriminate the 30°TO group from the sham group (Q^2= 0.56). The model also effectively separated the treatment group from the 30°TO group, as indicated by the highest Q^2 value (reaching 0.78) among all comparisons (Figure 6-8). However, there was less precision in separating the treated group from the sham group. The low Q^2 value (0.22) suggested a significant overlap between the two groups, indicating a tendency towards normal gait recovery in the

non-injured limb after treatment. The features with variable importance (VIP score > 1.0) in the optimal components are shown in

30ºTO group vs sham group ((Q2 =0.56)	VIP scores (Comp.1)	30ºTO group vs treatment group (Q2 =0.79)	VIP scores (Comp.1)	Sham group vs treatment group (Q2 =0.22)	VIP scores (Comp.1)
Paw Area at Peak Stance in sq. cm (cm2)	2.2333	Paw Area at Peak Stance in sq. cm (cm2)	1.9265	%PropelStance (%)	2.0785
Paw Area (cm2)	2.2333	Paw Area (cm2)	1.9265	%BrakeStance (%)	2.0785
MAX dA/dT (cm^2/s)	2.1798	MAX dA/dT (cm^2/s)	1.8441	%BrakeStride (%)	1.9786
Paw Width (cm)	2.1018	Paw Width Variability	1.6728	Gait Symmetry	1.9497
Paw Length (cm)	1.6727	Paw Length (cm)	1.5123	Brake (s)	1.8849
AFI (real#)	1.5864	%PropelStride (%)	1.4757	AFI (real#)	1.4903
Stance (s)	1.3393	Ataxia Coefficient	1.3056	Overlap Distance (cm)	1.4843
Paw Width Variability (cm)	1.286	Brake (s)	1.2954	Swing Duration CV (CV%)	1.4289
Propel (s)	1.1486	%PropelStance (%)	1.2884	Tau – Propulsion (s)	1.3201
%StanceStride (%)	1.037	%BrakeStance (%)	1.2884	Stride Length CV (CV%)	1.2593
%SwingStride (%)	1.037	Swing (s)	1.2601	%PropelStride (%)	1.2334
Stance/Swing	1.0359	%BrakeStride (%)	1.2209	Midline Distance (cm)	1.2287
		Stance/Swing	1.139	SLVar (cm)	1.2069
		Midline Distance (cm)	1.1301	Ataxia Coefficient	1.183
		%SwingStride (%)	1.0879	TFI	1.1404
		%StanceStride (%)	1.0879	SFI	1.1302
		Paw Width (cm)	1.0666	Paw Length Variability (cm)	1.0787
		Stride Length CV (CV%)	1.0632	StrideLength (cm)	1.0514
		Axis Distance (cm)	1.0334	Stride (s)	1.0377
		SLVar (cm)	0.97319	PawPlacementPositioning[PPP] (cm)	1.0083
		Paw Angle Variability (deg)	0.95242		
		StrideLength (cm)	0.77828		
		Stride (s)	0.76953		
		MIN dA/dT (cm^2/s)	0.73519		

.

Notably, important variables such as paw area at peak stance in sq. cm, max dA/dT, and several temporal features (such as %propel stride, %brake stance) which were selected in the three-group discrimination model (Section 6.3.1.3) consistently appear in the two-group right limb comparisons (

30ºTO group vs sham group ((Q2 =0.56)	VIP scores (Comp.1)	30ºTO group vs treatment group (Q2 =0.79)	VIP scores (Comp.1)	Sham group vs treatment group (Q2 =0.22)	VIP scores (Comp.1)
Paw Area at Peak Stance in sq. cm (cm2)	2.2333	Paw Area at Peak Stance in sq. cm (cm2)	1.9265	%PropelStance (%)	2.0785
Paw Area (cm2)	2.2333	Paw Area (cm2)	1.9265	%BrakeStance (%)	2.0785
MAX dA/dT (cm^2/s)	2.1798	MAX dA/dT (cm^2/s)	1.8441	%BrakeStride (%)	1.9786
Paw Width (cm)	2.1018	Paw Width Variability	1.6728	Gait Symmetry	1.9497
Paw Length (cm)	1.6727	Paw Length (cm)	1.5123	Brake (s)	1.8849
AFI (real#)	1.5864	%PropelStride (%)	1.4757	AFI (real#)	1.4903
Stance (s)	1.3393	Ataxia Coefficient	1.3056	Overlap Distance (cm)	1.4843
Paw Width Variability (cm)	1.286	Brake (s)	1.2954	Swing Duration CV (CV%)	1.4289
Propel (s)	1.1486	%PropelStance (%)	1.2884	Tau – Propulsion (s)	1.3201
%StanceStride (%)	1.037	%BrakeStance (%)	1.2884	Stride Length CV (CV%)	1.2593
%SwingStride (%)	1.037	Swing (s)	1.2601	%PropelStride (%)	1.2334
Stance/Swing	1.0359	%BrakeStride (%)	1.2209	Midline Distance (cm)	1.2287
		Stance/Swing	1.139	SLVar (cm)	1.2069
		Midline Distance (cm)	1.1301	Ataxia Coefficient	1.183
		%SwingStride (%)	1.0879	TFI	1.1404
		%StanceStride (%)	1.0879	SFI	1.1302
		Paw Width (cm)	1.0666	Paw Length Variability (cm)	1.0787
		Stride Length CV (CV%)	1.0632	StrideLength (cm)	1.0514
		Axis Distance (cm)	1.0334	Stride (s)	1.0377
		SLVar (cm)	0.97319	PawPlacementPositioning[PPP] (cm)	1.0083
		Paw Angle Variability (deg)	0.95242		
		StrideLength (cm)	0.77828		
		Stride (s)	0.76953		
		MIN dA/dT (cm^2/s)	0.73519		

). These parameters are considered highly sensitive markers in the comparison of the right limbs. However, the top contributory variables differ in the comparison between the sham group and the treatment group, with more variables related to temporal features.

30°TO group vs sham group ((Q^2 =0.56)	VIP scores (Comp.1)	30°TO group vs treatment group (Q^2 =0.79)	VIP scores (Comp.1)	Sham group vs treatment group (Q^2 =0.22)	VIP scores (Comp.1)
Paw Area at Peak Stance in sq. cm (cm^2)	2.2333	Paw Area at Peak Stance in sq. cm (cm^2)	1.9265	%PropelStance (%)	2.0785
Paw Area (cm^2)	2.2333	Paw Area (cm^2)	1.9265	%BrakeStance (%)	2.0785
MAX dA/dT (cm^2/s)	2.1798	MAX dA/dT (cm^2/s)	1.8441	%BrakeStride (%)	1.9786
Paw Width (cm)	2.1018	Paw Width Variability	1.6728	Gait Symmetry	1.9497
Paw Length (cm)	1.6727	Paw Length (cm)	1.5123	Brake (s)	1.8849
AFI (real#)	1.5864	%PropelStride (%)	1.4757	AFI (real#)	1.4903
Stance (s)	1.3393	Ataxia Coefficient	1.3056	Overlap Distance (cm)	1.4843
Paw Width Variability (cm)	1.286	Brake (s)	1.2954	Swing Duration CV (CV%)	1.4289
Propel (s)	1.1486	%PropelStance (%)	1.2884	Tau – Propulsion (s)	1.3201
%StanceStride (%)	1.037	%BrakeStance (%)	1.2884	Stride Length CV (CV%)	1.2593
%SwingStride (%)	1.037	Swing (s)	1.2601	%PropelStride (%)	1.2334
Stance/Swing	1.0359	%BrakeStride (%)	1.2209	Midline Distance (cm)	1.2287
		Stance/Swing	1.139	SLVar (cm)	1.2069
		Midline Distance (cm)	1.1301	Ataxia Coefficient	1.183
		%SwingStride (%)	1.0879	TFI	1.1404
		%StanceStride (%)	1.0879	SFI	1.1302
		Paw Width (cm)	1.0666	Paw Length Variability (cm)	1.0787
		Stride Length CV (CV%)	1.0632	StrideLength (cm)	1.0514
		Axis Distance (cm)	1.0334	Stride (s)	1.0377
		SLVar (cm)	0.97319	PawPlacementPositioning[PPP] (cm)	1.0083
		Paw Angle Variability (deg)	0.95242		
		StrideLength (cm)	0.77828		
		Stride (s)	0.76953		
		MIN dA/dT (cm^2/s)	0.73519		

Table 6-7: Gait feature selection (VIP > 1) in different components from the PLS-DA model for pairwise discriminatory separation between the 30°TO group, sham group, and treatment group in the right limb. The features are listed and ranked in descending order based on their VIP scores of component 1.

a

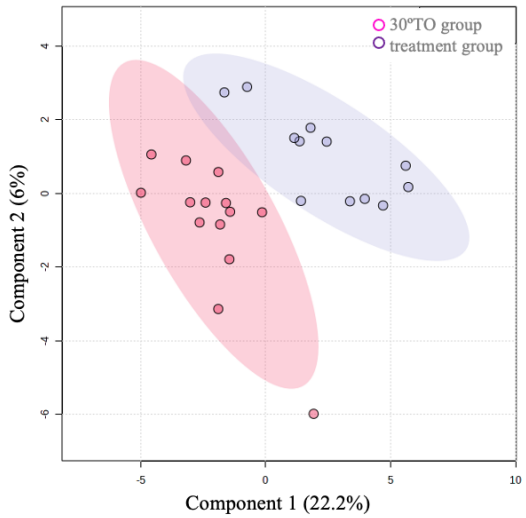

b

Measure	1 comps	2 comps	3 comps	4 comps	5 comps	6 comps
Accuracy	0.79667	0.74667	0.82	0.86	0.91	0.95
R^2	0.57152	0.84176	0.92515	0.95883	0.97451	0.97843
Q^2	0.35134	0.48044	0.70025	0.75671	0.76948	**0.78569**

Figure 6-8: PLS-DA model for discriminatory separation between right limb 30ºTO group and treatment group (best quality among all comparison) (a) 2D scores plot of the PLS-DA model illustrating class separation between two groups. (b) Cross validation: the model with 6 components is the optimal model for discriminatory separation.

6.3.3 Discriminate analysis between two treatment groups

This section aims to investigate whether the BMP treatment group and the APS treatment group can be effectively discriminated from all groups and to select the most important (contributory) variables. In Figure 6-9, PLS-DA was utilized to construct the predictive model. However, the predictive capability of the model is low (Q^2 <0.4.), indicating that the model is less effective to predict the sample's category based on the variation between current variables.

As mentioned in the methods (section 6.2.4), although there is no distinct discrimination, variables with a VIP value greater than 1 still significantly contribute to explaining the discrimination based on existing data. The most important (contributory) variables remain the paw area at peak stance and max dA/dT, consistently showing significant contributions across all discrimination models.

a

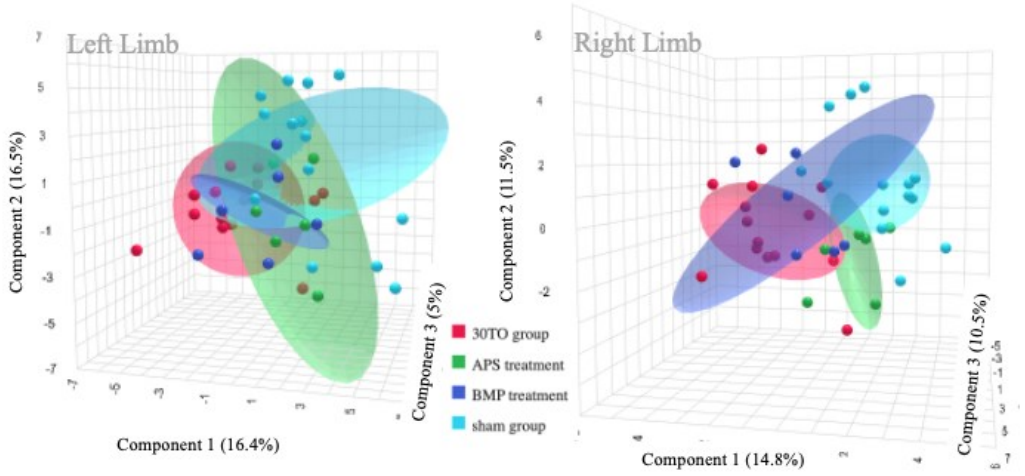

b

Measure	1 comps	2 comps	3 comps	4 comps	5 comps	Measure	1 comps	2 comps	3 comps	4 comps	5 comps
Accuracy	0.52778	0.61071	0.62579	0.7496	0.77817	Accuracy	0.525	0.565	0.65667	0.68167	0.665
R^2	0.45664	0.63086	0.7956	0.83557	0.86793	R^2	0.53288	0.73892	0.79754	0.8501	0.87864
Q^2	0.20932	0.28366	0.27547	**0.30732**	0.24748	Q^2	0.25082	0.39374	**0.3947**	0.31239	0.32854

Figure 6-9 PLS-DA model for discriminatory separation and cross-validation: sham (0ºTO) group, 30ºTO group, and 30ºTO group with BMP treatment or with APS treatment a. 3D scores plot of PLS-DA left limb model illustrating class separation between four groups. The coloured region displays the 95% confidence region. b. PLS-DA Cross-validation details: Q^2 <0.5 indicates the model lack effective predictiveness.

As described in the methods, Hierarchical Clustering is utilized in this study to illustrate the distance between groups when the PLS-DA plot does not effectively separate the groups. Subsequently, all variables were used for Hierarchical Clustering to group samples based on similarity, employing Euclidean distance as the measure of similarity. In Figure 6-10, it is observed that in the left limb, the samples from the 30ºTO group and sham group are clustered and separated from the other two groups.

The BMP and APS treatment groups are close to the sham group but cannot be distinctly clustered. In the right limb, the 30ºTO group is distinctly clustered but other three groups are mixed.

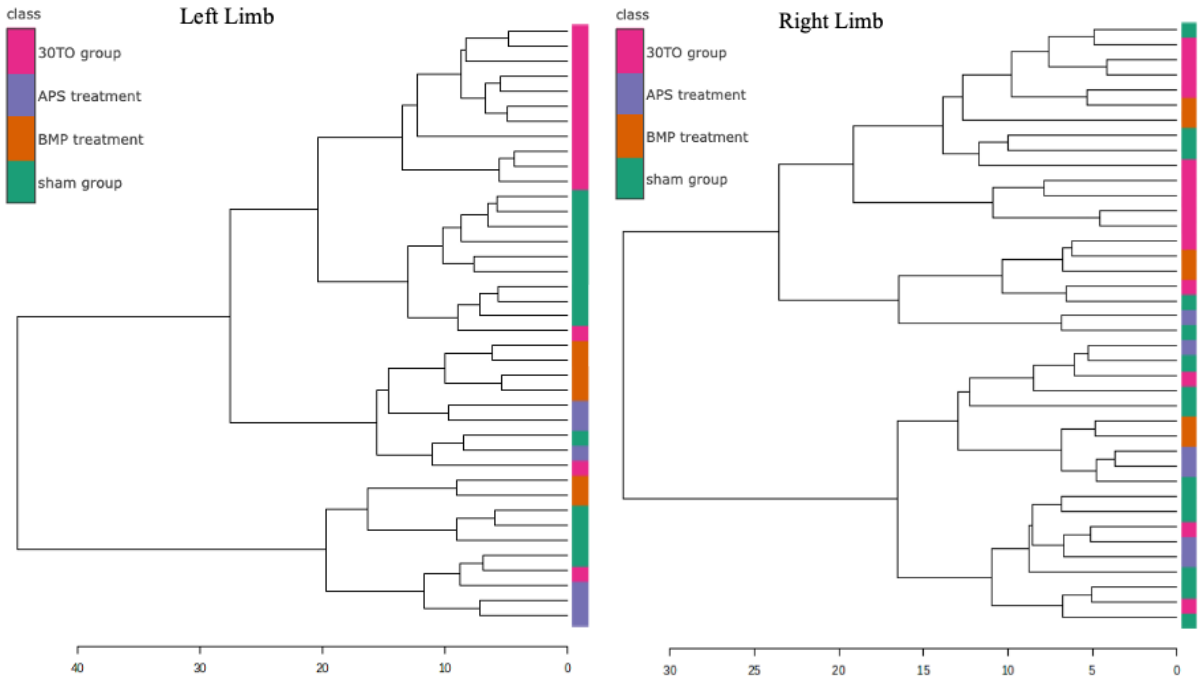

Figure 6-10: Hierarchical clustering dendrogram of the sample dataset for all groups. The samples are color-coded into four categories, the distance measure between branches indicates the level of dissimilarity between clusters; longer branches suggest greater dissimilarity, meaning the groups are less closely related.

To simplify the data and enhance clarity in group separation, only the important variables (VIP > 1) identified by the PLS-DA model were selected. The average values of each variable within each group were utilized to perform Hierarchical Clustering for the four groups. In the simplified model, the dendrogram shows that the 30ºTO branch is independent of the other three groups, with the Sham and 30ºTO groups showing the greatest difference (the farthest distance), and among the two treatments, APS is closer to Sham, as seen from Figure 6-11 and Figure 6-12.

The treated groups are in the same branch as the healthy group, with the APS group being closer to the sham group than the BMP group. This suggests that APS treatment may be more effective than BMP, particularly in recovering the gait coordination features. Furthermore, considering the intergroup differences and biological relevance, the study analysed the BMP-treatment group and the APS treatment group as a whole (called "30ºTO-treatment group") to simplify the model's complexity in Section 6.3.1, comparing them with the 30ºTO group (OA-affected gait) and Sham group (healthy gait).

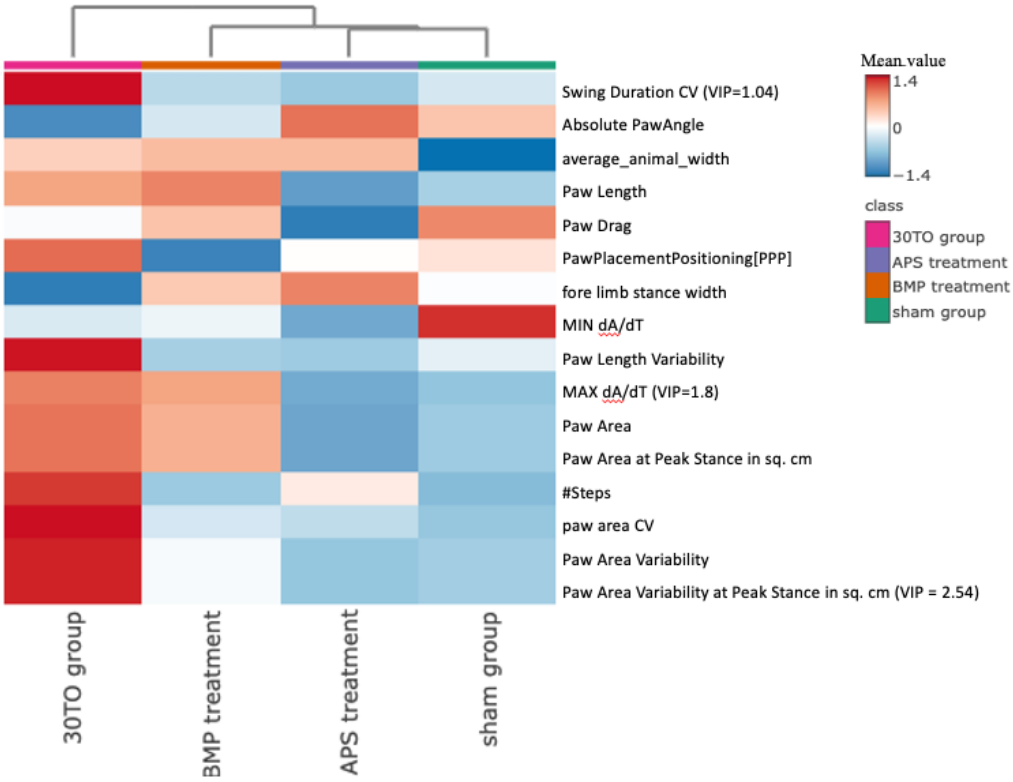

Figure 6-11. Hierarchical clustering heatmap of the **left limb** sample dataset for all groups (using the average value of each variable for each group). The samples are color-coded into four categories, with their classification displayed in the dendrogram. The colour gradient (from blue to red) represents the scaled value of the variables, ranging from low to high. The variables shown are the important variables (VIP > 1) identified by the PLS-DA model, arranged in ascending order of importance.

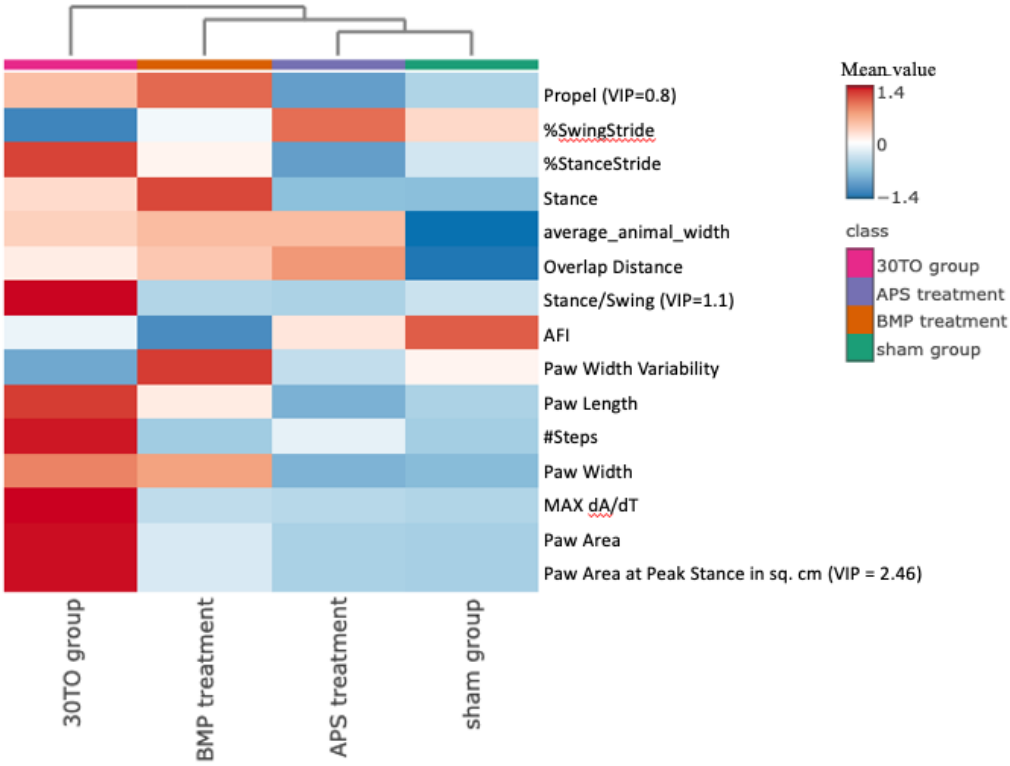

Figure 6-12. Hierarchical clustering heatmap of the **right limb** sample dataset for all groups (using the average value of each variable for each group). The samples are color-coded into four categories, with their classification displayed in the dendrogram. The colour gradient (from blue to red) represents the scaled value of the variables, ranging from low to high. The variables shown are the important variables (VIP > 1) identified by the PLS-DA model, arranged in ascending order of importance.

Additionally, PLS-DA analyses were conducted between these two treatment groups: the BMP-treatment group and the APS-treatment group. There is effective discrimination between the two groups in the left limb (Q^2=0.75), while in the right limb, they almost merged (Q^2= -0.05) (Figure 6-13a). In this comparison, the top contributory variables are different from the three groups PLS-DA in Section 6.3.1 and four groups' PLS-DA model in Section 6.3.3, with more variables related to gait coordination, such as Axis Distance, TFI, SFI, and AFI, ranking higher and providing more contribution in the discrimination model Table 6-8.

a

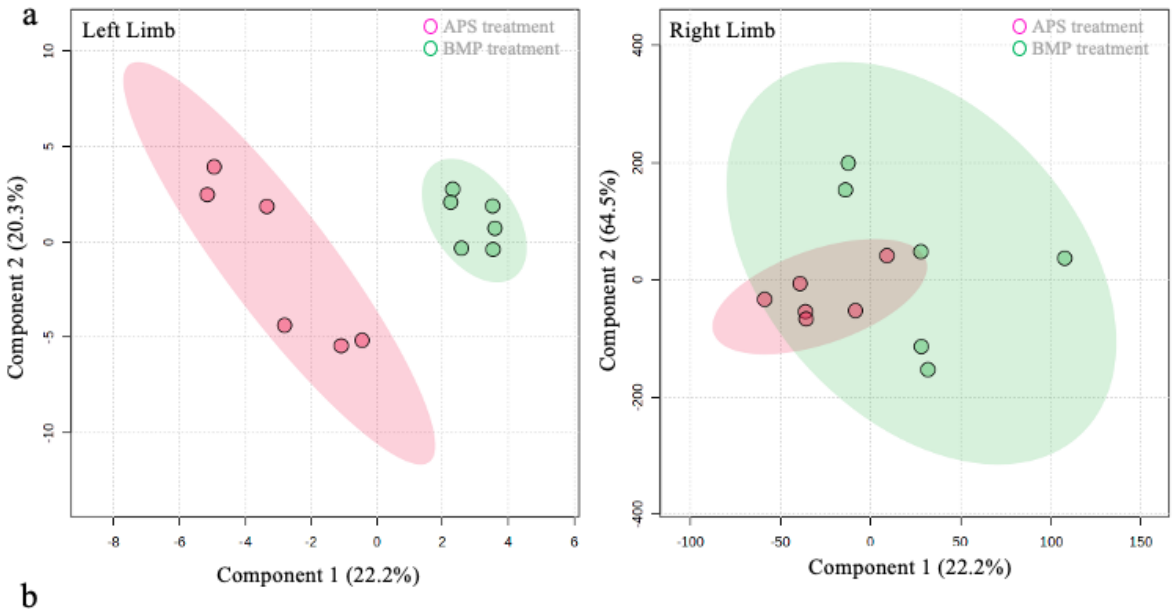

b

Left Limb

Measure	1 comps	2 comps	3 comps	4 comps	5 comps	6 comps	7 comps	8 comps
Accuracy	0.86667	0.93333	0.93333	0.93333	0.93333	0.93333	0.93333	0.93333
R^2	0.8345	0.96293	0.98838	0.99711	0.99948	0.99991	0.99997	1.0
Q^2	0.38466	0.55696	0.6551	0.68241	0.71289	0.73166	0.74605	**0.7468**

Right Limb

Measure	1 comps	2 comps	3 comps	4 comps	5 comps
Accuracy	0.625	0.625	0.75	0.875	0.75
R^2	0.42863	0.5127	0.7397	0.79821	0.81615
Q^2	-0.71325	-0.058349	-0.57952	-0.78166	-3.2599

Figure 6-13 PLS-DA model for discriminatory separation and cross-validation: BMP treatment group versus APS treatment group a. 2D scores plots of PLS-DA illustrating class separation between two groups for each limb. The coloured region displays the 95% confidence region. The two groups in the left limb are clearly separated, whereas they appear merged in the right limb. b. PLS-DA Cross-validation details: The left limb model demonstrates good quality with clear separation between groups. However, in the right limb model, the two groups lack effective predictiveness with a negative Q^2 value.

Contributory variables (Comp.1)	VIP Score	Contributory variables (Comp.1)	VIP Score
Axis Distance	1.8132	AFI	1.3515
Paw Length	1.7284	Stride Frequency	1.2735
PawPlacementPositioning[PPP]	1.6128	Paw Drag	1.1787
Paw Area at Peak Stance in sq. cm	1.5602	Paw Width Variability	1.122
Paw Area	1.5602	Swing	1.114
MAX dA/dT	1.5349	hind limb stance width	1.0962
TFI	1.5078	StanceWidth	1.0527
SFI	1.5023	Paw Area Variability at Peak Stance in sq. cm	1.0379
StrideLength	1.4606	Paw Area Variability	1.0379
Stride	1.4535	Stride Length CV	1.0319
SWVar	1.4248	Ataxia Coefficient	1.0287
Stance Width CV	1.3637	Gait Symmetry	1.0174

Table 6-8. Gait feature selection from the PLS-DA model for discriminating between the BMP treatment group and the APS treatment group in the left limb. The features with significant variable importance (VIP score > 1.0) in the first component are listed in descending order.

6.4 Discussion

This chapter analysed changes in gait features among rats with osteoarthritis (OA) and following pharmacological treatment. The discrimination model effectively differentiated between impaired and healthy gait in both limbs. However, it did not accurately classify treated versus OA-affected gait in the left limb, and treated versus normal gait in the right limb, as detailed in Sections 6.3.1 and 6.3.2. This indicates that gait in the left limb did not completely return to normal post-treatment, unlike the right (contralateral) limb.

Several gait features with significant variable importance were identified in Section 6.3.1.2. It was noted that both limbs possess important (contributory) variables in the gait coordination and paw feature (weight support) categories, with the right limb showing more pronounced differences. This suggests compensatory changes to the unaffected limb in weight distribution and support in quadrupeds. Among these variables, Paw Area at Peak Stance and Max dA/dT were consistently the most contributory variables across all discrimination models for both limbs. The study also observed differentiation between the two treatment groups, with the APS group exhibiting a closer similarity to the sham group, potentially indicating greater effectiveness in restoring gait coordination features (Section 6.3.2.2).

These results align with micro-CT and histological findings in characterizing group characteristics in OA and post-treatment conditions. Although these measures were not as sensitive in differentiating early-stage OA (10º TO group), these gait discrimination models, along with the identified gait features, are promising to serve as measurement tools for assessing the gait disturbances and progressive stage OA, and monitoring the effectiveness of treatments in rodent models in future studies.

6.4.1 Further explanation of the contributory gait features in the discrimination model

The contributory variables, particularly enriched in the gait coordination features category (such as Max dA/dT, paw placement positioning, midline distance) and paw features category (related to weight support, like paw area at peak stance, paw width variability), were found to be important (VIP>1) across all inter-group comparisons (Sections 6.3.1, 6.3.2, and 6.3.2.2) in both the left (Table 6-6) and right limbs (Table 6-7). Paw Area Variability, Paw Area at Peak Stance, and Max dA/dT emerged as the most contributory and consistent measurements. Notably, specific temporal markers showed importance exclusively in the right limbs.

Firstly, our study confirmed that OA can lead to changes on **paw area** related features, including Paw Area at Peak Stance, Paw Area Variability, and Paw Area Variability at Peak Stance. The change in paw area is a direct consequence of a shift in weight loading, with the non-OA areas bearing more weight to reduce pain. Rats experiencing chronic pain exhibit changes in the size of their fore and hind paws, with a reduced area in the rear paw and an increased area in the fore paw, although these changes are not pronounced (Coulthard et al., 2002). In our study, there was a significant increase in paw area (at peak stance) in the 30ºTO group in both hind limbs. The increase in paw area aims to enhance stability and balance by enlarging the contact surface with the ground. This adjustment can also be explained by changes in posture and tibia morphology in the left limb, characterized by a greater bending force, as detailed in the Chapter 5 Figure 5-21. After 30ºTO surgery, the rats adopted a lower incline forward position, with the centre of gravity shifting forward and downward. This shift explains the increased hind paw area, reduced swing time, and increased stance time in the 30ºTO surgery group (though these temporal features are not consistently important in all comparisons). **Paw Area Variability** has rarely been reported in gait studies. However, the measurement of paw area variability was found to be more sensitive (in left limbs) compared to measurements of paw area alone. It is observed that in the 0ºTO (sham) group, the paw area remains relatively consistent with each step. In contrast, in the 30ºTO group, tibia misalignment and OA appear to trigger a significant increase in paw area variability.

Secondly, the findings reveal **gait coordination features** (such as Max dA/dT, paw placement positioning, midline distance) substantially contribute to gait discrimination across all models, in OA rats and following treatment. A consistent increase in **Max dA/dT** was noted, which calculates the maximum rate of change of paw area in contact with the treadmill belt during the braking phase (initial stance time) (Figure 6-1). This result suggests that the left (OA) limb in 30ºTO surgery group undergoes rapid acceleration and deceleration when loading the limb on the treadmill. This can be explained through the pathomechanics of OA initiation discussed in Chapter 7. Rapid mechanical loading changes can produce excessive shear or tensile strains in the cartilage, leading to damage to the fibrous matrix. However, this novel parameter has not been discussed in the context of any disease in published data.

The measurement of dA/dT might potentially correlate with the rate of force development (RFD), a factor that has recently attracted attention in human gait studies. RFD (dF/dT) measures the capability of rapidly increasing force or torque during a voluntary contraction, reflecting the level of explosive muscle strength. It is calculated using the force or torque-time curves recorded during explosive voluntary contractions (Maffiuletti et al., 2016). As acquiring force data directly from the current treadmill is challenging, a separate study could be designed to examine the functional to focus on studying the functional relationship between force and paw area. This will help further understand how the metric dA/dT reflects changes in muscle strength and OA stages using data from the Digigait treadmill. For humans, a recent clinical study has confirmed that patients with severe knee OA would have a significantly reduced quadriceps RFD compared to those with early-stage knee OA, and the reduction in RFD is greater than the reduction in maximum quadriceps strength (Suzuki et al., 2022).

Paw placement positioning, which measures the extent of overlap between ipsilateral fore and hind paws during full stance, is typically minimal, close to zero if forelimb and hind limb stance widths are nearly equal. In OA animals, it increases, indicating that the width of the hind limbs during stance significantly exceeds that of the forelimbs, and it decreases after treatment, with APS treatment more closely resembling normal. Mechanically thinking, this increase can be explained by tibial malalignment in OA rats inducing a varus gait, which is adjusted for by the hind limb moving further laterally during gait, to try to minimise this overload on the medial compartment of the knee joint. Consequently, it is also observed that the forelimb stance width is reduced in OA rats to develop compensatory mechanisms to maintain balance and stability. The relationship between OA and gait coordination is clinically significant, as clinical studies have confirmed that patients with knee OA shows altered coordination patterns, increased coordination variability, and unstable motor control of the lower limb during walking (Wang et al., 2021).

Furthermore, other gait coordination parameters, such as TFI and SFI, rank higher and provide more contribution in the discrimination model between two treatment groups. These are equations based on multiple linear regression analysis originally developed to assess functional recovery after tibial or sciatic nerve injury. However, they can also be used to assess gait symmetry in this OA study. For instance, the equation for the Sciatic Function Index includes factors like paw width, paw length for each hind limb, and the distance between the 2nd and 4th toes. The prominence of these features in the discrimination model indicates that APS treatment is more effective in recovering gait coordination features than BMP treatment.Essentially, alterations in gait paw features (weight support) and gait coordination can be attributed to **compensatory mechanisms** adopted by the body to maintain mobility in OA and perhaps to unload the overloaded medial compartment, thus overloading the non-affected (right) limb. The compensatory mechanisms include: (1) The **right limb** (contralateral non-surgery hind limb) exhibited more significant inter-group differences for the same parameters than the left limb. This can be explained by OA-induced left joint pain and stiffness leading to compensatory gait patterns to

minimize discomfort. Thus, the right limb shows more distinct variations for the same variables compared to the left limb. As OA progresses, the degradation of joint cartilage and changes in joint structure can impair the function and range of motion of the affected limb, disrupting the overall coordinated gait. (2) Some specific parameters (temporal features) were only contributory to the contralateral (right) limb's gait results. Following treatment, there was an increase in swing time, %Brake Stance, and a decrease in %Propel Stance. A shorter braking phase in the OA gait indicates that the right limb rapidly decelerates motion during the initiation of the stance phase. Conversely, post-treatment, a longer braking phase suggests improved control and distribution of loading during stance, potentially leading to a reduced peak load. A longer %Propel Stance in the OA gait indicates that the right limb slowly accelerates motion to maintain forward movement. Following treatment, a shorter braking phase could imply increased strength and improved limb control. (3) Additionally, changes in gait were also detected in the **left forelimb**, specifically a decreased paw stance width, highlighting the importance of compensatory gait measurement in rodent gait analysis. Human studies show that pain avoidance can lead to long-term compensatory mechanisms, even after pain elimination (Farquhar et al., 2008). This phenomenon can be explained by the significantly longer swing time and decreased paw area observed in the OA group, which might result in a higher contact area when using the forelimb and consequently lead to a significantly decreased paw stance width in the forelimb. This increased reliance on the forelimbs may result in further atrophy of the hind limbs due to disuse (Farquhar et al., 2008). These findings underscore the importance of further studies analysing weight loading and gait changes considering all four limbs in quadrupeds, rather than focusing solely on the disease-affected limb.

6.4.2 Gait pattern changes depending on the model used to induce OA

Following the observed variability of gait patterns depending on this OA model, a review of current gait analysis studies using animal models to investigate OA-associated gait changes was conducted. The results of these studies vary, with limited consensus on the specific gait changes observed in OA models. Some studies, which induced OA using the MIA model, reported slower swing speed and longer swing time in the ipsilateral (target/injured/OA) limb compared to the contralateral (healthy) limb (Ferland et al., 2011b). Another study showed an imbalance in swing speed and contact area between the ipsilateral and contralateral limbs three weeks after MIA injection, with morphine rectifying the gait imbalance (Ishikawa et al., 2014). Additionally, the Limb Idleness Index (LII), calculating the combination of contact print area and swing duration ratios between the target side and contralateral side, showed significant differences between ACLT and sham groups six months post-surgery (Fu et al., 2012). In a repetitive loading-induced OA model, significant gait changes were observed only in the contralateral limbs, including increased stance time, stride time, stride length, and paw area from the second week after loading (Poulet et al., 2015). However, other studies reported that mice did not develop gait impairment up to eight weeks after destabilization of the medial meniscus (DMM) surgery-induced OA

(Malfait et al., 2010) and no difference between limbs in the ACLT model was noted (Ferland et al., 2011a).

Therefore, it is concluded that gait changes are more challenging to observe in biomechanically-induced OA models compared to chemically-induced OA models. This might be because the gait changes observed in the MIA model are primarily associated with pain, complicating the interpretation of whether the changes result from injury pain, OA pain, or altered joint biomechanics (Gerwin et al., 2010). Biomechanical models, on the other hand, involve a more moderate mode that requires longer periods to observe significant changes.

A review highlighted the heterogeneity of OA models concerning gait changes (Little and Zaki, 2012a). Currently, most gait analyses in animal models studying OA focus on OA pain behaviour, a symptomatic change, differing from those used to investigate OA's pathophysiology. In pathophysiology studies, models should ideally reflect natural structural joint damage. Thus, the initiation events are based on OA risk factors such as joint injury, aging, and sex. Conversely, many OA gait studies use chemically-induced models to trigger rapid chondrocyte apoptosis and joint pain (Lakes and Allen, 2016). Despite their effectiveness in studying pain outcomes, these models may not accurately reflect true OA changes. The fundamental cause of gait pattern changes is not merely inflammation-induced pain but the structural joint damage-induced instability (Hunter et al., 2013) and the regulatory mechanisms of cartilage erosion (McNamee et al., 2010). Unfortunately, very few gait studies have been conducted in biomechanically induced models. From the publish data working on biomechanical induced models, the gait changes after OA-induction are not very significant (Malfait et al., 2010), or can only be observed in the contralateral limb (Poulet et al., 2015). One study compared different models within the same lab and found different gait outcomes between the MIA and ACLT models (Ferland et al., 2011a).

Therefore, it is crucial to consider data from different preclinical models for precise translation into different subtypes of human OA (described in Chapter 1) (Dell'Isola et al., 2016). The chemically induced model, such as the MIA and carrageenan-induced arthritis models, present the inflammation-related OA phenotype, present stronger gait changes due to the strong relationship between OA pain and inflammation, which subsequently results in gait pattern changes (Dorman et al., 2014, Berryman et al., 2009a). Biomechanically induced animal models, which presented mechanical overloading phenotypes of OA, (as described in chapter 1, section 1.5.1) can subtyped to the 1) “primary” mechanically induced slow/progressive OA, where the chronic overloading OA is naturally occurring after long-term lower levels of increased loading (mechanical overuse), the gait changes are present in our study. 2) “secondary” PTOA after the acute high impact or trauma, above mentioned DMM and ACLT models are presented the gait data in the clinical phenotype (Malfait et al., 2010, Ferland et al., 2011a). It is important to note that chemically induced OA models might not be regarded as "true" OA models since they do not reflect real OA pathogenic changes, as described in Chapter 1, Section 1.5.1. Nonetheless, these chemical injection models, being less severe and offering high success rates, act as convenient

models for the preliminary development of gait measurements. These measurements can then be reliably utilized in more complex, surgically induced models that more closely resemble the real progression of OA, for additional validation and research.

6.4.3 Correlation of gait pattern changes with joint structural changes

Following the comparison of spatiotemporal data, a crucial aspect emerges: the correlation between gait pattern changes and joint structural changes, particularly in relation to subchondral bone damage result in micro-CT data in Chapter 5. At present, there is a scarcity of literature exploring this correlation in animal models. This study hypothesizes that changes in the subchondral bone may initially cause pain, subsequently leading to alterations in gait. This hypothesis is based on the theory that vascular growth in the subchondral bone during endochondral ossification may result in pain (Mapp and Walsh, 2012). This opens the way for gait analysis to be linked to microstructural joint damage, macro joint morphology changes, and ultimately, the pathogenesis of the disease.

Clinical data have provided some insights into structural changes associated with pain, which may indirectly elucidate the correlation between "micro bone changes" and gait pattern changes. MRI studies, for instance, have identified pathological changes, such as bone marrow lesions and synovitis, showing a strong correlation with pain symptoms (Hunter et al., 2013). Histopathological investigations have revealed increased angiogenesis in the subchondral bone (Mapp and Walsh, 2012). The presence of new vascular channels containing osteoclasts, osteoblasts, and growth factors breaching from the subchondral bone into the cartilage can stimulate inflammation, nerve growth, sensitization, and endochondral ossification (Suri and Walsh, 2012). Angiogenesis in the subchondral bone has been suggested as an indicator of OA pain (Ashraf et al., 2011a), providing a new avenue for understanding the relationship between structural changes and pain-induced gait changes.

Another issue is the translatability of gait results from animals to humans, questioning whether findings in this animal OA model can be applied to human OA conditions. This challenge is common in animal gait studies. The discrepancies between outcomes in preclinical animal studies and clinical human studies are not only due to differences in gait patterns between species but also because the model may not adequately reflect the molecular mechanisms or symptoms of human OA. Consequently, assessing the translatability of these gait data to human conditions remains a significant challenge at this juncture. The TO model used in this study is considered an optimal choice for effectively representing human OA pathology. Nevertheless, it requires further refinement to improve the translational relevance of gait outcome from this model. This includes a deeper exploration of the complex relationship between gait patterns and joint structural changes and enhancing gait measurements to more accurately reflect human OA condition.

Overall, this chapter establishes that TO-induced OA in rats results in marked gait alterations that can be quantitatively evaluated using specific gait metrics. It is evident that, while normal and OA-affected

gaits can be differentiated in both limbs, pharmacological interventions fail to fully restore the gait parameters to their normal state in the affected limb, indicating persistent abnormalities. A trend toward recovery is observed in the unaffected limb, suggesting the presence of compensatory mechanisms. Features such as paw area at peak stance and max dA/dT have emerged as consistent biomarkers across all comparisons, along with the discriminatory models, showing potential for future assessments of OA and the testing of novel therapeutics in rodent models. The discussion highlights the challenges involved in correlation between different scale results and translating findings from animal models to human conditions.

7 Untargeted LFQ-MS proteomics approach in characterising OA cartilage and serum changes

7.1 Summary

The aim of this chapter is to provide an in-depth analysis of differentially expressed proteins and their enriched biological processes across early and progressive stages of osteoarthritis (OA), in the 30°TO mechanically induced OA model, and to evaluate the effects of pharmacological treatments with BMP and APS. By confirming significant molecular alterations due mechanically induced OA, the chapter highlights key biological processes such as collagen formation, ECM degradation, endochondral ossification, inflammation, and metabolic changes. Furthermore, it is revealed that BMP and APS treatments modulate these processes through activation of different pathways, potentially reversing mechanical stress-induced remodelling and contributing to cartilage and bone homeostasis. Changes in these protein expressions, are likely linked to joint cartilage degradation (Chapter 4), structural alterations (Chapter 5), and gait pattern alternations (Chapter 6), in response to altered mechanical loading and OA progression. Compared to those macro-level measurements, proteomics provides a better understanding of the underlying mechanisms in the occurrence, progression, and reversal of OA, and in distinguishing the effects of BMP and APS treatments.

7.2 Introduction

As discussed in Chapter 1, Section 1.8.4, the identification of reliable biomarkers capable of detecting cartilage metabolism and inflammation is of paramount importance in OA research for assessing disease progression. One frequently mentioned and well-published biomarker is CTX-II, which has been investigated in both human (Meulenbelt et al., 2006a) and animal studies (Duclos et al., 2010a, Legrand et al., 2017). Type II collagen has also been considered an early indicator and an ideal surrogate for histological assessment in animal research (Legrand et al., 2017). However, a lack of consistency and absence of a gold-standard reference limit the use of these biomarkers in animal studies. Advances in proteomics and metabolomics techniques have facilitated the discovery of new OA biomarkers in human and animal studies (Parra-Torres et al., 2014c, De Sousa et al., 2017a), offering promise in enhancing the predictive capabilities of these tests.

It is commonly believed that most diseases have undergone some changes in the qualities and quantities of proteins before the clinical symptoms appear (Lescuyer et al., 2007). These proteins, which demonstrate relatively stable expression changes, are often referred to as disease "biomarkers". As this study focuses on mechanical stimuli rather than genetically driven changes, the investigation will concentrate on protein-level changes rather than the more complex gene-level changes. Accordingly,

proteomic methods are ideal for revealing global-scale protein-level alterations that can serve as references for OA onset and progression resulting from mechanical factors.

Mass spectrometry, an analytical method measuring the mass-to-charge ratio of ions, is frequently used in the diagnosis and treatment of protein-related diseases. It provides insights into qualitative and quantitative protein expression changes, serving as potential indicators of specific diseases (Lescuyer et al., 2007) (Anderson and Anderson, 1998) (Wysocki et al., 2005). However, the complexity of biological samples and the large dynamic range of protein concentrations challenge the full identification of components in a single analysis. Thus, an effective pre-separation step before mass spectrometry detection is critical. With the development of proteomics technology, liquid chromatography-tandem mass spectrometry (LC-MS) has emerged as a preferred technique in proteomic studies (Aebersold and Mann, 2016). Coupling high-performance liquid chromatography (HPLC) with mass spectrometry creates a highly automated system for the separation and identification of proteins and peptides (Mitulović and Mechtler, 2006).

Current research strategies in proteomic studies include the bottom-up method (qualitative proteomics) and the quantitative proteomics method (Chen and Pramanik, 2009). Bottom-up proteomics, which is based on mass spectrometry, is widely used for large-scale identification of unknown proteins, studying protein post-translational modifications, protein interactions, and the discovery and verification of disease biomarkers. This approach involves digesting complete protein mixtures into peptides, detecting the peptides using LC-MS, and matching the obtained fragmentation spectrum information with theoretical protein databases to identify peptide sequences (Zhang et al., 2013). Quantitative proteomics, on the other hand, aims to analyse the expression levels of proteins under different physiological or pathological conditions from a quantitative perspective (Chen and Pramanik, 2009) The peptides from different sources can be identified by the mass of the labelled peptides during the mass spectrometry scan. This enables accurate detection of protein expression in different states and absolute quantification of their abundance (Grossmann et al., 2010, Srivastava and Srivastava, 2005).

In this study, High-Performance Liquid Chromatography-Mass Spectrometry (HPLC-MS) was used with a label-free quantification (LFQ) approach for the proteomic analysis. This **semi-quantitative approach** opens up the possibility for identifying novel biomarkers exhibiting significant changes between experimental groups. Through the analysis of LFQ intensities, it is able to determine the relative abundance of proteins in biological samples within a single experimental round. This process provides valuable insights into the relative proteomic abundance alterations when comparing disease or treatment groups with control groups, without requiring a precise quantification of each individual marker. In the context of LFQ, the intensity refers to a protein's total non-normalized intensity (accounting for all peptides), divided by the number of measurable tryptic peptides. Protein intensities are then normalized to exclude outliers, thereby providing an accurate representation of ratio changes among the various

samples. This untargeted label-free quantification approach serves as an effective screening method to identify potential biomarkers for subsequent, more detailed investigation.

Based on the histological and micro-CT results presented in Chapters 4 and 5, the left limb in the 30°TO group exhibits osteotomy surgery-induced varus alignment (abnormal loading) and progressive-stage OA, while the right, no-surgery limb exhibits early-stage OA. Specifically, the varus alignment shifts the weight-bearing axis to the medial compartment of the knee, creating overloading and unloading conditions in the left knee. Comparisons can be made between the left lateral compartment (OA under unloading conditions) and the left medial compartment (OA under overloading conditions), as well as between the right (contralateral) lateral compartment (considered healthy cartilage) and the right medial compartment (considered early-stage OA).

Therefore, the aim of this chapter is to utilize this untargeted LFQ-MS proteomics approach to conduct a series of proteomic analyses, between the 30ºTO group, the 0ºTO (sham) group, and the treatment (BMP/APS) groups, as well as between their left and right limbs, lateral and medial compartments. This is to better understand the underlying molecular mechanisms in the occurrence, progression, and reversal of OA observed in histological (Chapter 4), imaging (Chapter 5) and gait (Chapter 6) evaluations. The second aim is to elucidate the molecular response to mechanical loading, and corelate it with the histological (Chapter 4) and imaging-level (Chapter 5) structural alterations, as well as gait pattern alterations (Chapter 6) in response to mechanical loading.

7.3 Methods

7.3.1 Sample collection

As described in Chapter 2, blood sample collection was conducted pre-operatively and monthly thereafter. Cartilage tissue was obtained at the end of the study after the rats had been sacrificed; these samples were used for LC-MS analysis.

In detail, the rat's tail was cleaned with warm water, and the rat was then placed in a 37°C incubator for 10 minutes, allowing the veins to become more visible. The rat was then restrained in a rodent restrainer. Half a millilitre (0.5 ml) of blood was collected from the caudal vein of each rat in a sterile environment using vacutainers at each visit. This blood was then centrifuged, and the serum was removed and stored in Eppendorf tubes in a 4 °C fridge for further sample processing. The samples were centrifuged at 1200g for 15 minutes. The serum was pipetted out and aliquoted into 50µl Eppendorf tubes. One aliquot was used immediately for LC/MS sample preparation, while the others were frozen at -80°C until needed. It has been demonstrated that long-term storage of plasma, with limited freeze/thaw cycles, does not significantly affect protein results in mass spectrometry (Mitchell et al., 2005).

For the harvesting of cartilage tissue, at week 20, following the sacrifice of the animal, the cartilage was cut into parallel strips from the weight bearing area of the tibia cartilage surface of each limb, medial and lateral compartment separately (Cicuttini et al., 2004, Folkesson et al., 2018). The strips were then snap-frozen in dry ice and stored at -80°C until subsequent protein extraction (Wilson et al., 2012).

7.3.2 Mass spectrometry sample processing

The label-free quantitation (LFQ) LC/MS proteomics method was used to analyze tissue (Vanquish HPLC, Thermo Fisher). The sample preparation steps for cartilage tissue followed general protocols outlined in recent literature (Dey et al., 2019, Wang et al., 2011, Wilson et al., 2012). The assay kits were all procured from Thermo Fisher. The steps included:

1. protein extraction and proteolysis: cartilage pieces were ground in lysis buffer and incubated overnight at 4°C. Afterward, the samples were centrifuged at 16,000g for 10 minutes, and the supernatant was collected; and
2. the 'EasyPep™ Mini MS Sample Prep Kit' was used for further trypsin digestion and stage-tip protocol.

After sample preparation, peptides, which are generally quite stable, were dried down in multi low adsorption plastic tubes in a vacuum freeze dryer and stored at −20 °C (Kraut et al., 2009).

7.3.3 Proteomics

Once the LC/MS schedule was confirmed, the sample was resuspended in 100 µl of 0.1% formic acid in water for LC-MS analysis. Samples were analysed with an LC column at a flow rate of 200 µl/min for separation, and a 3-hour gradient run in MS. Bovine serum albumin (BSA) control standards (Pierce™ BSA Protein Digest, Thermo Fisher) were routinely included in every run between every 3 samples to track the performance of the instrument.

7.3.4 Data processing

Protein identification and differential expression analysis were performed using the MaxQuant software package (Version 2.4.14.0, Max Plank Institute of Biochemistry, 2023), followed by Persure software (Version 2.0.11, Cox Lab, 2023) for comparing the relative amounts of proteins (LFQ ion intensity) between samples. Cluster analysis and biological pathway analysis were conducted based on the differentially expressed proteins.

A statistical method (Limma function in R 3.1.0) was used to identify genes encoding differentially expressed proteins between groups. Filtering identified proteins over-expressed or under-expressed by at least 2.0-fold, with p-values < 0.05 for comparisons between each group. Differentially expressed proteins were visualized using volcano plots in MetaboAnalyst (Version 6.0, McGill University, 2023)

and GraphPad Prism (Version 9.4.0, Dotmatics, 2022) . The DAVID homology tool (Sherman and Lempicki, 2009) and Gene Ontology (Ashburner et al., 2000) were used to assign molecular functions, biological processes, and cellular compartments to the identified proteins (Sherman and Lempicki, 2009).

Subsequently, protein enrichment pathway analysis was performed using functional clustering analysis of differentially expressed proteins (Metascape online software-v3.5, 2023)(Zhou et al., 2019), based on the Kyoto Encyclopedia of Genes and Genomes (KEGG), Reactome, or Gene Ontology databases. The significantly enriched pathways were summarized in a table to interpret the underlying biological mechanisms. The statistical methods used during the data processing are detailed in the following section (Section 7.3.5).

7.3.5 Statistical methods

Section 1: Calculation of the differential expression of proteins between the groups

As mentioned in the introduction, the label-free quantitation (LFQ) LC/MS proteomics method, a semi-quantitative approach used in this study, can only determine the relative abundance of proteins in biological samples within a single experimental round (max 12 samples in one round). Therefore, to maintain higher accuracy, comparisons between runs were avoided. It is not feasible to analyse all samples in one round or to compare every aspect of interest. Due to this limitation, the 30°TO (no treatment) group was analysed in the same rounds as the sham group for comparison. In characterizing the BMP-treated cartilage (Section 7.4.2), comparisons were made exclusively within BMP-treated group samples, specifically comparing left and right knees, medial and lateral compartments, excluding the sham group and the 30°TO (without treatment) group, as these were in different experimental rounds. A similar limitation in comparations applied to the APS-treated group (Section 7.4.3).

Differential expression of proteins between group comparations was calculated using the Limma function in R 3.1.0. This involved comparing various parameters, where the protein profile changes were represented by a general linear model for each protein. For instance, the log-ratios of protein “g” expression is $y_g = \log_2(R_g) - \log_2(G_g)$, where R_g and G_g are the protein expression levels in health and disease conditions, respectively.

The **Limma function** employs a general linear model approach, utilizing moderated t-statistics, moderated F-statistics, and log-odds of differential expression through empirical Bayes moderation of standard errors towards a common value. A simulation study by Smyth (2004) confirmed the robustness of this method, even with small sample sizes.

This function used the **empirical Bayes method** (eBays) to adjust residual variances of protein intensity between two groups towards a common value. The augmented degree of freedom for individual variances led to an increased power to detect differential expression, which was obtained from the

empirical Bayes moderation. This method can shrink the estimated sample variances towards a pooled estimate, resulting in far more stable inference when the number of arrays is small.

Given that fewer protein intensity replicates increase the variability, the eBayes step estimated the "average" variability over all proteins, adjusting down high variability proteins and adjusting up low variability proteins. The key steps are: 1) after obtaining the mean value of the two groups in "fit", the system estimated the overall distribution of the data (usually a beta distribution), and 2) this beta distribution was then used to represent the prior expectations for estimating each average.

The **moderated t-statistics** were used for calculating posterior odds statistics (posterior residual standard deviations), instead of the ordinary standard deviations. eBayes did not use ordinary (unmoderated) t-statistics because moderated t-statistics have better performance than the ordinary version. For each protein, a **contrast** was defined, which included the protein intensity value in 3 healthy samples and 3 disease samples. This set of contrasts was defined as the "fit" column in the R code, produced by the "LimFit" or "contrasts.Fit" function in R.

The **moderated t-statistics** are used to determine if the expression level of each protein (reflected as individual contrasts) significantly deviates from zero. In contrast, the **moderated F-statistic** assesses the collective null hypothesis that all contrasts across proteins are zero. This approach moderates the residual mean squares across genes, enhancing the reliability of statistical inferences. Although this method incorporates aspects of conventional ANOVA, such as t-statistics and F-statistics, it differs by applying empirical Bayes techniques to stabilize variance estimates, especially beneficial in studies with limited sample sizes.

"**Adjusted p-values**" were also computed after multiple comparisons to control the false discovery rate (FDR), which is commonly used in genomics and proteomics studies where many genes are tested simultaneously (Table 7-1). It included two steps: 1) individual ranks (ranking the mean difference between two groups) computed for each comparison after the t-test for each parameter, and 2) a two-stage linear step-up method (Benjamini et al., 2006) was applied targeting an FDR of 5%. Only genes with adjusted p-values ≤ 0.05 are considered statistically significant, ensuring that the overall rate of false positives (FDR) is kept at or below 5%. This yields a more conservative measure of significance, akin to the Benjamini-Hochberg correction method used in other circumstances. Hence, the differentiated proteins selected from the proteomics data for the subsequent pathway enrichment analysis are determined based on the adjusted p-value and log fold change (Log FC), depending on the specific requirements of each group's analysis.

The two-stage linear step-up approach first analyses the distribution of p-values to determine the proportion of null hypotheses that are accurate. Each parameter is then ranked based on its p-value. The adjusted p-value is calculated from p-value x rank, which leverages the p-value to enhance its ability to make a determination when a p-value is deemed insufficiently low to be considered a significant finding.

Table 7-1. Example of calculation of adjusted p-values

Gene	P-value	Rank	Adjusted p-value
Gene 1	0.080	5	=0.08*5/5=0.08
Gene 2	0.010	2	=0.01*5/2=0.025
Gene 3	0.002	1	=0.002*5/1=0.01
Gene 4	0.056	4	=0.056*5/4=0.07
Gene 5	0.034	3	=0.034*5/3=0.057

Section 2: Pathway enrichment analysis

Next, the differentially expressed proteins (selected from Section 1), were subjected to enrichment analysis for each comparison to identify biological pathways or processes significantly enriched with these proteins.

Statistical methods are used in this enrichment analysis. The first step involves **annotating the protein pathways**. Firstly, the proteins of interest, which are identified as differentially expressed between two conditions, are annotated using the Metascape analysis tool (Zhou et al., 2019). This tool matches the proteins to known biological pathways or processes, followed by mapping these annotations onto databases like the Kyoto Encyclopedia of Genes and Genomes (KEGG), Reactome, and Gene Ontology.

The next step is the **pathway enrichment analysis**. The Metascape tool identifies enriched pathways using a two-tailed Fisher's exact test to test the enrichment of the differentially expressed protein against all identified proteins. Specifically, this test compares the proportion of proteins of interest found in a specific pathway to the proportion expected by chance alone, considering the pathway's size and the total number of examined proteins. The statistical significance of pathway enrichment is determined using a p-value threshold of <0.05. Additionally, the pathways are classified into hierarchical categories according to the Metascape tool.

In the results section, each enrichment analysis (from each comparison of differentially expressed proteins) is listed in a table presenting the top potential pathways identified, ranked by the adjusted p-value of pathways enrichment. Pathways that exhibit representative biological processes related to OA are highlighted in red (

Table 7-4. Differentiated upregulated and down regulated genes (adjusted p-value < 0.05 and fold changes FC>2) when comparing the 30ºTO left knee (OA knee) with the 0ºTO left knee (healthy knee). The bolded genes are the top 10 with the most significant p-values.

Gene symbols	P value	group	Gene symbols	P value	group
Txndc17	2.07E-15	up	Vars	8.24E-07	down
Lypla2	2.72E-09	up	Gclm	2.93E-06	down
Rbm39	4.89E-09	up	Prep	2.66E-05	down
Psmb7	4.96E-09	up	Mgll	6.21E-05	down
Mtap	2.44E-07	up	Rras;Rras2	0.00011605	down
Nedd8	2.47E-07	up	Cd36	0.00031964	down

Acadm	9.83E-07	up	Plbd1	0.00031964	down
Pak2	9.83E-07	up	Tmpo	0.00032781	down
Atp6v1b2	4.65E-06	up	U2af2	0.00032923	down
Kif5b	7.92E-06	up	Eif3c	0.00046907	down
C5	8.04E-06	up	Rab2a	0.0011899	down
Txn2	1.09E-05	up	Ak3	0.00137563	down
Hdgfrp3	5.40E-05	up	Calu	0.00162574	down
D10Jhu81e	9.29E-05	up	Hsp90ab1	0.00170473	down
Mylk2	0.00011605	up	Flnb	0.00236575	down
Tuba1c;Tuba8	0.00023551	up	Pfkl	0.00314632	down
Crk	0.00032781	up	Cyb5r3	0.00460445	down
Prkacb	0.00038467	up	Slc25a11	0.00480434	down
Sephs1	0.00038467	up	Ap2s1	0.00496938	down
Ces1	0.00042352	up	Cfl1	0.00496938	down
Copе	0.00047049	up	Cotl1	0.00496938	down
Ppid	0.00054651	up	Psmd7	0.00525939	down
Sparc	0.00060884	up	Hnrnpc	0.00525939	down
Yars	0.0010528	up	Ehd2	0.00525939	down
Nit1	0.00170473	up	Lmna	0.0054498	down
Mybph	0.00191824	up	Suclg2	0.00557764	down
Col1a1	0.00239822	up	Acat1	0.00666657	down
Tpd52	0.00266218	up	Pea15a;Pea15	0.00666657	down
Adssl1	0.00303895	up	Mrc1	0.00666657	down
Rpe	0.00382914	up	Cilp	0.00666657	down
Rab5a	0.00393187	up	F13a1	0.00741743	down
Pdlim3	0.00401685	up	Gstp1;Gstp2	0.0075867	down
Txndc5	0.00460445	up	Ptbp1	0.0075867	down
Rrbp1	0.00461129	up	Psme1	0.00806975	down
Aldoa	0.00496938	up	Ube2l3	0.00809822	down
Tpi1	0.00521668	up	Methig1;mCG_20149;Mettl7a1;UbiE2;Mett l7a2	0.00813725	down
Rnh1	0.00525939	up	Glud1	0.00891487	down
Rpl8	0.00525939	up	Nap1l1	0.00973741	down
Adsl	0.00525939	up	Lmnb1	0.00985808	down
Capn1	0.00525939	up	Rtcb	0.00992345	down
H3f3c;H3f3a	0.00546061	up	Psmc5	0.01008918	down
Gm10320;Sec61b	0.00577054	up	Snx6	0.0104049	down
Col3a1	0.00645402	up	Psme2	0.01061846	down
Fscn1	0.006974	up	Lum	0.01066458	down
Fhl1	0.00809822	up	Rsu1	0.01093092	down
Got2	0.00823961	up	Tagln2	0.01102439	down
Nucb2	0.00906396	up	Ptrf	0.01102439	down
Col1a2	0.00992345	up	Lamc1	0.01106318	down
Tpm3	0.01008918	up	Etfa	0.01129435	down
Bin1	0.01061846	up	H2afy	0.01397084	down
Pygm	0.01061846	up	Hadhb	0.01397084	down
Ppp3ca;Ppp3cb	0.01061846	up	Cenpv	0.01397084	down
Gapdh;Gm3839	0.01292091	up	Ugdh	0.01426463	down
Myh8	0.01397084	up	Rap1b	0.01469834	down
Get4	0.01397084	up	Ap2b1	0.01596263	down
Tpm2	0.01397084	up	Rpn1	0.01605107	down
Pgm1;Pgm2	0.01397084	up	Cct8	0.01645979	down
Epb4.1l2;Epb41l2	0.01397084	up	Elavl1	0.01932009	down
Dynll1;BC048507;Dyn ll2	0.01416987	up	Phb	0.01951462	down
Sec13	0.01634264	up	Fbln1	0.02038648	down
Pkm	0.01932363	up	Hadha	0.02038648	down
Crabp2	0.01951462	up	Mapre1	0.0212615	down
Plod2	0.02426845	up	Ube2n	0.02248509	down
A2mp	0.02442485	up	Mvp	0.02321648	down
Cbr1	0.02676971	up	Tmed9	0.02323243	down
Ivd	0.02878361	up	Abhd5	0.0240549	down
Tceb1	0.03079792	up	Slc25a3	0.02426845	down
Ckmt2	0.03213418	up	Psmc2	0.02426845	down
Rpl14	0.0321724	up	Myh9	0.02426845	down
Eef1a2	0.03465496	up	Rpsa	0.02615636	down
Kars	0.03701331	up	Hsp90aa1	0.02620886	down
Blmh	0.03818193	up	Snd1	0.02692628	down
Pdgfrb	0.0403398	up	Atp2b1;Atp2b4;Atp2b3	0.03009483	down
Sorbs2	0.04336638	up	Uba1	0.03009483	down
Oat	0.04497057	up	Ppp2r1a	0.03165957	down
Zbed5;Chchd2	0.04764187	up	Ddx5	0.0321724	down
Myh4	0.04821126	up	Capza1	0.03321476	down
Tubb2a	0.04955647	up	Arpc4	0.03488554	down
Scrn1	0.05137905	up	Clu	0.03522974	down

	Aldh2	0.03598282	down
	Tns1	0.03701331	down
	Rps3	0.03701331	down
	Aoc3	0.03701331	down
	Glrx3	0.03701331	down
	Vps35	0.03802018	down
	Serpina3m;Serpina3k	0.0403398	down
	Capza2	0.04097764	down
	Blvrb	0.04174182	down
	Psmd12	0.04336638	down
	Atp5a1	0.04383393	down
	Arhgap1	0.04452513	down
	Psmb3	0.04576808	down
	Pdhb	0.04610957	down
	Angptl7	0.04715294	down
	Hnrnpm	0.04821126	down
	Rab5b	0.04821126	down
	Psmd3	0.04821126	down
	Nono	0.04821126	down
	Dusp3	0.04954178	down
	S100a6	0.05137905	down

Table 7-5). The "**Count**" column reflects the number of genes from the input list associated with each pathway or process. The "Gene symbols" column enumerates the identified genes enriched in each pathway or process. The "**Log P Value**" column displays the -log10 (p-value), where the adjusted p-values from the last step have been converted to -log10 (p-value) for easier visualization and interpretation, with values exceeding 1.30 indicating $p < 0.05$. The "**Term**" column denotes the serial number of specific biological processes or pathways as identified in databases.

7.4 Results

This section presents the biological pathways or processes that are significantly enriched with differentially expressed proteins in rat cartilage samples across various conditions of OA.

Initially, the section details the upregulated biological processes in the OA cartilage of the 30°TO group. It specifically evaluates the 30°TO-induced OA knee, including the left knee in the progressive stage of OA and the right knee in the early stage of OA, compared with the 0°TO sham group, where the cartilage remains in a healthy state (Section 7.4.1). The upregulated biological processes include collagen formation, extracellular matrix degradation, endochondral ossification, inflammatory-related process (e.g.,VEGFR2 signalling), and metabolic response. The summary results are listed in Table 7-2.

Subsequently, the analysis focuses on evaluating the upregulated biological processes in the left knee after pharmacological treatments within the 30°TO BMP-treated group (Section 7.4.2) and the 30°TO APS-treated group (Section 7.4.3). Within the 30°TO BMP-treated group, comparisons were conducted between the left lateral compartment (BMP-treated OA under unloading conditions), and the left medial compartment (BMP-treated OA under overloading conditions). The summary results are listed in Table 7-3 left. BMP treatment notably influences mechanically stressed-induced pathways, including RUNX and MAPK signalling, along with metabolic regulation by reducing fatty acid oxidation and enhancing glucose metabolism.

Within 30°TO APS -treated group, the summary results of the comparisons are listed in Table 7-3 right. It reveals APS treatment has a pronounced effect on collagen synthesis and the reestablishment of cartilage and bone homeostasis, marked by an increase in non-canonical Wnt signalling pathway and Rho GTPases signalling, and the suppression of TGF-beta signalling.

Table 7-2 Summary of the upregulated biological processes in each comparison between 30°TO and 0°TO, for both left and right limbs, presenting the OA condition. The numbers (area 1, area 2) in the figure indicate the comparison where area 1 is compared to area 2, suggesting that the upregulated pathways are enriched in area 1 relative to area 2. Each comparison is detailed in the subsequent results and tables in section 7.4.1. L= left limb, R=right limb, M=medial compartment, L= lateral compartment.

30ºTO L vs. 0ºTO L OA knee vs. healthy knee	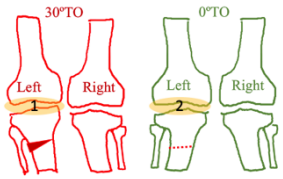	**Upregulated** biological process in OA cartilage ① 1) collagen formation (Type I collagen) 2) extracellular matrix degradation 3) endochondral ossification 4) ROBO signalling VEGFA-VEGFR2 signalling	**Table 7-4**

Table 7-3 Summary of the representative upregulated biological processes in each comparison within the BMP-treated group and the APS-treated group, presenting the OA condition. The numbers (area 1, area 2) in the figure indicate the comparison where area 1 is compared to area 2, suggesting that the upregulated pathways are enriched in area 1 relative to area 2. Each comparison is detailed in the subsequent results and tables in section 7.4.2 and section 7.4.3. L= left limb, R=right limb, M=medial compartment, L= lateral compartment.

	Upregulated pathways in BMP-treated cartilage		**Upregulated pathways in APS-treated cartilage**
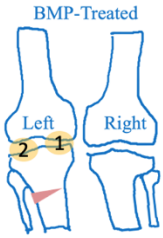	LM vs. LL (Table 7-7) BMP-treated OA in overloading condition vs. BMP-treated OA in unloading condition 1) Glycolysis / Gluconeogenesis pathway (high significant) 2) the response to interleukin-7	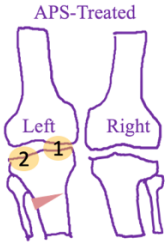	LM vs. LL (Table 7-11) APS-treated OA in overloading vs. APS-treated OA in unloading condition 1) Hedgehog signalling; 2) Interleukin-17A signalling (MMP3) 3) VEGFA-VEGFR2 signalling.
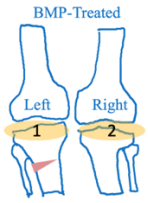	L vs. R (Table 7-9) BMP-treated OA vs. healthy 1) the KEAP1-NFE2L2 pathway 2) RUNX regulation 3) PTEN regulation 4) MAPK6/MAPK4 signalling 5) cellular responses to stress	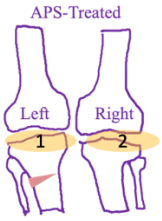	L vs. R (Table 7-13) APS-treated OA vs. Healthy 1) ROBO signalling 2) VEGFA-VEGFR2 signalling, 3) Wnt signalling 4) Collagen formation 5) MAPK6/MAPK4, KEAP1-NFE2L2, RUNX1 signalling. 6) TGF-beta receptor signalling (down regulation)

7.4.1 Enrichment analysis of OA cartilage

7.4.1.1 Upregulated and downregulated pathway in OA cartilage

As described in Chapter 4, OA occurs in 30°TO-induced OA model (progressive-stage left knee and early-stage in right knee), whereas the cartilage remains healthy in the 0°TO (sham surgery) group, as demonstrated by histology results. Comparing the proteome profiles of these two groups, among 2000 screened proteomes, 200 proteins were identified as differentially expressed between healthy cartilage and OA cartilage. The differential expression of these proteins is visualized in the volcano plot shown in Figure 7-1. A detailed comparison of the 30ºTO left knee to the sham group (Figure 7-1A) revealed

a significantly higher number of differentially expressed proteins compared to the 30ºTO contralateral (right) knee when compared to the sham group, and most differentiate proteins in the right knee is down regulated (shown as green plot in Figure 7-1B). This suggests that there were significant molecular changes in the left OA knee induced by varus malignment and the mechanical changes induced, changes that were not as pronounced in the contralateral knee.

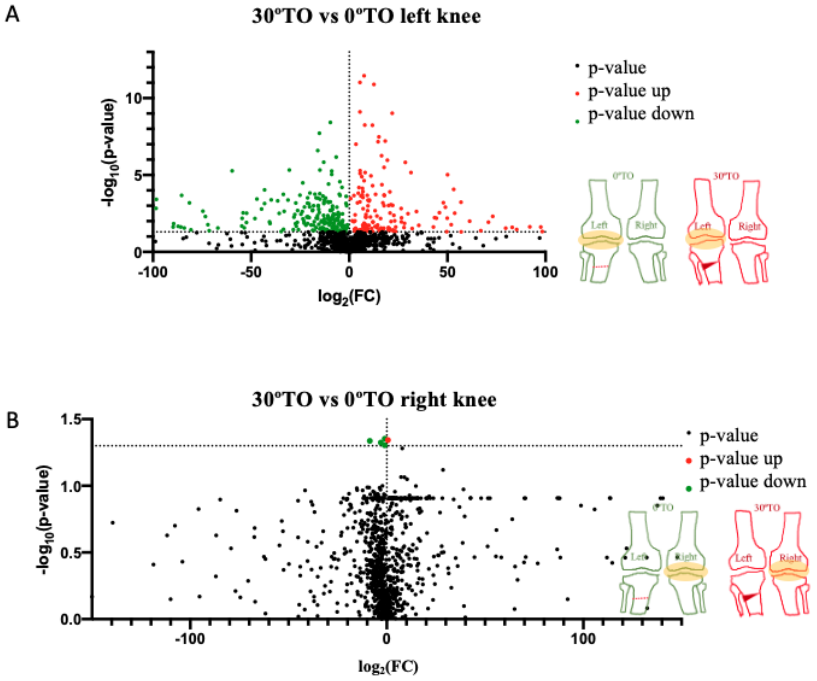

Figure 7-1. Volcano plot illustrating significant differentially expressed proteins in (a) 30ºTO left knee compared to the sham group left knee and (b) 30ºTO contralateral (right) knee compared to the sham group right knee. Please note that a small portion of data points may extend beyond the axis limits. Upregulated proteins (adjusted p-value< 0.05) are depicted in red, while downregulated proteins (adjusted p-value< 0.05) are indicated in green. Others are shown in black.

The differentiated proteins (p-value < 0.05 and fold changes FC>2) are selected (Table 7-4), and protein symbols were converted to their respective encoding genes for subsequent pathway enrichment analysis. Pathways enriched with upregulated genes are listed as upregulated pathways, and those enriched with downregulated genes are listed as downregulated pathways. When comparing the left knee samples in 30ºTO (OA) group to the 0°TO (healthy) group, the following biological processes were notably upregulated (a summary of pathways from Table 7-4 and Table 7-5):

1) collagen formation process, indicated by upregulated expression of Seprin H1, COL1A2, and COL3A1 genes upregulation;

2) degradation of the extracellular matrix (especially collagen degradation) , indicated by upregulated expression of the CTSB and CTSD genes;

3) endochondral ossification, indicated by the upregulation of SERPINH1, COL2A1, and STAT1 genes;

4) some inflammation processes, indicated by upregulatedVEGFA-VEGFR2 signalling, Interleukin-12 signalling, neutrophil degranulation;

5) ROBO signalling, indicated by upregulated expression of RPL and RPS genes.

Table 7-4. Differentiated upregulated and down regulated genes (adjusted p-value < 0.05 and fold changes FC>2) when comparing the 30ºTO left knee (OA knee) with the 0ºTO left knee (healthy knee). The bolded genes are the top 10 with the most significant p-values.

Gene symbols	P value	group	Gene symbols	P value	group
Txndc17	2.07E-15	up	Vars	8.24E-07	down
Lypla2	2.72E-09	up	Gclm	2.93E-06	down
Rbm39	4.89E-09	up	Prep	2.66E-05	down
Psmb7	4.96E-09	up	Mgll	6.21E-05	down
Mtap	2.44E-07	up	Rras;Rras2	0.00011605	down
Nedd8	2.47E-07	up	Cd36	0.00031964	down
Acadm	9.83E-07	up	Plbd1	0.00031964	down
Pak2	9.83E-07	up	Tmpo	0.00032781	down
Atp6v1b2	4.65E-06	up	U2af2	0.00032923	down
Kif5b	7.92E-06	up	Eif3c	0.00046907	down
C5	8.04E-06	up	Rab2a	0.0011899	down
Txn2	1.09E-05	up	Ak3	0.00137563	down
Hdgfrp3	5.40E-05	up	Calu	0.00162574	down
D10Jhu81e	9.29E-05	up	Hsp90ab1	0.00170473	down
Mylk2	0.00011605	up	Flnb	0.00236575	down
Tuba1c;Tuba8	0.00023551	up	Pfkl	0.00314632	down
Crk	0.00032781	up	Cyb5r3	0.00460445	down
Prkacb	0.00038467	up	Slc25a11	0.00480434	down
Sephs1	0.00038467	up	Ap2s1	0.00496938	down
Ces1	0.00042352	up	Cfl1	0.00496938	down
Cope	0.00047049	up	Cotl1	0.00496938	down
Ppid	0.00054651	up	Psmd7	0.00525939	down
Sparc	0.00060884	up	Hnrnpc	0.00525939	down
Yars	0.0010528	up	Ehd2	0.00525939	down
Nit1	0.00170473	up	Lmna	0.0054498	down
Mybph	0.00191824	up	Suclg2	0.00557764	down
Col1a1	0.00239822	up	Acat1	0.00666657	down
Tpd52	0.00266218	up	Pea15a;Pea15	0.00666657	down
Adssl1	0.00303895	up	Mrc1	0.00666657	down
Rpe	0.00382914	up	Cilp	0.00666657	down
Rab5a	0.00393187	up	F13a1	0.00741743	down
Pdlim3	0.00401685	up	Gstp1;Gstp2	0.0075867	down
Txndc5	0.00460445	up	Ptbp1	0.0075867	down
Rrbp1	0.00461129	up	Psme1	0.00806975	down
Aldoa	0.00496938	up	Ube2l3	0.00809822	down
Tpi1	0.00521668	up	Methig1;mCG_20149;Mettl7a1;UbiE2;Mettl7a2	0.00813725	down
Rnh1	0.00525939	up	Glud1	0.00891487	down
Rpl8	0.00525939	up	Nap1l1	0.00973741	down
Adsl	0.00525939	up	Lmnb1	0.00985808	down
Capn1	0.00525939	up	Rtcb	0.00992345	down
H3f3c;H3f3a	0.00546061	up	Psmc5	0.01008918	down
Gm10320;Sec61b	0.00577054	up	Snx6	0.0104049	down
Col3a1	0.00645402	up	Psme2	0.01061846	down
Fscn1	0.006974	up	Lum	0.01066458	down

Fhl1	0.00809822	up	Rsu1	0.01093092	down
Got2	0.00823961	up	Tagln2	0.01102439	down
Nucb2	0.00906396	up	Ptrf	0.01102439	down
Col1a2	0.00992345	up	Lamc1	0.01106318	down
Tpm3	0.01008918	up	Etfa	0.01129435	down
Bin1	0.01061846	up	H2afy	0.01397084	down
Pygm	0.01061846	up	Hadhb	0.01397084	down
Ppp3ca;Ppp3cb	0.01061846	up	Cenpv	0.01397084	down
Gapdh;Gm3839	0.01292091	up	Ugdh	0.01426463	down
Myh8	0.01397084	up	Rap1b	0.01469834	down
Get4	0.01397084	up	Ap2b1	0.01596263	down
Tpm2	0.01397084	up	Rpn1	0.01605107	down
Pgm1;Pgm2	0.01397084	up	Cct8	0.01645979	down
Epb4.1l2;Epb41l2	0.01397084	up	Elavl1	0.01932009	down
Dynll1;BC048507;Dynll2	0.01416987	up	Phb	0.01951462	down
Sec13	0.01634264	up	Fbln1	0.02038648	down
Pkm	0.01932363	up	Hadha	0.02038648	down
Crabp2	0.01951462	up	Mapre1	0.0212615	down
Plod2	0.02426845	up	Ube2n	0.02248509	down
A2mp	0.02442485	up	Mvp	0.02321648	down
Cbr1	0.02676971	up	Tmed9	0.02323243	down
Ivd	0.02878361	up	Abhd5	0.0240549	down
Tceb1	0.03079792	up	Slc25a3	0.02426845	down
Ckmt2	0.03213418	up	Psmc2	0.02426845	down
Rpl14	0.0321724	up	Myh9	0.02426845	down
Eef1a2	0.03465496	up	Rpsa	0.02615636	down
Kars	0.03701331	up	Hsp90aa1	0.02620886	down
Blmh	0.03818193	up	Snd1	0.02692628	down
Pdgfrb	0.0403398	up	Atp2b1;Atp2b4;Atp2b3	0.03009483	down
Sorbs2	0.04336638	up	Uba1	0.03009483	down
Oat	0.04497057	up	Ppp2r1a	0.03165957	down
Zbed5;Chchd2	0.04764187	up	Ddx5	0.0321724	down
Myh4	0.04821126	up	Capza1	0.03321476	down
Tubb2a	0.04955647	up	Arpc4	0.03488554	down
Scrn1	0.05137905	up	Clu	0.03522974	down
			Aldh2	0.03598282	down
			Tns1	0.03701331	down
			Rps3	0.03701331	down
			Aoc3	0.03701331	down
			Glrx3	0.03701331	down
			Vps35	0.03802018	down
			Serpina3m;Serpina3k	0.0403398	down
			Capza2	0.04097764	down
			Blvrb	0.04174182	down
			Psmd12	0.04336638	down
			Atp5a1	0.04383393	down
			Arhgap1	0.04452513	down
			Psmb3	0.04576808	down
			Pdhb	0.04610957	down
			Angptl7	0.04715294	down
			Hnrnpm	0.04821126	down
			Rab5b	0.04821126	down
			Psmd3	0.04821126	down
			Nono	0.04821126	down
			Dusp3	0.04954178	down
			S100a6	0.05137905	down

Table 7-5 Top upregulated pathways in OA cartilage samples (n=6), ranked by the p-value of pathway enrichment when comparing the 30ºTO left knee (OA knee) with the 0ºTO left knee (healthy knee). Pathways exhibiting representative biological processes related to OA, as identified in previous literature, are highlighted in bold. A Log P Value (equivalent to -log10 p-value) greater than 1.3 is considered significant. The "Term" column represents the serial number of specific biological processes or pathways as identified in databases. The "Count" column indicates the number of genes enriched from the input list. The "Gene symbols" column listed the enriched genes.

Term	Pathways	Log P Value	Count	Gene symbols
				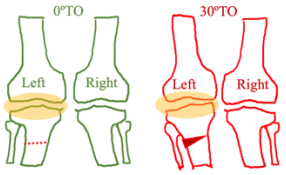
R-HSA-9010553	**Regulation of expression of SLITs and ROBOs**	12.49	13/172	Psma4, Rpl7, Rpl15, Rpl17, Rpl18a, Rpl19, Rpl24, Rpl38, Rps3a, Rps23, Rps25, Elob, Rpl23
GO:0097435	**supramolecular fiber organization**	10.66	18/569	Cacng2, Serpinh1, Cnn3, Col2a1, Csrp1, Dpysl3, Myh3, Myo10, Pls3, Tnnt3, Tpm1, Tpm4, Pdlim1, Arpc1b, Ldb3, Fkbp10, Scin
hsa04066	HIF-1 signalling pathway	4.05	5/109	Eno3, Ldha, Pfkm, Pgk1, Elob
R-HSA-70326	Glucose metabolism	3.23	4/93	Eno3, Pfkm, Pgk1, Pgam2
WP3888	**VEGFA-VEGFR2 signalling**	5.75	11/-	Calr, Csrp1, Ldha, P4hb, Pgk1, Rpl7, Rpl18a, Stat1, Txn, Copg1, Cycs
GO:0045861	negative regulation of proteolysis	5.11	9/323	Serpinh1, Ccrvab, Ctsb, Itih1, Itih4, Serpinb6, Serpine2, Rpl23, Park7
R-HSA-6798695	Neutrophil degranulation	4.51	10/-	Ctsb, Eef2, Mif, Serpinb6, Psap, S100a11, Surf4, Rab31, Erp44, Dpp7
WP474	**Endochondral ossification**	3.88	13/-	Serpinh1, Col2a1, Stat1, Scin, Capns1, Vcan, Ctsb, P4hb, Tnn, Fkbp10, Pepd, Actn3, Pls3
GO:0006979	response to oxidative stress	3.79	8/375	Cryab, Gpx7, Prdx1, Stat1, Tpm1, Pdlim1, Park7, Ero1a
R-HSA-381426	**Regulation of Insulin-like Growth Factor (IGF) transport and uptake by Insulin-like Growth Factor Binding Proteins (IGFBPs)**	3.77	5/125	Cp, Vcan, Nucb1, P4hb, Prkcs
R-HSA-1474244	**Extracellular matrix organization**	3.61	7/300	Capns1, Serpinh1, Col2a1, Vcan, Ctsb, P4hb, Tnn
WP4786	**Type I collagen synthesis in the context of osteogenesis imperfecta**	3.47	3/33	Serpinh1, P4hb, Fkbp10
R-HSA-1474290	Collagen formation	3.28	4/90	Serpinh1, Col2a1, Ctsb, P4hb
GO:0060349	**Bone morphogenesis**	2.11	3/98	Actn3, Serpinh1, Col2a1

7.4.2 Upregulated pathways in BMP-treated cartilage

The analysis of differentially expressed proteins in BMP-treated groups is presented next. As described in the methods section (Section 7.3.3), duo to the technical limitation, the comparison was confined

within a single experimental round. Therefore, the comparation is restricted in 30ºTO BMP-treated group, between left and right limbs, and the medial and lateral compartments,

Table 7-6 and Table 7-7 presents a detailed comparison focusing specifically on the BMP-treated left knee, distinguishing between the medial and lateral compartments. The left lateral compartment exhibits an OA condition under a state of unloading, while the left medial compartment shows an OA condition under overloading, both receiving BMP injection.

Highly expressed proteins in the BMP-treated OA cartilage are enriched in: 1) the Glycolysis / Gluconeogenesis pathway and 2) the response to interleukin-7 (Eno1, Hdgf, Hnrnph1). Notably, the Glycolysis/Gluconeogenesis pathway (Eno1, Aldh, ADH) is significantly more upregulated in this analysis (Table 7-7), despite already being active in the earlier analysis comparing the left medial compartment to the right lateral compartment (healthy) (Table 7-8).

The findings also highlight an upregulation of the biological process "response to interleukin-7," which is particularly pronounced in the left medial compartment of the BMP-treated group. This indicates that the IL-7 response is synergistically stimulated by the effects of BMP and overloading conditions.

Table 7-6 Differentiated upregulated genes when comparing left medial compartment (BMP-treated OA in overloading condition) with left lateral compartment (BMP treated OA in unloading condition). The bolded genes are the top 10 with the most significant p-values.

Upregulated gene	P value	Upregulated gene	P value
Rnf113a2;Rnf113a1	1.60E-14	Mcfd2	0.0004131
Myh8	1.02E-11	Psmd3	0.00106929
Ckap5	6.38E-09	Hdgf	0.00109123
Cryab	3.51E-08	Pfkl	0.00115625
Myom1	4.90E-08	Agl	0.00115927
Actn2	8.37E-08	Rps15	0.00124528
Srl	2.47E-07	Cdc37	0.00128242
Eef1a2	3.20E-07	Plod1	0.00142656
Ampd1	4.37E-07	Sypl2	0.00153759
Pdlim7	5.49E-07	Myot	0.00174372
Klhl41	2.00E-06	Ckmt2	0.00199884
Pkhd1	2.21E-06	Fndc1	0.00227609
Atp2a3	2.57E-06	Vps29	0.00228193
Glyr1	3.09E-06	Prkra	0.00262358
Anp32b	6.32E-06	Nes	0.00284233
Pfdn2	7.42E-06	Mrps5	0.00292131
Eno1	8.06E-06	B2m	0.00360789
Obscn	1.19E-05	Txndc12	0.00373724
Rpl8	1.56E-05	Col5a2	0.00385417

Pdlim5	2.03E-05	Acp5	0.00425525
Huwe1	2.04E-05	Trim72	0.00434676
Mybph	2.33E-05	Eif3g	0.00483766
Rpl24	2.64E-05	Lbh	0.00505676
Serpina3c	4.08E-05	Col11a2	0.0067089
Apobec2	4.68E-05	Fkbp3	0.00744761
Rps26	5.77E-05	C7	0.00745825
Aldoart1	0.00010053	Ivd	0.00975271
Ptms	0.00010301	Prcp	0.01086616
Aldh7a1	0.00010557	Kars	0.0130455
Bpgm	0.00010865	Sh3bgr	0.01403997
Hnrnph1	0.00012907	Npepl1	0.01471925
Atp1b3	0.00022259	Myo1d	0.01533235
Txnrd1	0.00026569	Cars	0.01915484
Capn1	0.00030873	Stmn1;Stmn2	0.02759307
Ptma	0.00031939	Golph3;Golph3l	0.03212428
Tpm1	0.00031939	Nedd4	0.04188381
Tuba1c	0.00041317	Acly	0.04471386

Table 7-7. Top upregulated pathways in BMP-treated knee in overloading condition (n=3), ranked by the p-value of pathway enrichment when comparing left medial compartment (BMP-treated OA in overloading condition) with left lateral compartment (BMP treated OA in unloading condition). Pathways exhibiting representative biological processes related to OA, as identified in previous literature, are highlighted in red. A Log P Value (equivalent to -log10 p-value) greater than 1.3 is considered significant. The "Term" column represents the serial number of specific biological processes or pathways as identified in databases. The "Count" column indicates the number of genes enriched from the input list. The "Gene symbols" column listed the enriched genes.

Term	Pathways	Log P value	Count	Gene symbols
				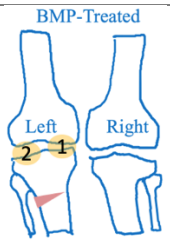
mmu00010	**Glycolysis / Gluconeogenesis**	4.90	9/-	Bpgm,Eno1,Pfkl,Aldh7a1,Aldoart1,Agl,Bcat2,Gpc1,Galns
GO:0006412	**translation**	4.80	17/-	Eef1a2,Rps15,Rpl8,Cars,Rps26,Eif3g,Rpl24,Ckap5,Mrps5,Kars,Acly,Apobec2,Psmd3,U2af2,Hnrnph1,Rnf113a1,C7
GO:0098760	**response to interleukin-7**	4.25	3/-	Eno1,Hdgf,Hnrnph1
GO:1901881	positive regulation of protein depolymerization	4.17	14/-	Actn2,Nes,Stmn2,Capn1,Cryab,Stmn1,Pfdn2,Tpm1,Ckap5,B2m,Col11a2,Col5a2,Klhl41,Myo1d
GO:0010927	cellular component assembly involved in morphogenesis	3.72	19/-	Actn2,Gpc1,Tpm1,Ckap5,Klhl41,Myh8,Atp1b3,Atp2a3,Myom1,Pdlim5,Trim72,Sypl2,Cryab,Pdlim7,Stmn1,Nes,Myot,Rpl24,Myo1d
R-MMU-6798695	Neutrophil degranulation	3.26	9/-	B2m,Capn1,Pfkl,Psmd3,Galns,Huwe1,Prcp,Agl,Acly
R-MMU-71291	Metabolism of amino acids and derivatives	3.05	8/-	Bcat2,Psmd3,Txnrd1,Ivd,Ckmt2,Aldh7a1,Cars,Kars

Table 7-9 contrasts the right limb (combining data from medial and lateral compartments) with the left limb (BMP-treated OA, combining data from medial and lateral compartments) in the 30°TO-BMP group. This comparison provides an overview of the effects of BMP treatment on OA knees relative to changes observed in the contralateral limb due to gait alterations. To enhance the robustness of the findings, this analysis includes a mixed sample from both medial and lateral compartments in each limb, thereby enlarging the sample size.

A greater number of pathways were identified with higher statistical significance. The top enriched pathways are 1) the KEAP1-NFE2L2 pathway, 2) RUNX regulation, 3) PTEN regulation, and 4) MAPK6/MAPK4 signalling, 5) cellular responses to stress (Eef1a1, Alb). Notably, RUNX signals (such

as RUNX1, RUNX2, and RUNX3), MAPK signalling, and KEAP1-NFE2L2 signalling, were significantly highly enriched in the left limb, both in the BMP-treated groups (Table 7-9) and later discussed APS-treated group (Table 7-13), with greater degree of enrichment observed in the BMP-treated group.

Table 7-8 Differentiated upregulated genes when comparing left limb (BMP-treated OA) with right limb (healthy). The bolded genes are the top 10 with the most significant p-values.

Upregulated gene	P value	Upregulated gene	P value
Tmsb10	0.00088035	Btf3	0.0240751
Cpn10-rs1;Hspe1	0.00136494	Rbp4	0.02443575
Tsc22d1	0.00232237	Ubqln1;Ubqln2	0.02477091
Cttn	0.00288444	Cnpy2	0.02508128
Psap	0.00290705	Ddost	0.02554951
Lamtor5	0.00316623	Cdh13	0.02598347
Map4	0.00431592	Afm	0.02795695
Aox2	0.00468911	Nucb2	0.02840182
Cfi	0.00564772	Psma4	0.02850252
Col3a1	0.00584104	Pabpc1	0.02895771
Blmh	0.00593115	Sparc	0.02951033
Lima1	0.00610602	Txn2	0.02955755
Ahnak	0.00627545	Ctsh	0.02975526
Lgals1	0.0073813	Ahsg	0.03134926
Dbi	0.00795113	Itih2	0.03202082
Sod2	0.00843826	Ppp3r1	0.03330437
Col5a1	0.00882059	S100a11	0.0345399
Lsm8	0.00897407	Rbbp4	0.03503088
Fus;Taf15	0.00922912	Rpl23a	0.03552367
Cast	0.00949215	Clec3b	0.03690027
Nit2	0.00950346	Gm20390;Nme2;Nme1	0.03719009
Glo1	0.0097257	Cp	0.03814868
Aga	0.01048117	Psma5	0.03841256
Dld	0.01051719	Igkv1-132	0.03917408
Ighv8-14;Ighv8-13;Ighv8-12	0.01058492	Sec13	0.03940957
Hpx	0.01095837	Sod1	0.03987326
Tf	0.01202402	Polr2i	0.04010009
Lsm3	0.01213993	Rps21	0.04076384
Rad23b	0.01218347	Nit1	0.04158542
Efhd2	0.01231022	Rpl38	0.04195952
Ighg2c;Ighg2b	0.01233137	Egfr	0.04242808
Rcn2	0.01325306	Ada	0.04312749
Xdh	0.01327203	Dnpep	0.04337842
Serpina3m;Serpina3k	0.01331799	Rpia	0.04374425
Gda	0.01353006	Calu	0.04378367
Alb	0.01381132	Sfpq	0.04398706
Nucb1	0.01686954	Mif	0.04400191
Fkbp7	0.01755296	Gc	0.04400521
Hprt1	0.01773525	Vapb	0.04450847
Lgals3bp	0.01779132	Ctsb	0.04486335
Ica;1300017J02Rik	0.01791498	Hnrnpk	0.04572277
Eif6	0.01861084	Pepd	0.04613423
Lap3	0.01960802	Lum	0.04721545
Manf	0.02097006	Naca	0.04729395
Gsr	0.02139927	Ces1e	0.04756652
Fkbp10	0.02161821	C3	0.04862094
Atp5d	0.02297871	Eif5a	0.04866549
Rrbp1	0.02391284	Lgmn	0.04879152

Table 7-9. Top upregulated pathways in BMP-treated knee (n=6), ranked by the p-value of pathway enrichment when comparing left limb (BMP-treated OA) with right limb (healthy). Pathways exhibiting representative biological processes related to OA, as identified in previous literature, are highlighted in red. A Log P Value (equivalent to -log10 p-value) greater than 1.3 is considered significant. The "Term" column represents the serial number of specific biological processes or pathways as identified in databases. The "Count" column indicates the number of genes enriched from the input list. The "Gene symbols" column listed the enriched genes.

Term	Pathways	Log P value	Count	Gene symbols
				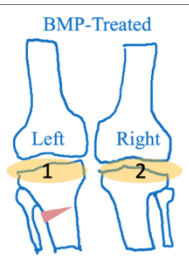
R-MMU-9711123	**Cellular response to chemical stress**	16.43	22/156	Alb,Cycs,Gsr,P4hb,Prdx1,Psma3,Psmb1,Psmb6,Psmb7,Psmc3,Sod1,Sod2,Psmd2,Txn1,Psma1,Psma4,Psma5,Psma7,Psmb3,Txn2,Psma8,Cox6b1
R-MMU-2262752	**Cellular responses to stress**	15.12	32/438	Alb,Cycs,Dync1i2,Eef1a1,Gsr,Hspa5,P4hb,Prdx1,Psma3,Psmb1,Psmb6,Psmb7,Psmc3,Rbbp4,Sod1,Sod2,Stip1,Psmd2,Tuba1b,Txn1,Psma1,Psma4,Psma5,Psma7,Psmb3,Txn2,Lamtor5,Dctn2,Psma8,Cox6b1,Sec13,Rbbp7
R-MMU-9755511	**KEAP1-NFE2L2 pathway**	11.10	13/75	Prdx1,Psma3,Psmb1,Psmb6,Psmb7,Psmc3,Psmd2,Psma1,Psma4,Psma5,Psma7,Psmb3,Psma8
R-MMU-8939236	**RUNX1** regulates transcription of genes involved in differentiation of HSCs	10.54	12/66	Psma3,Psmb1,Psmb6,Psmb7,Psmc3,Psmd2,Psma1,Psma4,Psma5,Psma7,Psmb3,Psma8
R-MMU-8939902	Regulation of **RUNX2** expression and activity	10.47	11/52	Psma3,Psmb1,Psmb6,Psmb7,Psmc3,Psmd2,Psma1,Psma4,Psma5,Psma7,Psmb3
R-MMU-8948751	Regulation of **PTEN** stability and activity	10.38	12/68	Psma3,Psmb1,Psmb6,Psmb7,Psmc3,Psmd2,Psma1,Psma4,Psma5,Psma7,Psmb3,Psma8
R-MMU-8941858	Regulation of **RUNX3** expression and activity	10.37	11/53	Psma3,Psmb1,Psmb6,Psmb7,Psmc3,Psmd2,Psma1,Psma4,Psma5,Psma7,Psmb3
R-MMU-5687128	MAPK6/MAPK4 signalling	10.00	12/73	Psma3,Psmb1,Psmb6,Psmb7,Psmc3,Psmd2,Psma1,Psma4,Psma5,Psma7,Psmb3,Psma8
GO:0030162	regulation of proteolysis	9.71	38/-	Ahsg,Serpinc1,Cast,Serpinh1,Cfl1,Cst3,Ctsb,Ctsh,Ctsl,Cycs,Dab2,Ecm1,F3,Serpind1,Itih1,Itih2,Itih3,Mug2,Lgmn,Psma3,Rad23b,Glg1,Sumo3,Serpina3k,Serpina3m,Clec3b,Xdh,Ubqln2,Ubqln1,Cpb2,Lamtor5,Sumo2,A2m,Spon1,Adipoq,Actb,Banf1,Mvp
R-MMU-6798695	Neutrophil degranulation	9.35	27/-	Aga,Ahsg,C3,Cst3,Ctsb,Ctsh,Ddost,Eef1a1,Gm2a,Mif,Nme2,Ctsa,Psap,Psmb1,Psmb7,Psmc3,Rab7,S100a11,Psmd2,Ttr,Psma5,Nit2,Prdx4,Copb1,Cotl1,Mvp,Txndc5

7.4.3 Upregulated pathways in APS-treated cartilage

The analysis of differentially expressed proteins in APS-treated groups is presented next. Table 7-11 compares the left lateral compartment with the left medial compartment in 30°TO APS group, presenting the comparison of OA under differing loading conditions in the knee post-APS treatment. The medial compartment is considered to be under overloading conditions, while the lateral compartment is considered to be under unloading conditions. High protein expression in APS-treated OA cartilage under overloading conditions was associated with: 1) Hedgehog signalling; 2) Interleukin-17A signalling (notably, high expression of MMP3 was detected); 3) VEGFA-VEGFR2 signalling. Cartilage degeneration process is notably active.

Table 7-10 Differentiated upregulated genes when comparing left medial compartment (APS-treated OA in overloading condition) with left lateral compartment (APS treated OA in unloading condition). The bolded genes are the top 10 with the most significant p-values.

Upregulated gene	P value	Upregulated gene	P value
Rplp2	1.63E-19	Crat	3.10E-10
Rpl35	2.31E-16	Krt10	3.14E-10
Ces1a	8.03E-16	Sec23ip	3.14E-10
Cbx1	5.01E-15	Dnajb11	4.17E-10
F13a1	9.86E-15	Leprel4;P3h4	4.84E-10
Rras;Rras2	1.94E-14	Hnrnpul1	4.84E-10
Txndc17	2.14E-14	Fkbp11	4.92E-10
Cpne8	3.22E-14	Mx2;Mx1	5.03E-10
Snrpa1	4.26E-14	Vps29	5.65E-10
Gstm2	4.56E-14	Eif4e	6.63E-10
Lasp1	4.72E-14	Hpcal1	7.84E-10
Mmp3;Mmp10	4.89E-14	Hnrnph1	8.18E-10
Arfip1	4.98E-14	Ppp1r14b	9.32E-10
Rab35	6.92E-14	Hmgb2	2.52E-09
Crabp2	7.19E-14	Sorbs2	2.65E-09
Serpine2;Serpinb3c	7.32E-14	Papss2	3.17E-09
Ilf3;Strbp	7.32E-14	Gclc	3.17E-09
Iars2	8.07E-14	Vasp	5.24E-09
Srp54c;Srp54	8.92E-14	Myl6b	6.40E-09
Ighv8-14;Ighv8-13;Ighv8-9;Ighv8-6;Ighv8-12;Ighv8-5;Ighv8-11	9.10E-14	Rcc1	6.89E-09
Rtn3	9.48E-14	Vapa	1.27E-08
Swap70	9.68E-14	Btf3l4	1.78E-08
Rdx	9.88E-14	Mme	2.58E-08
Tax1bp3	1.03E-13	Api5	6.06E-08
Lrrc15	1.36E-13	Wars	6.06E-08
C8a	1.39E-13	Eif3m	1.00E-07
Rbm8a	1.49E-13	Rcn3	1.15E-07
Pin1	1.93E-13	Ubap2l	1.77E-07
Csnk2a1	2.75E-13	Fahd1	3.40E-07
Farsb	3.23E-13	Fam49b	3.40E-07
Ktn1	4.41E-13	St13	6.51E-07
Cnpy4	4.96E-13	Arf5	8.10E-07
Ppp1r9b	8.58E-13	Phpt1	1.36E-06
Rhog	1.18E-12	Actr1a	3.50E-06
Akr1b8;Akr1b10	1.37E-12	Tceb1	4.61E-06

Efemp2	1.54E-12	C2	6.45E-06
Pgrmc2	1.61E-12	Eif3i	1.27E-05
Cisd1	1.89E-12	Rcn1	1.74E-05
Sub1	1.97E-12	Hp1bp3	5.65E-05
Crtap	2.05E-12	Arfgap3	6.56E-05
Cltb	2.14E-12	Nln	7.88E-05
F9	2.67E-12	Snrnp70	8.93E-05
Erh	3.06E-12	Serpinf1	0.00023056
Gm20503;Gng10	3.09E-12	Rap1a	0.000553
Ankfy1	3.36E-12	Apmap	0.00060954
Stab1	3.62E-12	Mtap	0.00063897
Rtn4	4.50E-12	Mesdc2	0.0008029
Grn	4.74E-12	Nsf	0.00352936
Mycbp	6.17E-12	Pcna	0.00377415
Igf2r	9.21E-12	Eif3g	0.00461719
Ube2m	1.11E-11	Dynlrb1	0.00504693
Pmm2	1.34E-11	Pcbp2	0.00638814
Cuta	1.53E-11	Lgalsl;Pick1	0.00653568
Scamp2	1.76E-11	Ctsl	0.00654576
Ppp3r1	2.03E-11	Sephs1	0.0073273
Fbl	2.73E-11	Gmppb	0.00964412
Ahcyl1;Ahcyl2	3.20E-11	Rpl19	0.00982368
Rnpep	4.10E-11	Dnaja2	0.0112444
Upf1	4.10E-11	Anp32b	0.0116778
Lmcd1	4.72E-11	Pcmt1	0.01709479
Nhp2l1	4.88E-11	Rpl31	0.0172758
Adss	7.79E-11	Yars	0.02457142
Tuba1a;Tuba3a	7.79E-11	Azgp1	0.0280373
Magohb;Magoh	1.32E-10	Acan	0.03568276
Immt	1.32E-10	Hadhb	0.03581577
Sgta	1.59E-10	Eif3j1;Eif3j2	0.03649112
Snx12	1.87E-10	Alpl	0.04746276
Ppt1	2.40E-10	Pdcd6	0.04927138
Fermt3	2.74E-10		

Table 7-11. Top upregulated pathways in APS-treated knee in overloading condition (n=3), ranked by the p-value of pathway enrichment when comparing left medial compartment (APS-treated OA in overloading condition) with left lateral compartment (APS treated OA in unloading condition). Pathways exhibiting representative biological processes related to OA, as identified in previous literature, are highlighted in red. A Log P Value (equivalent to -log10 p-value) greater than 1.3 is considered significant. The "Term" column represents the serial number of specific biological processes or pathways as identified in databases. The "Count" column indicates the number of genes enriched from the input list. The "Gene symbols" column listed the enriched genes.

Term	**Pathways**	**Log P value**	**Count**	**Gene symbols**
R-HSA-72766	Translation	4.87	13/-	Eif4e, Eif4ebp1, Rpl32, Srp14, Srp54, Vars1, Atp1b1, Ppp3r1, Tsg101, Tuba1a, Ap1m1, Timm13, H1-3

WP5242	**Comprehensive IL-17A signalling**	2.49	3/-	Mmp3,Ppp1r14b,Rras2
R-MMU-5358351	Signalling by Hedgehog	2.12	3/138	Prkar2b,Tuba1a,Tuba3a
WP3888	**VEGFA-VEGFR2 signalling**	2.13	4/-	Eif4e, Gpc1, Ptma, Srp54

Finally, Table 7-13 contrasts the right limb with the left limb (OA with APS treatment), showcasing the effects of APS treatment on OA knees against the contralateral limb. Interestingly, the degeneration and collagen formation processes are far more active in this left versus right limb comparison, more so than in the intra-knee comparison provided in the previous table (Table 7-11). In comparison to BMP treatment, APS treatment appears to contribute more significantly to collagen synthesis and EGFR and interleukin-related inflammation processes, while suppressing TGF-beta signalling.

High protein expression in APS-treated OA cartilage was associated with 1. ROBO signalling 2. VEGFA-VEGFR2 signalling, 3. Wnt signalling 4. Supramolecular fibre organisation and Type 1 collagen formation process 5. MAPK6/MAPK4 signalling, KEAP1-NFE2L2 pathway, RUNX1 pathway. A downregulation of TGF-beta receptor signalling was also observed. Additionally, the β-catenin -independent Wnt signalling pathway and Rho GTPases signalling were activated, with the typical genes (e.g., RAC1, RAC3, RHOG, CDC42) significantly increased in APS-treated OA knee (left knee).

Beyond cartilage protein-related biological processes, the results also revealed upregulated translation-related pathways in both OA (Table 7-5) and APS-treated knees (Table 7-13), such as L13a-mediated translational silencing of ceruloplasmin expression and ribosome dysfunction.

Table 7-12 Differentiated upregulated genes when comparing left limb (APS-treated OA) with right limb (healthy). The bolded genes are the top 10 with the most significant p-values.

Upregulated gene	P value	Upregulated gene	P value
Psmb9	1.12E-28	Cops4	1.28E-05
Nedd8	3.19E-23	Lypla1	1.49E-05
Mtap	2.30E-21	Arpc5l	2.38E-05
Hook3	2.78E-20	Nras;Kras;Hras	3.32E-05
Gale	9.08E-19	F9	3.68E-05
Wars	4.78E-18	Atp6v1h	4.33E-05
Vps4b	3.74E-15	Gcn1l1	4.52E-05
Qdpr	4.74E-15	Pin1	5.36E-05
Api5	4.74E-15	Sgta	5.86E-05
Ubap2l	6.86E-15	Lypla2	7.01E-05
Vbp1	2.99E-14	Erh	7.12E-05
Gid8	8.71E-14	Paics	7.52E-05
Sfxn3	1.65E-13	Fkbp2	7.69E-05
Rcc1	3.45E-13	Rhog	9.23E-05
Ube2i	5.38E-13	Rbm8a	9.62E-05
Ethe1	8.06E-13	Parp3	0.00013418
Hpcal1	2.08E-12	Psme2	0.00017628
Ppp1r14b	4.02E-12	Rpe	0.00031043
Tor1aip1	5.44E-12	Dnajc3	0.00043482
Nhp2l1	5.44E-12	Mmp3;Mmp10	0.0004548
Tuba1a;Tuba3a	1.39E-11	Hist1h3a	0.00057793

Rap1a	1.39E-11	Sec11a	0.0006981
Vasp	1.40E-11	Hexa	0.00118554
Ppt1	1.98E-11	Ctsb	0.00135439
Hmgb2	1.98E-11	Sar1b	0.00136627
Coro7	2.78E-11	Rpl22	0.00183532
Grn	2.78E-11	Aldh1l2	0.00263441
Vps29	3.74E-11	Afm	0.0026803
Vars	5.49E-11	Ctsh	0.00299252
Sec23ip	5.72E-11	Rtn3	0.00319985
Stat6	5.72E-11	Hnrnph1	0.00364347
Carhsp1	6.45E-11	Tm9sf3	0.00432526
Rpl22l1	7.50E-11	Cdc37	0.00468658
Plod3	8.80E-11	Caprin1	0.00471798
Nsfl1c	1.73E-10	Lamtor5	0.00487554
Snx12	5.93E-10	Srgap2;Srgap1	0.0053912
Fbl	5.96E-10	Dhx9	0.00635566
Txnrd1	9.57E-10	Tuba1c;Tuba8	0.00661781
Rtn4	1.17E-09	Tubb6	0.00681473
Timp2	1.36E-09	Itgb2	0.00742138
Eif4e	1.38E-09	Gls	0.00839025
Rars	1.38E-09	Cald1	0.00867674
Fis1	2.22E-09	Gaa	0.00871524
Cbx3	2.52E-09	Scp2	0.00871524
Srsf3	2.52E-09	Ostf1	0.00898789
Sec61a1	2.52E-09	Aldh7a1	0.00900428
Magohb;Magoh	2.90E-09	Rbm3	0.01120681
Dnajb11	3.17E-09	Lgmn	0.01120681
Tnfaip8	3.38E-09	Sod2	0.01155168
Pdlim4	4.15E-09	Vwa5a	0.01155168
Lpp	5.42E-09	Atp6v0c	0.01245515
Fubp1	6.51E-09	Papss1	0.01391934
Qars	7.67E-09	Lamtor1	0.01391934
Immt	8.39E-09	Atp6v1b2	0.01412419
Rnpep	9.53E-09	Rpl14	0.01453309
Ahcyl1;Ahcyl2	1.09E-08	Psmc1	0.01573375
Akr1b8;Akr1b10	1.18E-08	Prmt1	0.01573375
Hk3	1.55E-08	Cndp2	0.01725942
Kpna3	1.66E-08	Mbnl1;Mbnl2	0.01748184
Itpa	2.06E-08	Sorbs2	0.01867018
Mapre2	2.42E-08	Ctsd	0.02148171
Lsm4	4.68E-08	Cnpy4	0.02520965
Ubqln1;Ubqln2;Ubqln4	5.05E-08	Ndrg1	0.02526313
Igf2r	5.65E-08	Ppp1cb	0.02526313
Cirbp	8.98E-08	Sar1a	0.02555486
Zyx	8.98E-08	Rpl19	0.02567992
Inf2	9.65E-08	Timm8a1;Timm8a2	0.02755862
Crip2	1.10E-07	P3h1;Lepre1	0.02903937
Mycbp	1.18E-07	Atp6v1a	0.03215428
Gmppa	1.21E-07	Ugt1a6b;Ugt1a6;	0.03329291
Sdf4	1.35E-07	Rps15	0.03329291
Eif3e	1.35E-07	Npepl1	0.03329421
Numa1	1.39E-07	Ak2	0.03329421
Snrpd1	1.66E-07	Sfxn1	0.0336283
Pygb	2.10E-07	Mogs	0.0336984
Crtap	2.47E-07	Atp6v0d1	0.0360731
Pgrmc2	2.48E-07	Hp1bp3	0.03649781
Nop58	2.68E-07	Tax1bp3	0.03659669
Aldh18a1	2.97E-07	Cnn2	0.03698915
Chmp4b	3.20E-07	Gorasp2	0.03934544
Snrnp200	4.02E-07	Hnrnpul1	0.04035462
Wdr61	5.04E-07	Acaa1b;Acaa1a	0.04113213
Sf3a3	5.30E-07	Rpl15	0.04174306
Pdcd4	1.04E-06	S100a11	0.04205133

Rab1b	1.08E-06	Pak2	0.04275028
Aldoc	1.28E-06	Snx9	0.04309312
Galk1	1.50E-06	Vapa	0.04373342
Diap1;Diaph1	2.24E-06	Rab31	0.04564904
Pmm2	2.26E-06	Gnpda1	0.04564904
Sf3b3	2.90E-06	Fam129b	0.04579341
Serbp1	2.91E-06	Ckb	0.04694288
Pld3	3.06E-06	Psmc2	0.0471432
Cthrc1	3.28E-06	Sars	0.04769191
Gpx8	5.01E-06	Sf3b5	0.04862847
Gart	5.12E-06	Cbx1	0.04896692
Upp1	7.72E-06	Pitrm1	0.04929314
Txndc17	1.02E-05	Abracl	0.04944586

Table 7-13. Top upregulated pathways in APS-treated knee (n=6), ranked by the p-value of pathway enrichment when comparing left limb (APS-treated OA) with right limb (healthy). Pathways exhibiting representative biological processes related to OA, as identified in previous literature, are highlighted in red. A Log P Value (equivalent to -log10 p-value) greater than 1.3 is considered significant. The "Term" column represents the serial number of specific biological processes or pathways as identified in databases. The "Count" column indicates the number of genes enriched from the input list. The "Gene symbols" column listed the enriched genes.

Term	Pathways	Log P value	Count	Gene symbols
				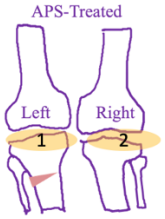
R-HSA-376176	**Signalling by ROBO receptors**	45.80	197/-	Cdc42, Eif4g1, Gspt1, Rpsa, Magoh, Rpl10a, Pak2, Prkacb, Psma2, Psmb1, Psmb9, Psmc2, Psmd2, Psmd12, Psme2, Rac1, Rpl3, Rpl4, Rpl5, Tubb2a, ... Hexb, Ppt1, Vapa, Gnptab, Nt5c2, Nagk, Aldh1l2, C8a, Mmp3, Mx1
R-HSA-156827	**L13a-mediated translational silencing of Ceruloplasmin expression**	41.67	39/112	Eif2s3, Eif4e, Eif4g1, Eif3e, Rpsa, Rpl10a, Rpl3, Rpl4, Rpl5, Rpl6, Rpl7, Rpl7a, Rpl9, Rpl12, Rpl15, Rpl17, Rpl18, Rpl18a, Rpl19, Rpl22, Rpl27a, Rpl31, Rplp1, Rps2, Rps3a, Rps4x, Rps7, Rps11, Rps12, Rps15, Rps27, Eif3c, Eif3j, Rpl14, Rpl23, Eif3m, Pabpc1, Rps27l, Rpl22l1
R-HSA-6798695	Neutrophil degranulation	33.79	58/-	Acaa1, Ap2a2, Aldoc, Rhog, Atp6v0c, Cnn2, Copb1, Ctsb, Ctsd, Ctsh, Ctsz, Diaph1, Eef2, Stom, Fth1, Ftl, Gaa, Glb1, Grn, Hexb, Hk3, Hmgb1, Igf2r, Itgav, Itgb2, Nras, Ctsa, Ppia, Dnajc3, Psma2, Psmb1, Psmc2, Psmd2, Psmd12, Pygb, Rac1, Rap1a, Rap2b, S100a11, Serpinb3, Surf4, Timp2, Vapa, Cap1, Prdx4, Pgrmc1, Rab31, Erp44, Cyfip1, Cotl1, Ostf1, Dbnl, Lamtour1, Nit2, Rap2c, Txndc5, Arl8a, Tubb
WP3888	**VEGFA-VEGFR2 signalling**	20.81	42/-	Ap2a1, Calr, Cdc42, Crip2, Ctnna1, Ctnnd1, Eif4e, Eif4g1, Eprs1, Hmgb1, Hras, Itgav, Mmp10, Nap1l1, Rpl10a, P4hb, Pak2, Ppp3ca, Rac1, Rap1a, Rpl5, Rpl7, Rpl18a, Rps11, Sars1, Fscn1, Sod2, Stat1, Stat6, Txn, Plod3, Atp6v0d1, Qki, Ubap2l, Ndrg1, Hyou1, Copg1, Pabpc1, Snd1, Txndc5, Arpc5l, Tuba1c
R-HSA-72649	Translation initiation complex formation	18.29	47/-	Eif2s3, Eif4e, Eif4g1, Eif3e, Rpsa, Rps2, Rps3a, Rps4x, Rps7, Rps11, Rps12, Rps15, Rps27, Eif3c, Eif3j, Eif3m, Pabpc1, Rps27l, Ap2a1, Ap2a2, Ap2b1, Comt, Hnrnpa1, Prmt1, Pcbp2, Ppia, Sec13, Snrpd1, Snrpd3, Stat1, Ube2i, Mogs, Sec24d, Sec23a, Ganab, Sar1b, Chmp4b, Tubb, Fbl, Snu13, Nop58, Rpl5, Rpl6, Rpl7, Rpl7a, Rpl14, Ddx17
R-HSA-194315	**Signalling by Rho GTPases**	13.80	43/-	Rhog, Cdc42, Ckb, Ctnna1, Diaph1, Dync1i2, Cttn, Stom, Ktn1, Pafah1b1, Pak2, Pin1, Rac1, Rac3, Rps27, Sec13, Tmpo, Tubb2a, Tuba1a, H2ac14, H3c1, Arpc1b, Pgrmc2, Cdc37, Mapre1, Swap70, Cyfip1, Scfd1, Srgap2, Tor1aip1, Cyfip2, Tax1bp3, Cops4, Ankfy1, Tuba8, Lamtor1, H2aj, Nsfl1c, Srgap1, Tubb6, Tuba1c, Tuba3e, Cpne8
GO:0097435	**Supramolecular fiber organization**	10.77	44/-	Rhog, Cald1, Cdc42, Cnn2, Cnn3, Diaph1, Fus, Hnrnpa1, Lcp1, Myh3, Numa1, P4ha1, Pafah1b1, Rac1, Rac3, Fscn1, Vasp, Zyx, Tuba1a, Plod3, Arpc1b, Cap1, Ctrap, P3h4, Mapre1, Swap70, Tardbp, Efemp2, Lima1, Myoz1, Inf2, Coro7, Arpc5l, Hook3, Actn3, Calr, Cttn, Kras, Rap2a, Pdlim4, Pacsin2, Dbnl, Phpt1, Srgap2
R-MMU-2262752	Cellular responses to stress	10.59	45/438	Alb, Atp6v1b2, Atp6v0d1, Atp6v0c, Cybb, Eif2s1, H1f3, H1f0, Hmox1, Dnaja1, Psmb9, Nup62, Psma2, Psmb1, Psmb7, Psme2, Psmd3, Tuba1a, Tuba3a, Tubb3, Tubb4a, Uba52, Ubb, Ubc, Psmc4, Psma4, Tcirg1, Bag3, Txn2, H1f5, Atp6v1c1, Psmd6, Gpx7, Map1lc3b, Tubb6, Gpx8, Lrpprc, Rps27a, Lamtor2, Xpo1, Camk2d, Atp6v1h, Tubb4b, Dync1li1, Vcp
R-HSA-447115	Interleukin-12 family signalling	10.28	12/57	Cdc42, Cnn2, Lcp1, Mtap, P4hb, Pak2, Ppia, Psme2, Snrpa1, Sod2, Stat1, Pdcd4
R-HSA-3858494	**Beta-catenin independent**	9.98	17/146	Ap2a1, Ap2a2, Ap2b1, Gnb1, Gnb2, Gng10, Kras, Ppp3ca, Psma2, Psmb1, Psmb9, Psmc2, Psmd2, Psmd12, Psme2, Rac1, Rac3

	WNT signalling			
R-HSA-195721	**Signalling by WNT**	7.99	22/331	Ap2a1, Ap2a2, Ap2b1, Csnk2a1, Gnb1, Gnb2, Gng10, Kras, Ppp3ca, Psma2, Psmb1, Psmb9, Psmc2, Psmd2, Psmd12, Psme2, Rac1, Rac3, H2ac14, H3c1, Vps29, H2aj
R-HSA-5687128	**MAPK6/MAPK4 signalling**	6.94	11/89	Cdc42, Pak2, Prkacb, Psma2, Psmb1, Psmb9, Psmc2, Psmd2, Psmd12, Psme2, Rac1
R-HSA-5358351	Signalling by Hedgehog	6.29	13/149	P4hb, Prkacb, Psma2, Psmb1, Psmb9, Psmc2, Psmd2, Psmd12, Psme2, Tubb2a, Tuba1a, Tubb6, Tuba1c
R-HSA-9755511	**KEAP1-NFE2L2 pathway**	6.12	11/107	Csnk2a1, Hmox1, Psma2, Psmb1, Psmb9, Psmc2, Psmd2, Psmd12, Psme2, Txnrd1, Dpp3
R-HSA-8878171	Transcriptional regulation by RUNX1	4.73	14/237	Csnk2a1, Prmt1, Psma2, Psmb1, Psmb9, Psmc2, Psmd2, Psmd12, Psme2, Smarcc1, Smarcc2, H2ac14, H3c1, H2aj
WP4786	Type I collagen synthesis in the context of osteogenesis imperfecta	5.02	6/33	P4ha1, P4hb, Plod1, Plod2, Ctrap, P3h1
R-MMU-445989	TAK1-dependent IKK and NF-kappa-B activation	3.87	7/35	Hmgb1, Uba52, Ubb, Ubc, Usp14, Rps27a, Ube2n
R-MMU-2173788	Downregulation of TGF-beta receptor signalling	2.90	4/15	Uba52, Ubb, Ubc, Rps27a

7.5 Discussion

This chapter delves into the characterization of differentially expressed proteins and biological processes across various stages of OA — early-stage (right knee in the 30°TO group) and progressive stage (left knee in the 30°TO group) — and examines the effects of pharmacological treatments (30°TO BMP group and 30°TO APS group). The findings validate significant molecular level changes within the OA model induced by varus malalignment (mechanical stress), highlighting processes such as collagen formation, extracellular matrix degradation, endochondral ossification, inflammatory-related process (e.g., VEGFR2 signalling), and metabolic response.

Moreover, it is evident that mechanically induced remodelling in OA can be mitigated through early pharmacological interventions, but cannot completely halt OA progression if the mechanical stimuli persist. BMP treatment notably influences mechanically stressed-induced pathways, including RUNX and MAPK signalling, along with metabolic regulation by reducing fatty acid oxidation and enhancing

glucose metabolism. Conversely, APS treatment has a pronounced effect on collagen synthesis and the reestablishment of cartilage and bone homeostasis, marked by an increase in non-canonical Wnt signalling pathway and Rho GTPases signalling, and the suppression of TGF-beta signalling.

The following discussion aims to deepen the understanding of the biological processes enhanced in OA cartilage and how pharmacological treatments modulate these processes. These processes will be correlated with evidence from previous chapters on joint cartilage degradation (Chapter 4), structural alterations (Chapter 5), and alterations in gait patterns (Chapter 6). Additionally, it will compare these findings with those from other studies, offering a richer context for the observed molecular dynamics in OA pathogenesis and treatment.

7.5.1 Understanding enhanced biological processes in OA cartilage

Mechanical forces influence cellular metabolism and potentially incite tissue remodelling by triggering a cascade of reactions in cells, a process known as mechano-transduction (Stoltz et al., 2018). In the OA cartilage, the activated biological processes primarily involve collagen formation, collagen degradation (CTSB, CTSD), VEGFA-VEGFR2 signalling, endochondral ossification (SERPINH1, COL2A1, STAT1), and inflammation processes, including Interleukin-12 signalling (not very significant) and neutrophil degranulation.

The findings related to cartilage processes in 30°TO left knee reveal a co-existence of cartilage formation, degradation, and endochondral ossification processes, consistent with the histology results (Chapter 4, Section 4.5.1). Specifically, cartilage formation is associated with SERPINH1, COL1A2, COL3A1 upregulation, degradation is associated with CTSB, CTSD upregulation, and endochondral ossification correlates with SERPINH1, COL2A1, STAT1, SCIN upregulation.

Previous studies confirmed that expression levels of type I collagen α2 chain (COL1A2), and type III collagen α1 chain (COL3A1) genes increased in OA cartilage, and differences correlated with radiographic measures of OA severity (Clements et al., 2009). Matrix-regulatory agents such as Serpin H1 might contribute to abnormal chondrogenesis, thereby contributing to OA development (Rocha et al., 2013). In addition, Cathepsin B (CTSB) is a lysosomal cysteine protease involved in proteolysis. It has been recognized as a marker of the dedifferentiated chondrocyte phenotype and plays a role in cartilage destruction in OA, as well as pathological proteolysis in rheumatoid arthritis (Baici et al., 2005).

The results indicate an increase in VEGFA-VEGFR2 signalling in both OA knee (more significant) and APS-treated knee, with the medial compartment showing more significant upregulation. This aligns with previous studies that confirmed the increased expression of VEGF-A and VEGFR2 in ACLT-induced OA rats, correlating with OA severity (Qian et al., 2021). Additionally, it has been demonstrated that mechanical force acting on human chondrocytes can induce VEGF expression (Beckmann et al., 2014). Healthy articular cartilage does not contain any blood vessels, but angiogenesis has been observed at

the osteochondral junction and in non-calcified cartilage in OA (Walsh et al., 2007). The expression of VEGF in chondrocytes is a critical characteristic of OA, distinguishing it from rheumatoid arthritis (RA) (Walsh et al., 2010). Inhibitors of VEGF-receptor 1 have shown to reduce pain in experimental models of OA (Das et al., 2018).

VEGF is somewhat unique in that it appears to perform distinct functions in cartilage and bone development. In articular cartilage, VEGF is required for chondrocyte differentiation into a persistent phenotype (Col2a1-expressing cells), but it does not appear to play a significant role in maintaining the cartilage phenotype after its formation (Nagao et al., 2017). Some studies suggest that OA cartilage might lose its resistance to vascular invasion, which distinguishes it from normal articular cartilage and may play a critical role in OA pathogenesis (Smith et al., 2003). However, in the growth plate, VEGF and HIF-1α act coordinately as survival factors for chondrocytes, maintaining cartilage metabolism in hypoxic regions (Maes et al., 2012). VEGF is also expressed by hypertrophic chondrocytes for timely ossification of primary and secondary centers in endochondral bones.

This may explain why VEGF signalling remains significantly upregulated in the APS treatment group; under APS treatment, VEGF might play a suppression role in hypertrophic chondrocytes ossification. In a prior study regarding PRP (a cell product similar to APS), it was demonstrated that PRP exerts an antifibrotic effect, preventing the transformation of fibroblasts into myofibroblasts by increasing VEGFA-VEGFR signalling and thereby interfering with TGF-β1/Smad3 fibrosis signalling (Chellini et al., 2018).

Concerning the interleukin signalling and neutrophil degranulation identified in the study, these contribute to chronic inflammation. Low-level inflammation in knee cartilage is thought to play a critical role in OA development. The IL-12 signal is a pro-inflammatory pathway that, along with the VEGF signal, is associated with poor knee function and knee pain (Nees et al., 2019). Dysregulated neutrophil activation is reported to contribute to chronic inflammation and pathology of autoimmune diseases, such as rheumatoid arthritis (Fresneda Alarcon et al., 2021). However, the understanding of how this low-grade inflammation is maintained in the OA joint and whether the inflammatory pattern varies among different OA subtypes is limited (Moradi et al., 2015).

Interestingly, Robo signalling is the most enriched signalling pathway in both APS-treated OA limbs (in the APS treatment group) and in OA left limbs (in the 30ºTO group). Robo signalling was recently discovered to play a role in regulating bone metabolism, preserving a dynamic balance between bone formation and bone resorption through acting on osteoclasts and osteoblasts (Kim and Koh, 2019). The Rac1 Rho GTPase, identified in this analysis, is a major downstream molecular signal of the Robo receptor (Shin et al., 2020, Jiang et al., 2022).

Finally, it is noteworthy that the right knee samples in 30ºTO group, classified as early-stage OA with minor cartilage defects based on histology results (Chapter 4), showed a suppression of the cartilage

degradation pathways that were active in the left knee samples (section 7.4.1.1). This suppression of degenerative processes likely contributes to chondrocyte stability and maintenance of the cartilage matrix, possibly halting or slowing the progression of OA. Therefore, these findings reveal significant variations in the regulation of key biological processes between progressive and early OA conditions. These differences could potentially offer insights into the pathophysiology of OA and inform future therapeutic strategies.

7.5.2 Characterizing the effects of BMP treatment on OA cartilage biology

Next, this work delves into the upregulated biological processes or pathways in BMP-treated cartilage, shedding light on the dual role of BMP in both promoting cartilage repair after mechanical injury (Dell'Accio et al., 2006) and initiating chondrocyte hypertrophy and osteophyte formation when the cartilage repair is complete (Scharstuhl et al., 2003), which were concluded from previous histology (Chapter 4) and micro CT (Chapter 5) results. Very few *in vivo* studies report how BMP affects the OA process. There is one study that reported a significant increase in BMPs and Runx-2 in an exercise-induced OA model, suggesting that BMP potentially upregulates the expression of Runx-2. Nonetheless, whether this regulation depends on either the Wnt or MAPK pathway necessitates further research.

This discussion subsequently explores the influence of BMP signalling on metabolism. While many studies address the role of metabolism (including glucose, amino acid and fatty acid metabolism) in disease (Zoch et al., 2016, Wei et al., 2015) the effect of bone formation pathways like BMP signal on glucose and fatty acid metabolism in cartilage and bone homeostasis is still largely unknown. Therefore, the results of BMP treatment are explained based on the evidence of how BMP signalling controls whole-body metabolism.

Interestingly, BMP signaling has been documented to play a dual role in either promoting or repressing fatty acid oxidation (Yang et al., 2020). BMP-4 treatment can repress the expression of β-oxidation genes (such as Acadm, Acadvl, Hadha, and Hadhb) in brown pre-adipocytes (Modica et al., 2016). The data (high expression of Acadm and Adadyl gene in non-BMP treated tissue) strongly aligns with the notion that BMP signaling represses fatty acid metabolism. On the other hand, BMP-4 and BMP-7 were found to stimulate mitochondrial activity and fatty acid uptake in mature brown adipocytes (Townsend et al., 2013), suggesting a complicated relationship between BMP and fatty acid metabolism in bone homeostasis of OA disease.

Regarding glucose metabolism's support of bone formation and collagen synthesis (Zoch et al., 2016, Wei et al., 2015), a recent study reported that BMP-2 can upregulate glucose metabolism by increasing the glucose transporter Glut1's expression level, resulting in chondrocyte proliferation and hypertrophy during endochondral bone ossification (Lee et al., 2018). Although the link between BMP signalling and metabolism is not fully understood, this study might provide a new perspective for identifying prognostic biomarkers and therapeutic targets, where energy metabolism might be a novel downstream

mechanism of the BMP signalling pathway in regulating cartilage homeostasis. Further studies are needed to clarify how BMP signalling affects fatty acid metabolism in cartilage and bone homeostasis.

The results also indicate an upregulation in the "interleukin-7 response" biological process in the left medial compartment of the BMP-treated group, when compared both to the left lateral compartment and to the right limb. It seems that IL-7 response is stimulated by BMP effects and overloading conditions together. IL-7, produced by articular chondrocytes and upregulated in OA patients (Long et al., 2008), is known to induce the production of metalloproteinase (MMP)-13 and the release of proteoglycan from cartilage (van Roon and Lafeber, 2008). However, the (patho)physiological triggers for IL-7 production in chondrocytes *in vivo* have yet to be elucidated. The results suggest that mechanical stress add BMP may play a role in this process.

Additionally, the KEAP1-NFE2L2 pathway is highly enriched in BMP/APS treated left limbs compared to right limbs. NF-E2-related factor 2 (Nrf2) is a sensitive redox transcription factor, and Kelch-like ECH-associated protein 1 (Keap1) is its specific repressor. The KEAP1-NFE2L2 pathway (also called Nrf2/Keap1) plays a key role in regulating cellular responses to oxidative stress (Motohashi and Yamamoto, 2004). This pathway is known to mitigate oxidative stress, thereby protecting against chronic inflammation and cancer. Future investigations could further elucidate these observations (Hintsala et al., 2016, Zhang et al., 2015).

Runt-related transcription factors (RUNX) such as RUNX1, RUNX2, and RUNX3, and MAPK signalling, were significant upregulated in the left limb for both the BMP-treated group and APS treated group, with the former (BMP-treated group) showing much more significance. The interplay between RUNX and MAPK signalling plays a crucial role in mechanical stress-induced OA pathogenesis, by controlling the expression of genes that regulate cell differentiation and progression through the cell cycle (Komori et al., 1997). RUNX-2 has been reported to promote bone mineralization by triggering osteoblast differentiation, and it contributes to OA pathogenesis by inducing chondrocyte hypertrophy and breakdown of the extracellular matrix after joint instability (Kamekura et al., 2006, Franceschi and Xiao, 2003). Furthermore, the MAPK signalling pathway can activate RUNX-2, playing a crucial role in the early differentiation of osteoblasts in response to mechanical stress (Meyers et al., 2004, Fan et al., 2006).

Recent reports have shown that RUNX is an upstream regulator of mechanical stress-induced ADAMTS-5 and MMP13, both of which are critical proteases in cartilage matrix degradation (Saito et al., 2013). However, it is disheartening that inhibitors of ADAMTS and MMP do not show significant clinical benefits in OA, likely because inhibiting a specific degradative activity does not suppress the underlying tissue catabolism, but rather promotes an irreversible extracellular matrix (ECM) loss (Burrage and Brinckerhoff, 2007). Therefore, a wider target, such as their upstream regulators RUNX

could be the potential target for OA therapy (Saito et al., 2013). However, the regulatory mechanisms of mechanical stress effect on these signalling are unclear, warranting further investigation.

In this study, a significant upregulation of Col11a2, indicative of collagen formation, was noted in both BMP and APS-treated groups. The upregulated expression of Col11a2 and the corresponding enhancement of the supramolecular fiber organization, as indicated by the Gene Ontology (GO) analysis, could be interpreted as an attempt by the cartilage to restore its organization and stability. Col XI collagen is known to contribute to the mechanical properties of cartilage tissue (Holyoak et al., 2018, Lawrence et al., 2018). However, whether this upregulation has a positive or negative impact is not known.

Type XI collagen, a fibrillary collagen, influences the formation of Type II collagen (the primary collagen type in cartilage) and Type I collagen collagen (Luo and Karsdal, 2016). The presence of Type XI collagen is crucial for organizing and reinforcing the Type II collagen fibril network. This network forms a dense ECM that provides structural support to chondrocytes (Lawrence et al., 2018). A previous study showed that the absence of col11a2 in zebrafish negatively affected the mechanical properties of the developing joint, leading to premature OA (Lawrence et al., 2018). However, another study produced opposite results, revealing that cartilage tissue with Col11a1 gene depletion demonstrated reduced load-induced cartilage damage, thinner and less dense cortical bone, and thicker cartilage (Holyoak et al., 2018). As such, further research is necessary to definitively determine the impact of Type XI collagen on cartilage health and stability.

7.5.3 Exploring the role of APS treatment in regulating biological processes in OA cartilage

This study further investigated the changes of protein intensity after autologous platelet solutions (APS) treatment; there are few studies that look into the changes of cartilage proteins after APS injection in OA individuals. This is the first report which extensively investigated the protein expression differences before and after APS injections. The differentiated protein profiles reveal a general reduction in the previously discussed pathogenic pathways in OA, and an emergence of pathways potentially implicated in cartilage repair and remodeling. The activated biological processes primarily involve 1) Collagen formation (Col11a2), 2) Beta-catenin independent WNT signalling 3) ROBO signalling (MMP3), and 4) KEAP1-NFE2L2 pathway. The significant alterations in protein expression after APS treatment seem to suggest a shift in biological processes towards tissue repair and reestablishment of homeostasis.

The APS therapy has been reported to have regenerative potential in in vitro studies. APS injection has shown to protect cartilage explants and inhibit MMP-13 production from IL-1α and TNF-α-induced cartilage degradation (Bertone et al., 2014, Woodell-May et al., 2011).

In this study, the non-canonical Wnt signalling pathway and Rho GTPases signalling were activated, with the typical genes (e.g., RAC1, RAC3, RHOG, CDC42) significantly increased in APS-treated OA

knee (left knee). Although there is no published data about the effects of Rho GTPases on OA, RAC1 and CDC42 have been identified to play a positive role in chondrogenesis and chondrocytes, functioning in promoting the N-cadherin-mediated chondrocyte condensation (Woods et al., 2007), and upregulating MMP 13 and COLX activity (Wang and Beier, 2005). Based on this evidence, this study suggests that Rho GTPases signalling might play a critical role in OA development, and may not only be limited to cartilage degradation but also involve in cartilage repair, remodelling, and osteochondral bone remodelling. The definitive role and its cross-link with Wnt signalling need to be further investigated. It can be a potential marker and target for modulating the signalling.

Canonical Wnt signalling, which has shown upregulation in OA cartilage, has been well established to induce chondrocyte maturation, hypertrophy, and endochondral ossification during OA development (Day et al., 2005, Zhu et al., 2013). The activation of bone calcification, as well as the expression of MMPs and VEGF, require the activation of canonical Wnt signalling during bone formation (Tamamura et al., 2005). In chondrocyte development, most studies support that Wnt/β-catenin signalling may lead to cartilage matrix catabolism and a shift in the stable phenotype of chondrocytes (Yuasa et al., 2008). However, in APS-treated OA cartilage, a significant upregulation of the non-canonical Wnt signalling pathway (β-catenin-independent Wnt signalling) was identified in addition to the still present canonical Wnt signalling for cartilage degeneration process (Table 7-13). It is noteworthy that while β-catenin-independent Wnt signalling is also upregulated in OA cartilage in the study, it is not among the most significantly upregulated pathways.

Compared to the well-recognized canonical Wnt signalling, the non-canonical Wnt signalling pathway has attracted relatively less focus. It is characterized as being β-catenin/TCF-independent and functions through the action of Rho GTPases to promote cell organization in a specific orientation (Fanto et al., 2000). Recent studies indicate that Rho GTPases have a crucial role in chondrocyte growth, maturation, and death in bone development (Wang and Beier, 2005). Most studies support that Rho GTPases accelerate the chondrocyte terminal differentiation (hypertrophic change) in the growth plate (Wang and Beier, 2005), but whether it plays a positive regulation or antagonistic effect on chondrocyte development in articular cartilage and osteoarthritis is still poorly understood (Woods et al., 2005).

In addition to cartilage and bone harmonizing related biological processes, the results show that upregulated proteins are also enriched in translation-related pathways in both OA knees and APS-treated knees, such as L13a-mediated translational silencing of ceruloplasmin expression and ribosome dysfunction. Previously, it was believed that major proteomic expression changes, both upregulated and downregulated protein synthesis, were primarily due to changes in mRNA transcriptomics, and numerous studies focused on transcriptomic changes in OA. However, it was only recently demonstrated that protein synthesis can also be regulated at the level of ribosome activity (van den Akker et al., 2022). This study confirmed that ribosome protein translation activity is elevated in the early stages of OA and can persist to later stages (Katsara et al., 2017), aligning with the findings in this research. Nevertheless,

given the complexity of ribosome mechanisms and the fact that research in this field related to osteoarthritis is only just emerging (van den Akker et al., 2022), further studies are needed to clarify the alterations in ribosome biogenesis and function related to osteoarthritis pathogenesis. As the central hub of cellular protein synthesis, the ribosome might be a potential target contributing to osteoarthritis treatment (Venturi and Montanaro, 2020).

7.5.4 Characterizing the overloading effects on left medial compartment of OA cartilage

As discussed in Chapters 1 and 5, the varus alignment causes the weight-bearing axis to deviate from the joint centre, shifting it to the medial compartment, thereby replicating a natural mechanical overloading condition in the medial compartment of the left limb. This section correlates the molecular response to this abnormal mechanical loading stimuli with histological (Chapter 4) and imaging-level (Chapter 5) structural alterations, as well as with gait pattern alterations (Chapter 6) in response to mechanical loading, in the 30°TO group and BMP/APS-treated groups.

In the **30°TO group**, the left knee, which presents varus alignment, displays a significantly higher number of differentially expressed proteins compared to the sham group, while the number of differentiated proteins was low in the right (contralateral) knee (Section 7.4.1.1). These findings align with histological and micro-CT analyses, where the right knee did not exhibit significant changes in cartilage (Chapter 4) or subchondral bone volume (Chapter 5) measurements. Nevertheless, gait analysis in Chapter 6 revealed significant alterations in several gait parameters, some of which were not evident in the left gait, suggesting a compensatory mechanism in the contralateral gait. This discrepancy prompts further exploration of gait compensatory mechanisms in OA and their potential to address the limitations of biological changes in the right knee.

Based on the analysis, the 30°TO left knee (both compartments) exhibited significant upregulation of collagen formation and bone ossification-related pathways. Subsequently, when comparing the medial compartment with the lateral compartment in the 30°TO left knee (Section 7.4.1), collagen formation was significantly upregulated in the medial compartment (overloading condition), but bone ossification did not show differential upregulation, suggesting that bone ossification is not localized to the mechanically stimulated overloaded area but occurs in both compartments. This is corroborated by the results presented in Chapter 5, Figure 5-10, which demonstrated a significant reduction in bone volume in both compartments, with no notable difference between the left medial and lateral compartments. However, clear differences in collagen changes between these compartments (more significant in medical compartment) are consistent with histological results (Chapter 0), raising questions about the dynamic equilibrium between matrix synthesis and bone breakdown under varying loading conditions in OA.Comparing the left medial compartment to the lateral compartment of the **BMP-treated group** revealed a significant upregulation in the “interleukin-7 response” and “gluconeogenesis” biological processes under the overloading condition with BMP treatment (Section 7.4.2). This indicates that both

the IL-7 and glucose responses are stimulated by the combined effects of BMP and overloading. IL-7, which is produced by articular chondrocytes and upregulated in OA patients (Long et al., 2008), is implicated in the induction of MMP-13 production and proteoglycan release from cartilage cartilage (van Roon and Lafeber, 2008). Yet, the precise triggers for IL-7 production in chondrocytes *in vivo* remain unclear, suggesting a potential role for the combined mechanical stress and BMP in this process.

When comparing the left medial compartment to the lateral compartment of the **APS-treated group**, pathways related to collagen degradation and the IL-17 pathway, along with high MMP-3 expression, were notably active, whereas collagen formation was more dominant in the entire left limb compared to the right limb in this APS-treated group (Section 7.4.3). This indicates that although APS treatment appears effective in promoting collagen formation, it may not completely halt cartilage degradation if the mechanical overloading stimuli persist.

7.5.5 Proteomics results among different animal models.

7.5.5.1 The model in this study is a mechanically induced OA model

The extra-joint surgery in this study was designed to minimize inflammation noise due to the surgery procedure. It is confirmed there is an acute inflammation and prolonged low-level inflammation up to 4 weeks in the circulating blood. However, without harvesting cartilage post-surgery, it remains uncertain if the cartilage inflammation is unregulated at other timepoints in this model.

There is still evidence that helps distinguish whether the OA in this model arises from mechanical factors rather than inflammatory factors. Fn1 and MMP (related to inflammation response) were detected in the 5-month cartilage proteomics results, but they were not differentially expressed. Moreover, although interleukin-related pathways slightly increased, genes specifically related to inflammation were not detected as differentially regulated. Therefore, it can be inferred that there wasn't a detectable inflammation signal difference between the unoperated and operated limbs.

In contrast, in the mechanically-induced model with intra-articular surgery - the MMT model (Salazar-Noratto et al., 2019b), a variety of inflammatory downstream molecules including IL1, Tnfα, Spp1, and MMPs are upregulated, but they were not differentiated in the OA model in this thesis. This current model, therefore, can be described as a mechanically induced model generally not associated with substantial inflammation. It presents a purely mechanical OA condition and evaluate how the biomechanical environment in isolation affects OA onset without intra-articular damage.

The limitation of this cartilage proteomics study is the single harvest timepoint (at week 20 explored in this work. Therefore, there might be molecular changes (stages) that were not captured. It remains necessary to distinguish whether these changes are indeed from mechanical stress or if they are the downstream of inflammatory processes. A useful approach for future research could be to harvest the

cartilage at earlier timepoints after the surgery. Despite these limitations, this work provides a baseline for cartilage molecular changes in a purely mechanical-induced OA model.

7.5.5.2 Proteomics results of OA cartilage in other models

There have been very few cartilage proteomics studies conducted on rat models. The pathways detected in this mechanically-induced model differ significantly from those in the MIA-induced model. This is primarily due to the fact that the MIA-induced OA model has been confirmed to exhibit dramatic differences from human OA at the transcriptome level (Barve et al., 2007). That study confirmed that matrix degradation and inflammatory genes are upregulated in the MIA model to a much greater extent than in human OA tissue (Barve et al., 2007).

The results of the model in this thesis are more similar to proteomic studies in other mechanically induced OA models (Parra-Torres et al., 2014b, Salazar-Noratto et al., 2019a, Duclos et al., 2010a). For instance, in the partial meniscectomy followed by high-impact exercise (representing early-stage OA), most differentially expressed proteins and enriched pathways detected in that model were also differentially expressed in this study's model. Examples include glycolysis and energy metabolism, cartilage matrix remodelling (Col2a1), and cellular responses to stress (Parra-Torres et al., 2014c). Therefore, apart from a few inflammatory downstream molecules that are more significant in other mechanical models (as discussed above), there are no other notable differences between this extra-articular cartilage mechanical model (purely mechanically induced) and other intra-articular cartilage surgery-induced mechanical models (mechanically and inflammation-induced) at later harvest timepoints (OA progressive stage).

7.5.5.3 Proteomics studies on human cartilage

Although there are very few animal studies of OA cartilage proteomics, several human studies have compared normal individuals and patients with osteoarthritis. Differentially expressed proteins are mainly involved in the extracellular matrix(ECM) turnover, such as activated protease expression in OA cartilage (Wu et al., 2007), and glycolysis and energy production, such as alcohol dehydrogenase (ADH) and enolase (ENOA) (Guo et al., 2008). These activated biological process and molecules are consistent with findings in the model in this thesis. Similarly, another study compared the proteomic profiles of cartilage from different cartilage disorders and found similar qualitative profiles in patients with early OA, rheumatoid arthritis, or chondrosarcoma. Several of the shared proteins identified were found to participate in metabolism (ADH, ADK, ENOA) and extracellular matrix cartilage composition (Vincourt et al., 2006).

However, human donors are usually in an advanced stage of OA. Therefore, some inflammation and degradative products, such as COMP, aggrecan (ACAN), and fibronectin (FN), which were suggested as potential OA biomarkers (Garcia et al., 2006), and found to be more abundant in the deep area than

the superficial area (Cillero-Pastor et al., 2013) were not differentially expressed in the model in this thesis.

In summary, this chapter has elucidated the complex biological processes and pathways activated in osteoarthritic cartilage and following APS/BMP treatments, highlighting the roles of mechanical stress and therapeutic interventions in modulating cartilage repair and homeostasis. The proteomics analysis revealed key differences in molecular responses between mechanically induced models and those influenced by inflammation, offering insights into OA's progressive and repair mechanism. It highlights the discovery of key processes such as collagen formation, extracellular matrix degradation, endochondral ossification, inflammation, and metabolic responses across early-stage and progressive stages of OA, as well as after BMP and APS treatments. The analysis reveals that mechanical stress-induced remodelling in OA can be mitigated by these treatments, with BMP affecting mechanically stressed pathways and metabolic regulation, and APS significantly enhancing collagen synthesis and cartilage and bone homeostasis through pathways like non-canonical Wnt signalling and Rho GTPases signalling. But the treatments cannot completely halt OA progression if the mechanical stimuli persist. By comparing these findings with human OA studies, the research provides a valuable link between experimental models and clinical reality, underscoring the potential for developing targeted therapies based on these molecular insights.

8 Conclusion

8.1 Summary of findings

OA is a prevalent joint disease and a leading cause of disability worldwide (Abramoff and Caldera, 2020). Due to its complex nature with various biological and mechanical influences, there are challenges in developing a long-term overloading model to mimic the natural pathogenesis of OA and finding consistent measurements for monitoring and interpreting OA conditions.

A review of the literature in Chapter 1 highlighted confusion in categorizing mechanically-induced OA preclinical models, as well as in the terminology and description linking the model to OA clinical phenotypes. This review identified that the mechanical overload OA phenotype should be further subcategorized into post-traumatic and chronic overloading OA. Currently, there is no representative model that closely mimics the natural mechanical condition of the mechanical overloading phenotype of OA. The overuse of post-traumatic osteoarthritis (PTOA) models and chemical injection models, which induce an acute intra-articular inflammatory response to trigger OA, may present distinct etiologies and disease progression.

Based on the review's findings, there is a highlighted inadequacy of current models in presenting chronic overloading. Therefore, the objective of this PhD thesis was to develop a tibial malalignment-induced OA model to create a model of chronic primary OA resulting from natural chronic overloading, with varying levels of severity. This model, for the first time, addresses the deficiencies of previous mechanical OA models, offering a promising approach to present the chronic natural course of primary OA (Chapter 2). The model was then used to assess histological cartilage degradation (Chapter 4), radiographic structural changes (Chapter 5), gait patterns (Chapter 6), and cytokine levels (Chapter 7) in this long-term overloading-induced OA model. Finally, the model was utilized to evaluate the response to pharmacological treatments (throughout Chapters 4-7).

This study explains a series of OA joint changes primarily through mechanical interactions. The 30º-varus alignment increases loading in the medial compartment, leading to the activation of cartilage degradation, fabrication and endochondral ossification biological processes, resulting in cartilage loss (thickness and elasticity reduction) in the medial compartment of the operated leg. This, in turn, increases the mechanical loads in the subchondral bone. To accommodate these new mechanical requirements, the system modifies bone mass and distribution via bone resorption or remodelling. the vascular growth process in the subchondral bone during endochondral ossification. Additionally, there are compensatory changes to the unaffected limb in weight distribution and support in quadrupeds. This opens the way to linking microstructural joint damage, gait analysis, and ultimately, the pathogenesis and molecular changes of the disease.

Firstly, the study successfully established a **tibia osteotomy (TO) model** with confirmed tibial varus malalignment with different degree (0º, 10º, 30º) in the left hind limb at five months (20 weeks) post-osteotomy. Additionally, a workflow for developing autologous protein solution (APS) biologics was confirmed, demonstrating successful preparation of APS therapy from individual rats throughout the course of disease. APS, known for its anti-inflammatory properties, and BMP, a single-target growth factor, were selected to potentially prevent the onset of OA in the model.

Next, Histological analysis revealed distinct cartilage changes in response to tibial malalignment. The sham group displayed a homogeneous proteoglycan-rich matrix throughout the entire cartilage. The left limb of 10º tibial TO group and right limb of 10º TO group exhibited early-stage OA characteristics, with intact cartilage surface but focal superficial fibrillation. In contrast, the 30º tibial osteotomy group showed progressive OA with a layered pattern. The superficial layer of the OA cartilage displayed decreased matrix staining (proteoglycan loss), while the middle layer showed increased staining, suggesting chondrocyte hypertrophy. Vertical fissures and matrix loss extended to the deep layer of the cartilage. The treatment groups displayed intermediate cartilage characteristics, with APS treatment showing greater proximity to healthy cartilage and BMP treatment resembling the repair stage of hypertrophic differentiation. BMP treatment resulted in focal cartilage thickness increase, particularly in the central weight-bearing zone, while APS treatment led to uniformly increased cartilage thickness with an intact surface. In the microscope results, it was observed that in the 30ºTO-BMP treatment group, chondrocyte size (fibrocartilaginous and osseous tissue) significantly increased compared to both the 30ºTO group and the 30ºTO-APS treatment group. This suggests that BMP treatment in OA can help cartilage repair but may also enhance chondrophyte formation. In contrast, the 30ºTO group with APS treatment recovered the cartilage well, displaying uniformly increased cartilage thickness with an intact and even surface.

Micro-CT analysis unveiled a series of changes in joint mechanics primarily driven by mechanical interactions. The 30º malalignment increased loading in the medial compartment, leading to cartilage loss and subsequent modifications in subchondral bone to accommodate the new mechanical requirements. These modifications included an increase in subchondral bone plate (Sb.P) thickness, a decrease in trabecular bone volume fraction (BV/TV), a decrease in trabecular bone thickness (Tb.Th), and an increase in in trabecular spacing (Tb.Sp). Osteophytes, indicative of joint stabilizing and remodelling due to the mechanical imbalance, were observed in the periphery of the medial compartment. BMP treatment showed potential remodelling effects on subchondral bone repair with significant Sb.P decrease and increased Tb.Th and Tb.Sp. In contrast, the APS treatment group showed minimal changes in trabecular bone structure, suggesting a limited impact on remodelling. It is concluded that malalignment appears to stimulate osteophyte formation, with BMP administration potentially enhancing this growth.

Gait analysis was validated as an effective approach for assessing OA severity in the biomechanical OA model and following pharmacological treatment. The discrimination model effectively differentiated between impaired and healthy gait in both limbs. After treatment, the gait in the left limb did not completely return to normal, unlike the right (contralateral) limb. It was noted that both limbs possess important (contributory) variables in the gait coordination and paw feature (weight support) categories, with the right limb showing more pronounced differences. This suggests compensatory changes to the unaffected limb in weight distribution and support in quadrupeds. Among these variables, Paw Area at Peak Stance and Max dA/dT were consistently the most contributory variables across all discrimination models for both limbs. The study also observed differentiation between the two treatment groups, with the APS group exhibiting a closer similarity to the sham group, potentially indicating greater effectiveness in restoring gait coordination features.

Finally, Untargeted LFQ-MS proteomics characterized proteomic changes in rat serum and articular cartilage within the OA model induced by varus malalignment (mechanical stress). Serum proteomics revealed a progression from acute systemic inflammation, inflammation elimination to OA initiation in the model, effectively isolating the effects of surgery-induced local inflammation from the onset of OA. This effectively separates OA induction in this model from inflammatory artifacts—a frequent critique of most mechanical OA models. The cartilage proteomics highlighting the processes relevant to OA pathogenesis and mechanical tress, including collagen formation, extracellular matrix degradation, endochondral ossification, inflammatory-related process (e.g., VEGFR2 signalling), and metabolic response. Moreover, it is evident that mechanically induced remodelling in OA can be mitigated through early pharmacological interventions, but cannot completely halt OA progression if the mechanical stimuli persist. BMP treatment notably influences mechanically stressed-induced pathways, including RUNX and MAPK signalling, along with metabolic regulation by reducing fatty acid oxidation and enhancing glucose metabolism. Conversely, APS treatment has a pronounced effect on collagen synthesis and the reestablishment of cartilage and bone homeostasis, marked by an increase in non-canonical Wnt signalling pathway and Rho GTPases signalling, and the suppression of TGF-beta signalling.

The comprehensive exploration of OA in our study is underscored by the intricate correlations between the histopathological, imaging, biomechanical, and molecular analyses conducted across the chapters (Figure 8-1). Chapter 2's establishment of a tibial malalignment-induced OA model sets the foundation, with Chapters 3's introduction of BMP and APS treatments directly influencing the outcomes observed in the subsequent analyses. The histopathology results presented in Chapter 4, identified as the gold standard for assessing OA, not only validate the model but also correlate with the subchondral bone changes observed in micro-CT (Chapter 5), the alterations in gait patterns (Chapter 6), and the proteomic changes (Chapter 7). The micro-CT findings elucidate the structural adaptations in the bone that correspond to the severity of cartilage degradation, which are in turn reflected in the altered gait

mechanics, underscoring the biomechanical consequences of joint malalignment (abnormal loading stimuli) and subsequent OA progression. Gait pattern alterations, highlighted by markers such as paw area at peak stance and max dA/dT, bridge the macroscopic structural changes with functional outcomes, and gait compensatory mechanisms have the potential to address the limitations of biological changes in the contralateral knee assessment. Furthermore, the proteomic data offer a molecular dimension that correlates with the histological and imaging findings, providing a deeper understanding of the biological processes underpinning the structural and biomechanical changes observed. Together, these correlated findings offer a comprehensive overview of the mechanical factor (varus alignment) on OA pathogenesis and treatment efficacy, reinforcing the interconnectedness of the tissue-level changes, biomechanical functions, and molecular responses.

The caveats of the study include the limited animal sample size, which did not allow for more accurate predictive statistics in proteomics and selection of markers. Additionally, limitations in some equipment, such as microscope imaging and IHC, restricted our further analysis of chondrocyte repair differentiation. These limitations and the need for further studies will be discussed in Section 8.2.

In summary, this study uniquely confirms the impact of tibial malalignment, a mechanical factor, on OA development within a mechanically induced rodent OA model. Different degrees of malalignment were induced to create a model of chronic primary OA resulting from natural chronic overloading, with varying levels of severity. This model is confirmed to induce OA without significant experimental intra-articular trauma, thereby presenting the natural OA process and enabling the detection of early-stage OA changes in the absence of such inflammatory artifacts. This research also marks the first instance of using autologous protein solution therapy in experimental rodents, characterizing comprehensive biological and mechanical changes in the OA joint following APS and BMP injections. The OA joints exhibit a dualistic state, characterized by concurrent articular cartilage degradation and subchondral bone remodelling, alongside new osteophytic cartilage/osteophyte formation, complicating the application of biological treatments. BMP may play a dual role in OA; while potentially promoting chondrogenesis and subchondral bone repair in early-stage OA, it could also significantly contribute to the development of osteophytic cartilage/osteophytes in later stages. Conversely, APS emerges as a promising option for OA treatment, demonstrating significant therapeutic effects in this study by addressing both cartilage degradation and the formation of new osteophytic cartilage.

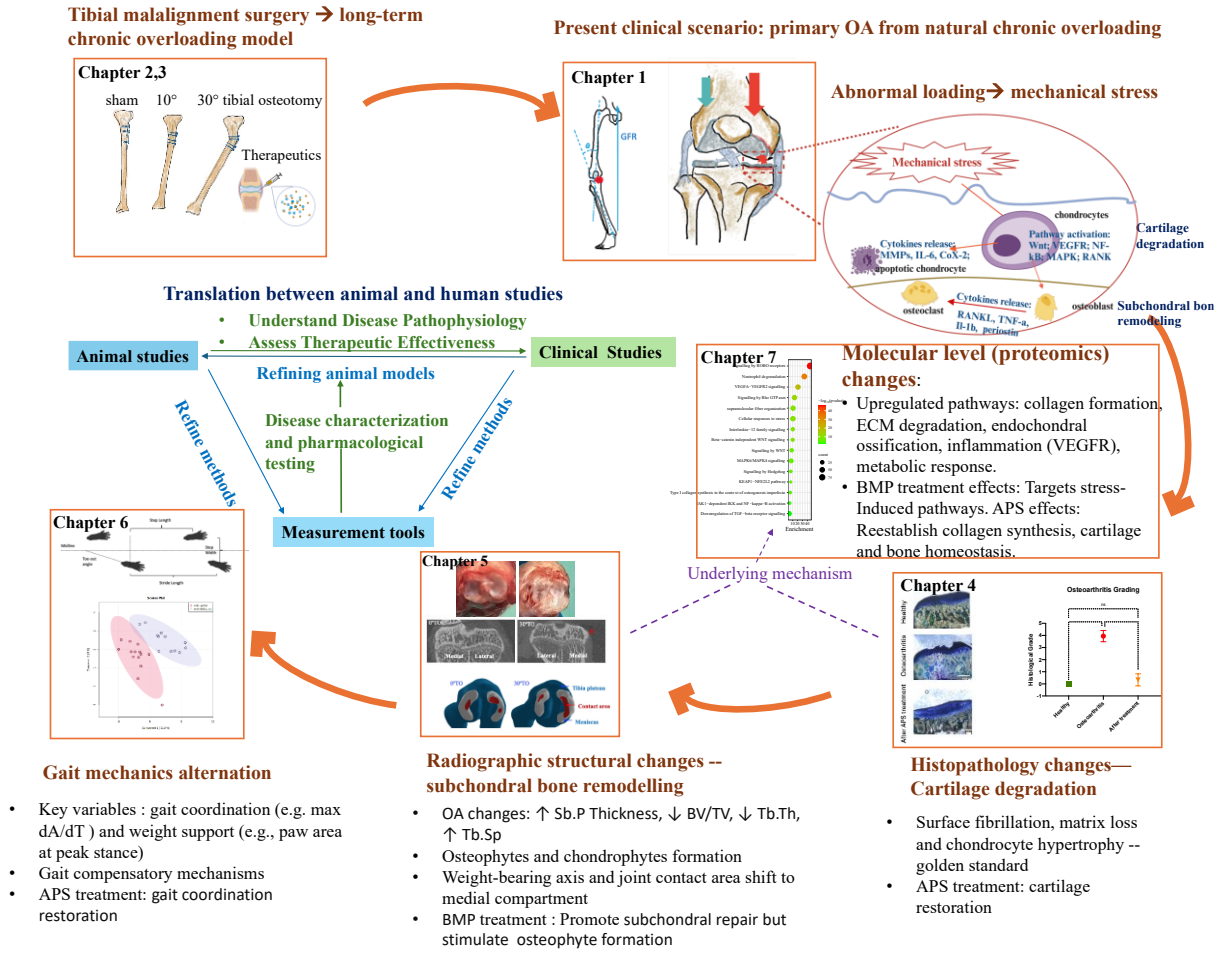

Figure 8-1 Comprehensive overview of thesis flow and the development of the chronic overload OA model. This figure connects the array of measurement outcomes from each chapter, showing how OA changes and treatments are evaluated. It also illustrates the transition from animal models to clinical relevance.

8.2 Perspectives and future works

Based on the biological and biomechanical outcomes from this thesis and the techniques developed, future research directions can be proposed. These directions are poised to provide further insights into the structural, mechanical, and molecular changes occurring in OA, encompassing diagnosis, pathogenesis, and therapy.

8.2.1 Further development of chondrophytes as an OA marker in MRI imaging

Based on the macroscopic dissection results of knee cartilage presented in Chapter 4, the potential of chondrophytes as an early-stage OA marker detectable via MRI is promising, offering significant advancements in human OA diagnostics. Currently, chondrophytes are challenging to detect with CT/micro-CT and tend to be overlooked in standard histological assessments due to their typical location in the posterior margin area. MRI, particularly using the T2 sequence, is adept at imaging regions of

cartilage that exhibit swelling (Calvo et al., 2004) or chondrophyte-related hypertrophy (Panzer et al., 2012), with the capacity to differentiate fat and water-rich tissue (oedema) contrasts effectively.

While radiographic features like joint space narrowing, osteophyte formation, cysts, and subchondral sclerosis are established markers of OA in X-rays and CT scans, MRI's role in OA diagnostics is growing, especially in the assessment of bone and soft tissue pathologies. Its ability to visualize detailed cartilage, subchondral BMLs, synovium, menisci, ligaments, and quantify glycosaminoglycan (GAG) in cartilage (Wang et al., 2018c, Link et al., 2017a, Brimmo et al., 2016b, Chaudhari et al., 2020), makes it invaluable for early OA detection and monitoring. However, the characterization of chondrophytes via MRI in OA assessments is rare, partly due to the high cost and operational constraints of MRI, which often limit the examination to single scan directions to minimize scan time. Typically, MRI studies focus on coronal section images to highlight joint space variations and cartilage thickness, yet sagittal or axial planes might be better suited for identifying posteriorly located chondrophytes (Accart et al., 2022, Panzer et al., 2012) .

The hypothesis proposed is that chondrophytes could serve as pre-radiographic markers for OA, indicating loading imbalances and an association with the high incidence of radiographic OA (the clinical definition of OA). Moreover, MRI-specific markers like subchondral bone edema, already associated with early OA indicators in clinical research (Libicher et al., 2005a), highlight MRI's transformative potential in OA diagnosis and treatment evaluation. This marker, prominent and easily identifiable in MRI images, has been observed in 71.5% of OA patients and is correlated with microdamage in subchondral trabecular bone, underscoring its diagnostic significance (Felson et al., 2001a). Further studies are needed to establish standard criteria for assessing OA characteristics in MRI and its scan sequences. Efficient image acquisition and postprocessing tools can reduce the scan time and help extend these imaging methods and their subsequent analysis techniques to study larger human population cohorts. This development could significantly impact the early detection of OA and the assessment of therapeutic efficacy, addressing the current limitations in OA imaging diagnostics and advancing our understanding of the disease's progression.

8.2.2 Deepening the understanding of the gait characteristics in OA rat model

For a better understanding of the gait pattern changes associated with loading changes, OA and its post-treatment effects, expanding the current spatial-temporal measurements to include 3D kinematics, kinetics and musculoskeletal modelling is crucial. The 3D kinematics, including knee adduction moments (KAM) and knee flexion moments (KFM), along with kinetics such as vertical ground reaction force (GRF) and medial knee joint contact force (derived from musculoskeletal modelling), need to be accurately quantified using an optical motion capture system and an anatomical model of the rat musculature. Deepening the understanding of gait characteristics in the OA rat model involves motion analysis, force analysis, and musculoskeletal dynamics to derive internal loading on tissues

(Eftaxiopoulou et al., 2014b, Cleather and Bull, 2011, Howard et al., 2000). Furthermore, the established rodent musculoskeletal model from the work of Britzman (2017) could be used for translating the kinematic and kinetics data.

Combining these spatiotemporal, kinematic, and dynamic analyses with existing rodent musculoskeletal models (Britzman et al., 2018b, Johnson et al., 2008) will allow for a more nuanced measurement of subtle gait changes (Eftaxiopoulou et al., 2014b). Furthermore, integrating these analyses with computational finite element modeling can provide tissue-specific insights into local biomechanical overload, a technique that has found extensive application in human studies (Zanjani-Pour et al., 2020a) and shows promise for preclinical rodent models of chronic overload OA. This approach will enhance our ability to quantify the complex biomechanical interplay in OA progression and evaluate the biomechanical outcomes of therapeutic interventions.

8.2.3 Deepening the understanding of OA pathogenesis from histology and proteomics perspective

Enhancing the understanding of OA pathogenesis is crucial for the development of advanced treatment strategies and diagnostic approaches. According to the **histological results** presented in Chapter 4, future studies should prioritize using immunohistochemistry to examine proteins that show significant differential expression in our proteomic analyses across various cartilage layers (identified as damaged, fibrillated, or intact layers). Using specific primary antibodies for immunostaining will assist in visualizing the different stages of chondrocytes across cartilage zones. Immunohistochemical markers such as Collagen II and aggrecan, which is associated with maintaining the chondrocyte phenotype, could be selectively detected in healthy articular cartilage. MMPs, RUNX2, and COL10, indicative of chondrocyte-hypertrophy and endochondral ossification, could be selectively to detect cartilage degradation during OA progression (Park et al., 2021).

Proteomics provides a semi-quantitative method to differentiate OA samples and evaluate treatment efficacy based on differentially expressed genes and enriched biological pathways, showing great promise for exploring the early mechanisms of OA and distinguishing the effectiveness of various therapies. Upcoming studies are expected to utilize LC-MS with Tandem Mass Tag (TMT)-labelled quantitative methods for accurate quantification of biomarkers identified in the OA model, and Gene Set Enrichment Analysis (GSEA) method to represents the enrichment of all gene sets' expression matrices in a pathway. Discovering and validating these markers in extensive studies could lead to the inclusion of a set of biomarkers for developing a diagnostic scoring scale, algorithm, or discrimination model. Additional proteomic studies are needed to elucidate the transition from chondrophyte to hypertrophic chondrocyte stages and ultimately to endochondral ossification. Understanding how modulation of these genes can affect chondrocyte hypertrophy may open new paths to mitigate degeneration or enhance desired repair processes (to permanent phenotype chondrocyte) in osteoarthritis,

providing significant insights into the disease's pathogenesis and potential treatments (Burr, 2004, Park et al., 2021, Aghajanian and Mohan, 2018).

8.2.4 Clinical translation

The established varus alignment model, which offers a chronic overloading scenario, presents the chronic natural course of primary OA. This marks a significant advancement in the preclinical study of early OA changes in non-trauma related, slowly progressive OA, and its early-stage interventions. Utilizing this model, future research can investigate the effectiveness of novel therapeutic strategies or molecular drugs. The application of micro-CT imaging has shown potential in early detection of OA-induced changes in subchondral bone, suggesting its utility for early diagnosis and monitoring treatment effectiveness in animal models through non-invasive techniques.

In the area of therapeutic strategies, this thesis establishes that OA results from or driven by mechanical factors such as femoral-tibia malalignment. Therefore, further translational studies could focus on biomechanical-based treatments for OA, with the goal of restoring biomechanics. This could involve reversing knee malalignment and joint overloading conditions, or realigning the weight-bearing line (WBL) to alleviate pain and decelerate disease progression. These strategies hold potential for broad application in clinical settings. As introduced in Chapter 1, such biomechanical-based approaches involve conservative interventions (physical methods) frequently utilized in the early stages of OA or for its prevention, such as knee braces and strengthening the lateral hamstring muscle; surgical interventions such as high tibia osteotomy or knee arthroplasty are options for patients whose symptoms are beyond conservative control. Additionally, as discussed regarding APS and BMP biologics injections (Chapter 7), it is evident that mechanically induced remodelling in OA can be moderated by early pharmacological interventions, but these cannot fully halt OA progression if the mechanical stimuli continue. Thus, it may be inferred that there exists a biomechanical threshold below which only APS treatment might be effective, whereas above it, realignment surgery (i.e., restoring the biomechanics), with the addition of APS treatment, may be necessary. This hypothesis requires further investigation in this animal model and clinical studies and could be a significant point for translation into clinical use.

Further studies are also encouraged to refine the therapeutic approaches of BMP and APS biologics treatments, with a focus on optimizing these strategies for different OA stages. This endeavor may include comprehensive research into their long-term effects and safety profiles. The concept of maintaining the chondrocyte phenotype to inhibit hypertrophic differentiation introduces a new avenue in cartilage repair and OA therapies. Investigating the regulatory mechanisms of the BMP and Wnt pathways (endochondral ossification-related pathways), and utilizing inhibitory factors such as GREM1 (inhibit BMP expression and hypertrophic process) could provide innovative methods to uphold chondrocyte stability and avert osteophyte development (Fajardo et al., 2009, Davidson et al., 2007).

Progressing towards personalized OA treatments is vital, guided by a comprehensive understanding of the biomechanical, biochemical, and proteomic changes in the disease. Future efforts can be directed at customizing treatments to the individual's specific OA conditions. Considering OA's multifactorial nature, a customized therapeutic approach that aligns treatment strategies with the disease stage, prior joint damage, excessive biomechanical loading, genetic predispositions, or metabolic factors could significantly improve management strategies. This personalized approach could be particularly advantageous in discerning which patients are better suited for structural preservation interventions, such as mitigating overloading conditions, and those who might benefit more from anti-inflammatory symptomatic strategies or localized injections for cartilage repair. Such an approach ensures optimized treatment outcomes that are closely aligned with each patient’s clinical situation and the progression of their disease.

In summary, this study assessed histological cartilage degradation, radiographic structural changes, gait scores, and cytokine levels in a long-term overloading-induced OA model, and evaluated the responses to APS and BMP treatment. The five key perspectives provided offer a comprehensive framework for future research in OA, covering a range of innovative approaches. The potential of chondrophytes as early-stage OA markers in MRI imaging is promising for enhancing diagnostic practices by offering precise, non-invasive insights into joint pathology. Advanced histological and proteomic studies are expected to yield significant insights into the OA pathogenesis mechanisms and potential treatments. Exploring proteomics with the TMT-labelled quantitative method for precise biomarker quantification is anticipated to identify novel biomarkers and therapeutic targets. Moreover, investigating gait characteristics in OA rat models aims to improve biomechanical analysis, facilitating detailed correlations between locomotor function and disease progression. Together, these perspectives are set to significantly advance the understanding of OA, improve diagnostic accuracy, and inform the development of targeted, effective treatments, and clinical translation.

9 References

AABOE, J., BLIDDAL, H., MESSIER, S. P., ALKJAER, T. & HENRIKSEN, M. 2011. Effects of an intensive weight loss program on knee joint loading in obese adults with knee osteoarthritis. *Osteoarthritis and Cartilage,* 19**,** 822-828.

ABRAMOFF, B. & CALDERA, F. E. 2020. Osteoarthritis: Pathology, Diagnosis, and Treatment Options. *Medical Clinics,* 104**,** 293-311.

ACCART, N., DAWSON, J., OBRECHT, M., LAMBERT, C., FLUECKIGER, M., KREIDER, J., HATAKEYAMA, S., RICHARDS, P. J. & BECKMANN, N. 2022. Degenerative joint disease induced by repeated intra-articular injections of monosodium urate crystals in rats as investigated by translational imaging. *Scientific Reports,* 12**,** 157.

ADEYEMI, W. J. & OLAYAKI, L. A. 2017. Effects of single or combined administration of salmon calcitonin and omega-3 fatty acids vs. diclofenac sodium in sodium monoiodoacetate-induced knee osteoarthritis in male Wistar rats. *J Basic Clin Physiol Pharmacol,* 28**,** 573-582.

AEBERSOLD, R. & MANN, M. 2016. Mass-spectrometric exploration of proteome structure and function. *Nature,* 537**,** 347-355.

AGHAJANIAN, P. & MOHAN, S. 2018. The art of building bone: emerging role of chondrocyte-to-osteoblast transdifferentiation in endochondral ossification. *Bone research,* 6**,** 19.

AGRAWAL, V., OH, J., MILIAN, E., KIM, K., ELTOUKHY, M. & BEST, T. 2019. A Novel Biomechanical Marker for Determining the Severity of Knee Osteoarthritis by Quantifying Shock Absorption at the Knee. *Osteoarthritis and Cartilage,* 27**,** S67-S67.

AIGNER, T., COOK, J., GERWIN, N., GLASSON, S., LAVERTY, S., LITTLE, C., MCILWRAITH, W. & KRAUS, V. 2010. Histopathology atlas of animal model systems–overview of guiding principles. *Osteoarthritis and Cartilage,* 18**,** S2-S6.

AIGNER, T., DIETZ, U., STöSS, H. & VON DER MARK, K. 1995. Differential expression of collagen types I, II, III, and X in human osteophytes. *Laboratory investigation; a journal of technical methods and pathology,* 73**,** 236-243.

ALI, T. S., PRASADAM, I., XIAO, Y. & MOMOT, K. I. 2018. Progression of Post-Traumatic Osteoarthritis in rat meniscectomy models: Comprehensive monitoring using MRI. *Scientific Reports,* 8.

ALLEN, K. D., CHAN, K. M., YARMOLA, E. G., SHAH, Y. Y. & PARTAIN, B. D. 2020. The effects of age on the severity of joint damage and intra-articular inflammation following a simulated medial meniscus injury in 3, 6, and 9 month old male rats. *Connect Tissue Res,* 61**,** 82-94.

ALLEN, K. D., MATA, B. A., GABR, M. A., HUEBNER, J. L., ADAMS, S. B., KRAUS, V. B., SCHMITT, D. O. & SETTON, L. A. 2012. Kinematic and dynamic gait compensations resulting from knee instability in a rat model of osteoarthritis. *Arthritis Research & Therapy,* 14.

ALTMAN, R., ASCH, E., BLOCH, D., BOLE, G., BORENSTEIN, D., BRANDT, K., CHRISTY, W., COOKE, T. D., GREENWALD, R., HOCHBERG, M. & ET AL. 1986. Development of criteria for the classification and reporting of osteoarthritis. Classification of osteoarthritis of the knee.

Diagnostic and Therapeutic Criteria Committee of the American Rheumatism Association. *Arthritis Rheum,* 29**,** 1039-49.

AMENDOLA, A. & PANARELLA, L. 2005. High tibial osteotomy for the treatment of unicompartmental arthritis of the knee. *The Orthopedic Clinics of North America,* 36**,** 497-504.

ANDERSON, N. L. & ANDERSON, N. G. 1998. Proteome and proteomics: new technologies, new concepts, and new words. *Electrophoresis,* 19**,** 1853-1861.

ANDRIACCHI, T. P. 2012. Osteoarthritis: Probing knee OA as a system responding to a stimulus. *Nat Rev Rheumatol,* 8**,** 371-2.

ANDRIACCHI, T. P., MüNDERMANN, A., SMITH, R. L., ALEXANDER, E. J., DYRBY, C. O. & KOO, S. 2004. A framework for the in vivo pathomechanics of osteoarthritis at the knee. *Ann Biomed Eng,* 32**,** 447-57.

APPLETON, C. T., PITELKA, V., HENRY, J. & BEIER, F. 2007. Global analyses of gene expression in early experimental osteoarthritis. *Arthritis Rheum,* 56**,** 1854-68.

ARMIENTO, A. R., ALINI, M. & STODDART, M. J. 2019. Articular fibrocartilage-Why does hyaline cartilage fail to repair? *Advanced drug delivery reviews,* 146**,** 289-305.

ARZI, B., WISNER, E. R., HUEY, D. J., KASS, P. H., HU, J. & ATHANASIOU, K. A. 2012. A proposed model of naturally occurring osteoarthritis in the domestic rabbit. *Lab Animal,* 41**,** 20-25.

ASHBURNER, M., BALL, C. A., BLAKE, J. A., BOTSTEIN, D., BUTLER, H., CHERRY, J. M., DAVIS, A. P., DOLINSKI, K., DWIGHT, S. S., EPPIG, J. T., HARRIS, M. A., HILL, D. P., ISSEL-TARVER, L., KASARSKIS, A., LEWIS, S., MATESE, J. C., RICHARDSON, J. E., RINGWALD, M., RUBIN, G. M. & SHERLOCK, G. 2000. Gene ontology: tool for the unification of biology. The Gene Ontology Consortium. *Nat Genet,* 25**,** 25-9.

ASHRAF, S., MAPP, P. I. & WALSH, D. A. 2011a. Contributions of angiogenesis to inflammation, joint damage, and pain in a rat model of osteoarthritis. *Arthritis & Rheumatism,* 63**,** 2700-2710.

ASHRAF, S., WIBBERLEY, H., MAPP, P. I., HILL, R., WILSON, D. & WALSH, D. A. 2011b. Increased vascular penetration and nerve growth in the meniscus: a potential source of pain in osteoarthritis. *Annals of the rheumatic diseases,* 70**,** 523-529.

BAICI, A., LANG, A., ZWICKY, R. & MüNTENER, K. Cathepsin B in osteoarthritis: uncontrolled proteolysis in the wrong place. Seminars in arthritis and rheumatism, 2005. 24-28.

BALEMANS, W. & VAN HUL, W. 2002. Extracellular regulation of BMP signaling in vertebrates: a cocktail of modulators. *Developmental biology,* 250**,** 231-250.

BARVE, R., MINNERLY, J., WEISS, D., MEYER, D., AGUIAR, D., SULLIVAN, P., WEINRICH, S. & HEAD, R. 2007. Transcriptional profiling and pathway analysis of monosodium iodoacetate-induced experimental osteoarthritis in rats: relevance to human disease. *Osteoarthritis and cartilage,* 15**,** 1190-1198.

BECKMANN, R., HOUBEN, A., TOHIDNEZHAD, M., KWEIDER, N., FRAGOULIS, A., WRUCK, C. J., BRANDENBURG, L. O., HERMANNS-SACHWEH, B., GOLDRING, M. B., PUFE, T. & JAHR,

H. 2014. Mechanical Forces Induce Changes in VEGF and VEGFR-1/sFlt-1 Expression in Human Chondrocytes. *International Journal of Molecular Sciences,* 15**,** 15456-15474.

BEITZEL, K., ALLEN, D., APOSTOLAKOS, J., RUSSELL, R. P., MCCARTHY, M. B., GALLO, G. J., COTE, M. P. & MAZZOCCA, A. D. 2015. US definitions, current use, and FDA stance on use of platelet-rich plasma in sports medicine. *The journal of knee surgery,* 28**,** 029-034.

BENDELE, A. M. 2001. Animal models of osteoarthritis. *J Musculoskelet Neuronal Interact,* 1**,** 363-76.

BENJAMINI, Y., KRIEGER, A. M. & YEKUTIELI, D. 2006. Adaptive linear step-up procedures that control the false discovery rate. *Biometrika,* 93**,** 491-507.

BENNELL, K., HUNTER, D. J. & VICENZINO, B. 2012. Long-term effects of sport: preventing and managing OA in the athlete. *Nat Rev Rheumatol,* 8**,** 747-52.

BERENBAUM, F. 2013. Osteoarthritis as an inflammatory disease (osteoarthritis is not osteoarthrosis!). *Osteoarthritis Cartilage,* 21**,** 16-21.

BERENBAUM, F., EYMARD, F. & HOUARD, X. 2013. Osteoarthritis, inflammation and obesity. *Curr Opin Rheumatol,* 25**,** 114-8.

BERGHOLT, N. L., LYSDAHL, H., LIND, M. & FOLDAGER, C. B. 2019. A standardized method of applying toluidine blue metachromatic staining for assessment of chondrogenesis. *Cartilage,* 10**,** 370-374.

BERRYMAN, E., HARRIS, R., MOALLI, M. & BAGI, C. 2009a. Digigait quantitation of gait dynamics in rat rheumatoid arthritis model. *J Musculoskelet Neuronal Interact,* 9**,** 89-98.

BERRYMAN, E. R., HARRIS, R. L., MOALLI, M. & BAGI, C. M. 2009b. Digigait (TM) quantitation of gait dynamics in rat rheumatoid arthritis model. *Journal of Musculoskeletal & Neuronal Interactions,* 9**,** 89-98.

BERTONE, A. L., ISHIHARA, A., ZEKAS, L. J., WELLMAN, M. L., LEWIS, K. B., SCHWARZE, R. A., BARNABA, A. R., SCHMALL, M. L., KANTER, P. M. & GENOVESE, R. L. 2014. Evaluation of a single intra-articular injection of autologous protein solution for treatment of osteoarthritis in horses. *American journal of veterinary research,* 75**,** 141-151.

BIANCO, D., TODOROV JR, A., ČENGIć, T., PAGENSTERT, G., SCHäREN, S., NETZER, C., HüGLE, T. & GEURTS, J. 2018. Alterations of subchondral bone progenitor cells in human knee and hip osteoarthritis lead to a bone sclerosis phenotype. *International journal of molecular sciences,* 19**,** 475.

BIERMA-ZEINSTRA, S. M. & VAN MIDDELKOOP, M. 2017. Osteoarthritis: In search of phenotypes. *Nat Rev Rheumatol,* 13**,** 705-706.

BLANEY DAVIDSON, E. N., VITTERS, E. L., VAN BEUNINGEN, H. M., VAN DE LOO, F. A., VAN DEN BERG, W. B. & VAN DER KRAAN, P. M. 2007. Resemblance of osteophytes in experimental osteoarthritis to transforming growth factor beta-induced osteophytes: limited role of bone morphogenetic protein in early osteoarthritic osteophyte formation. *Arthritis Rheum,* 56**,** 4065-73.

BLASIOLI, D. J. & KAPLAN, D. L. 2014. The roles of catabolic factors in the development of osteoarthritis. *Tissue Engineering Part B: Reviews,* 20**,** 355-363.

BLOKS, N. G., DICKS, A., HARISSA, Z., NELISSEN, R. G., HAJMOUSA, G., RAMOS, Y. F., DE ALMEIDA, R. C., GUILAK, F. & MEULENBELT, I. 2024. Hyper-physiologic mechanical cues, as an osteoarthritis disease-relevant environmental perturbation, cause a critical shift in set points of methylation at transcriptionally active CpG sites in neo-cartilage organoids. *Clinical Epigenetics,* 16**,** 64.

BOEGARD, T. 1998. Rudling 0, Petersson IF, Jonsson K. Correlation between radiographically diagnosed osteophytes and magnetic resonance detected cartilage defects in the tibiofemoral joint. *Ann Rheum Dis,* 57**,** 401-7.

BOTTER, S., VAN OSCH, G., WAARSING, J., DAY, J., VERHAAR, J., POLS, H., VAN LEEUWEN, J. & WEINANS, H. 2006a. Quantification of subchondral bone changes in a murine osteoarthritis model using micro-CT. *Biorheology,* 43**,** 379-388.

BOTTER, S. M., VAN OSCH, G. J., WAARSING, J. H., DAY, J. S., VERHAAR, J. A., POLS, H. A., VAN LEEUWEN, J. P. & WEINANS, H. 2006b. Quantification of subchondral bone changes in a murine osteoarthritis model using micro-CT. *Biorheology,* 43**,** 379-88.

BOYAN, B. D., TOSI, L. L., COUTTS, R. D., ENOKA, R. M., HART, D. A., NICOLELLA, D. P., BERKLEY, K. J., SLUKA, K. A., KWOH, C. K., O'CONNOR, M. I., KOHRT, W. M. & RESNICK, E. 2013. Addressing the gaps: sex differences in osteoarthritis of the knee. *Biology of Sex Differences,* 4**,** 4.

BREDERSON, J. D., CHU, K. L., XU, J., NIKKEL, A. L., MARKOSYAN, S., JARVIS, M. F., EDELMAYER, R., BITNER, R. S. & MCGARAUGHTY, S. 2018. Characterization and comparison of rat monosodium iodoacetate and medial meniscal tear models of osteoarthritic pain. *Journal of Orthopaedic Research,* 36**,** 2109-2117.

BREW, C. J., CLEGG, P. D., BOOT-HANDFORD, R. P., ANDREW, J. G. & HARDINGHAM, T. 2010. Gene expression in human chondrocytes in late osteoarthritis is changed in both fibrillated and intact cartilage without evidence of generalised chondrocyte hypertrophy. *Annals of the Rheumatic Diseases,* 69**,** 234-240.

BRIMMO, O. A., PFEIFFER, F., BOZYNSKI, C. C., KUROKI, K., COOK, C., STOKER, A., SHERMAN, S. L., MONIBI, F. & COOK, J. L. 2016a. Development of a Novel Canine Model for Posttraumatic Osteoarthritis of the Knee. *J Knee Surg,* 29**,** 235-41.

BRIMMO, O. A., PFEIFFER, F., BOZYNSKI, C. C., KUROKI, K., COOK, C., STOKER, A., SHERMAN, S. L., MONIBI, F. & COOK, J. L. 2016b. Development of a novel canine model for posttraumatic osteoarthritis of the knee. *The journal of knee surgery,* 29**,** 235-241.

BRITZMAN, D. 2017. *Biomechanics and Osteoarthritis: A Novel Rat Model.* Doctor of Philosophy, Imperial College London.

BRITZMAN, D., IGAH, I., EFTAXIOPOULOU, T., MACDONALD, W. & BULL, A. M. 2018a. Tibial osteotomy as a mechanical model of primary osteoarthritis in rats. *Scientific reports,* 8**,** 1-8.

BRITZMAN, D., IGAH, I., EFTAXIOPOULOU, T., MACDONALD, W. & BULL, A. M. J. 2018b. Tibial Osteotomy as a Mechanical Model of Primary Osteoarthritis in Rats. *Scientific Reports,* 8.

BROUWER, G., TOL, A. V., BERGINK, A., BELO, J., BERNSEN, R., REIJMAN, M., POLS, H. & BIERMA‐ZEINSTRA, S. 2007a. Association between valgus and varus alignment and the

development and progression of radiographic osteoarthritis of the knee. *Arthritis & rheumatism,* 56**,** 1204-1211.

BROUWER, G. M., VAN TOL, A. W., BERGINK, A. P., BELO, J. N., BERNSEN, R. M., REIJMAN, M., POLS, H. A. & BIERMA-ZEINSTRA, S. M. 2007b. Association between valgus and varus alignment and the development and progression of radiographic osteoarthritis of the knee. *Arthritis Rheum,* 56**,** 1204-11.

BROUWER, R. W., HUIZINGA, M. R., DUIVENVOORDEN, T., VAN RAAIJ, T. M., VERHAGEN, A. P., BIERMA-ZEINSTRA, S. M. & VERHAAR, J. A. 2014a. Osteotomy for treating knee osteoarthritis. *Cochrane Database Syst Rev***,** CD004019.

BROUWER, R. W., HUIZINGA, M. R., DUIVENVOORDEN, T., VAN RAAIJ, T. M., VERHAGEN, A. P., BIERMA‐ZEINSTRA, S. M. & VERHAAR, J. A. 2014b. Osteotomy for treating knee osteoarthritis. *Cochrane Database of Systematic Reviews*.

BROWN, S. B., HORNYAK, J. A., JUNGELS, R. R., SHAH, Y. Y., YARMOLA, E. G., ALLEN, K. D. & SHARMA, B. 2020. Characterization of Post-Traumatic Osteoarthritis in Rats Following Anterior Cruciate Ligament Rupture by Non-Invasive Knee Injury (NIKI). *J Orthop Res,* 38**,** 356-367.

BROWN, T. D., JOHNSTON, R. C., SALTZMAN, C. L., MARSH, J. L. & BUCKWALTER, J. A. 2006. Posttraumatic osteoarthritis: a first estimate of incidence, prevalence, and burden of disease. *J Orthop Trauma,* 20**,** 739-44.

BRZUSEK, D. & PETRON, D. 2008. Treating knee osteoarthritis with intra-articular hyaluronans. *Current medical research and opinion,* 24**,** 3307-3322.

BURR, D. B. 2004. Anatomy and physiology of the mineralized tissues: role in the pathogenesis of osteoarthrosis. *Osteoarthritis and cartilage,* 12**,** 20-30.

BURRAGE, P. & BRINCKERHOFF, C. 2007. Molecular targets in osteoarthritis: metalloproteinases and their inhibitors. *Current drug targets,* 8**,** 293-303.

BUSH, P. G. & HALL, A. C. 2003. The volume and morphology of chondrocytes within non-degenerate and degenerate human articular cartilage. *Osteoarthritis and cartilage,* 11**,** 242-251.

CAKE, M. A., APPLEYARD, R. C., READ, R. A., SMITH, M. M., MURRELL, G. A. & GHOSH, P. 2005. Ovariectomy alters the structural and biomechanical properties of ovine femoro-tibial articular cartilage and increases cartilage iNOS. *Osteoarthritis Cartilage,* 13**,** 1066-75.

CALVO, E., PALACIOS, I., DELGADO, E., SANCHEZ-PERNAUTE, O., LARGO, R., EGIDO, J. & HERRERO-BEAUMONT, G. 2004. Histopathological correlation of cartilage swelling detected by magnetic resonance imaging in early experimental osteoarthritis. *Osteoarthritis and cartilage,* 12**,** 878-886.

CAPPOZZO, A. 1984. Gait analysis methodology. *Human movement science,* 3**,** 27-50.

CARMO, A., KLEINER, A., COSTA, P. & BARROS, R. 2012a. Three-dimensional kinematic analysis of upper and lower limb motion during gait of post-stroke patients. *Brazilian Journal of Medical and Biological Research,* 45**,** 537-545.

CARMO, A. A., KLEINER, A. F. R., DA COSTA, P. H. L. & BARROS, R. M. L. 2012b. Three-dimensional kinematic analysis of upper and lower limb motion during gait of post-stroke patients. *Brazilian Journal of Medical and Biological Research,* 45**,** 537-545.

CARTER, D. & BEAUPRE, G. 2001. Mechanobiology of Skeletal Development, Aging, and Regeneration. Cambridge University Press, Cambridge.

CARTER, D. R., BEAUPRé, G. S., WONG, M., SMITH, R. L., ANDRIACCHI, T. P. & SCHURMAN, D. J. 2004. The Mechanobiology of Articular Cartilage Development and Degeneration. *Clinical Orthopaedics and Related Research®,* 427**,** S69-S77.

CARTER, D. R. & WONG, M. 1988. The role of mechanical loading histories in the development of diarthrodial joints. *J Orthop Res,* 6**,** 804-16.

CARTER, D. R. & WONG, M. 2003. Modelling cartilage mechanobiology. *Philos Trans R Soc Lond B Biol Sci,* 358**,** 1461-71.

CASTANEDA, S., CALVO, E., LARGO, R., GONZALEZ-GONZALEZ, R., DE LA PIEDRA, C., DIAZ-CURIEL, M. & HERRERO-BEAUMONT, G. 2008. Characterization of a new experimental model of osteoporosis in rabbits. *J Bone Miner Metab,* 26**,** 53-9.

CASTANEDA, S., LARGO, R., CALVO, E., BELLIDO, M., GOMEZ-VAQUERO, C. & HERRERO-BEAUMONT, G. 2010. Effects of estrogen deficiency and low bone mineral density on healthy knee cartilage in rabbits. *J Orthop Res,* 28**,** 812-8.

CASTAñEDA, S., ROMAN-BLAS, J. A., LARGO, R. & HERRERO-BEAUMONT, G. 2012. Subchondral bone as a key target for osteoarthritis treatment. *Biochemical pharmacology,* 83**,** 315-323.

CHAHLA, J., CINQUE, M. E., PIUZZI, N. S., MANNAVA, S., GEESLIN, A. G., MURRAY, I. R., DORNAN, G. J., MUSCHLER, G. F. & LAPRADE, R. F. 2017. A call for standardization in platelet-rich plasma preparation protocols and composition reporting: a systematic review of the clinical orthopaedic literature. *JBJS,* 99**,** 1769-1779.

CHAPURLAT, R., GARNERO, P., SORNAY-RENDU, E., ARLOT, M., CLAUSTRAT, B. & DELMAS, P. 2000. Longitudinal study of bone loss in pre-and perimenopausal women: evidence for bone loss in perimenopausal women. *Osteoporosis International,* 11**,** 493-498.

CHAPURLAT, R. D. 2014. Treatment of postmenopausal osteoporosis with odanacatib. *Expert opinion on pharmacotherapy,* 15**,** 559-564.

CHAPURLAT, R. D. & CONFAVREUX, C. B. 2016. Novel biological markers of bone: from bone metabolism to bone physiology. *Rheumatology,* 55**,** 1714-1725.

CHARAN, J. & KANTHARIA, N. D. 2013. How to calculate sample size in animal studies? *Journal of pharmacology & pharmacotherapeutics,* 4**,** 303-306.

CHAUDHARI, A. S., KOGAN, F., PEDOIA, V., MAJUMDAR, S., GOLD, G. E. & HARGREAVES, B. A. 2020. Rapid knee MRI acquisition and analysis techniques for imaging osteoarthritis. *Journal of Magnetic Resonance Imaging,* 52**,** 1321-1339.

CHELLINI, F., TANI, A., VALLONE, L., NOSI, D., PAVAN, P., BAMBI, F., ZECCHI ORLANDINI, S. & SASSOLI, C. 2018. Platelet-Rich Plasma Prevents In Vitro Transforming Growth Factor-β1-Induced Fibroblast to Myofibroblast Transition: Involvement of Vascular

Endothelial Growth Factor (VEGF)-A/VEGF Receptor-1-Mediated Signaling †. *Cells,* 7**,** 142.

CHEN, G. & PRAMANIK, B. N. 2009. Application of LC/MS to proteomics studies: current status and future prospects. *Drug Discovery Today,* 14**,** 465-471.

CHEN, J. H., LIU, C., YOU, L. & SIMMONS, C. A. 2010. Boning up on Wolff's Law: mechanical regulation of the cells that make and maintain bone. *J Biomech,* 43**,** 108-18.

CHENG, F., YAN, F. F., LIU, Y. P., CONG, Y., SUN, K. F. & HE, X. M. 2019. Dexmedetomidine inhibits the NF-kappaB pathway and NLRP3 inflammasome to attenuate papain-induced osteoarthritis in rats. *Pharm Biol,* 57**,** 649-659.

CHRISTIANSEN, B. A. 2016. Effect of micro-computed tomography voxel size and segmentation method on trabecular bone microstructure measures in mice. *Bone Rep,* 5**,** 136-40.

CHRISTIANSEN, B. A., ANDERSON, M. J., LEE, C. A., WILLIAMS, J. C., YIK, J. H. N. & HAUDENSCHILD, D. R. 2012. Musculoskeletal changes following non-invasive knee injury using a novel mouse model of post-traumatic osteoarthritis. *Osteoarthritis and Cartilage,* 20**,** 773-782.

CHRISTIANSEN, B. A., GUILAK, F., LOCKWOOD, K. A., OLSON, S. A., PITSILLIDES, A. A., SANDELL, L. J., SILVA, M. J., VAN DER MEULEN, M. C. H. & HAUDENSCHILD, D. R. 2015. Non-invasive mouse models of post-traumatic osteoarthritis. *Osteoarthritis and Cartilage,* 23**,** 1627-1638.

CHU, C. R., SHETH, S., ERHART-HLEDIK, J. C., DO, B., TITCHENAL, M. R. & ANDRIACCHI, T. P. 2018. Mechanically stimulated biomarkers signal cartilage changes over 5 years consistent with disease progression in medial knee osteoarthritis patients. *J Orthop Res,* 36**,** 891-897.

CHUBINSKAYA, S., HURTIG, M. & RUEGER, D. C. 2007. OP-1/BMP-7 in cartilage repair. *International orthopaedics,* 31**,** 773-781.

CICUTTINI, F. M., WLUKA, A. E., WANG, Y. & STUCKEY, S. 2004. Longitudinal study of changes in tibial and femoral cartilage in knee osteoarthritis. *Arthritis & Rheumatism: Official Journal of the American College of Rheumatology,* 50**,** 94-97.

CILLERO‐PASTOR, B., EIJKEL, G. B., KISS, A., BLANCO, F. J. & HEEREN, R. M. 2013. Matrix‐assisted laser desorption ionization–imaging mass spectrometry: A new methodology to study human osteoarthritic cartilage. *Arthritis & Rheumatism,* 65**,** 710-720.

CLEATHER, D. J. & BULL, A. M. J. 2011. An Optimization-Based Simultaneous Approach to the Determination of Muscular, Ligamentous, and Joint Contact Forces Provides Insight into Musculoligamentous Interaction. *Annals of Biomedical Engineering,* 39**,** 1925-1934.

CLEMENTS, D. N., FITZPATRICK, N., CARTER, S. D. & DAY, P. J. R. 2009. Cartilage gene expression correlates with radiographic severity of canine elbow osteoarthritis. *The Veterinary Journal,* 179**,** 211-218.

COMINELLI, F. & PIZARRO, T. T. 1997. Interleukin-1 receptor antagonist: a "novel" acute phase protein with antiinflammatory activities. *J Clin Invest,* 99**,** 2813.

COOKE, T. D., SLED, E. A. & SCUDAMORE, R. A. 2007a. Frontal plane knee alignment: a call for standardized measurement. *J Rheumatol,* 34**,** 1796-801.

COOKE, T. D. V., SLED, E. A. & SCUDAMORE, R. A. 2007b. Frontal plane knee alignment: a call for standardized measurement. *Journal of Rheumatology,* 34**,** 1796-1801.

COPE, P. J., OURRADI, K., LI, Y. & SHARIF, M. 2019. Models of osteoarthritis: the good, the bad and the promising. *Osteoarthritis Cartilage,* 27**,** 230-239.

COULTHARD, P., PLEUVRY, B. J., BREWSTER, M., WILSON, K. L. & MACFARLANE, T. V. 2002. Gait analysis as an objective measure in a chronic pain model. *J Neurosci Methods,* 116**,** 197-213.

COURTEIX, D., LESPESSAILLES, E., PERES, S. L., OBERT, P., GERMAIN, P. & BENHAMOU, C. 1998. Effect of physical training on bone mineral density in prepubertal girls: a comparative study between impact-loading and non-impact-loading sports. *Osteoporosis international,* 8**,** 152-158.

COURTIES, A., GUALILLO, O., BERENBAUM, F. & SELLAM, J. 2015. Metabolic stress-induced joint inflammation and osteoarthritis. *Osteoarthritis and Cartilage,* 23**,** 1955-1965.

COVENTRY, M. 1985a. Upper tibial osteotomy for osteoarthritis. *JBJS,* 67**,** 1136-1140.

COVENTRY, M. B. 1985b. Upper tibial osteotomy for osteoarthritis. *J Bone Joint Surg Am,* 67**,** 1136-40.

COWIN, S. C. 1986. Wolff's law of trabecular architecture at remodeling equilibrium.

CULLEY, K. L., DRAGOMIR, C. L., CHANG, J., WONDIMU, E. B., COICO, J., PLUMB, D. A., OTERO, M. & GOLDRING, M. B. 2015. Mouse models of osteoarthritis: surgical model of posttraumatic osteoarthritis induced by destabilization of the medial meniscus. *Methods Mol Biol,* 1226**,** 143-73.

DAI, G., WANG, S., LI, J., LIU, C. & LIU, Q. 2006. The validity of osteoarthritis model induced by bilateral ovariectomy in guinea pig. *J Huazhong Univ Sci Technolog Med Sci,* 26**,** 716-9.

DAS NEVES BORGES, P., FORTE, A. E., VINCENT, T. L., DINI, D. & MARENZANA, M. 2014. Rapid, automated imaging of mouse articular cartilage by microCT for early detection of osteoarthritis and finite element modelling of joint mechanics. *Osteoarthritis Cartilage,* 22**,** 1419-28.

DAS NEVES BORGES, P., VINCENT, T. L. & MARENZANA, M. 2017. Automated assessment of bone changes in cross-sectional micro-CT studies of murine experimental osteoarthritis. *PloS one,* 12**,** e0174294.

DAS, V., KC, R., LI, X., I, O. S., VAN WIJNEN, A. J., KROIN, J. S., PYTOWSKI, B., APPLEGATE, D. T., VOTTA-VELIS, G., RIPPER, R. L., PARK, T. J. & IM, H. J. 2018. Blockade of Vascular Endothelial Growth Factor Receptor-1 (Flt-1), Reveals a Novel Analgesic For Osteoarthritis-Induced Joint Pain. *Gene Rep,* 11**,** 94-100.

DATI, F., SCHUMANN, G., THOMAS, L., AGUZZI, F., BAUDNER, S., BIENVENU, J., BLAABJERG, O., BLIRUP-JENSEN, S., CARLSTRöM, A. & HYLTOFT-PETERSEN, P. 1996. Consensus of a group of professional societies and diagnostic companies on guidelines for interim reference ranges for 14 proteins in serum based on the standardization against the

IFCC/BCR/CAP reference material (CRM 470). *European Journal of Clinical Chemistry and Clinical Biochemistry,* 34**,** 517-520.

DAVIDSON, E. B., VITTERS, E., VAN BEUNINGEN, H., VAN DE LOO, F., VAN DEN BERG, W. & VAN DER KRAAN, P. 2007. Resemblance of osteophytes in experimental osteoarthritis to transforming growth factor β–induced osteophytes: limited role of bone morphogenetic protein in early osteoarthritic osteophyte formation. *Arthritis & Rheumatism: Official Journal of the American College of Rheumatology,* 56**,** 4065-4073.

DAY, J., DING, M., VAN DER LINDEN, J., HVID, I., SUMNER, D. & WEINANS, H. 2001a. A decreased subchondral trabecular bone tissue elastic modulus is associated with pre-arthritic cartilage damage. *Journal of orthopaedic research,* 19**,** 914-918.

DAY, J. S., DING, M., VAN DER LINDEN, J. C., HVID, I., SUMNER, D. R. & WEINANS, H. 2001b. A decreased subchondral trabecular bone tissue elastic modulus is associated with pre-arthritic cartilage damage. *J Orthop Res,* 19**,** 914-8.

DAY, T. F., GUO, X., GARRETT-BEAL, L. & YANG, Y. 2005. Wnt/β-catenin signaling in mesenchymal progenitors controls osteoblast and chondrocyte differentiation during vertebrate skeletogenesis. *Developmental cell,* 8**,** 739-750.

DE SOUSA, E., DOS SANTOS JUNIOR, G., DUARTE, M., MOURA NETO, V. & AGUIAR, D. 2017a. Metabolomics as a promising tool for early osteoarthritis diagnosis. *Brazilian journal of medical and biological research,* 50**,** e6485.

DE SOUSA, E. B., DOS SANTOS, G. C., DUARTE, M. E. L., NETO, V. M. & AGUIAR, D. P. 2017b. Metabolomics as a promising tool for early osteoarthritis diagnosis. *Brazilian Journal of Medical and Biological Research,* 50.

DELL'ACCIO, F., DE BARI, C., EL TAWIL, N. M., BARONE, F., MITSIADIS, T. A., O'DOWD, J. & PITZALIS, C. 2006. Activation of WNT and BMP signaling in adult human articular cartilage following mechanical injury. *Arthritis research & therapy,* 8**,** 1-13.

DELL'ISOLA, A., ALLAN, R., SMITH, S. L., MARREIROS, S. S. & STEULTJENS, M. 2016. Identification of clinical phenotypes in knee osteoarthritis: a systematic review of the literature. *BMC Musculoskelet Disord,* 17**,** 425.

DELP, S. L., ANDERSON, F. C., ARNOLD, A. S., LOAN, P., HABIB, A., JOHN, C. T., GUENDELMAN, E. & THELEN, D. G. 2007. OpenSim: open-source software to create and analyze dynamic simulations of movement. *IEEE Trans Biomed Eng,* 54**,** 1940-50.

DEY, K. K., WANG, H., NIU, M., BAI, B., WANG, X., LI, Y., CHO, J. H., TAN, H., MISHRA, A., HIGH, A. A., CHEN, P. C., WU, Z., BEACH, T. G. & PENG, J. 2019. Deep undepleted human serum proteome profiling toward biomarker discovery for Alzheimer's disease. *Clin Proteomics,* 16**,** 16.

DOMANDER, R., FELDER, A. A. & DOUBE, M. 2021. BoneJ2-refactoring established research software. *Wellcome Open Research,* 6.

DORMAN, C. W., KRUG, H. E., FRIZELLE, S. P., FUNKENBUSCH, S. & MAHOWALD, M. L. 2014. A comparison of DigiGait™ and TreadScan™ imaging systems: assessment of pain using gait analysis in murine monoarthritis. *J Pain Res,* 7**,** 25-35.

DOUGHERTY, R. & KUNZELMANN, K.-H. 2007. Computing local thickness of 3D structures with ImageJ. *Microscopy and Microanalysis,* 13**,** 1678-1679.

DUCLOS, M., ROUALDES, O., CARARO, R., ROUSSEAU, J., ROGER, T. & HARTMANN, D. 2010a. Significance of the serum CTX-II level in an osteoarthritis animal model: a 5-month longitudinal study. *Osteoarthritis and Cartilage,* 18**,** 1467-1476.

DUCLOS, M. E., ROUALDES, O., CARARO, R., ROUSSEAU, J. C., ROGER, T. & HARTMANN, D. J. 2010b. Significance of the serum CTX-II level in an osteoarthritis animal model: a 5-month longitudinal study. *Osteoarthritis and Cartilage,* 18**,** 1467-1476.

EFTAXIOPOULOU, T., MACDONALD, W., BRITZMAN, D. & BULL, A. M. 2014a. Gait compensations in rats after a temporary nerve palsy quantified using temporo-spatial and kinematic parameters. *Journal of Neuroscience Methods,* 232**,** 16-23.

EFTAXIOPOULOU, T., MACDONALD, W., BRITZMAN, D. & BULL, A. M. J. 2014b. Gait compensations in rats after a temporary nerve palsy quantified using temporo-spatial and kinematic parameters. *Journal of Neuroscience Methods,* 232**,** 16-23.

ERHART, J. C., MüNDERMANN, A., ELSPAS, B., GIORI, N. J. & ANDRIACCHI, T. P. 2008. A variable-stiffness shoe lowers the knee adduction moment in subjects with symptoms of medial compartment knee osteoarthritis. *Journal of biomechanics,* 41**,** 2720-2725.

ERHART-HLEDIK, J. C., FAVRE, J. & ANDRIACCHI, T. P. 2015. New insight in the relationship between regional patterns of knee cartilage thickness, osteoarthritis disease severity, and gait mechanics. *Journal of Biomechanics,* 48**,** 3868-3875.

ERHART-HLEDIK, J. C., FAVRE, J., ASAY, J. L., SMITH, R. L., GIORI, N. J., MüNDERMANN, A. & ANDRIACCHI, T. P. 2012. A relationship between mechanically-induced changes in serum cartilage oligomeric matrix protein (COMP) and changes in cartilage thickness after 5 years. *Osteoarthritis Cartilage,* 20**,** 1309-15.

ESTAI, M. A., SOELAIMAN, I. N., SHUID, A. N., DAS, S., ALI, A. M. & SUHAIMI, F. H. 2011. Histological changes in the fracture callus following the administration of water extract of piper sarmentosum (daun kadok) in estrogen-deficient rats. *Iran J Med Sci,* 36**,** 281-8.

FAJARDO, M., LIU, C.-J. & EGOL, K. 2009. Levels of expression for BMP-7 and several BMP antagonists may play an integral role in a fracture nonunion: a pilot study. *Clinical Orthopaedics and Related Research®,* 467**,** 3071-3078.

FAN, X., RAHNERT, J. A., MURPHY, T. C., NANES, M. S., GREENFIELD, E. M. & RUBIN, J. 2006. Response to mechanical strain in an immortalized pre‐osteoblast cell is dependent on ERK1/2. *Journal of cellular physiology,* 207**,** 454-460.

FANTO, M., WEBER, U., STRUTT, D. I. & MLODZIK, M. 2000. Nuclear signaling by Rac and Rho GTPases is required in the establishment of epithelial planar polarity in the Drosophila eye. *Current Biology,* 10**,** 979-S1.

FARQUHAR, S. J., REISMAN, D. S. & SNYDER-MACKLER, L. 2008. Persistence of altered movement patterns during a sit-to-stand task 1 year following unilateral total knee arthroplasty. *Physical therapy,* 88**,** 567-579.

FATÁS, M. A., FRANQUELO, P. & FRANQUELO, R. 2008. Anomalous Flotation of Separator Gel: Density or Viscosity? *Clinical Chemistry,* 54**,** 771-772.

FAUL, F., ERDFELDER, E., BUCHNER, A. & LANG, A. G. 2009. Statistical power analyses using G*Power 3.1: tests for correlation and regression analyses. *Behav Res Methods,* 41**,** 1149-60.

FDA, U. 1999. Guidance for industry: clinical development programs for drugs, devices, and biological products for the treatment of rheumatoid arthritis (RA). *Food and Drug Administration, Rockville, MD, USA*.

FELSON, D. T., CHAISSON, C. E., HILL, C. L., TOTTERMAN, S. M., GALE, M. E., SKINNER, K. M., KAZIS, L. & GALE, D. R. 2001a. The association of bone marrow lesions with pain in knee osteoarthritis. *Annals of internal medicine,* 134**,** 541-549.

FELSON, D. T., CHAISSON, C. E., HILL, C. L., TOTTERMAN, S. M. S., GALE, M. E., SKINNER, K. M., KAZIS, L. & GALE, D. R. 2001b. The association of bone marrow lesions with pain in knee osteoarthritis. *Annals of Internal Medicine,* 134**,** 541-549.

FERLAND, C., LAVERTY, S., BEAUDRY, F. & VACHON, P. 2011a. Gait analysis and pain response of two rodent models of osteoarthritis. *Pharmacology Biochemistry and Behavior,* 97**,** 603-610.

FERLAND, C. E., LAVERTY, S., BEAUDRY, F. & VACHON, P. 2011b. Gait analysis and pain response of two rodent models of osteoarthritis. *Pharmacology Biochemistry and Behavior,* 97**,** 603-610.

FIGUEROA, D., ESPINOSA, M., CALVO, R., SCHEU, M., VALDERRAMA, J. J., GALLEGOS, M. & CONGET, P. 2014. Treatment of acute full-thickness chondral defects with high molecular weight hyaluronic acid; an experimental model. *Rev Esp Cir Ortop Traumatol,* 58**,** 261-6.

FILARDO, G., KON, E., LONGO, U. G., MADRY, H., MARCHETTINI, P., MARMOTTI, A., VAN ASSCHE, D., ZANON, G. & PERETTI, G. M. 2016. Non-surgical treatments for the management of early osteoarthritis. *Knee Surgery, Sports Traumatology, Arthroscopy,* 24**,** 1775-1785.

FIRESTEIN, G. S., BUDD, R. C., GABRIEL, S. E., MCINNES, I. B. & O'DELL, J. R. 2016. *Kelley and Firestein's textbook of rheumatology*, Elsevier Health Sciences.

FLANIGAN, D. C., HARRIS, J. D., BROCKMEIER, P. M. & SISTON, R. A. 2010. The Effects of Lesion Size and Location on Subchondral Bone Contact in Experimental Knee Articular Cartilage Defects in a Bovine Model. *Arthroscopy-the Journal of Arthroscopic and Related Surgery,* 26**,** 1655-1661.

FLECHER, X., PARRATTE, S., AUBANIAC, J.-M. & ARGENSON, J.-N. A. 2006. A 12-28-year followup study of closing wedge high tibial osteotomy. *Clinical Orthopaedics and Related Research®,* 452**,** 91-96.

FOLKESSON, E., TURKIEWICZ, A., ENGLUND, M. & ÖNNERFJORD, P. 2018. Differential protein expression in human knee articular cartilage and medial meniscus using two different proteomic methods: a pilot analysis. *BMC Musculoskeletal Disorders,* 19**,** 416.

FRANCESCHI, R. T. & XIAO, G. 2003. Regulation of the osteoblast-specific transcription factor, Runx2: Responsiveness to multiple signal transduction pathways. *Journal of cellular biochemistry,* 88**,** 446-454.

FRANSES, R., MCWILLIAMS, D., MAPP, P. & WALSH, D. 2010. Osteochondral angiogenesis and increased protease inhibitor expression in OA. *Osteoarthritis and Cartilage,* 18**,** 563-571.

FRESNEDA ALARCON, M., MCLAREN, Z. & WRIGHT, H. L. 2021. Neutrophils in the Pathogenesis of Rheumatoid Arthritis and Systemic Lupus Erythematosus: Same Foe Different M.O. *Frontiers in Immunology,* 12.

FRISBIE, D. D., AL-SOBAYIL, F., BILLINGHURST, R. C., KAWCAK, C. E. & MCILWRAITH, C. W. 2008. Changes in synovial fluid and serum biomarkers with exercise and early osteoarthritis in horses. *Osteoarthritis Cartilage,* 16**,** 1196-204.

FROST, H. M. 1988. Vital biomechanics: proposed general concepts for skeletal adaptations to mechanical usage. *Calcified tissue international,* 42**,** 145-156.

FU, S. C., CHEUK, Y. C., HUNG, L. K. & CHAN, K. M. 2012. Limb Idleness Index (LII): a novel measurement of pain in a rat model of osteoarthritis. *Osteoarthritis and Cartilage,* 20**,** 1409-1416.

FURMAN, B. D., STRAND, L., HEMBREE, W. C., WARD, B. D., GUILAK, F. & OLSON, S. A. 2007. Joint degeneration following closed Intraarticular fracture in the mouse knee: A model of posttraumatic arthritis. *Journal of Orthopaedic Research,* 25**,** 578-592.

GAASBEEK, R. D., GROEN, B. E., HAMPSINK, B., VAN HEERWAARDEN, R. J. & DUYSENS, J. 2007. Valgus bracing in patients with medial compartment osteoarthritis of the knee: a gait analysis study of a new brace. *Gait & posture,* 26**,** 3-10.

GABUSI, E., MANFERDINI, C., GRASSI, F., PIACENTINI, A., CATTINI, L., FILARDO, G., LAMBERTINI, E., PIVA, R., ZINI, N. & FACCHINI, A. 2012. Extracellular calcium chronically induced human osteoblasts effects: specific modulation of osteocalcin and collagen type XV. *Journal of cellular physiology,* 227**,** 3151-3161.

GARCIA, B. A., PLATT, M. D., BORN, T. L., SHABANOWITZ, J., MARCUS, N. A. & HUNT, D. F. 2006. Protein profile of osteoarthritic human articular cartilage using tandem mass spectrometry. *Rapid Communications in Mass Spectrometry: An International Journal Devoted to the Rapid Dissemination of Up‐to‐the‐Minute Research in Mass Spectrometry,* 20**,** 2999-3006.

GARDINER, B. S., WOODHOUSE, F. G., BESIER, T. F., GRODZINSKY, A. J., LLOYD, D. G., ZHANG, L. & SMITH, D. W. 2016. Predicting Knee Osteoarthritis. *Ann Biomed Eng,* 44**,** 222-33.

GBD 2017 DISEASE AND INJURY INCIDENCE AND PREVALENCE COLLABORATORS 2018. Global, regional, and national incidence, prevalence, and years lived with disability for 354 diseases and injuries for 195 countries and territories, 1990-2017: a systematic analysis for the Global Burden of Disease Study 2017. *Lancet,* 392**,** 1789-1858.

GE, Z., HU, Y., HENG, B. C., YANG, Z., OUYANG, H., LEE, E. H. & CAO, T. 2006. Osteoarthritis and therapy. *Arthritis care & research,* 55**,** 493-500.

GELSE, K., EKICI, A., CIPA, F., SWOBODA, B., CARL, H., OLK, A., HENNIG, F. & KLINGER, P. 2012a. Molecular differentiation between osteophytic and articular cartilage–clues for a transient and permanent chondrocyte phenotype. *Osteoarthritis and cartilage,* 20**,** 162-171.

GELSE, K., EKICI, A. B., CIPA, F., SWOBODA, B., CARL, H. D., OLK, A., HENNIG, F. F. & KLINGER, P. 2012b. Molecular differentiation between osteophytic and articular cartilage – clues for a transient and permanent chondrocyte phenotype. *Osteoarthritis and Cartilage,* 20**,** 162-171.

GELSE, K., SöDER, S., EGER, W., DIEMTAR, T. & AIGNER, T. 2003. Osteophyte development—molecular characterization of differentiation stages. *Osteoarthritis and cartilage,* 11**,** 141-148.

GERWIN, N., BENDELE, A. M., GLASSON, S. & CARLSON, C. S. 2010. The OARSI histopathology initiative – recommendations for histological assessments of osteoarthritis in the rat. *Osteoarthritis and Cartilage,* 18**,** S24-S34.

GILBERT, S. J. & BLAIN, E. J. 2018. Chapter 4 - Cartilage mechanobiology: How chondrocytes respond to mechanical load. *In:* VERBRUGGEN, S. W. (ed.) *Mechanobiology in Health and Disease.* Academic Press.

GILBERTSON, E. M. 1975. Development of periarticular osteophytes in experimentally induced osteoarthritis in the dog. A study using microradiographic, microangiographic, and fluorescent bone-labelling techniques. *Ann Rheum Dis,* 34**,** 12-25.

GLASSON, S. S. 2007. In vivo osteoarthritis target validation utilizing genetically-modified mice. *Current drug targets,* 8**,** 367-376.

GLASSON, S. S., BLANCHET, T. J. & MORRIS, E. A. 2007. The surgical destabilization of the medial meniscus (DMM) model of osteoarthritis in the 129/SvEv mouse. *Osteoarthritis Cartilage,* 15**,** 1061-9.

GŁODEK, J., ADAMIAK, Z. & PRZEWORSKI, A. 2016. Magnetic Resonance Imaging of Reptiles, Rodents, and Lagomorphs for Clinical Diagnosis and Animal Research. *Comp Med,* 66**,** 216-9.

GLYN-JONES, S., PALMER, A. J., AGRICOLA, R., PRICE, A. J., VINCENT, T. L., WEINANS, H. & CARR, A. J. 2015. Osteoarthritis. *Lancet,* 386**,** 376-87.

GOETZ, J. E., COLEMAN, M. C., FREDERICKS, D. C., PETERSEN, E., MARTIN, J. A., MCKINLEY, T. O. & TOCHIGI, Y. 2017. Time-dependent loss of mitochondrial function precedes progressive histologic cartilage degeneration in a rabbit meniscal destabilization model. *J Orthop Res,* 35**,** 590-599.

GOLDRING, M., OTERO, M., TSUCHIMOCHI, K., IJIRI, K. & LI, Y. 2008. Defining the roles of inflammatory and anabolic cytokines in cartilage metabolism. *Annals of the rheumatic diseases,* 67**,** iii75-iii82.

GOLDRING, M. B. 2001. Anticytokine therapy for osteoarthritis. *Expert opinion on biological therapy,* 1**,** 817-829.

GOLDRING, M. B. 2006. Update on the biology of the chondrocyte and new approaches to treating cartilage diseases. *Best practice & research Clinical rheumatology,* 20**,** 1003-1025.

GOLDRING, M. B. 2012. Chondrogenesis, chondrocyte differentiation, and articular cartilage metabolism in health and osteoarthritis. *Therapeutic advances in musculoskeletal disease,* 4**,** 269-285.

GOLDRING, M. B., CULLEY, K. L., WONDIMU, E. & OTERO, M. 2017. Chapter 3 - Cartilage and Chondrocytes. *In:* FIRESTEIN, G. S., BUDD, R. C., GABRIEL, S. E., MCINNES, I. B. & O'DELL, J. R. (eds.) *Kelley and Firestein's Textbook of Rheumatology (Tenth Edition).* Elsevier.

GOLDRING, M. B. & GOLDRING, S. R. 2010. Articular cartilage and subchondral bone in the pathogenesis of osteoarthritis. *Annals of the New York Academy of Sciences,* 1192**,** 230-237.

GOLDRING, M. B. & OTERO, M. 2011. Inflammation in osteoarthritis. *Current opinion in rheumatology,* 23**,** 471.

GRATAL, P., MEDIERO, A., SáNCHEZ-PERNAUTE, O., PRIETO-POTIN, I., LAMUEDRA, A., HERRERO-BEAUMONT, G. & LARGO, R. 2019. Chondrocyte enlargement is a marker of osteoarthritis severity. *Osteoarthritis and Cartilage,* 27**,** 1229-1234.

GRIFFIN, T. M. & GUILAK, F. 2005. The role of mechanical loading in the onset and progression of osteoarthritis. *Exerc Sport Sci Rev,* 33**,** 195-200.

GROSSMANN, J., ROSCHITZKI, B., PANSE, C., FORTES, C., BARKOW-OESTERREICHER, S., RUTISHAUSER, D. & SCHLAPBACH, R. 2010. Implementation and evaluation of relative and absolute quantification in shotgun proteomics with label-free methods. *Journal of proteomics,* 73**,** 1740-1746.

GRUNDNES, O. & REIKERåS, O. 1993. Effects of instability on bone healing: Femoral osteotomies studied in rats. *Acta Orthopaedica Scandinavica,* 64**,** 55-58.

GUILAK, F. 2011. Biomechanical factors in osteoarthritis. *Best Practice & Research in Clinical Rheumatology,* 25**,** 815-823.

GUO, D., TAN, W., WANG, F., LV, Z., HU, J., LV, T., CHEN, Q., GU, X., WAN, B. & ZHANG, Z. 2008. Proteomic analysis of human articular cartilage: identification of differentially expressed proteins in knee osteoarthritis. *Joint Bone Spine,* 75**,** 439-444.

HALDER, A., KUTZNER, I., GRAICHEN, F., HEINLEIN, B., BEIER, A. & BERGMANN, G. 2012. Influence of limb alignment on mediolateral loading in total knee replacement: in vivo measurements in five patients. *J Bone Joint Surg Am,* 94**,** 1023-9.

HAMAI, S., MORO-OKA, T. A., MIURA, H., SHIMOTO, T., HIGAKI, H., FREGLY, B. J., IWAMOTO, Y. & BANKS, S. A. 2009. Knee kinematics in medial osteoarthritis during in vivo weight-bearing activities. *J Orthop Res,* 27**,** 1555-61.

HANDIN, R. I., LUX, S. E. & STOSSEL, T. P. 2003. *Blood: principles and practice of hematology*, Lippincott Williams & Wilkins.

HAYAMI, T., PICKARSKI, M., ZHUO, Y., WESOLOWSKI, G. A., RODAN, G. A. & DUONG, L. T. 2006a. Characterization of articular cartilage and subchondral bone changes in the rat anterior cruciate ligament transection and meniscectomized models of osteoarthritis. *Bone,* 38**,** 234-243.

HAYAMI, T., PICKARSKI, M., ZHUO, Y., WESOLOWSKI, G. A., RODAN, G. A. & DUONG, L. T. 2006b. Characterization of articular cartilage and subchondral bone changes in the rat anterior cruciate ligament transection and meniscectomized models of osteoarthritis. *Bone,* 38**,** 234-43.

HEIDEN, T. L., LLOYD, D. G. & ACKLAND, T. R. 2009. Knee joint kinematics, kinetics and muscle co-contraction in knee osteoarthritis patient gait. *Clin Biomech (Bristol, Avon),* 24**,** 833-41.

HERMAN, B. V. & GIFFIN, J. R. 2016. High tibial osteotomy in the ACL-deficient knee with medial compartment osteoarthritis. *J Orthop Traumatol,* 17**,** 277-85.

HINMAN, R. S., BOWLES, K. A., PAYNE, C. & BENNELL, K. L. 2008. Effect of length on laterally-wedged insoles in knee osteoarthritis. *Arthritis Care & Research: Official Journal of the American College of Rheumatology,* 59**,** 144-147.

HINMAN, R. S., MAY, R. L. & CROSSLEY, K. M. 2006. Is there an alternative to the full-leg radiograph for determining knee joint alignment in osteoarthritis? *Arthritis Care & Research: Official Journal of the American College of Rheumatology,* 55**,** 306-313.

HINTSALA, H.-R., JOKINEN, E., HAAPASAARI, K.-M., MOZA, M., RISTIMÄKI, A., SOINI, Y., KOIVUNEN, J. & KARIHTALA, P. 2016. Nrf2/Keap1 pathway and expression of oxidative stress lesions 8-hydroxy-2'-deoxyguanosine and nitrotyrosine in melanoma. *Anticancer Research,* 36**,** 1497-1506.

HOEGH-ANDERSEN, P., TANKO, L. B., ANDERSEN, T. L., LUNDBERG, C. V., MO, J. A., HEEGAARD, A. M., DELAISSE, J. M. & CHRISTGAU, S. 2004. Ovariectomized rats as a model of postmenopausal osteoarthritis: validation and application. *Arthritis Research & Therapy,* 6**,** R169-R180.

HOLYOAK, D. T., CHLEBEK, C., KIM, M. J., WRIGHT, T. M., OTERO, M. & VAN DER MEULEN, M. C. H. 2019. Low-level cyclic tibial compression attenuates early osteoarthritis progression after joint injury in mice. *Osteoarthritis Cartilage,* 27**,** 1526-1536.

HOLYOAK, D. T., OTERO, M., ARMAR, N. S., ZIEMIAN, S. N., OTTO, A., CULLINANE, D., WRIGHT, T. M., GOLDRING, S. R., GOLDRING, M. B. & VAN DER MEULEN, M. C. H. 2018. Collagen XI mutation lowers susceptibility to load-induced cartilage damage in mice. *J Orthop Res,* 36**,** 711-720.

HORKAY, F. 2012. Interactions of Cartilage Extracellular Matrix Macromolecules. *J Polym Sci B Polym Phys,* 50**,** 1699-1705.

HORTON, W. 2003. The biology of bone growth. *Lancet,* 362**,** 560-569.

HOWARD, C. S., BLAKENEY, D. C., MEDIGE, J., MOY, O. J. & PEIMER, C. A. 2000. Functional assessment in the rat by ground reaction forces. *Journal of Biomechanics,* 33**,** 751-757.

HUISKES, R., RUIMERMAN, R., VAN LENTHE, G. H. & JANSSEN, J. D. 2000. Effects of mechanical forces on maintenance and adaptation of form in trabecular bone. *Nature,* 405**,** 704-706.

HUNT, M. A., CHARLTON, J. M. & ESCULIER, J. F. 2020. Osteoarthritis year in review 2019: mechanics. *Osteoarthritis and Cartilage,* 28**,** 267-274.

HUNTER, D. J. & BIERMA-ZEINSTRA, S. 2019. Osteoarthritis. *Lancet,* 393**,** 1745-1759.

HUNTER, D. J., GUERMAZI, A., ROEMER, F., ZHANG, Y. & NEOGI, T. 2013. Structural correlates of pain in joints with osteoarthritis. *Osteoarthritis and cartilage,* 21**,** 1170-1178.

HUNTER, D. J., PIKE, M. C., JONAS, B. L., KISSIN, E., KROP, J. & MCALINDON, T. 2010a. Phase 1 safety and tolerability study of BMP-7 in symptomatic knee osteoarthritis. *BMC musculoskeletal disorders,* 11**,** 1-8.

HUNTER, D. J., PIKE, M. C., JONAS, B. L., KISSIN, E., KROP, J. & MCALINDON, T. 2010b. Phase 1 safety and tolerability study of BMP-7 in symptomatic knee osteoarthritis. *BMC Musculoskeletal Disorders,* 11**,** 232.

IIJIMA, H., AOYAMA, T., ITO, A., TAJINO, J., NAGAI, M., ZHANG, X., YAMAGUCHI, S., AKIYAMA, H. & KUROKI, H. 2014. Destabilization of the medial meniscus leads to subchondral bone defects and site-specific cartilage degeneration in an experimental rat model. *Osteoarthritis Cartilage,* 22**,** 1036-43.

IIJIMA, H., ITO, A., NAGAI, M., TAJINO, J., YAMAGUCHI, S., KIYAN, W., NAKAHATA, A., ZHANG, J., WANG, T., AOYAMA, T., NISHITANI, K. & KUROKI, H. 2017. Physiological exercise loading suppresses post-traumatic osteoarthritis progression via an increase in bone morphogenetic proteins expression in an experimental rat knee model. *Osteoarthritis and Cartilage,* 25**,** 964-975.

INOUE, S., AKAGI, M., ASADA, S., MORI, S., ZAIMA, H. & HASHIDA, M. 2016. The valgus inclination of the tibial component increases the risk of medial tibial condylar fractures in unicompartmental knee arthroplasty. *The Journal of arthroplasty,* 31**,** 2025-2030.

ISHIKAWA, G., NAGAKURA, Y., TAKESHITA, N. & SHIMIZU, Y. 2014. Efficacy of drugs with different mechanisms of action in relieving spontaneous pain at rest and during movement in a rat model of osteoarthritis. *European Journal of Pharmacology,* 738**,** 111-117.

ISSA, R. I. & GRIFFIN, T. M. 2012. Pathobiology of obesity and osteoarthritis: integrating biomechanics and inflammation. *Pathobiol Aging Age Relat Dis,* 2.

JACKSON, D. W., GROOD, E. S., GOLDSTEIN, J. D., ROSEN, M. A., KURZWEIL, P. R., CUMMINGS, J. F. & SIMON, T. M. 1993. A Comparison of Patellar Tendon Autograft and Allograft Used for Anterior Cruciate Ligament Reconstruction in the Goat Model. *American Journal of Sports Medicine,* 21**,** 176-185.

JACOBS, B. Y., DUNNIGAN, K., PIRES-FERNANDES, M. & ALLEN, K. D. 2017. Unique spatiotemporal and dynamic gait compensations in the rat monoiodoacetate injection and medial meniscus transection models of knee osteoarthritis. *Osteoarthritis Cartilage,* 25**,** 750-758.

JACOBS, B. Y., KLOEFKORN, H. E. & ALLEN, K. D. 2014. Gait analysis methods for rodent models of osteoarthritis. *Curr Pain Headache Rep,* 18**,** 456.

JEON, B., KIM, J.-M., KIM, J.-M., LEE, C.-R., KIM, K.-A. & BIN, S.-I. 2015. An osteophyte in the tibial plateau is a risk factor for allograft extrusion after meniscus allograft transplantation. *The American Journal of Sports Medicine,* 43**,** 1215-1221.

JI, Q., ZHENG, Y., ZHANG, G., HU, Y., FAN, X., HOU, Y., WEN, L., LI, L., XU, Y. & WANG, Y. 2019. Single-cell RNA-seq analysis reveals the progression of human osteoarthritis. *Annals of the rheumatic diseases,* 78**,** 100-110.

JIANG, L., SUN, J. & HUANG, D. 2022. Role of Slit/Robo Signaling pathway in Bone Metabolism. *Int J Biol Sci,* 18**,** 1303-1312.

JIMENEZ, P. A., GLASSON, S. S., TRUBETSKOY, O. V. & HAIMES, H. B. 1997. Spontaneous osteoarthritis in Dunkin Hartley guinea pigs: histologic, radiologic, and biochemical changes. *Lab Anim Sci,* 47**,** 598-601.

JOHNSON, F. & WAUGH, W. 1979. Method for routine clinical assessment of knee-joint forces. *Medical and Biological Engineering and Computing,* 17**,** 145-154.

JOHNSON, R. & POOLE, A. 1988a. Degenerative changes in dog articular cartilage induced by a unilateral tibial valgus osteotomy. *Experimental pathology,* 33**,** 145-164.

JOHNSON, R. G. & POOLE, A. R. 1988b. Degenerative changes in dog articular cartilage induced by a unilateral tibial valgus osteotomy. *Exp Pathol,* 33**,** 145-64.

JOHNSON, W. L., JINDRICH, D. L., ROY, R. R. & REGGIE EDGERTON, V. 2008. A three-dimensional model of the rat hindlimb: musculoskeletal geometry and muscle moment arms. *J Biomech,* 41**,** 610-9.

JONES, D., LEIVSETH, G. & TENBOSCH, J. 1995. Mechano-reception in osteoblast-like cells. *Biochemistry and cell biology,* 73**,** 525-534.

JONES, I. A., TOGASHI, R., WILSON, M. L., HECKMANN, N. & VANGSNESS, C. T., JR. 2019. Intra-articular treatment options for knee osteoarthritis. *Nat Rev Rheumatol,* 15**,** 77-90.

KAHN, D., MITTELSTAEDT, D., MATYAS, J., QU, X., LEE, J. H., BADAR, F., LES, C., ZHUANG, Z. & XIA, Y. 2016. Meniscus Induced Cartilaginous Damage and Non-linear Gross Anatomical Progression of Early-stage Osteoarthritis in a Canine Model. *Open Orthop J,* 10**,** 690-705.

KAMEKURA, S., HOSHI, K., SHIMOAKA, T., CHUNG, U., CHIKUDA, H., YAMADA, T., UCHIDA, M., OGATA, N., SEICHI, A., NAKAMURA, K. & KAWAGUCHI, H. 2005. Osteoarthritis development in novel experimental mouse models induced by knee joint instability. *Osteoarthritis Cartilage,* 13**,** 632-41.

KAMEKURA, S., KAWASAKI, Y., HOSHI, K., SHIMOAKA, T., CHIKUDA, H., MARUYAMA, Z., KOMORI, T., SATO, S., TAKEDA, S. & KARSENTY, G. 2006. Contribution of runt‐related transcription factor 2 to the pathogenesis of osteoarthritis in mice after induction of knee joint instability. *Arthritis & Rheumatism: Official Journal of the American College of Rheumatology,* 54**,** 2462-2470.

KATSURAGI, J., SASHO, T., YAMAGUCHI, S., SATO, Y., WATANABE, A., AKAGI, R., MURAMATSU, Y., MUKOYAMA, S., AKATSU, Y. & FUKAWA, T. 2015. Hidden osteophyte formation on plain X-ray is the predictive factor for development of knee osteoarthritis after 48 months–data from the Osteoarthritis Initiative. *Osteoarthritis and Cartilage,* 23**,** 383-390.

KEAN, C., HINMAN, R., BOWLES, K. & BENNELL, K. 2011. 22 ABILITY OF PEAK KNEE ADDUCTION MOMENT AND KNEE ADDUCTION MOMENT IMPULSE TO DISTINGUISH BETWEEN CLINICAL AND STRUCTURAL DISEASE SEVERITY. *Osteoarthritis and Cartilage.* UK.

KEMPER, A., TRUMBLE, T., BOYCE, M., BROWN, M. & MCCOY, A. 2019. Altered synovial gene expression reflects early changes in post-traumatic osteoarthritis in a novel animal model. *Osteoarthritis and Cartilage,* 27**,** S291-S292.

KERNOZEK, T., TORRY, M., SHELBURNE, K., DURALL, C. J. & WILLSON, J. 2013. From the gait laboratory to the rehabilitation clinic: translation of motion analysis and modeling data

to interventions that impact anterior cruciate ligament loads in gait and drop landing. *Crit Rev Biomed Eng,* 41**,** 243-58.

KETTELKAMP, D. B. & CHAO, E. 1972. A method for quantitative analysis of medial and lateral compression forces at the knee during standing. *Clinical Orthopaedics and Related Research (1976-2007),* 83**,** 202-213.

KHARB, A., SAINI, V., JAIN, Y. & DHIMAN, S. 2011. A review of gait cycle and its parameters. *IJCEM International Journal of Computational Engineering & Management,* 13**,** 78-83.

KHORASANI, M. S., DIKO, S., HSIA, A. W., ANDERSON, M. J., GENETOS, D. C., HAUDENSCHILD, D. R. & CHRISTIANSEN, B. A. 2015. Effect of alendronate on post-traumatic osteoarthritis induced by anterior cruciate ligament rupture in mice. *Arthritis Res Ther,* 17**,** 30.

KIAPOUR, A., KIAPOUR, A. M., KAUL, V., QUATMAN, C. E., WORDEMAN, S. C., HEWETT, T. E., DEMETROPOULOS, C. K. & GOEL, V. K. 2014. Finite element model of the knee for investigation of injury mechanisms: development and validation. *J Biomech Eng,* 136**,** 011002.

KIM, B.-J. & KOH, J.-M. 2019. Coupling factors involved in preserving bone balance. *Cellular and Molecular Life Sciences,* 76**,** 1243-1253.

KIM, Y., BRODT, M. D., TANG, S. Y. & SILVA, M. J. 2021. MicroCT for Scanning and Analysis of Mouse Bones. *Skeletal Development and Repair: Methods and Protocols***,** 169-198.

KIMMERLING, K. A., FURMAN, B. D., MANGIAPANI, D. S., MOVERMAN, M. A., SINCLAIR, S. M., HUEBNER, J. L., CHILKOTI, A., KRAUS, V. B., SETTON, L. A., GUILAK, F. & OLSON, S. A. 2015. Sustained Intra-Articular Delivery of Il-1ra from a Thermally-Responsive Elastin-Like Polypeptide as a Therapy for Post-Traumatic Arthritis. *European Cells & Materials,* 29**,** 124-140.

KING, W., BENDELE, A., MAROHL, T. & WOODELL-MAY, J. 2017. Human blood-based anti-inflammatory solution inhibits osteoarthritis progression in a meniscal-tear rat study. *J Orthop Res,* 35**,** 2260-2268.

KING, W., CAWOOD, K. & BOOKMILLER, M. 2021. The use of autologous protein solution (Pro-Stride®) and leukocyte-rich platelet-rich plasma (Restigen®) in canine medicine. *Veterinary Medicine: Research and Reports***,** 53-65.

KLOPPENBURG, M. & BERENBAUM, F. 2020. Osteoarthritis year in review 2019: epidemiology and therapy. *Osteoarthritis Cartilage,* 28**,** 242-248.

KNIGHTS, C. B., GENTRY, C. & BEVAN, S. 2012. Partial medial meniscectomy produces osteoarthritis pain-related behaviour in female C57BL/6 mice. *Pain,* 153**,** 281-292.

KNOOP, J., STEULTJENS, M. P., VAN DER LEEDEN, M., VAN DER ESCH, M., THORSTENSSON, C. A., ROORDA, L. D., LEMS, W. F. & DEKKER, J. 2011. Proprioception in knee osteoarthritis: a narrative review. *Osteoarthritis Cartilage,* 19**,** 381-8.

KO, F. C., DRAGOMIR, C., PLUMB, D. A., GOLDRING, S. R., WRIGHT, T. M., GOLDRING, M. B. & VAN DER MEULEN, M. C. 2013. In vivo cyclic compression causes cartilage degeneration and subchondral bone changes in mouse tibiae. *Arthritis Rheum,* 65**,** 1569-78.

KOKEBIE, R., AGGARWAL, R., LIDDER, S., HAKIMIYAN, A. A., RUEGER, D. C., BLOCK, J. A. & CHUBINSKAYA, S. 2011. The role of synovial fluid markers of catabolism and anabolism in osteoarthritis, rheumatoid arthritis and asymptomatic organ donors. *Arthritis research & therapy,* 13**,** R50.

KOMORI, T., YAGI, H., NOMURA, S., YAMAGUCHI, A., SASAKI, K., DEGUCHI, K., SHIMIZU, Y., BRONSON, R., GAO, Y.-H. & INADA, M. 1997. Targeted disruption of Cbfa1 results in a complete lack of bone formation owing to maturational arrest of osteoblasts. *cell,* 89**,** 755-764.

KON, E., ENGEBRETSEN, L., VERDONK, P., NEHRER, S. & FILARDO, G. 2018. Clinical Outcomes of Knee Osteoarthritis Treated With an Autologous Protein Solution Injection: A 1-Year Pilot Double-Blinded Randomized Controlled Trial. *Am J Sports Med,* 46**,** 171-180.

KOROTKYI, O., VOVK, A., BLOKHINA, O., DVORSHCHENKO, K., FALALYEYEVA, T., ABENAVOLI, L. & OSTAPCHENKO, L. 2019. Effect of Chondroitin Sulfate on Blood Serum Cytokine Profile during Carrageenan-induced Edema and Monoiodoacetate-induced Osteoarthritis in Rats. *Rev Recent Clin Trials,* 14**,** 50-55.

KRAUS, V. B., HUEBNER, J. L., DEGROOT, J. & BENDELE, A. 2010. The OARSI histopathology initiative - recommendations for histological assessments of osteoarthritis in the guinea pig. *Osteoarthritis Cartilage,* 18 Suppl 3**,** S35-52.

KRAUT, A., MARCELLIN, M., ADRAIT, A., KUHN, L., LOUWAGIE, M., KIEFFER-JAQUINOD, S., LEBERT, D., MASSELON, C. D., DUPUIS, A., BRULEY, C., JAQUINOD, M., GARIN, J. & GALLAGHER-GAMBARELLI, M. 2009. Peptide storage: are you getting the best return on your investment? Defining optimal storage conditions for proteomics samples. *J Proteome Res,* 8**,** 3778-85.

KREIPKE, T. C., RIVERA, N. C., GARRISON, J. G., EASLEY, J. T., TURNER, A. S. & NIEBUR, G. L. 2014. Alterations in trabecular bone microarchitecture in the ovine spine and distal femur following ovariectomy. *J Biomech,* 47**,** 1918-21.

KRISHNAN, V., BRYANT, H. U. & MACDOUGALD, O. A. 2006. Regulation of bone mass by Wnt signaling. *The Journal of clinical investigation,* 116**,** 1202-1209.

KUJALA, U. M., KAPRIO, J. & SARNA, S. 1994. Osteoarthritis of weight bearing joints of lower limbs in former elite male athletes. *BMJ,* 308**,** 231-4.

KURENKOVA, A. D., ROMANOVA, I. A., KIBIRSKIY, P. D., TIMASHEV, P. & MEDVEDEVA, E. V. 2022. Strategies to Convert Cells into Hyaline Cartilage: Magic Spells for Adult Stem Cells. *International Journal of Molecular Sciences,* 23**,** 11169.

KUYINU, E. L., NARAYANAN, G., NAIR, L. S. & LAURENCIN, C. T. 2016a. Animal models of osteoarthritis: classification, update, and measurement of outcomes. *Journal of orthopaedic surgery and research,* 11**,** 19.

KUYINU, E. L., NARAYANAN, G., NAIR, L. S. & LAURENCIN, C. T. 2016b. Animal models of osteoarthritis: classification, update, and measurement of outcomes. *J Orthop Surg Res,* 11**,** 19.

KYOSTIO-MOORE, S., NAMBIAR, B., HUTTO, E., EWING, P. J., PIRAINO, S., BERTHELETTE, P., SOOKDEO, C., MATTHEWS, G. & ARMENTANO, D. 2011. STR/ort Mice, a Model for

Spontaneous Osteoarthritis, Exhibit Elevated Levels of Both Local and Systemic Inflammatory Markers. *Comparative Medicine,* 61**,** 346-355.

LAHM, A., UHL, M., EDLICH, M., ERGGELET, C., HABERSTROH, J. & KREUZ, P. C. 2005. An experimental canine model for subchondral lesions of the knee joint. *Knee,* 12**,** 51-55.

LAKES, E. H. & ALLEN, K. D. 2016. Gait analysis methods for rodent models of arthritic disorders: reviews and recommendations. *Osteoarthritis and cartilage,* 24**,** 1837-1849.

LAMPROPOULOU-ADAMIDOU, K., LELOVAS, P., KARADIMAS, E. V., LIAKOU, C., TRIANTAFILLOPOULOS, I. K., DONTAS, I. & PAPAIOANNOU, N. A. 2014. Useful animal models for the research of osteoarthritis. *Eur J Orthop Surg Traumatol,* 24**,** 263-71.

LANYON, L. 1996. Using functional loading to influence bone mass and architecture: objectives, mechanisms, and relationship with estrogen of the mechanically adaptive process in bone. *Bone,* 18**,** S37-S43.

LAPVETELAINEN, T., HYTTINEN, M. M., SAAMANEN, A. M., LANGSJO, T., SAHLMAN, J., FELSZEGHY, S., VUORIO, E. & HELMINEN, H. J. 2002. Lifelong voluntary joint loading increases osteoarthritis in mice housing a deletion mutation in type II procollagen gene, and slightly also in non-transgenic mice. *Annals of the Rheumatic Diseases,* 61**,** 810-817.

LAPVETELAINEN, T., NEVALAINEN, T., PARKKINEN, J. J., AROKOSKI, J., KIRALY, K., HYTTINEN, M., HALONEN, P. & HELMINEN, H. J. 1995. Lifelong Moderate Running Training Increases the Incidence and Severity of Osteoarthritis in the Knee-Joint of C57bl Mice. *Anatomical Record,* 242**,** 159-165.

LAURENT, D., WASVARY, J., RUDIN, M., O'BYRNE, E. & PELLAS, T. 2003. In vivo assessment of macromolecular content in articular cartilage of the goat knee. *Magn Reson Med,* 49**,** 1037-46.

LAVIGNE, P., BENDERDOUR, M., LAJEUNESSE, D., REBOUL, P., SHI, Q., PELLETIER, J. P., MARTEL-PELLETIER, J. & FERNANDES, J. C. 2005. Subchondral and trabecular bone metabolism regulation in canine experimental knee osteoarthritis. *Osteoarthritis Cartilage,* 13**,** 310-7.

LAWRENCE, E. A., KAGUE, E., AGGLETON, J. A., HARNIMAN, R. L., RODDY, K. A. & HAMMOND, C. L. 2018. The mechanical impact of col11a2 loss on joints; col11a2 mutant zebrafish show changes to joint development and function, which leads to early-onset osteoarthritis. *Philosophical Transactions of the Royal Society B: Biological Sciences,* 373**,** 20170335.

LEE, J. H., FITZGERALD, J. B., DIMICCO, M. A. & GRODZINSKY, A. J. 2005. Mechanical injury of cartilage explants causes specific time‐dependent changes in chondrocyte gene expression. *Arthritis & Rheumatism: Official Journal of the American College of Rheumatology,* 52**,** 2386-2395.

LEE, K. M., PRASAD, V., ACHUTHAN, A., FLEETWOOD, A. J., HAMILTON, J. A. & COOK, A. D. 2020. Targeting GM-CSF for collagenase-induced osteoarthritis pain and disease in mice. *Osteoarthritis Cartilage,* 28**,** 486-491.

LEE, S.-Y., ABEL, E. D. & LONG, F. 2018. Glucose metabolism induced by Bmp signaling is essential for murine skeletal development. *Nature communications,* 9**,** 4831.

LEEMAN, M., CHOI, J., HANSSON, S., STORM, M. U. & NILSSON, L. 2018. Proteins and antibodies in serum, plasma, and whole blood-size characterization using asymmetrical flow field-flow fractionation (AF4). *Anal Bioanal Chem,* 410**,** 4867-4873.

LEGRAND, C. B., LAMBERT, C. J., COMBLAIN, F. V., SANCHEZ, C. & HENROTIN, Y. E. 2017. Review of Soluble Biomarkers of Osteoarthritis: Lessons From Animal Models. *Cartilage,* 8**,** 211-233.

LESCUYER, P., HOCHSTRASSER, D. & RABILLOUD, T. 2007. How shall we use the proteomics toolbox for biomarker discovery? *Journal of proteome research,* 6**,** 3371-3376.

LESPASIO, M. J., PIUZZI, N. S., HUSNI, M. E., MUSCHLER, G. F., GUARINO, A. & MONT, M. A. 2017a. Knee Osteoarthritis: A Primer. *Perm J,* 21**,** 16-183.

LESPASIO, M. J., PIUZZI, N. S., HUSNI, M. E., MUSCHLER, G. F., GUARINO, A. & MONT, M. A. 2017b. Knee Osteoarthritis: A Primer. *The Permanente journal,* 21**,** 16-183.

LEWIS, J. S., HEMBREE, W. C., FURMAN, B. D., TIPPETS, L., CATTEL, D., HUEBNER, J. L., LITTLE, D., DEFRATE, L. E., KRAUS, V. B., GUILAK, F. & OLSON, S. A. 2011. Acute joint pathology and synovial inflammation is associated with increased intra-articular fracture severity in the mouse knee. *Osteoarthritis and Cartilage,* 19**,** 864-873.

LI, B. & ASPDEN, R. M. 1997. Composition and mechanical properties of cancellous bone from the femoral head of patients with osteoporosis or osteoarthritis. *Journal of bone and mineral research,* 12**,** 641-651.

LI, G., YIN, J., GAO, J., CHENG, T. S., PAVLOS, N. J., ZHANG, C. & ZHENG, M. H. 2013a. Subchondral bone in osteoarthritis: insight into risk factors and microstructural changes. *Arthritis Research & Therapy,* 15**,** 223.

LI, G., YIN, J., GAO, J., CHENG, T. S., PAVLOS, N. J., ZHANG, C. & ZHENG, M. H. 2013b. Subchondral bone in osteoarthritis: insight into risk factors and microstructural changes. *Arthritis research & therapy,* 15**,** 1-12.

LI, G. Y., YIN, J. M., GAO, J. J., CHENG, T. S., PAVLOS, N. J., ZHANG, C. Q. & ZHENG, M. H. 2013c. Subchondral bone in osteoarthritis: insight into risk factors and microstructural changes. *Arthritis Research & Therapy,* 15.

LI, Y., FRANK, E. H., WANG, Y., CHUBINSKAYA, S., HUANG, H.-H. & GRODZINSKY, A. J. 2013d. Moderate dynamic compression inhibits pro-catabolic response of cartilage to mechanical injury, tumor necrosis factor-α and interleukin-6, but accentuates degradation above a strain threshold. *Osteoarthritis and Cartilage,* 21**,** 1933-1941.

LI, Y. & XU, L. 2015. Advances in understanding cartilage remodeling. *F1000Res,* 4**,** 642.

LIBICHER, M., IVANCIC, M., HOFFMANN, M. & WENZ, W. 2005a. Early changes in experimental osteoarthritis using the Pond-Nuki dog model: technical procedure and initial results of in vivo MR imaging. *European Radiology,* 15**,** 390-394.

LIBICHER, M., IVANCIC, M., HOFFMANN, V. & WENZ, W. 2005b. Early changes in experimental osteoarthritis using the Pond-Nuki dog model: technical procedure and initial results of in vivo MR imaging. *European Radiology,* 15**,** 390-394.

LINK, T. M., NEUMANN, J. & LI, X. 2017a. Prestructural cartilage assessment using MRI. *Journal of Magnetic Resonance Imaging,* 45**,** 949-965.

LINK, T. M., NEUMANN, J. & LI, X. J. 2017b. Prestructural cartilage assessment using MRI. *Journal of Magnetic Resonance Imaging,* 45**,** 949-965.

LITTLE, C. B. & HUNTER, D. J. 2013. Post-traumatic osteoarthritis: from mouse models to clinical trials. *Nature Reviews Rheumatology,* 9**,** 485-497.

LITTLE, C. B. & ZAKI, S. 2012a. What constitutes an “animal model of osteoarthritis” – the need for consensus? *Osteoarthritis and Cartilage,* 20**,** 261-267.

LITTLE, C. B. & ZAKI, S. 2012b. What constitutes an "animal model of osteoarthritis"--the need for consensus? *Osteoarthritis Cartilage,* 20**,** 261-7.

LIU, Y., SHAH, K. M. & LUO, J. 2021. Strategies for articular cartilage repair and regeneration. *Frontiers in Bioengineering and Biotechnology,* 9**,** 1328.

LIUKKONEN, M. K., MONONEN, M. E., TANSKA, P., SAARAKKALA, S., NIEMINEN, M. T. & KORHONEN, R. K. 2017. Application of a semi-automatic cartilage segmentation method for biomechanical modeling of the knee joint. *Comput Methods Biomech Biomed Engin,* 20**,** 1453-1463.

LOBOA, E. G., WREN, T. A. L., BEAUPRé, G. S. & CARTER, D. R. 2003. Mechanobiology of soft skeletal tissue differentiation—a computational approach of a fiber-reinforced poroelastic model based on homogeneous and isotropic simplifications. *Biomechanics and Modeling in Mechanobiology,* 2**,** 83-96.

LOCKWOOD, K. A., CHU, B. T., ANDERSON, M. J., HAUDENSCHILD, D. R. & CHRISTIANSEN, B. A. 2014. Comparison of loading rate-dependent injury modes in a murine model of post-traumatic osteoarthritis. *J Orthop Res,* 32**,** 79-88.

LOESER, R. F., COLLINS, J. A. & DIEKMAN, B. O. 2016. Ageing and the pathogenesis of osteoarthritis. *Nature Reviews Rheumatology,* 12**,** 412.

LONG, D., BLAKE, S., SONG, X.-Y., LARK, M. & LOESER, R. F. 2008. Human articular chondrocytes produce IL-7 and respond to IL-7 with increased production of matrix metalloproteinase-13. *Arthritis research & therapy,* 10**,** 1-10.

LUO, Y. Y. & KARSDAL, M. A. 2016. Chapter 11 - Type XI Collagen. *In:* KARSDAL, M. A. (ed.) *Biochemistry of Collagens, Laminins and Elastin.* Academic Press.

LYDON, H., GETGOOD, A. & HENSON, F. M. D. 2017. Healing of Osteochondral Defects via Endochondral Ossification in an Ovine Model. *CARTILAGE,* 10**,** 94-101.

MA, Y., YAO, Y., ZHONG, N., ANGWA, L. M. & PEI, J. 2020. The dose-time effects of fluoride on the expression and DNA methylation level of the promoter region of BMP-2 and BMP-7 in rats. *Environ Toxicol Pharmacol,* 75**,** 103331.

MADRY, H., VAN DIJK, C. N. & MUELLER-GERBL, M. 2010. The basic science of the subchondral bone. *Knee Surgery, Sports Traumatology, Arthroscopy,* 18**,** 419-433.

MAERZ, T., KURDZIEL, M. D., DAVIDSON, A. A., BAKER, K. C., ANDERSON, K. & MATTHEW, H. W. 2015. Biomechanical Characterization of a Model of Noninvasive, Traumatic Anterior Cruciate Ligament Injury in the Rat. *Ann Biomed Eng,* 43**,** 2467-76.

MAES, C., ARALDI, E., HAIGH, K., KHATRI, R., VAN LOOVEREN, R., GIACCIA, A. J., HAIGH, J. J., CARMELIET, G. & SCHIPANI, E. 2012. VEGF‐independent cell‐autonomous functions of

HIF-1α regulating oxygen consumption in fetal cartilage are critical for chondrocyte survival. *Journal of Bone and Mineral Research,* 27**,** 596-609.

MAFFIULETTI, N. A., AAGAARD, P., BLAZEVICH, A. J., FOLLAND, J., TILLIN, N. & DUCHATEAU, J. 2016. Rate of force development: physiological and methodological considerations. *Eur J Appl Physiol,* 116**,** 1091-116.

MALEMUD, C. J. 2010. Anticytokine therapy for osteoarthritis: evidence to date. *Drugs & aging,* 27**,** 95-115.

MALFAIT, A.-M. & MILLER, R. E. 2020. Why we should study osteoarthritis pain in experimental models in both sexes. *Osteoarthritis and cartilage,* 28**,** 397-399.

MALFAIT, A. M., LITTLE, C. B. & MCDOUGALL, J. J. 2013. A commentary on modelling osteoarthritis pain in small animals. *Osteoarthritis and Cartilage,* 21**,** 1316-1326.

MALFAIT, A. M., RITCHIE, J., GIL, A. S., AUSTIN, J. S., HARTKE, J., QIN, W., TORTORELLA, M. D. & MOGIL, J. S. 2010. ADAMTS-5 deficient mice do not develop mechanical allodynia associated with osteoarthritis following medial meniscal destabilization. *Osteoarthritis and Cartilage,* 18**,** 572-580.

MALY, M. R., ACKER, S. M., TOTTERMAN, S., TAMEZ-PENA, J., STRATFORD, P. W., CALLAGHAN, J. P., ADACHI, J. D. & BEATTIE, K. A. 2015. Knee adduction moment relates to medial femoral and tibial cartilage morphology in clinical knee osteoarthritis. *J Biomech,* 48**,** 3495-501.

MANKIN, H. J., DORFMAN, H., LIPPIELLO, L. & ZARINS, A. 1971. Biochemical and metabolic abnormalities in articular cartilage from osteo-arthritic human hips: II. Correlation of morphology with biochemical and metabolic data. *JBJS,* 53**,** 523-537.

MANKIN, H. J., JOHNSON, M. & LIPPIELLO, L. 1981a. Biochemical and metabolic abnormalities in articular cartilage from osteoarthritic human hips. III. Distribution and metabolism of amino sugar-containing macromolecules. *The Journal of bone and joint surgery. American volume,* 63**,** 131-139.

MANKIN, H. J., JOHNSON, M. E. & LIPPIELLO, L. 1981b. Biochemical and metabolic abnormalities in articular cartilage from osteoarthritic human hips. III. Distribution and metabolism of amino sugar-containing macromolecules. *J Bone Joint Surg Am,* 63**,** 131-9.

MAPP, P. I. & WALSH, D. A. 2012. Mechanisms and targets of angiogenesis and nerve growth in osteoarthritis. *Nature Reviews Rheumatology,* 8**,** 390-398.

MARTAY, J. L., PALMER, A. J., BANGERTER, N. K., CLARE, S., MONK, A. P., BROWN, C. P. & PRICE, A. J. 2018. A preliminary modeling investigation into the safe correction zone for high tibial osteotomy. *The Knee,* 25**,** 286-295.

MASON, R. M., CHAMBERS, M. G., FLANNELLY, J., GAFFEN, J. D., DUDHIA, J. & BAYLISS, M. T. 2001. The STR/ort mouse and its use as a model of osteoarthritis. *Osteoarthritis and Cartilage,* 9**,** 85-91.

MASOUROS, S., MCDERMOTT, I., AMIS, A. & BULL, A. 2008. Biomechanics of the meniscus-meniscal ligament construct of the knee. *Knee surgery, sports traumatology, arthroscopy,* 16**,** 1121-1132.

MASTBERGEN, S. C., MARIJNISSEN, A. C., VIANEN, M. E., VAN ROERMUND, P. M., BIJLSMA, J. W. & LAFEBER, F. P. 2006. The canine 'groove' model of osteoarthritis is more than simply the expression of surgically applied damage. *Osteoarthritis and Cartilage,* 14**,** 39-46.

MATUSKA, A., O'SHAUGHNESSEY, K., KING, W. & WOODELL-MAY, J. 2013. Autologous solution protects bovine cartilage explants from IL-1α- and TNFα-induced cartilage degradation. *J Orthop Res,* 31**,** 1929-35.

MCALINDON, T. E., DRIBAN, J., HENROTIN, Y., HUNTER, D., JIANG, G.-L., SKOU, S. T., WANG, S. & SCHNITZER, T. 2015. OARSI clinical trials recommendations: design, conduct, and reporting of clinical trials for knee osteoarthritis. *Osteoarthritis and cartilage,* 23**,** 747-760.

MCCOY, A. M. 2015a. Animal Models of Osteoarthritis: Comparisons and Key Considerations. *Veterinary Pathology,* 52**,** 803-818.

MCCOY, A. M. 2015b. Animal Models of Osteoarthritis:Comparisons and Key Considerations. *Veterinary Pathology,* 52**,** 803-818.

MCDOUGALL, J. J., SCHUELERT, N. & BOWYER, J. 2010. Cathepsin K inhibition reduces CTXII levels and joint pain in the guinea pig model of spontaneous osteoarthritis. *Osteoarthritis Cartilage,* 18**,** 1355-7.

MCERLAIN, D. D., APPLETON, C. T., LITCHFIELD, R. B., PITELKA, V., HENRY, J. L., BERNIER, S. M., BEIER, F. & HOLDSWORTH, D. W. 2008. Study of subchondral bone adaptations in a rodent surgical model of OA using in vivo micro-computed tomography. *Osteoarthritis Cartilage,* 16**,** 458-69.

MCERLAIN, D. D., MILNER, J. S., IVANOV, T. G., JENCIKOVA-CELERIN, L., POLLMANN, S. I. & HOLDSWORTH, D. W. 2011. Subchondral cysts create increased intra-osseous stress in early knee OA: A finite element analysis using simulated lesions. *Bone,* 48**,** 639-46.

MCERLAIN, D. D., ULICI, V., DARLING, M., GATI, J. S., PITELKA, V., BEIER, F. & HOLDSWORTH, D. W. 2012. An in vivo investigation of the initiation and progression of subchondral cysts in a rodent model of secondary osteoarthritis. *Arthritis Research & Therapy,* 14.

MCILWRAITH, C. W., FRISBIE, D. D. & KAWCAK, C. E. 2012. The horse as a model of naturally occurring osteoarthritis. *Bone & Joint Research,* 1**,** 297-309.

MCINTYRE, J. A., JONES, I. A., HAN, B. & VANGSNESS JR, C. T. 2018. Intra-articular mesenchymal stem cell therapy for the human joint: a systematic review. *The American journal of sports medicine,* 46**,** 3550-3563.

MCNAMEE, K. E., BURLEIGH, A., GOMPELS, L. L., FELDMANN, M., ALLEN, S. J., WILLIAMS, R. O., DAWBARN, D., VINCENT, T. L. & INGLIS, J. J. 2010. Treatmentof murine osteoarthritis withTrkAd5 reveals a pivotal rolefor nerve growth factor in non-inflammatory joint pain. *PAIN®,* 149**,** 386-392.

MCNULTY, M. A., LOESER, R. F., DAVEY, C., CALLAHAN, M. F., FERGUSON, C. M. & CARLSON, C. S. 2012. Histopathology of naturally occurring and surgically induced osteoarthritis in mice. *Osteoarthritis Cartilage,* 20**,** 949-56.

MELVILLE, K. M., ROBLING, A. G. & VAN DER MEULEN, M. C. 2015. In vivo axial loading of the mouse tibia. *Methods Mol Biol,* 1226**,** 99-115.

MERINO, R., RODRIGUEZ-LEON, J., MACIAS, D., GANAN, Y., ECONOMIDES, A. & HURLE, J. 1999. The BMP antagonist Gremlin regulates outgrowth, chondrogenesis and programmed cell death in the developing limb. *Development,* 126**,** 5515-5522.

MEULENBELT, I., KLOPPENBURG, M., KROON, H. M., HOUWING-DUISTERMAAT, J. J., GARNERO, P., LE GRAVERAND, M. H., DEGROOT, J. & SLAGBOOM, P. 2006a. Urinary CTX-II levels are associated with radiographic subtypes of osteoarthritis in hip, knee, hand, and facet joints in subject with familial osteoarthritis at multiple sites: the GARP study. *Annals of the rheumatic diseases,* 65**,** 360-365.

MEULENBELT, I., KLOPPENBURG, M., KROON, H. M., HOUWING-DUISTERMAAT, J. J., GARNERO, P., LE GRAVERAND, M. P. H., DEGROOT, J. & SLAGBOOM, P. E. 2006b. Urinary CTX-II levels are associated with radiographic subtypes of osteoarthritis in hip, knee, hand, and facet joints in subject with familial osteoarthritis at multiple sites: the GARP study. *Annals of the Rheumatic Diseases,* 65**,** 360-365.

MEYERS, V. E., ZAYZAFOON, M., GONDA, S. R., GATHINGS, W. E. & MCDONALD, J. M. 2004. Modeled microgravity disrupts collagen I/integrin signaling during osteoblastic differentiation of human mesenchymal stem cells. *Journal of cellular biochemistry,* 93**,** 697-707.

MILLER, R. E., LU, Y., TORTORELLA, M. D. & MALFAIT, A.-M. 2013a. Genetically engineered mouse models reveal the importance of proteases as osteoarthritis drug targets. *Current rheumatology reports,* 15**,** 350.

MILLER, R. E., LU, Y. Z., TORTORELLA, M. D. & MALFAIT, A. M. 2013b. Genetically Engineered Mouse Models Reveal the Importance of Proteases as Osteoarthritis Drug Targets. *Current Rheumatology Reports,* 15.

MITCHELL, B. L., YASUI, Y., LI, C. I., FITZPATRICK, A. L. & LAMPE, P. D. 2005. Impact of freeze-thaw cycles and storage time on plasma samples used in mass spectrometry based biomarker discovery projects. *Cancer Inform,* 1**,** 98-104.

MITULOVIĆ, G. & MECHTLER, K. 2006. HPLC techniques for proteomics analysis—a short overview of latest developments. *Briefings in Functional Genomics,* 5**,** 249-260.

MODICA, S., STRAUB, L. G., BALAZ, M., SUN, W., VARGA, L., STEFANICKA, P., PROFANT, M., SIMON, E., NEUBAUER, H. & UKROPCOVA, B. 2016. Bmp4 promotes a brown to white-like adipocyte shift. *Cell reports,* 16**,** 2243-2258.

MOGIL, J. S. 2009. Animal models of pain: progress and challenges. *Nature Reviews Neuroscience,* 10**,** 283-294.

MOHAN, G., PERILLI, E., KULIWABA, J. S., HUMPHRIES, J. M., PARKINSON, I. H. & FAZZALARI, N. L. 2011. Application of in vivo micro-computed tomography in the temporal characterisation of subchondral bone architecture in a rat model of low-dose monosodium iodoacetate-induced osteoarthritis. *Arthritis Research & Therapy,* 13**,** R210.

MOODIE, J. P., STOK, K. S., MüLLER, R., VINCENT, T. L. & SHEFELBINE, S. J. 2011. Multimodal imaging demonstrates concomitant changes in bone and cartilage after destabilisation of the medial meniscus and increased joint laxity. *Osteoarthritis Cartilage,* 19**,** 163-70.

MORADI, B., ROSSHIRT, N., TRIPEL, E., KIRSCH, J., BARIé, A., ZEIFANG, F., GOTTERBARM, T. & HAGMANN, S. 2015. Unicompartmental and bicompartmental knee osteoarthritis show different patterns of mononuclear cell infiltration and cytokine release in the affected joints. *Clin Exp Immunol,* 180**,** 143-54.

MOTOHASHI, H. & YAMAMOTO, M. 2004. Nrf2–Keap1 defines a physiologically important stress response mechanism. *Trends in molecular medicine,* 10**,** 549-557.

MURPHY, G. & LEE, M. 2005. What are the roles of metalloproteinases in cartilage and bone damage? *Annals of the rheumatic diseases,* 64**,** iv44-iv47.

NAGAO, M., HAMILTON, J. L., KC, R., BERENDSEN, A. D., DUAN, X., CHEONG, C. W., LI, X., IM, H.-J. & OLSEN, B. R. 2017. Vascular Endothelial Growth Factor in Cartilage Development and Osteoarthritis. *Scientific Reports,* 7**,** 13027.

NEES, T. A., ROSSHIRT, N., ZHANG, J. A., REINER, T., SORBI, R., TRIPEL, E., WALKER, T., SCHILTENWOLF, M., HAGMANN, S. & MORADI, B. 2019. Synovial Cytokines Significantly Correlate with Osteoarthritis-Related Knee Pain and Disability: Inflammatory Mediators of Potential Clinical Relevance. *Journal of Clinical Medicine,* 8**,** 1343.

NEOGI, T., BOWES, M. A., NIU, J., DE SOUZA, K. M., VINCENT, G. R., GOGGINS, J., ZHANG, Y. & FELSON, D. T. 2013. Magnetic resonance imaging-based three-dimensional bone shape of the knee predicts onset of knee osteoarthritis: data from the osteoarthritis initiative. *Arthritis Rheum,* 65**,** 2048-58.

NIE, Y., YU, Q. & SHEN, B. 2021. Impact of Tibial Component Coronal Alignment on Knee Joint Biomechanics Following Fixed‐bearing Unicompartmental Knee Arthroplasty: A Finite Element Analysis. *Orthopaedic Surgery,* 13**,** 1423-1429.

NIEHOFF, A., OFFERMANN, M., DARGEL, J., SCHMIDT, A., BRüGGEMANN, G. P. & BLOCH, W. 2008. Dynamic and static mechanical compression affects Akt phosphorylation in porcine patellofemoral joint cartilage. *Journal of Orthopaedic Research,* 26**,** 616-623.

NILSSON, O., PARKER, E. A., HEGDE, A., CHAU, M., BARNES, K. M. & BARON, J. 2007. Gradients in bone morphogenetic protein-related gene expression across the growth plate. *Journal of Endocrinology,* 193**,** 75-84.

NOROUZI, N., BHAKTA, H. C. & GROVER, W. H. 2017. Sorting cells by their density. *PloS one,* 12**,** e0180520.

O'SHAUGHNESSEY, K., MATUSKA, A., HOEPPNER, J., FARR, J., KLAASSEN, M., KAEDING, C., LATTERMANN, C., KING, W. & WOODELL-MAY, J. 2014a. Autologous protein solution prepared from the blood of osteoarthritic patients contains an enhanced profile of anti-inflammatory cytokines and anabolic growth factors. *J Orthop Res,* 32**,** 1349-55.

O'SHAUGHNESSEY, K., MATUSKA, A., HOEPPNER, J., FARR, J., KLAASSEN, M., KAEDING, C., LATTERMANN, C., KING, W. & WOODELL‐MAY, J. 2014b. Autologous protein solution prepared from the blood of osteoarthritic patients contains an enhanced profile of anti‐inflammatory cytokines and anabolic growth factors. *Journal of Orthopaedic Research,* 32**,** 1349-1355.

O'SHAUGHNESSEY, K. M., PANITCH, A. & WOODELL-MAY, J. E. 2011. Blood-derived anti-inflammatory protein solution blocks the effect of IL-1β on human macrophages in vitro. *Inflamm Res,* 60**,** 929-36.

OESTERGAARD, S., SONDERGAARD, B. C., HOEGH-ANDERSEN, P., HENRIKSEN, K., QVIST, P., CHRISTIANSEN, C., TANKO, L. B. & KARSDAL, M. A. 2006. Effects of ovariectomy and estrogen therapy on type II collagen degradation and structural integrity of articular cartilage in rats - Implications of the time of initiation. *Arthritis and Rheumatism,* 54**,** 2441-2451.

OHTORI, S., ORITA, S., YAMAUCHI, K., EGUCHI, Y., OCHIAI, N., KISHIDA, S., KUNIYOSHI, K., AOKI, Y., NAKAMURA, J. & ISHIKAWA, T. 2015. Efficacy of direct injection of etanercept into knee joints for pain in moderate and severe knee osteoarthritis. *Yonsei Medical Journal,* 56**,** 1379-1383.

ORHAN, C., JUTURU, V., SAHIN, E., TUZCU, M., OZERCAN, I. H., DURMUS, A. S., SAHIN, N. & SAHIN, K. 2021. Undenatured Type II Collagen Ameliorates Inflammatory Responses and Articular Cartilage Damage in the Rat Model of Osteoarthritis. *Front Vet Sci,* 8**,** 617789.

OTSU, N. 1979. A Threshold Selection Method from Gray-Level Histograms. *IEEE Transactions on Systems, Man, and Cybernetics,* 9**,** 62-66.

OVERLEY, B. D. & BEIDEMAN, T. C. 2015. Painful osteophytes, ectopic bone, and pain in the malleolar gutters following total ankle replacement: management and strategies. *Clinics in Podiatric Medicine and Surgery,* 32**,** 509-516.

PALAZZO, C., NGUYEN, C., LEFEVRE-COLAU, M. M., RANNOU, F. & POIRAUDEAU, S. 2016. Risk factors and burden of osteoarthritis. *Ann Phys Rehabil Med,* 59**,** 134-138.

PALMIERI-SMITH, R. M., THOMAS, A. C., KARVONEN-GUTIERREZ, C. & SOWERS, M. F. 2010. Isometric Quadriceps Strength in Women with Mild, Moderate, and Severe Knee Osteoarthritis. *American Journal of Physical Medicine & Rehabilitation,* 89**,** 541-548.

PANULA, H. E., HELMINEN, H. J. & KIVIRANTA, I. 1997a. Slowly progressive osteoarthritis after tibial valgus osteotomy in young beagle dogs. *Clin Orthop Relat Res***,** 192-202.

PANULA, H. E., HELMINEN, H. J. & KIVIRANTA, I. 1997b. Slowly progressive osteoarthritis after tibial valgus osteotomy in young beagle dogs. *Clinical orthopaedics and related research***,** 192-202.

PANZER, S., AUGAT, P., ATZWANGER, J. & HERGAN, K. 2012. 3-T MRI assessment of osteophyte formation in patients with unilateral anterior cruciate ligament injury and reconstruction. *Skeletal Radiology,* 41**,** 1597-1604.

PARK, S., BELLO, A., ARAI, Y., AHN, J., KIM, D., CHA, K.-Y., BAEK, I., PARK, H. & LEE, S.-H. 2021. Functional Duality of Chondrocyte Hypertrophy and Biomedical Application Trends in Osteoarthritis. *Pharmaceutics,* 13**,** 1139.

PARRA-TORRES, N. M., CAZARES-RAGA, F. E. & KOURI, J. B. 2014a. Proteomic analysis of rat cartilage: the identification of differentially expressed proteins in the early stages of osteoarthritis. *Proteome Sci,* 12**,** 55.

PARRA-TORRES, N. M., CáZARES-RAGA, F. E. & KOURI, J. B. 2014b. Proteomic analysis of rat cartilage: the identification of differentially expressed proteins in the early stages of osteoarthritis. *Proteome science,* 12**,** 1-12.

PARRA-TORRES, N. M., CáZARES-RAGA, F. E. & KOURI, J. B. 2014c. Proteomic analysis of rat cartilage: the identification of differentially expressed proteins in the early stages of osteoarthritis. *Proteome Science,* 12**,** 55.

PAS, H. I., WINTERS, M., HAISMA, H. J., KOENIS, M. J., TOL, J. L. & MOEN, M. H. 2017. Stem cell injections in knee osteoarthritis: a systematic review of the literature. *British journal of sports medicine,* 51**,** 1125-1133.

PEDOIA, V., HAEFELI, J., MORIOKA, K., TENG, H. L., NARDO, L., SOUZA, R. B., FERGUSON, A. R. & MAJUMDAR, S. 2017. TOPOLOGICAL DATA ANALYSIS TO PREDICT CARTILAGE LESION PROGRESSION IN KNEE OSTEOARTHRITIS. *Osteoarthritis and Cartilage,* 25**,** S240-S241.

PEREIRA, J. E., CABRITA, A. M., FILIPE, V. M., BULAS-CRUZ, J., COUTO, P. A., MELO-PINTO, P., COSTA, L. M., GEUNA, S., MAURICIO, A. C. & VAREJAO, A. S. 2006. A comparison analysis of hindlimb kinematics during overground and treadmill locomotion in rats. *Behav Brain Res,* 172**,** 212-8.

PING, S. H., TIAN, F. M., LIU, H., SUN, Q., SHAO, L. T., LIAN, Q. Q. & ZHANG, L. 2021. Raloxifene inhibits the overexpression of TGF-β1 in cartilage and regulates the metabolism of subchondral bone in rats with osteoporotic osteoarthritis. *Bosn J Basic Med Sci,* 21**,** 284-293.

PISKIN, A., GULBAHAR, M. Y., TOMAK, Y., GULMAN, B., HOKELEK, M., KERIMOGLU, S., KOKSAL, B., ALIC, T. & KABAK, Y. B. 2007. Osteoarthritis models after anterior cruciate ligament resection and medial meniscectomy in rats. A histological and immunohistochemical study. *Saudi Med J,* 28**,** 1796-802.

PITCHER, T., SOUSA-VALENTE, J. & MALCANGIO, M. 2016. The Monoiodoacetate Model of Osteoarthritis Pain in the Mouse. *J Vis Exp*.

PITSILLIDES, A. A. & BEIER, F. 2011. Cartilage biology in osteoarthritis—lessons from developmental biology. *Nature Reviews Rheumatology,* 7**,** 654-663.

PORTILLO, A. L., HOGG, R. & ASHKAR, A. A. 2021. Production of human CAR-NK cells with lentiviral vectors and functional assessment in vitro. *STAR protocols,* 2**,** 100956.

POULET, B. 2016. Non-invasive Loading Model of Murine Osteoarthritis. *Curr Rheumatol Rep,* 18**,** 40.

POULET, B., DE SOUZA, R., KENT, A. V., SAXON, L., BARKER, O., WILSON, A., CHANG, Y. M., CAKE, M. & PITSILLIDES, A. A. 2015. Intermittent applied mechanical loading induces subchondral bone thickening that may be intensified locally by contiguous articular cartilage lesions. *Osteoarthritis and Cartilage,* 23**,** 940-948.

POULET, B., DE SOUZA, R., KNIGHTS, C. B., GENTRY, C., WILSON, A. M., BEVAN, S., CHANG, Y. M. & PITSILLIDES, A. A. 2014a. Modifications of gait as predictors of natural osteoarthritis progression in STR/Ort mice. *Arthritis & rheumatology,* 66**,** 1832-1842.

POULET, B., HAMILTON, R. W., SHEFELBINE, S. & PITSILLIDES, A. A. 2011a. Characterizing a novel and adjustable noninvasive murine joint loading model. *Arthritis & Rheumatism,* 63**,** 137-147.

POULET, B., HAMILTON, R. W., SHEFELBINE, S. & PITSILLIDES, A. A. 2011b. Characterizing a novel and adjustable noninvasive murine joint loading model. *Arthritis Rheum,* 63**,** 137-47.

POULET, B., SOUZA, R., KNIGHT, C., WILSON, A., BEVAN, S., CHANG, Y. & PITSILLIDES, A. 2014b. Gait analysis in Str/ort mice reveals modified paw area as a predictor of natural osteoarthritis progression. *ARTHRITIS AND RHEUMATISM,* 66.

POULET, B., WESTERHOF, T. A. T., HAMILTON, R. W., SHEFELBINE, S. J. & PITSILLIDES, A. A. 2013. Spontaneous osteoarthritis in Str/ort mice is unlikely due to greater vulnerability to mechanical trauma. *Osteoarthritis and Cartilage,* 21**,** 756-763.

PRITZKER, K. P. 2003. Pathology of osteoarthritis. *Osteoarthritis,* 2**,** 49-58.

PRITZKER, K. P. H., GAY, S., JIMENEZ, S. A., OSTERGAARD, K., PELLETIER, J. P., REVELL, P. A., SALTER, D. & VAN DEN BERG, W. B. 2006. Osteoarthritis cartilage histopathology: grading and staging. *Osteoarthritis and Cartilage,* 14**,** 13-29.

PROFFEN, B. L., MCELFRESH, M., FLEMING, B. C. & MURRAY, M. M. 2012. A comparative anatomical study of the human knee and six animal species. *Knee,* 19**,** 493-9.

PUCHA, K. A., MCKINNEY, J. M., FULLER, J. M. & WILLETT, N. J. 2020. Characterization of OA development between sexes in the rat medial meniscal transection model. *Osteoarthritis and Cartilage Open,* 2**,** 100066.

QIAN, J. J., XU, Q., XU, W. M., CAI, R. & HUANG, G. C. 2021. Expression of VEGF-A Signaling Pathway in Cartilage of ACLT-induced Osteoarthritis Mouse Model. *J Orthop Surg Res,* 16**,** 379.

QIN, Y., HE, J., XIA, L., GUO, H. & HE, C. 2013. Effects of electro-acupuncture on oestrogen levels, body weight, articular cartilage histology and MMP-13 expression in ovariectomised rabbits. *Acupunct Med,* 31**,** 214-21.

RAMME, A. J., LENDHEY, M., RAYA, J. G., KIRSCH, T. & KENNEDY, O. D. 2016. A novel rat model for subchondral microdamage in acute knee injury: a potential mechanism in post-traumatic osteoarthritis. *Osteoarthritis Cartilage,* 24**,** 1776-1785.

RAMME, A. J., LENDHEY, M. S., STRAUSS, E. J. & KENNEDY, O. D. 2018. A Biomechanical Study of Two Distinct Methods of Anterior Cruciate Ligament Rupture, and a Novel Surgical Reconstruction Technique, in a Small Animal Model of Posttraumatic Osteoarthritis. *J Knee Surg,* 31**,** 43-49.

RAMME, A. J., VOSS, K., LESPORIS, J., LENDHEY, M. S., COUGHLIN, T. R., STRAUSS, E. J. & KENNEDY, O. D. 2017. Automated Bone Segmentation and Surface Evaluation of a Small Animal Model of Post-Traumatic Osteoarthritis. *Ann Biomed Eng,* 45**,** 1227-1235.

REEVES, N. D. & BOWLING, F. L. 2011. Conservative biomechanical strategies for knee osteoarthritis. *Nature Reviews Rheumatology,* 7**,** 113.

REIMANN, I. 1973a. Experimental osteoarthritis of the knee in rabbits induced by alteration of the load-bearing. *Acta Orthop Scand,* 44**,** 496-504.

REIMANN, I. 1973b. Experimental osteoarthritis of the knee in rabbits induced by alteration of the load-bearing. *Acta Orthopaedica Scandinavica,* 44**,** 496-504.

RICHMOND, S. A., FUKUCHI, R. K., EZZAT, A., SCHNEIDER, K., SCHNEIDER, G. & EMERY, C. A. 2013. Are joint injury, sport activity, physical activity, obesity, or occupational activities predictors for osteoarthritis? A systematic review. *J Orthop Sports Phys Ther,* 43**,** 515-B19.

RO, J. Y., ZHANG, Y., TRICOU, C., YANG, D., DA SILVA, J. T. & ZHANG, R. 2019. Age and Sex Differences in Acute and Osteoarthritis-Like Pain Responses in Rats. *The Journals of Gerontology: Series A,* 75**,** 1465-1472.

ROBBINS, S. M., MORELLI, M., MARTINEAU, P. A., ST-ONGE, N., BOILY, M., DIMENTBERG, R. & ANTONIOU, J. 2019. A comparison of muscle activation and knee mechanics during gait between patients with non-traumatic and post-traumatic knee osteoarthritis. *Osteoarthritis Cartilage,* 27**,** 1033-1042.

ROBIN, D. M. C. 2017. ESTABLISHMENT OF A RAT MODEL OF TEMPOROMANDIBULAR JOINT OSTEOARTHRITIS USING INTRAARTICULAR INJECTION OF COMPLETE FREUND'S ADJUVANT. *UNEJ e-Proceeding***,** 190-193.

ROCHA, B., CALAMIA, V., MATEOS, J., FERNáNDEZ-PUENTE, P., LOURIDO, L., FERNáNDEZ-COSTA, C., FERNáNDEZ-LóPEZ, C., OREIRO, N., RUIZ-ROMERO, C. & BLANCO, F. 2013. THU0024 Differences between healthy and osteoarthritis proteomic profiles of bone marrow mesenchymal stem cells undergoing chondrogenesis. *Annals of the Rheumatic Diseases,* 71**,** 161-161.

RODAN, G. A. 1991. Perspectives: mechanical loading, estrogen deficiency, and the coupling of bone formation to bone resorption. *Journal of Bone and Mineral Research,* 6**,** 527-530.

RODRIGUES-NETO, H. R., ANDRADE-JUNIOR, E. F., FEITOSA-JUNIOR, D. J. S., VALENTE, A. L., XAVIER, T. C., ALHO, B. C. D. N., TEIXEIRA, R. K. C., MORIYA, F. V. & BARROS, R. S. R. M. D. 2016. Comparison of Three Experimental Models for Rat Osteoarthritis Induction. *Journal of Biosciences and Medicines,* Vol.04No.12**,** 8.

ROEMER, F. W., ECKSTEIN, F., HAYASHI, D. & GUERMAZI, A. 2014a. The role of imaging in osteoarthritis. *Best Pract Res Clin Rheumatol,* 28**,** 31-60.

ROEMER, F. W., ECKSTEIN, F., HAYASHI, D. & GUERMAZI, A. 2014b. The role of imaging in osteoarthritis. *Best practice & research Clinical rheumatology,* 28**,** 31-60.

ROEMER, F. W., GUERMAZI, A., NIU, J., ZHANG, Y., MOHR, A. & FELSON, D. T. 2012a. Prevalence of magnetic resonance imaging-defined atrophic and hypertrophic phenotypes of knee osteoarthritis in a population-based cohort. *Arthritis Rheum,* 64**,** 429-37.

ROEMER, F. W., GUERMAZI, A., NIU, J., ZHANG, Y., MOHR, A. & FELSON, D. T. 2012b. Prevalence of magnetic resonance imaging – defined atrophic and hypertrophic phenotypes of knee osteoarthritis in a population - based cohort. *Arthritis & Rheumatism,* 64**,** 429-437.

ROEMER, F. W., KWOH, C. K., HANNON, M. J., HUNTER, D. J., ECKSTEIN, F., FUJII, T., BOUDREAU, R. M. & GUERMAZI, A. 2015. What comes first? Multitissue involvement leading to radiographic osteoarthritis: magnetic resonance imaging-based trajectory analysis over four years in the osteoarthritis initiative. *Arthritis Rheumatol,* 67**,** 2085-96.

RöNN, K., REISCHL, N., GAUTIER, E. & JACOBI, M. 2011. Current surgical treatment of knee osteoarthritis. *Arthritis,* 2011.

ROOS, E. M., HERZOG, W., BLOCK, J. A. & BENNELL, K. L. 2011. Muscle weakness, afferent sensory dysfunction and exercise in knee osteoarthritis. *Nat Rev Rheumatol,* 7**,** 57-63.

ROUSSEAU, J.-C. & DELMAS, P. D. 2007. Biological markers in osteoarthritis. *Nature Clinical Practice Rheumatology,* 3**,** 346-356.

ROUX, W. 1895. *Gesammelte Abhandlungen über Entwicklungsmechanik der Organismen von Wilhelm Roux*, W. Engelmann.

RUNDELL, S. A., BAARS, D. C., PHILLIPS, D. M. & HAUT, R. C. 2005. The limitation of acute necrosis in retro-patellar cartilage after a severe blunt impact to the in vivo rabbit patello-femoral joint. *J Orthop Res,* 23**,** 1363-9.

RUTGERS, M., VAN PELT, M., DHERT, W., CREEMERS, L. B. & SARIS, D. 2010a. Evaluation of histological scoring systems for tissue-engineered, repaired and osteoarthritic cartilage. *Osteoarthritis and cartilage,* 18**,** 12-23.

RUTGERS, M., VAN PELT, M. J., DHERT, W. J., CREEMERS, L. B. & SARIS, D. B. 2010b. Evaluation of histological scoring systems for tissue-engineered, repaired and osteoarthritic cartilage. *Osteoarthritis Cartilage,* 18**,** 12-23.

RUTHERFORD, D., HUBLEY-KOZEY, C. & STANISH, W. 2010. The neuromuscular demands of altering foot progression angle during gait in asymptomatic individuals and those with knee osteoarthritis. *Osteoarthritis and cartilage,* 18**,** 654-661.

SAGAWA JR, Y., ARMAND, S., LUBBEKE, A., HOFFMEYER, P., FRITSCHY, D., SUVA, D. & TURCOT, K. 2013. Associations between gait and clinical parameters in patients with severe knee osteoarthritis: A multiple correspondence analysis. *Clinical biomechanics,* 28**,** 299-305.

SAGAWA, Y., ARMAND, S., LUBBEKE, A., HOFFMEYER, P., FRITSCHY, D., SUVA, D. & TURCOT, K. 2013. Associations between gait and clinical parameters in patients with severe knee osteoarthritis: A multiple correspondence analysis. *Clinical Biomechanics,* 28**,** 299-305.

SAITO, T., NISHIDA, K., FURUMATSU, T., YOSHIDA, A., OZAWA, M. & OZAKI, T. 2013. Histone deacetylase inhibitors suppress mechanical stress-induced expression of RUNX-2 and ADAMTS-5 through the inhibition of the MAPK signaling pathway in cultured human chondrocytes. *Osteoarthritis and cartilage,* 21**,** 165-174.

SALAZAR-NORATTO, G., DE NIJS, N., STEVENS, H., GIBSON, G. & GULDBERG, R. 2019a. Regional gene expression analysis of multiple tissues in an experimental animal model of post-traumatic osteoarthritis. *Osteoarthritis and cartilage,* 27**,** 294-303.

SALAZAR-NORATTO, G. E., DE NIJS, N., STEVENS, H. Y., GIBSON, G. & GULDBERG, R. E. 2019b. Regional gene expression analysis of multiple tissues in an experimental animal model of post-traumatic osteoarthritis. *Osteoarthritis and Cartilage,* 27**,** 294-303.

SALAZAR-NORATTO, G. E., DE NIJS, N., STEVENS, Y., GIBSON, G. & GULDBERG, R. E. 2019c. Regional gene expression analysis of multiple tissues in an experimental animal model of post-traumatic osteoarthritis. *Osteoarthritis and Cartilage,* 27**,** 294-303.

SAMPSON, S., REED, M., SILVERS, H., MENG, M. & MANDELBAUM, B. 2010. Injection of platelet-rich plasma in patients with primary and secondary knee osteoarthritis: a pilot study. *American Journal of Physical Medicine & Rehabilitation,* 89**,** 961-969.

SANDELL, L. J. & AIGNER, T. 2001a. Articular cartilage and changes in arthritis: cell biology of osteoarthritis. *Arthritis Research & Therapy,* 3**,** 107.

SANDELL, L. J. & AIGNER, T. 2001b. Articular cartilage and changes in arthritis. An introduction: cell biology of osteoarthritis. *Arthritis Res,* 3**,** 107-13.

SANDER, K., LAYHER, F., ANDERS, C., ROTH, A., BABISCH, J., SCHOLLE, H. & KINNE, R. 2012a. Gait analysis after minimally invasive total hip arthroplasty. *Der Orthopade,* 41**,** 365-376.

SANDER, K., LAYHER, F., ANDERS, C., ROTH, A., BABISCH, J., SCHOLLE, H. C. & KINNE, R. W. 2012b. Gait analysis after minimally invasive total hip arthroplasty. *Orthopade,* 41**,** 365-+.

SANTOSO, M. B. & WU, L. 2017. Unicompartmental knee arthroplasty, is it superior to high tibial osteotomy in treating unicompartmental osteoarthritis? A meta-analysis and systemic review. *J Orthop Surg Res,* 12**,** 50.

SARAGAGLIA, D., BLAYSAT, M., INMAN, D. & MERCIER, N. 2011. Outcome of opening wedge high tibial osteotomy augmented with a Biosorb® wedge and fixed with a plate and screws in 124 patients with a mean of ten years follow-up. *International orthopaedics,* 35**,** 1151-1156.

SAXBY, D. J. & LLOYD, D. G. 2017. Osteoarthritis year in review 2016: mechanics. *Osteoarthritis and Cartilage,* 25**,** 190-198.

SCHARSTUHL, A., GLANSBEEK, H. L., VAN BEUNINGEN, H. M., VITTERS, E. L., VAN DER KRAAN, P. M. & VAN DEN BERG, W. B. 2002. Inhibition of endogenous TGF-beta during experimental osteoarthritis prevents osteophyte formation and impairs cartilage repair. *J Immunol,* 169**,** 507-14.

SCHARSTUHL, A., VITTERS, E. L., VAN DER KRAAN, P. M. & VAN DEN BERG, W. B. 2003. Reduction of osteophyte formation and synovial thickening by adenoviral overexpression of transforming growth factor β/bone morphogenetic protein inhibitors during experimental osteoarthritis. *Arthritis & Rheumatism: Official Journal of the American College of Rheumatology,* 48**,** 3442-3451.

SCHENKER, M. L., MAUCK, R. L., AHN, J. & MEHTA, S. 2014. Pathogenesis and Prevention of Posttraumatic Osteoarthritis After Intra-articular Fracture. *Journal of the American Academy of Orthopaedic Surgeons,* 22**,** 20-28.

SCHIPPLEIN, O. & ANDRIACCHI, T. 1991a. Interaction between active and passive knee stabilizers during level walking. *Journal of orthopaedic research,* 9**,** 113-119.

SCHIPPLEIN, O. D. & ANDRIACCHI, T. P. 1991b. Interaction between active and passive knee stabilizers during level walking. *J Orthop Res,* 9**,** 113-9.

SCHMITZ, N., LAVERTY, S., KRAUS, V. & AIGNER, T. 2010a. Basic methods in histopathology of joint tissues. *Osteoarthritis and cartilage,* 18**,** S113-S116.

SCHMITZ, N., LAVERTY, S., KRAUS, V. B. & AIGNER, T. 2010b. Basic methods in histopathology of joint tissues. *Osteoarthritis and Cartilage,* 18**,** S113-S116.

SERRA, C. I. & SOLER, C. 2019. Animal Models of Osteoarthritis in Small Mammals. *Vet Clin North Am Exot Anim Pract,* 22**,** 211-221.

SERRA, C. I., SOLER, C., CARRILLO, J. M., SOPENA, J. J., REDONDO, J. I. & CUGAT, R. 2014. Effect of autologous platelet-rich plasma on the repair of full-thickness articular defects in rabbits (vol 21, pg 1730, 2013). *Knee Surgery Sports Traumatology Arthroscopy,* 22**,** 1710-1710.

SHARMA, L., SONG, J., DUNLOP, D., FELSON, D., LEWIS, C. E., SEGAL, N., TORNER, J., COOKE, T. D. V., HIETPAS, J. & LYNCH, J. 2010. Varus and valgus alignment and incident and progressive knee osteoarthritis. *Annals of the rheumatic diseases,* 69**,** 1940-1945.

SHARMA, L., SONG, J., FELSON, D. T., CAHUE, S., SHAMIYEH, E. & DUNLOP, D. D. 2001. The role of knee alignment in disease progression and functional decline in knee osteoarthritis. *JAMA,* 286**,** 188-95.

SHEFELBINE, S. J., AUGAT, P., CLAES, L. & BECK, A. 2005. Intact fibula improves fracture healing in a rat tibia osteotomy model. *Journal of Orthopaedic Research,* 23**,** 489-493.

SHERMAN, B. & LEMPICKI, R. 2009. Systematic and integrative analysis of large gene lists using DAVID bioinformatics resources. *Nat Protoc,* 4**,** 44-57.

SHIN, B., KUPFERMAN, J., SCHMIDT, E., POLLEUX, F., DELANY, A. M. & LEE, S. K. 2020. Rac1 inhibition via Srgap2 restrains inflammatory osteoclastogenesis and limits the clastokine, SLIT3. *Journal of Bone and Mineral Research,* 35**,** 789-800.

SHINMEI, M., ITO, K., MATSUYAMA, S., YOSHIHARA, Y. & MATSUZAWA, K. 1993. Joint fluid carboxy-terminal type II procollagen peptide as a marker of cartilage collagen biosynthesis. *Osteoarthritis and cartilage,* 1**,** 121-128.

SHOJI, H. & INSALL, J. 1973a. High tibial osteotomy for osteoarthritis of the knee with valgus deformity. *JBJS,* 55**,** 963-973.

SHOJI, H. & INSALL, J. 1973b. High tibial osteotomy for osteoarthritis of the knee with valgus deformity. *J Bone Joint Surg Am,* 55**,** 963-73.

SINUSAS, K. 2012. Osteoarthritis: diagnosis and treatment. *American family physician,* 85**,** 49-56.

SLEMENDA, C., BRANDT, K. D., HEILMAN, D. K., MAZZUCA, S., BRAUNSTEIN, E. M., KATZ, B. P. & WOLINSKY, F. D. 1997. Quadriceps weakness and osteoarthritis of the knee. *Annals of Internal Medicine,* 127**,** 97-+.

SMITH, J., WILSON, A. & THOMAS, N. 2013a. Osteotomy around the knee: evolution, principles and results. *Knee Surgery, Sports Traumatology, Arthroscopy,* 21**,** 3-22.

SMITH, J. O., OREFFO, R. O., CLARKE, N. M. & ROACH, H. I. 2003. Changes in the antiangiogenic properties of articular cartilage in osteoarthritis. *Journal of Orthopaedic Science,* 8**,** 849-857.

SMITH, J. O., WILSON, A. J. & THOMAS, N. P. 2013b. Osteotomy around the knee: evolution, principles and results. *Knee Surg Sports Traumatol Arthrosc,* 21**,** 3-22.

SMYTH, G. K. 2004. Linear models and empirical bayes methods for assessing differential expression in microarray experiments. *Statistical applications in genetics and molecular biology,* 3.

SNIEKERS, Y. H., WEINANS, H., VAN OSCH, G. J. V. M. & VAN LEEUWEN, J. P. T. M. 2010. Oestrogen is important for maintenance of cartilage and subchondral bone in a murine model of knee osteoarthritis. *Arthritis Research & Therapy,* 12.

SOKI, F. N., YOSHIDA, R., PAGLIA, D. N., DUONG, L. T., HANSEN, M. F. & DRISSI, H. 2018. Articular cartilage protection in Ctsk-/-mice is associated with cellular and molecular changes in subchondral bone and cartilage matrix. *Journal of Cellular Physiology,* 233**,** 8666-8676.

SRIVASTAVA, S. & SRIVASTAVA, R.-G. 2005. Proteomics in the forefront of cancer biomarker discovery. *Journal of proteome research,* 4**,** 1098-1103.

STAINES, K. A., POLLARD, A. S., MCGONNELL, I. M., FARQUHARSON, C. & PITSILLIDES, A. A. 2013. Cartilage to bone transitions in health and disease. *J Endocrinol,* 219**,** R1-r12.

STAINES, K. A., POULET, B., WENTWORTH, D. N. & PITSILLIDES, A. A. 2017. The STR/ort mouse model of spontaneous osteoarthritis - an update. *Osteoarthritis and Cartilage,* 25**,** 802-808.

STEWART, R. C., BANSAL, P. N., ENTEZARI, V., LUSIC, H., NAZARIAN, R. M., SNYDER, B. D. & GRINSTAFF, M. W. 2013. Contrast-enhanced CT with a high-affinity cationic contrast agent for imaging ex vivo bovine, intact ex vivo rabbit, and in vivo rabbit cartilage. *Radiology,* 266**,** 141-50.

STOLTZ, J.-F., MAGDALOU, J., GEORGE, D., CHEN, Y., LI, Y., DE ISLA, N., HE, X. & REMOND, Y. 2018. Influence of mechanical forces on bone: introduction to mechanobiology and mechanical adaptation concept. *Journal of Cellular Immunotherapy,* 4**,** 10-12.

STRASSLE, B. W., MARK, L., LEVENTHAL, L., PIESLA, M. J., JIAN LI, X., KENNEDY, J. D., GLASSON, S. S. & WHITESIDE, G. T. 2010. Inhibition of osteoclasts prevents cartilage loss and pain in a rat model of degenerative joint disease. *Osteoarthritis and Cartilage,* 18**,** 1319-1328.

SUKUR, E., TALU, C., AKMAN, Y. E., CIRCI, E., OZTURKMEN, Y. & TUZUNER, T. 2016. Comparison of the chondroprotective effect of a novel hydrogel compound and traditional hyaluronate on rat cartilage in a papain-induced osteoarthritis model. *Acta Orthop Traumatol Turc,* 50**,** 458-63.

SURI, S. & WALSH, D. A. 2012. Osteochondral alterations in osteoarthritis. *Bone,* 51**,** 204-211.

SUZUKI, Y., IIJIMA, H., NAKAMURA, M. & AOYAMA, T. 2022. Rate of force development in the quadriceps of individuals with severe knee osteoarthritis: a preliminary cross-sectional study. *Plos one,* 17**,** e0262508.

SVALA, E., LöFGREN, M., SIHLBOM, C., RüETSCHI, U., LINDAHL, A., EKMAN, S. & SKIöLDEBRAND, E. 2015. An inflammatory equine model demonstrates dynamic changes of immune response and cartilage matrix molecule degradation in vitro. *Connective tissue research,* 56**,** 315-325.

SWAIN, S., SARMANOVA, A., MALLEN, C., KUO, C. F., COUPLAND, C., DOHERTY, M. & ZHANG, W. 2020. Trends in incidence and prevalence of osteoarthritis in the United Kingdom:

findings from the Clinical Practice Research Datalink (CPRD). *Osteoarthritis and Cartilage,* 28**,** 792-801.

SWäRD, P., KOSTOGIANNIS, I., NEUMAN, P., VON PORAT, A., BOEGåRD, T. & ROOS, H. 2010. Differences in the radiological characteristics between post-traumatic and non-traumatic knee osteoarthritis. *Scand J Med Sci Sports,* 20**,** 731-9.

SYLVEN, B. 1954. Metachromatic dye-substrate interactions. *Journal of Cell Science,* 3**,** 327-358.

SZYMAńSKA, E., SACCENTI, E., SMILDE, A. K. & WESTERHUIS, J. A. 2012. Double-check: validation of diagnostic statistics for PLS-DA models in metabolomics studies. *Metabolomics,* 8**,** 3-16.

TAKEUCHI, R., UMEMOTO, Y., ARATAKE, M., BITO, H., SAITO, I., KUMAGAI, K., SASAKI, Y., AKAMATSU, Y., ISHIKAWA, H. & KOSHINO, T. 2010. A mid term comparison of open wedge high tibial osteotomy vs unicompartmental knee arthroplasty for medial compartment osteoarthritis of the knee. *Journal of Orthopaedic Surgery and Research,* 5**,** 65.

TAMAMURA, Y., OTANI, T., KANATANI, N., KOYAMA, E., KITAGAKI, J., KOMORI, T., YAMADA, Y., COSTANTINI, F., WAKISAKA, S. & PACIFICI, M. 2005. Developmental regulation of Wnt/β-catenin signals is required for growth plate assembly, cartilage integrity, and endochondral ossification. *Journal of Biological Chemistry,* 280**,** 19185-19195.

TANAMAS, S., HANNA, F. S., CICUTTINI, F. M., WLUKA, A. E., BERRY, P. & URQUHART, D. M. 2009. Does knee malalignment increase the risk of development and progression of knee osteoarthritis? A systematic review. *Arthritis Rheum,* 61**,** 459-67.

TARDIF, G., HUM, D., PELLETIER, J. P., BOILEAU, C., RANGER, P. & MARTEL‐PELLETIER, J. 2004. Differential gene expression and regulation of the bone morphogenetic protein antagonists follistatin and gremlin in normal and osteoarthritic human chondrocytes and synovial fibroblasts. *Arthritis & Rheumatism: Official Journal of the American College of Rheumatology,* 50**,** 2521-2530.

TEEPLE, E., JAY, G. D., ELSAID, K. A. & FLEMING, B. C. 2013. Animal models of osteoarthritis: challenges of model selection and analysis. *AAPS J,* 15**,** 438-46.

TEMP, J., LABUZ, D., NEGRETE, R., SUNKARA, V. & MACHELSKA, H. 2020a. Pain and knee damage in male and female mice in the medial meniscal transection-induced osteoarthritis. *Osteoarthritis Cartilage,* 28**,** 475-485.

TEMP, J., LABUZ, D., NEGRETE, R., SUNKARA, V. & MACHELSKA, H. 2020b. Pain and knee damage in male and female mice in the medial meniscal transection-induced osteoarthritis. *Osteoarthritis and Cartilage,* 28**,** 475-485.

TETSWORTH, K. & PALEY, D. 1994. Malalignment and degenerative arthropathy. *Orthop Clin North Am,* 25**,** 367-77.

THELIN, N., HOLMBERG, S. & THELIN, A. 2006. Knee injuries account for the sports-related increased risk of knee osteoarthritis. *Scandinavian Journal of Medicine & Science in Sports,* 16**,** 329-333.

THOMAS, A. C., HUBBARD-TURNER, T., WIKSTROM, E. A. & PALMIERI-SMITH, R. M. 2017. Epidemiology of Posttraumatic Osteoarthritis. *J Athl Train,* 52**,** 491-496.

THOMAS, C. M., FULLER, C. J., WHITTLES, C. E. & SHARIF, M. 2007. Chondrocyte death by apoptosis is associated with cartilage matrix degradation. *Osteoarthritis and Cartilage,* 15**,** 27-34.

TOWNSEND, K. L., AN, D., LYNES, M. D., HUANG, T. L., ZHANG, H., GOODYEAR, L. J. & TSENG, Y.-H. 2013. Increased mitochondrial activity in BMP7-treated brown adipocytes, due to increased CPT1-and CD36-mediated fatty acid uptake. *Antioxidants & redox signaling,* 19**,** 243-257.

TVEIT, M., ROSENGREN, B. E., NILSSON, J. A. & KARLSSON, M. K. 2012. Former Male Elite Athletes Have a Higher Prevalence of Osteoarthritis and Arthroplasty in the Hip and Knee Than Expected. *American Journal of Sports Medicine,* 40**,** 527-533.

UNGER, M. D., MURTHY, N. S., KANWAR, R., STRAND, K. A., MAUS, T. P. & BEUTLER, A. S. 2018. Clinical magnetic resonance-enabled characterization of mono-iodoacetate-induced osteoarthritis in a large animal species. *Plos One,* 13.

VAN DEN AKKER, G. G. H., CARON, M. M. J., PEFFERS, M. J. & WELTING, T. J. M. 2022. Ribosome dysfunction in osteoarthritis. *Current Opinion in Rheumatology,* 34**,** 61-67.

VAN DER KRAAN, P. M. & VAN DEN BERG, W. B. 2007. Osteophytes: relevance and biology. *Osteoarthritis and cartilage,* 15**,** 237-244.

VAN ROON, J. A. & LAFEBER, F. P. 2008. Role of interleukin-7 in degenerative and inflammatory joint diseases. *Arthritis Res Ther,* 10**,** 107.

VAN TUNEN, J. A., DELL'ISOLA, A., JUHL, C., DEKKER, J., STEULTJENS, M. & LUND, H. 2016. Biomechanical factors associated with the development of tibiofemoral knee osteoarthritis: protocol for a systematic review and meta-analysis. *BMJ Open,* 6**,** e011066.

VAN TUNEN, J. A. C., DELL'ISOLA, A., JUHL, C., DEKKER, J., STEULTJENS, M., THORLUND, J. B. & LUND, H. 2018. Association of malalignment, muscular dysfunction, proprioception, laxity and abnormal joint loading with tibiofemoral knee osteoarthritis - a systematic review and meta-analysis. *Bmc Musculoskeletal Disorders,* 19.

VAN ZEE, K. J., KOHNO, T., FISCHER, E., ROCK, C. S., MOLDAWER, L. L. & LOWRY, S. F. 1992. Tumor necrosis factor soluble receptors circulate during experimental and clinical inflammation and can protect against excessive tumor necrosis factor alpha in vitro and in vivo. *Proceedings of the National Academy of Sciences,* 89**,** 4845-4849.

VEDI, V. & WOODELL-MAY, J. 2020. Prospective post market data collection on patients with knee osteoarthrtis treated with autologous protein solution (APS)(progress III study). *Osteoarthritis and Cartilage,* 28**,** S156.

VENTURI, G. & MONTANARO, L. 2020. How altered ribosome production can cause or contribute to human disease: the spectrum of ribosomopathies. *Cells,* 9**,** 2300.

VERDELIS, K., LUKASHOVA, L., ATTI, E., MAYER-KUCKUK, P., PETERSON, M. G. E., TETRADIS, S., BOSKEY, A. L. & VAN DER MEULEN, M. C. H. 2011. MicroCT morphometry analysis of mouse cancellous bone: Intra- and inter-system reproducibility. *Bone,* 49**,** 580-587.

VERSUS ARTHRITIS 2019. The state of musculoskeletal health 2019. Chesterfield, UK: Arthritis Care and Arthritis Research UK.

VERZIJL, N., DEGROOT, J., THORPE, S. R., BANK, R. A., SHAW, J. N., LYONS, T. J., BIJLSMA, J. W., LAFEBER, F. P., BAYNES, J. W. & TEKOPPELE, J. M. 2000. Effect of collagen turnover on the accumulation of advanced glycation end products. *J Biol Chem,* 275**,** 39027-31.

VILENSKY, J. A., O'CONNOR, B. L., BRANDT, K. D., DUNN, E. A., ROGERS, P. I. & DELONG, C. A. 1994. Serial kinematic analysis of the unstable knee after transection of the anterior cruciate ligament: temporal and angular changes in a canine model of osteoarthritis. *J Orthop Res,* 12**,** 229-37.

VINA, E. R. & KWOH, C. K. 2018a. Epidemiology of osteoarthritis: literature update. *Current opinion in rheumatology,* 30**,** 160-167.

VINA, E. R. & KWOH, C. K. 2018b. Epidemiology of osteoarthritis: literature update. *Curr Opin Rheumatol,* 30**,** 160-167.

VINCOURT, J.-B., LIONNETON, F., KRATASSIOUK, G., GUILLEMIN, F., NETTER, P., MAINARD, D. & MAGDALOU, J. 2006. Establishment of a reliable method for direct proteome characterization of human articular cartilage. *Molecular & Cellular Proteomics,* 5**,** 1984-1995.

VRINTEN, D. H. & HAMERS, F. F. 2003a. 'CatWalk'automated quantitative gait analysis as a novel method to assess mechanical allodynia in the rat; a comparison with von Frey testing. *Pain,* 102**,** 203-209.

VRINTEN, D. H. & HAMERS, F. F. T. 2003b. 'CatWalk' automated quantitative gait analysis as a novel method to assess mechanical allodynia in the rat; a comparison with von Frey testing. *Pain,* 102**,** 203-209.

WALLACE, I. J., WORTHINGTON, S., FELSON, D. T., JURMAIN, R. D., WREN, K. T., MAIJANEN, H., WOODS, R. J. & LIEBERMAN, D. E. 2017. Knee osteoarthritis has doubled in prevalence since the mid-20th century. *Proc Natl Acad Sci U S A,* 114**,** 9332-9336.

WALSH, D. A., BONNET, C., TURNER, E., WILSON, D., SITU, M. & MCWILLIAMS, D. 2007. Angiogenesis in the synovium and at the osteochondral junction in osteoarthritis. *Osteoarthritis and cartilage,* 15**,** 743-751.

WALSH, D. A., MCWILLIAMS, D. F., TURLEY, M. J., DIXON, M. R., FRANSèS, R. E., MAPP, P. I. & WILSON, D. 2010. Angiogenesis and nerve growth factor at the osteochondral junction in rheumatoid arthritis and osteoarthritis. *Rheumatology (Oxford),* 49**,** 1852-61.

WALSH, M. C. & CHOI, Y. 2014. Biology of the RANKL–RANK–OPG system in immunity, bone, and beyond. *Frontiers in immunology,* 5**,** 511.

WANG, B., LIU, Q., WISE, B. L., KE, Y., XING, D., XU, Y., ZHANG, Y. & LIN, J. 2018a. Valgus malalignment and prevalence of lateral compartmental radiographic knee osteoarthritis (OA): The Wuchuan OA study. *International journal of rheumatic diseases,* 21**,** 1385-1390.

WANG, C., GUO, K., GAO, D., KANG, X., JIANG, K., LI, Y., SUN, L., ZHANG, S., SUN, C., LIU, X., WU, W., YANG, P. & LIU, Y. 2011. Identification of transaldolase as a novel serum biomarker for hepatocellular carcinoma metastasis using xenografted mouse model and clinic samples. *Cancer Lett,* 313**,** 154-66.

WANG, G. & BEIER, F. 2005. Rac1/Cdc42 and RhoA GTPases antagonistically regulate chondrocyte proliferation, hypertrophy, and apoptosis. *Journal of Bone and Mineral Research,* 20**,** 1022-1031.

WANG, N., BADAR, F. & XIA, Y. 2018b. Compressed sensing in quantitative determination of GAG concentration in cartilage by microscopic MRI. *Magn Reson Med,* 79**,** 3163-3171.

WANG, N., BADAR, F. & XIA, Y. 2018c. Compressed sensing in quantitative determination of GAG concentration in cartilage by microscopic MRI. *Magnetic resonance in medicine,* 79**,** 3163-3171.

WANG, W., YE, R., XIE, W., ZHANG, Y., AN, S., LI, Y. & ZHOU, Y. 2022. Roles of the calcified cartilage layer and its tissue engineering reconstruction in osteoarthritis treatment. *Frontiers in Bioengineering and Biotechnology,* 10.

WANG, Y., ZHANG, K., ZENG, J. & YAN, S. 2021. Coordination of lower limbs in patients with knee osteoarthritis during walking. *Gait Posture,* 83**,** 160-166.

WANSTRATH, A. W., HETTLICH, B. F., SU, L., SMITH, A., ZEKAS, L. J., ALLEN, M. J. & BERTONE, A. L. 2016. Evaluation of a Single Intra-Articular Injection of Autologous Protein Solution for Treatment of Osteoarthritis in a Canine Population. *Vet Surg,* 45**,** 764-74.

WEI, J., SHIMAZU, J., MAKINISTOGLU, M. P., MAURIZI, A., KAJIMURA, D., ZONG, H., TAKARADA, T., IEZAKI, T., PESSIN, J. E. & HINOI, E. 2015. Glucose uptake and Runx2 synergize to orchestrate osteoblast differentiation and bone formation. *Cell,* 161**,** 1576-1591.

WEI, L., DE BRI, E., LUNDBERG, A. & SVENSSON, O. 1998a. Mechanical load and primary guinea pig osteoarthrosis. *Acta Orthopaedica Scandinavica,* 69**,** 351-357.

WEI, L., DE BRI, E., LUNDBERG, A. & SVENSSON, O. 1998b. Mechanical load and primary guinea pig osteoarthrosis. *Acta Orthop Scand,* 69**,** 351-7.

WEI, L., FLEMING, B. C., SUN, X. J., TEEPLE, E., WU, W., JAY, G. D., ELSAID, K. A., LUO, J. M., MACHAN, J. T. & CHEN, Q. A. 2010. Comparison of Differential Biomarkers of Osteoarthritis with and without Posttraumatic Injury in the Hartley Guinea Pig Model. *Journal of Orthopaedic Research,* 28**,** 900-906.

WEI, Y. & BAI, L. 2016. Recent advances in the understanding of molecular mechanisms of cartilage degeneration, synovitis and subchondral bone changes in osteoarthritis. *Connective tissue research,* 57**,** 245-261.

WENDLER, A. & WEHLING, M. 2010. The translatability of animal models for clinical development: biomarkers and disease models. *Curr Opin Pharmacol,* 10**,** 601-6.

WHITTLE, M. W. 1993. Gait analysis. *The soft tissues.* Elsevier.

WHITTLE, M. W. 2014. *Gait analysis: an introduction,* Oxford, UK, Butterworth-Heinemann.

WILSON, R., NORRIS, E. L., BRACHVOGEL, B., ANGELUCCI, C., ZIVKOVIC, S., GORDON, L., BERNARDO, B. C., STERMANN, J., SEKIGUCHI, K. & GORMAN, J. J. 2012. Changes in the chondrocyte and extracellular matrix proteome during post-natal mouse cartilage development. *Molecular & Cellular Proteomics,* 11.

WOLF, A., DEDMAN, D., CAMPBELL, J., BOOTH, H., LUNN, D., CHAPMAN, J. & MYLES, P. 2019. Data resource profile: Clinical Practice Research Datalink (CPRD) Aurum. *International Journal of Epidemiology,* 48**,** 1740-1740g.

WOODELL-MAY, J., MATUSKA, A., OYSTER, M., WELCH, Z., O'SHAUGHNESSEY, K. & HOEPPNER, J. 2011. Autologous protein solution inhibits MMP-13 production by IL-1β and TNFα-stimulated human articular chondrocytes. *Journal of Orthopaedic Research,* 29**,** 1320-1326.

WOODS, A., WANG, G. & BEIER, F. 2005. RhoA/ROCK signaling regulates Sox9 expression and actin organization during chondrogenesis. *Journal of Biological Chemistry,* 280**,** 11626-11634.

WOODS, A., WANG, G., DUPUIS, H., SHAO, Z. & BEIER, F. 2007. Rac1 signaling stimulates N-cadherin expression, mesenchymal condensation, and chondrogenesis. *Journal of Biological Chemistry,* 282**,** 23500-23508.

WU, J., LIU, W., BEMIS, A., WANG, E., QIU, Y., MORRIS, E. A., FLANNERY, C. R. & YANG, Z. 2007. Comparative proteomic characterization of articular cartilage tissue from normal donors and patients with osteoarthritis. *Arthritis & Rheumatism: Official Journal of the American College of Rheumatology,* 56**,** 3675-3684.

WYSOCKI, V. H., RESING, K. A., ZHANG, Q. & CHENG, G. 2005. Mass spectrometry of peptides and proteins. *Methods,* 35**,** 211-222.

XU, X., LI, X., LIANG, Y., OU, Y., HUANG, J., XIONG, J., DUAN, L. & WANG, D. 2019. Estrogen Modulates Cartilage and Subchondral Bone Remodeling in an Ovariectomized Rat Model of Postmenopausal Osteoarthritis. *Med Sci Monit,* 25**,** 3146-3153.

XU, Z., CHEN, T., LUO, J., DING, S., GAO, S. & ZHANG, J. 2017. Cartilaginous Metabolomic Study Reveals Potential Mechanisms of Osteophyte Formation in Osteoarthritis. *Journal of Proteome Research,* 16**,** 1425-1435.

YAKHDANI, H. R. F., BAFGHI, H. A., MEIJER, O. G., BRUIJN, S. M., VAN DEN DIKKENBERG, N., STIBBE, A. B., VAN ROYEN, B. J. & VAN DIEEN, J. H. 2010. Stability and variability of knee kinematics during gait in knee osteoarthritis before and after replacement surgery. *Clinical Biomechanics,* 25**,** 230-236.

YANG, J., UEHARU, H. & MISHINA, Y. 2020. Energy metabolism: A newly emerging target of BMP signaling in bone homeostasis. *Bone,* 138**,** 115467.

YING, Y., QI, X. & ZHAO, G.-Q. 2001. Induction of primordial germ cells from murine epiblasts by synergistic action of BMP4 and BMP8B signaling pathways. *Proceedings of the National Academy of Sciences,* 98**,** 7858-7862.

YUASA, T., OTANI, T., KOIKE, T., IWAMOTO, M. & ENOMOTO-IWAMOTO, M. 2008. Wnt/β-catenin signaling stimulates matrix catabolic genes and activity in articular chondrocytes: its possible role in joint degeneration. *Laboratory investigation,* 88**,** 264-274.

ZANJANI-POUR, S., GIORGI, M. & DALL'ARA, E. 2020a. Development of Subject Specific Finite Element Models of the Mouse Knee Joint for Preclinical Applications. *Front Bioeng Biotechnol,* 8**,** 558815.

ZANJANI-POUR, S., GIORGI, M. & DALL'ARA, E. 2020b. Development of subject specific finite element models of the mouse knee joint for preclinical applications. *Frontiers in bioengineering and biotechnology,* 8**,** 558815.

ZENG, X. L., MA, L. M., LIN, Z. F., HUANG, W. H., HUANG, Z. Q., ZHANG, Y. & MAO, C. B. 2017. Relationship between Kellgren-Lawrence score and 3D kinematic gait analysis of patients with medial knee osteoarthritis using a new gait system. *Scientific Reports,* 7.

ZERWEKH, J. E., RUML, L. A., GOTTSCHALK, F. & PAK, C. Y. 1998. The effects of twelve weeks of bed rest on bone histology, biochemical markers of bone turnover, and calcium homeostasis in eleven normal subjects. *Journal of Bone and Mineral Research,* 13**,** 1594-1601.

ZHANG, Y., FONSLOW, B. R., SHAN, B., BAEK, M.-C. & YATES III, J. R. 2013. Protein analysis by shotgun/bottom-up proteomics. *Chemical reviews,* 113**,** 2343-2394.

ZHANG, Y., PIZZUTE, T. & PEI, M. 2014. Anti-inflammatory strategies in cartilage repair. *Tissue Engineering Part B: Reviews,* 20**,** 655-668.

ZHANG, Z., ZHOU, S., JIANG, X., WANG, Y.-H., LI, F., WANG, Y.-G., ZHENG, Y. & CAI, L. 2015. The role of the Nrf2/Keap1 pathway in obesity and metabolic syndrome. *Reviews in Endocrine and Metabolic Disorders,* 16**,** 35-45.

ZHOU, Y., ZHOU, B., PACHE, L., CHANG, M., KHODABAKHSHI, A. H., TANASEICHUK, O., BENNER, C. & CHANDA, S. K. 2019. Metascape provides a biologist-oriented resource for the analysis of systems-level datasets. *Nat Commun,* 10**,** 1523.

ZHU, S., LIU, H., WU, Y., HENG, B. C., CHEN, P., LIU, H. & OUYANG, H. W. 2013. Wnt and Rho GTPase signaling in osteoarthritis development and intervention: implications for diagnosis and therapy. *Arthritis Res Ther,* 15**,** 217.

ZHU, X., CHAN, Y. T., YUNG, P. S., TUAN, R. S. & JIANG, Y. 2021. Subchondral bone remodeling: a therapeutic target for osteoarthritis. *Frontiers in cell and developmental biology,* 8**,** 607764.

ZOCH, M. L., ABOU, D. S., CLEMENS, T. L., THOREK, D. L. & RIDDLE, R. C. 2016. In vivo radiometric analysis of glucose uptake and distribution in mouse bone. *Bone research,* 4**,** 1-8.